A computer controlled quenching simulator for observing phase transformation kinetics in metals by electrical resistance measurements

Mark A. Todd

A thesis submitted in partial fulfilment of the requirements for the degree of

Doctor of Philosophy

The University of Sheffield

Faculty of Engineering

Department of Materials Science and Engineering

March 2018

Abstract

The commonly used method of dilatometry to study the martensitic transformation leads to inaccuracies in the measured transformation temperatures and kinetics due to temperature gradients within the sample. Samples studied using commercial dilatometers are often of insufficient size to allow mechanical testing.

This thesis details work to design and construct an instrument that overcomes the limitations of commercial dilatometers for the study of the martensitic phase transformation in steel.

An introduction to why the study of the martensitic phase transformation is important to the new generation of automotive press hardened steels is presented. A review of the techniques that have been used in the literature to study the martensitic transformation kinetics including metallography, dilatometry, resistivity, thermal, acoustic emission, X-ray, and neutron diffraction follows.

A case is then presented as to why electrical resistivity measurements may be the best technique for the small scale metallurgical laboratory. Details of the construction of a machine that uses phase angle control of a 2000 A alternating current for the Joule (resistance) heating of samples suitable for thin sheet tensile testing are presented. The heating system of this machine has a predicted maximum heating rate of 50°C/s for 2 mm thick steel. The constructed machine is able to perform the heat treatments either in vacuum or an inert atmosphere, and uses argon quenching to achieve a cooling rate in excess of 40°C/s for a 2 mm thick sample. The heat treatment is fully computer controlled.

The results show that the phase transformations in pure cobalt, pure titanium, and a eutectoid steel are clearly observable using electrical resistance measurements. The effect of the transformation kinetics on the measured transformation temperatures is summarized. A detailed analysis of the effect of the common mode electrical noise of the small measurement

voltage is presented, along with suggestions about how to improve the accuracy of such measurements.

Acknowledgements

I would like to thank my supervisor, Professor Mark Rainforth, for his enduring guidance, knowledge of all things steel, and his faith that despite the many problems the machine would one day live.

I am grateful to the many technicians in the Faculty of Engineering who have contributed to this project. I would like to thank all of the foundry technicians: Kyle Arnold, Dean Haylock, Neil Hind, Lisa Hollands, and Ian Watts, for assistance with the many unusual demands of this project. I am grateful to Paul Hawksworth and John Lowndes for assistance with the vacuum system, to Paul Bentley for his guidance with the many electrical problems, and to Wayne Frankish for his expert views on the mechanical design. I would like to thank Ben Palmer for performing the DTA analysis that is included in chapter 5. I would especially like to thank Frank Fletcher for sharing with me some of his vast experience and knowledge of practical electronics, wiring the modules to the highest possible standard, invaluable assistance with fault finding, and general moral support through the many challenges.

I would like to thank Professor Iain Todd for his understanding during the writing of this thesis.

I am grateful to the Advanced Metallic Systems Centre for Doctoral Training, the Engineering and Physical Science Research Council, and ArcelorMittal for financially supporting this project.

Above all I would like to thank my family for their support and encouragement in all things. I am indebted to my wife Eunju for her support throughout the PhD, and especially during the writing of this thesis. I am grateful to my daughter Seraphina, for her beautiful smile and personality that always improve everything; she was a wonderful distraction when writing.

Abbreviations

AAF	Anti-aliasing filter.
AC	Alternating current.
ADC	Analogue to digital converter.
ALM	Additive layer manufacture.
API	Application programming interface.
BJT	Bipolar junction transistor.
BSPP	British Standard pipe parallel (thread).
BSPT	British Standard pipe tapered (thread).
CAD	Computer aided design.
CAN	Controller area network.
CFD	Computational fluid dynamics.
CMOS	Complementary metal-oxide semiconductor.
CMRR	Common mode rejection ratio.
CPU	Central processing unit.
CSA	Cross sectional area.
DAC	Digital to analogue converter.
DAQ	Data acquisition (system).
DC	Direct current.
EBSD	Electron back-scatter diffraction.
EDM	Electro-discharge machining.
FEM	Finite element method.
IL	Intermediate language.
LCD	Liquid crystal display.
LED	Light emitting diode.
MOSFET	Metal-oxide semiconductor field effect transistor.
MOV	Metal-oxide varistor.
PC	Personal computer.
PCB	Printed circuit board.
PLC	Programmable logic controller.
PTFE	Polytetrafluoroethylene.
PVC	Polyvinyl chloride.
PWM	Pulse width modulation.
QSCP	Quenching Simulator Control Panel software.
RCD	Residual current device.

RTD	Resistance temperature detector.
SEM	Scanning electron microscope.
SMPS	Switched mode power supply.
SR	Set-reset.
TEM	Transmission electron microscope.
TMP	Turbo molecular pump.
TRIAC	A three terminal AC switch. Like a bidirectional thyristor.
TVS	Transient voltage suppressor.
USB	Universal serial bus.
VAC	Alternating current (RMS) voltage.
VDC	Direct current voltage.
XLPE	Cross-linked polyethylene.
XRD	X-ray diffraction.

Contents

1 Introduction

This project started as an investigation into steel alloys for press hardening. It developed into its current form in response to the perceived inadequacies of available methods for studying the kinetics of the martensitic phase transformation.

When the historic use of electrical resistivity measurements was read about, the question I asked was *how difficult can it really be to measure resistance?* Well, the answer it turns-out, is a lot more difficult, and a lot more expensive than one might imagine!

Measuring the resistance of something sat on a bench in a lab is not that difficult. A hand held multimeter can be bought for a few pounds that will measure resistance above an ohm. Even measuring the micro-ohm resistances of a piece of metal can be achieved with an off-the-shelf micro-ohmmeter for relatively little money. However, that off-the-shelf unit will take measurements very slowly, and will soon start to fail in the presence of even small amounts of electromagnetic interference.

Much of the complexity of this project has not been on measuring the phase transformations using resistance measurements, but has been all the engineering necessary to get to that point. The cost and time implications of deciding that the experiments should take place in a vacuum chamber cannot be underestimated. The time taken to design the vacuum chamber, find a suitable manufacturer, receive the chamber, and assemble the system was the best part of a year. The difficulty of moving signals, gas, coolant, and especially a 2000 A electrical current into the chamber added considerable challenges.

The approach of splitting the control system into a series of modules has delivered a system that is effective and easily expandable. However, the time taken to design and prototype the circuit, produce the PCB artwork, program the firmware, have the PCB manufactured, assemble the

PCB, wire the enclosure, test and rectify any faults took more than six months for each control module.

The Quenching Simulator Control Panel has been designed to enable the user to operate the machine in a simple manner, but the complicated code required to make a simple user experience is about 8000 lines long.

This thesis will initially explore some of the different methods for measuring the martensitic transformation in chapter two. Chapter three will detail the construction of the machine, and explain why problems were tackled in a certain way. The fourth chapter will detail the calibration procedures that were performed to increase the accuracy of the results. Chapter five will give details of the machine performance, and the sixth chapter will discuss some of the issues that have arisen from this project.

My hope is that the engineering detail presented in this thesis will enable someone else to attempt a similar task much more expeditiously.

2 Literature review

2.1 Advanced high strength automotive steels

Recent years have seen increasing use of advanced high strength steels (AHSS) in automotive structures. The main reasons for the increased use of AHSS are summarized by Kuziak et al. [1] as being: 1) improved fuel efficiency from reduced vehicle weight; 2) improved passenger safety; and 3) the competition to steel from light-weight materials such as aluminium and plastics. In addition to high strength, the other main requirement for an AHSS to be used for an automotive structural component is sufficient press formability [2] of the material to allow the manufacture of complex geometries without problems such as cracking or spring-back. A variety of different AHSS have been developed that combine both high strength and good formability, these include DP (Dual Phase), CP (Complex Phase), TRIP (Transformation Induced Plasticity), TWIP (Twinning Induced Plasticity) and PH (Press Hardened, also referred to as Hot Stamped).

DP steels consist of a ferrite matrix with between 10 to 40wt% of martensite, martensite-austenite or bainite. The strength and ductility are primarily controlled by the size and distribution of the second phase particles, with both the strength and ductility of the steels increasing with decreasing particle size [1].

Similar to DP steels, CP steels contain particles of a phase different to that of the matrix. CP steels contain a greater fraction of second phase than DP steels and may have a bainitic matrix for increased strength [1].

TRIP steels, as delivered to the press, contain 50 – 55wt% ferrite, 30 – 35wt% bainite, 7 – 15wt% retained austenite and less than 5% martensite. TRIP steels contain retained austenite with M_s (the start temperature of the martensitic transformation) below the pressing temperature, but M_d (the highest temperature that the martensitic transformation can be made to start due to deformation of the steel) above the pressing temperature. The retained austenite improves the ductility of the steel during the pressing operation, but the deformation that occurs during the pressing operation causes the retained austenite to transform to martensite, leaving a hardened component in the finished shape [1].

Increased press formability is achieved in TWIP steels by the use of a fully austenitic microstructure that can deform by twinning during the pressing operation enabling greater plastic deformation before damage (improved ductility). The formation of twins during pressing increases the strength of the steel as the twins interfere with subsequent dislocation movement [3].

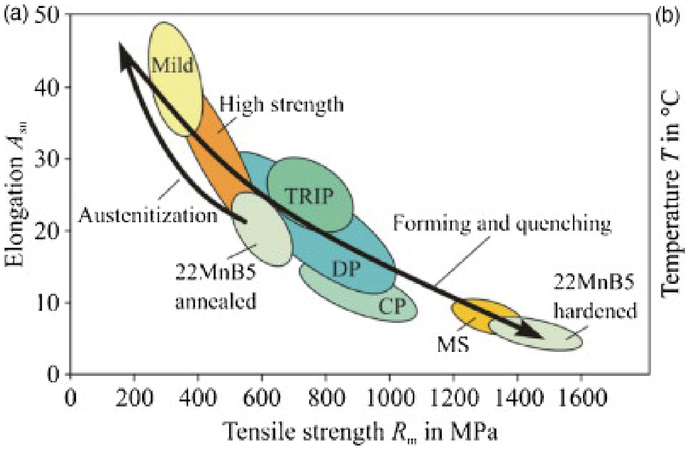

Figure 2.1 - Mechanical properties of some common automotive structural steels. Figure reproduced with permission from Karbasian and Tekkaya [4].

Press hardened steels were originally developed in the late 1970's for the production of saw blades and lawnmower blades, but have found increasing use in automotive structural components such as B-pillar and door reinforcement bars, which has seen their use rise from approximately 3 million parts / year in 1987 to approximately 107 million parts / year in 2007 [4]. The currently popular press hardened 22MnB5 steels, such as Usibor 1500, contain approximately 0.23wt% C, 1.18wt% Mn, 0.002wt% B [4] and are delivered to the automotive manufacturer with a mixed ferrite – pearlite microstructure. In the direct press hardening process the automotive manufacturer will fully austenitize the blank, before simultaneous forming and quenching in the die. As can be seen from Figure 2.1, austenitization of the blank will increase the ductility (and hence formability) of the blank, whereas the quenching will lead to a martensitic microstructure with considerably higher strength than in the as delivered state. The indirect press hardening procedure is broadly similar to the direct route, but prior to austenitization the blank is pre-formed at room temperature close to the required shape, before being die quenched. Both the direct and indirect press hardening process routes allow the manufacture of complex shapes in a material with a UTS of up to 1500 MPa [4], that would not otherwise be amenable to such complex pressing due to poor formability.

2.2 *The martensitic transformation in steels*

Martensite is formed by first heating steel to a temperature at which the crystal structure has transformed to face centred cubic (austenite). The austenitized steel is then quickly cooled (quenched), and rapidly changes crystal structure by a diffusionless transformation to a body centred tetragonal crystal structure (martensite). It can be seen from Figure 2.2 that the austenite must be quenched rapidly to avoid any diffusional transformation products and ensure a fully martensitic microstructure.

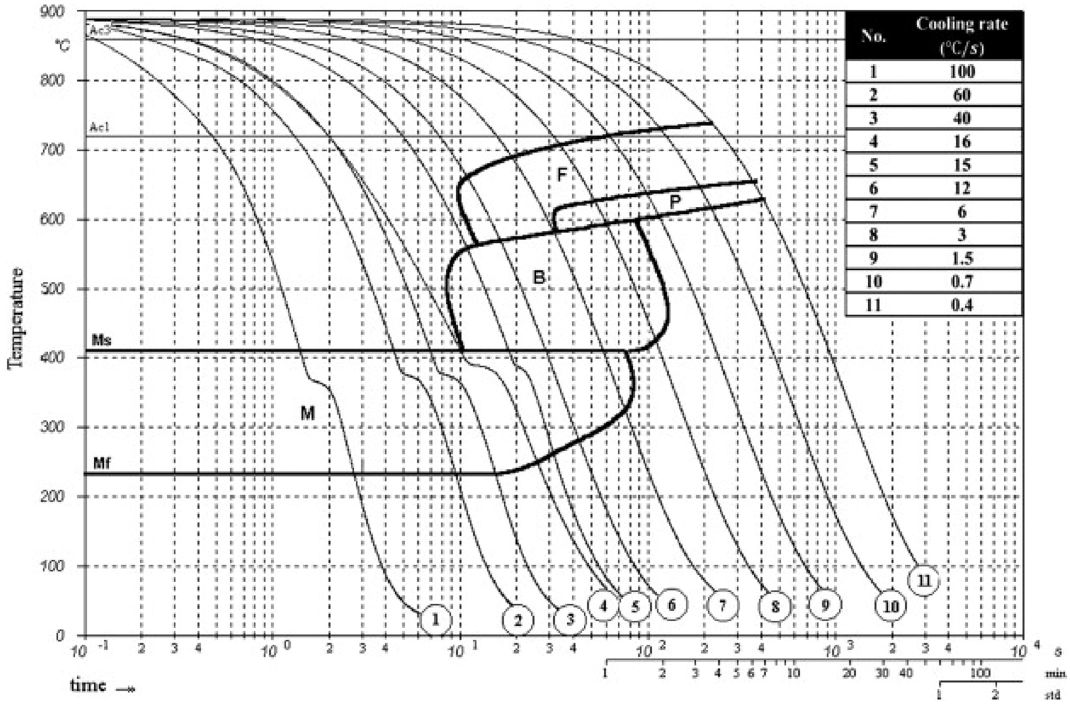

No.	Cooling rate (°C/s)
1	100
2	60
3	40
4	16
5	15
6	12
7	6
8	3
9	1.5
10	0.7
11	0.4

Figure 2.2 – The continuous cooling transformation (CCT) diagram for a 22MnB5 steel. The diagram includes martensite (M), bainite (B), ferrite (F), perlite (P), and austenite (unlabelled) phase regions. Figure reproduced with permission from Nikravesh [5].

As the martensitic transformation is diffusionless, the transformation can occur at very low temperatures, for example Kaufman and Cohen [6] report that an iron-nickel alloy containing 31.9wt% nickel has a transformation start temperature of just 50 K. Bunshah and Mehl [7] found that the martensitic transformation proceeds very rapidly, with individual plates growing at about one-third the speed of sound. This rapid transformation progress means that the carbon atoms that can be accommodated interstitially in the high temperature austenite do not have time to diffuse out of the iron crystals and become trapped. As the body centred cubic crystal structure of iron is unable to accommodate carbon items interstitially, the distortion caused by the trapped carbon atoms in the martensite leads to the crystal lattice becoming body centred tetragonal.

Bain [8] explained that the face centred cubic crystal structure of austenite can also be described using the body centred tetragonal Bravais lattice (see Figure 2.3). The resultant body centred tetragonal structure can be made to match the dimensions of the martensite unit cell by shortening the height and stretching the base; this strain that converts the face centre cubic austenite to the body centred cubic / tetragonal martensite is referred to as the Bain strain.

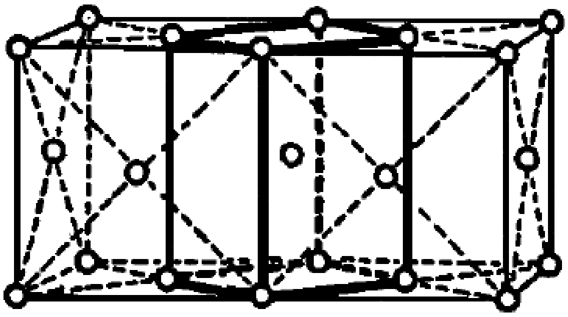

Figure 2.3 – The face centred cubic crystal of austenite can also be described using the body centred tetragonal Bravais lattice. Figure reproduced from Bain [8].

Kurdjumow and Sachs [9] found that there is a specific orientation relationship between the parent austenite and the martensite crystal structures. The orientation relationship is specified as a plane in the austenite lattice that is parallel to a plane in the martensite lattice: $\{111\}_\gamma || \{011\}_{\alpha'}$; and a pair of directions in the two lattices that are also parallel:

$<011>_{\gamma}||<111>_{\alpha'}$. Although the homogeneous Bain strain is able to explain the change in Bravais lattice, it does not account for the orientation relationship. As explained by Bowles and Barrett [10], Kurdjumow and Sachs went on to suggest an alternative to the Bain strain which is a shear of $(111)_{\gamma}$ $[\bar{1}\bar{1}2]_{\gamma}$ to produce a body centred tetragonal lattice, followed by a shear of $(1\bar{1}2)_{\alpha'}$ $[\bar{1}11]_{\alpha'}$ to produce the final body centred cubic / tetragonal lattice (see Figure 2.4). The shears proposed by Kurdjumow and Sachs account for the orientation-relationship and lead to approximately the correct martensite lattice.

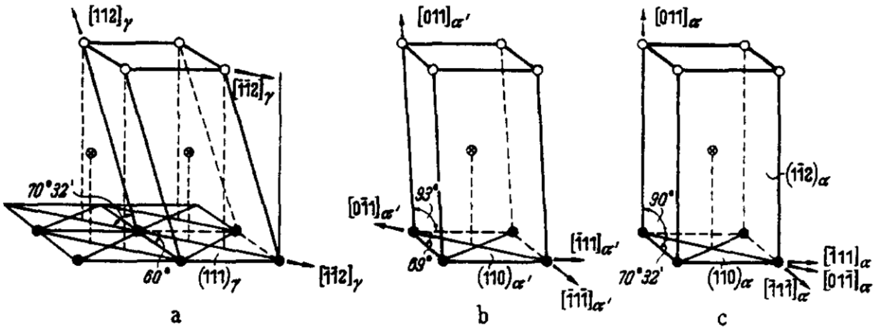

Figure 2.4 – The shears proposed by Kurdjumow and Sachs to explain the transformation from austenite to martensite. Figure (a) shows the face centred cubic austenite, (b) shows the tetragonal martensite, and (c) is the body centred cubic ferrite. Figure reproduced with permission from Bowles and Barrett [10].

Greninger and Troiano [11] investigated the austenite plane on which martensite formed (referred to as the habit plane) for four steels containing between 0.35 and 1.78wt% carbon. They found that only the habit plane of the low carbon steel was approximately $\{111\}_{\gamma}$, which meant that the initial shear on the $\{111\}_{\gamma}$ plane proposed by Kurdjumow and Sachs was not able to explain the habit plane in the other alloys. By studying the tilting of a martensite crystals at the surface of polished samples, Greninger and Troiano [12] went on to suggest that the transformation could be explained by an initial shear on the habit plane to account for the shape change, followed by second shear on the (112) plane in the $[11\bar{1}]$ direction to convert the triclinic lattice to a body centred tetragonal lattice. They found that these two shears could account for the orientation relationship and habit planes, but that an additional expansion was needed to account for the change in lattice parameters from the austenite to martensite.

Bowles and MacKenzie [13] developed a complex phenomenological theory to relate the final martensite structure to the parent austenite using vector algebra. In Bowles and MacKenzie's theory the martensitic transformation can be described as an initial homogeneous strain on the habit plane and a dilatation normal to the habit plane to give the correct shape change, followed by second strain to give the correct crystal structure. The second strain is only required to yield the correct martensite lattice, and any shape change that would be caused by this second strain is cancelled either by slip or twinning.

2.3 The morphology of ferrous martensite

The crystal structure of ferrous martensite (α') is body centred tetragonal (BCT) [14], which in a low carbon steel will normally be arranged as laths whose crystallographic orientation will be described by the Kurdjumow-Sachs relationship as being approximately $\{111\}_{\gamma}||\{011\}_{\alpha'}$ with $<011>_{\gamma}||<111>_{\alpha'}$ [9][14].

The greater the amount of carbon that is present in the alloy, the greater the amount of distortion that is caused when the carbon is trapped during quenching, and the more tetragonal the martensite crystal structure. Roberts [15] published an empirical equation (equation 2.1) that describes the level of tetragonality (c/a) as a function of the weight percent of carbon in the alloy (x).

$$c/a = 1 + 0.045x \qquad 2.1$$

Ferrous martensite may assume different morphologies (Figure 2.5), which may also have different orientation relationships, the chosen morphology appearing to be dictated by M_s [16, 17], which will itself be significantly influenced by alloy composition [14]. Lath martensite possesses a high dislocation density and is normally arranged with parallel laths that are tightly spaced with no retained austenite in between the individual laths [18]. The martensite morphology appears to influence whether the transformation is athermal, isothermal or burst, although it is not clear why the relationship exists [19].

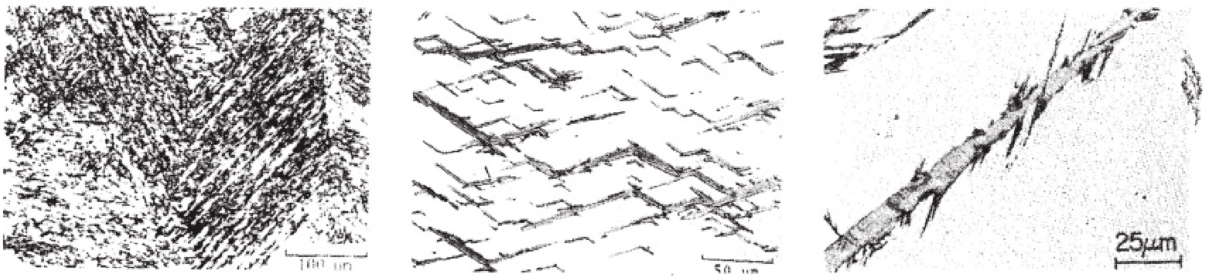

(a) lath α' (b) butterfly α' (c) $(225)_A$ type plate α'

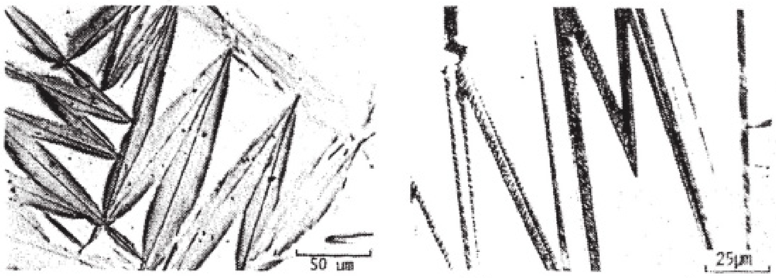

(d) lenticular α' (e) thin plate α'

Figure 2.5 – Optical micrographs of the different morphologies of ferrous martensite. Figure reproduced with permission from Maki [17].

2.4 The strength of ferrous martensite

The main benefits of ferrous martensite are the very high strength and hardness levels that can be achieved. The main strengthening mechanism in ferrous martensite is due to the solid solution strengthening by interstitial carbon [20]. Figure 2.6 is a plot of yield strength against carbon content, which demonstrates the crucial role of carbon in strengthening martensite.

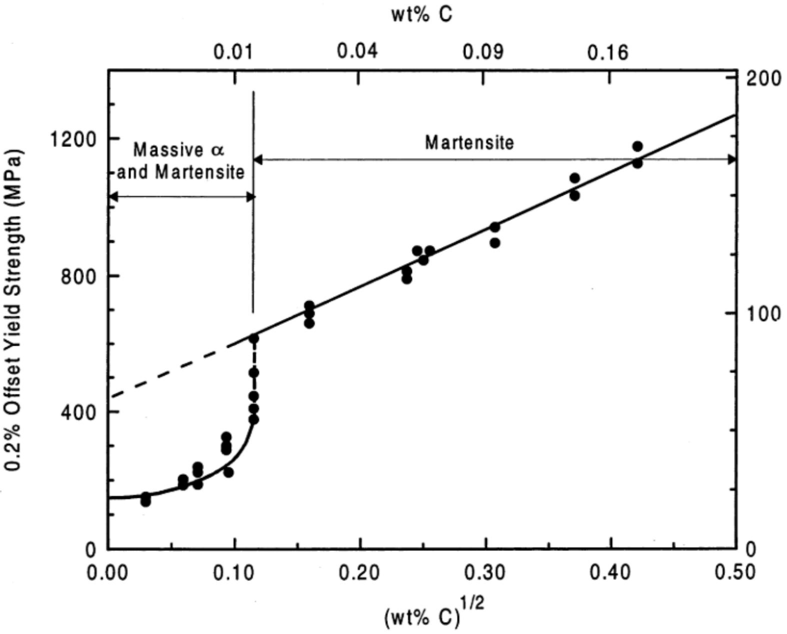

Figure 2.6 – The yield strength of low carbon steels versus the carbon content. Figure reproduced with permission from Krauss [21].

Solid solution strengthening by interstitial carbon is not the only mechanism responsible for the strength of martensite. Other strengthening mechanisms include solution hardening by substitutional elements, precipitation hardening, strengthening by substructure, and microplastic deformation and rapid work hardening [20]. The role of substructure is highlighted by Figure 2.7, which plots the yield strength as a function of packet size.

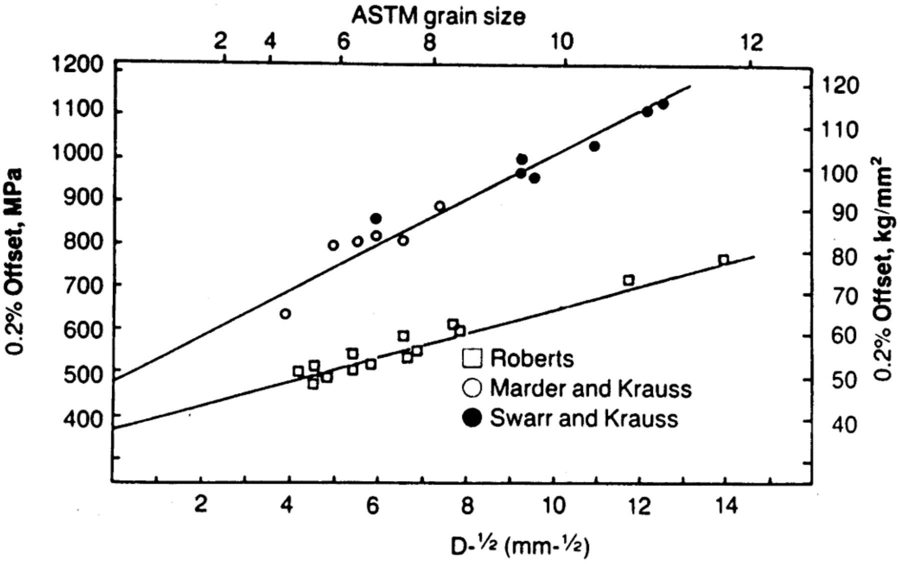

Figure 2.7 – The yield strength versus packet size. The data from Roberts is for a Fe-Mn alloy, the other data is for a Fe-0.2C alloy. Figure reproduced with permission from Krauss [21].

2.5 The martensitic transformation start temperature and kinetics

Greninger and Troiano [22] studied the kinetics of the martensitic transformation and found that in a steel containing 0.82wt% C that the rate of cooling had no appreciable effect on the either the start temperature or on the fraction of the alloy transformed at any given temperature; this result, which suggests that the martensitic transformation is athermal, has been confirmed in the literature for a variety of steels containing between 0.09 and 0.88wt% C [23, 24]. Greninger and Troiano [22] also found that for any given quenching temperature that the martensite that will be transformed at that temperature was present “a fraction of a second after the specimen has reached the quenching-bath temperature” and that the fraction transformed to martensite did not increase with isothermal holding. However, Greninger and Troiano did observe further microstructural changes after significant isothermal holding periods (e.g. 600 hours at 120°C), which they describe as being due to diffusional processes, but the resultant microstructure could not be definitively identified as being martensitic by the metallographic method used (lower bainite formation below M_s has been observed by Van Bohemen et al. [25]). The martensitic transformation in steels is not exclusively athermal, for example Babu et al. [26] found that in a steel containing 0.39C, 0.7Mn, 0.28Si, 0.76Cr, 1.7Ni, 0.2Mb, 0.22wt% Cu that “the martensite reaction did not stop when the cooling was arrested within 2 seconds of quenching, and that some retained austenite did transform isothermally in the next few seconds, before the onset of the bainite reaction”. The carbon content is one factor that may have a significant influence on the nature of the martensitic transformation as reported by Fisher and Corderoy [19], where an alloy containing 25Ni 0.02wt% C transformed athermally, but when decarburized became isothermal with “a ten-fold increase in cooling rate depressing M_s by up to 10°C”. Fisher and Corderoy argue that the athermal characteristics of the martensitic transformation in iron-based alloys is due to dynamic thermal stabilization, where below M_s, martensite embryos can nucleate isothermally, but that the transformation will only progress “i) if stabilized embryos can transform isothermally once the temperature is lowered significantly below the stabilization temperature-that is, if thermal stabilization simply lowers the embryo potency without also altering the mechanism of the critical nucleation step, or ii) if the rate of thermal stabilization does not sufficiently exceed the rate of isothermal nucleation of autocatalytic embryos." An alternative theory for the athermal nature of the martensitic transformation is given by Van Bohemen and Sietsma [27] who reason that as the transformed martensite strengthens the retained austenite due to the strain associated with the shape change [28], the transformation becomes athermal as the strengthened martensite inhibits further martensite growth until the driving force is increased by further cooling. Equation 2.2 describes the transformation kinetics of athermal martensite, published by Koistinen and Marburger [29], which relates the fraction of the alloy transformed to martensite (X_m) to the temperature to which the alloy has been quenched (T_q) below the transformation start temperature (M_s) by the rate parameter (α_m = -1.10 x 10^{-2} °C^{-1}).

$$X_m = 1 - \exp\left[\alpha_m\left(M_s - T_q\right)\right] \qquad 2.2$$

Breinan and Ansell [30] investigated the link between the austenite strength and M_s in a steel containing 0.96C, 0.69Mn, 5.3Cr, 1.07wt% Mo by work hardening the austenite above M_d and found that M_s decreased approximately linearly with increasing austenite flow stress, which they reasoned was due to the plastic deformation affecting either the ease of nucleation or the ease of growth and not due to any change in chemical free energy. In the same piece of work, Breinan and Ansell also found that for a range of seven different alloys containing between 0.14 and 2.12C and 4.80 and 13.60wt% Cr that M_s decreased with the increasing austenite flow stress of the different alloys. Early investigations into the effect of the austenite grain size on the start temperature of the martensitic transformation presented inconclusive evidence, such the work of Digges [31], which did not find any link between M_s and the austenite grain size as varied by austenitization temperature. However, more recent work, such as that of Umemoto and Owen [32], has shown that larger austenite grain sizes due to increased austenitizing temperatures lead to an increase in M_s. Nichol et al. [33] demonstrated that the depression in M_s was due to the austenite grain size refinement and not from some other effect caused by the change in austenitization temperature; the austenite grain size was varied independently of austenitization temperature by the inclusion of between 0 and 3wt% Y_2O_3 to act as nucleation sites. Nichol et al. also showed that the change in austenite grain size was accompanied by a change in the austenite yield strength at 327°C (which was above M_d), agreeing with the earlier work of Breinen and Ansell [30] on the effect of austenite strength on M_s. Similar results are also reported by Brofman and Ansell [34], who argue that the depression of M_s with decreasing austenite grain size is due to Hall-Petch strengthening of the austenite. Maweja et al. [35] found that lower values of M_s were also associated with a higher strength final product, which in five armour steels exhibited an improved performance in ballistic tests, this being attributed to the resultant finer martensite structures showing greater resistance to crack propagation.

2.6 Measurement of the start temperature of the martensitic transformation

There are a number of different experimental techniques that appear in the literature for determining M_s and observing the progress of the transformation, some of the most common being by metallography, by dilatometry, by electrical resistivity, by magnetic effects, and by thermal methods.

2.6.1 Metallographic

The metallographic method devised by Greninger and Troiano [22] was “based on the fact that tempered martensite and un-tempered martensite are easily differentiated microscopically after nital etching (picral is unsuited for this task) because the former etches dark brown and the latter is almost un-attacked and remains white”. Greninger and Troiano performed a series of experiments that involved quenching different samples of an alloy into an isothermal bath that was held at a range of temperatures and for a range of times; the samples then being tempered at a temperature above the quench temperature, causing the martensite formed in the isothermal bath to transform to tempered martensite. The samples were then quenched to room temperature, causing the remaining austenite to transform to martensite. The volume fraction of martensite transformed in the isothermal bath could be calculated as it was differentiated from the quenched and tempered martensite. Use of the metallographic method was more prevalent in some of the earlier publications, such as Meyerson [24], but has also been used more recently to investigate the spatial distribution of martensite formation[27]. Burke [36] is critical of the metallographic techniques for determining M_s stating that they are "of poor accuracy, are slow and tedious". Furthermore, the metallographic techniques rely on being able to distinguish tempered martensite from other possible transformation products by optical inspection alone and in alloys that may contain lower bainite it may not be possible to accurately distinguish the two phases [26].

2.6.2 Dilatometry

Dilatometric measurements rely on measuring the dilatation that accompanies the martensitic transformation due to the different densities of the austenite and the martensite. Dilatometric techniques have been seen as most useful for studying low temperature phase transformations [37] or have been criticized for their poor sensitivity. Commercial push rod dilatometers are now available that can detect a strain of $\varepsilon = 7.1 \times 10^{-6}$ [38] and as such can offer an off-the-shelf solution for studying the martensitic transformation for samples that are frequently prepared as small cylinders [25, 27, 38]. Dilatometric data may contain significant amounts of noise, which according to Yang and Bhadeshia [38] leads to significant variation in the value of M_s when this temperature is defined as being the point at which the temperature – dilatation data departs from the thermal contraction in the pure austenite region. Yang and Bhadeshia propose taking an offset of 1 vol% transformed to martensite to the thermal contraction of pure austenite and defining M_s as being the intercept of the offset line and the dilatometric data. Their experimental results show a reduction in the standard deviation of M_s from 43°C to 12°C, although it should be pointed out that there is some inconsistency within these calculations regarding the calculation of the thermal contraction of austenite, which may amplify the reported improvement. An alternative approach to determining M_s from dilatometric data has been proposed by Van Bohemen et al. [25] of calculating the fraction transformed to martensite from a ratio of mixtures approach to the dilatation at any given temperature compared to the measured thermal expansivities of the pure martensite and austenite phases; the Koistinen and Marburger equation [29] is then fitted to this data by adjusting M_s and α_m.

2.6.3 Resistivity

The first researchers to accurately observe the changes in electrical resistivity during phase transformations in iron were Burgess and Kellberg [39], who measured the resistivity of pure iron during slow cooling (0.06°C/s) and heating (0.10°C/s). They observed abrupt changes in resistivity at the Curie point and gradual changes at A_{c3} ($\alpha + \gamma \rightarrow \gamma$ temperature) and A_{r3} ($\gamma \rightarrow \alpha + \gamma$ temperature). McReynolds [40] subsequently used changes in electrical resistivity to determine M_s and to observe the kinetics of the transformation in a series of four steels containing between 0.09 and 0.88wt% C and 0.26 and 4.53wt% Mn. McReynolds argued that the relationship between electrical resistivity and the fraction transformed to martensite would depend upon the arrangement of the two phases, giving formulae to relate the two variables for cases where the phases are electrically parallel, electrically in series or where the phases are arranged electrically in some combination of series and parallel. Electrical resistivity techniques have been used to determine M_s by a number of researchers in steel [41, 42], in iron-nickel alloys [6, 32], and in CuZnAl memory shape alloys [43]. In addition to the advantage of being relatively simple to implement, electrical resistivity methods can also be used to observe precipitation kinetics [44-46] and have been reported as being able to accurately determine M_s to within ±0.3°C (with twenty determinations for a single sample showing a spread of ±1.5°C) [19] and to better than 3°C [34]. Garn and Flashen [47] describe that "as a material undergoes a phase transformation, the thermal coefficient of electrical resistance changes because of a change in the electronic energy levels or, in some cases, because of a change in the mobility of ions within the lattice”; however, it would appear that in steels and in other iron-based alloys that the change in electrical resistivity is most easily observed when accompanied by a change in magnetic properties [39, 42].

2.6.4 Magnetic

Nagler and Wood [48] initially used magnetic techniques to determine M_s by exploiting the change in magnetic permeability that accompanies the martensitic transformation in steel, which they observed by placing the sample within the magnetic field generated by a first electromagnetic coil and observing the voltage generated in the winding of a second electromagnetic coil, between whose poles the samples had been placed: the change in permeability being assumed directly proportional to the fraction transformed to martensite. Breinan and Ansell [30] used a technique similar to Nagler and Wood, and other researches have used alternative techniques to observe the change in permeability, such as using the sample as the core for an inductor within an oscillator and measuring the resonant frequency [26]. Another technique based on changes in permeability used an array of smaller electromagnets and co-located Hall effect sensors to image the phase transformation on a rolling-stand run-out table [49], albeit that in the latter piece of work the authors were interested in observing a combination of phase transformations not just the martensitic. It is worth noting that the applied magnetic field used in these early techniques may in itself affect M_s: Kakeshita et al. [50] found that in an iron-nickel alloy that M_s could be raised by as much as 73.3°C in a magnetic field of 26.98 MA/m.

Christien et al. [51] used the change in paramagnetic to ferromagnetic as the steel was cooled from austenite to martensite to determine M_S. The experimental procedure involved heating and cooling the sample in a thermobalance whilst a magnet was suspended above the sample. As the steel became more ferromagnetic, the magnetic force between the sample and the magnet reduced the apparent weight of the sample. A disadvantage of this method is that the austenitic transformation upon heating can only be detected when this occurs below the Currie temperature.

In the recent work of Goldenstein et al. [52], M_s is determined in an iron-nickel alloy by observing spontaneous magnetic emission (SME) that arises from the re-arrangement of magnetic domain walls accompanying the phase transformation without any externally applied magnetic fields. Goldenstein et al. claim that “The higher M_s temperature determined by SME shows the increased sensitivity of the method, which does not depend on a critical transformed volume, as is the case for electrical resistivity and magnetic susceptibility [permeability] measurements."

2.6.5 Thermal

Thermal methods for determining M_s rely upon the detection of heat that is evolved during the transformation from austenite to martensite and as such have an advantage over the previously described methods in that they rely on observing a direct effect of the transformation and not the property of some secondary variable that varies in an unknown way to the progress of the transformation [36]. Digges [31] attempted to observe the heat evolved during transformation by recording the time-temperature curves of steel alloys during quenching, and looking for the point of inflection in those curves as the start of heat evolution and hence the transformation start temperature. Digges noted that the point of inflection was not always sufficiently sharp to accurately determine M_s, something that was also found by Meyerson [24] who repeated the method of Digges. Bodin and Marchal [53] attempted to use differential scanning calorimetry (DSC) and differential thermal analysis (DTA) to more accurately determine transformation temperature for the austenite to ferrite transformation, but this approach required accurate knowledge of the specific heats of both austenite and ferrite to enable the calculation of effective heat transfer coefficient. In addition to the complexity of the approach of Bodin and

Marchal, the achievable cooling rates in DSC or DTA limit the range of martensite transforming alloys that could be studied by such an approach.

2.6.6 Acoustic emission

The shear produced by the martensitic transformation produces sound that was used by Speich and Fisher [54] to observe the martensitic transformation 28wt% Ni, 0.11wt% C steel, which has an M_s below room temperature. Homogenized samples were submerged in a cooled flask and the acoustic emission was recorded by the use of a piezoelectric sensor. The sample temperature was recorded using a type T thermocouple and electrical resistance was simultaneously measured using a four-wire technique with a constant current. Samples were quenched to a range of decreasing temperatures to increase the volume fraction of transformed martensite, which was measured using optical techniques. They found that the acoustic emission occurred in bursts of sound, and that each emission came from the formation of approximately 15 martensite plates. Speich and Fisher use the electrical resistance measurements to estimate the volume fraction of transformed martensite and used that information to show that the rate of acoustic emission reduces with an increasing fraction of transformed martensite. However, the formula that Speich and Fisher have used is the formula that McReynolds [40] indicates is suitable only where the austenite and martensite phases are electrically in series. McReynolds suggests that given the random orientation of the martensite plates that a more accurate formula would be to use the average value for the series and parallel formulae. Had Speich and Fisher used the formula suggested by McReynolds, they would have calculated a lower volume fraction of transformed at temperatures between M_s and M_f, which would have counteracted the trend in declining acoustic emission that they reported.

Van Bohemen et al. [55] made use of acoustic emission to observe the effect of austenite grain size on the martensitic transformation temperature. The authors again made use of a piezoelectric sensor to record the acoustic emission, but as the alloys studied began to transform to martensite at elevated temperatures, it was necessary to connect the piezoelectric sensor via a metallic waveguide to protect the sensor from the heat. The heating and cooling was performed using a Gleeble thermo-mechanical simulator that allowed the simultaneous recording of dilatation data. The authors found that the transformation start temperatures as measured by acoustic emission demonstrated good agreement with those found by dilatometry.

2.6.7 Diffraction

X-ray diffraction is a well-established technique to determine the volume fraction of transformed martensite in quenched steel samples [56]. Epp et al. [57] performed in situ X-ray diffraction at the European Synchrotron Radiation Facility on a AISI 5120 steel (0.2wt%C) that was quenched from 900°C at a rate of approximately 65°C/s. The sample was heated using Joule heating, and the quench cooling rate was achieved without the use of a quenching fluid by conductive heat loss through the sample clamps. The samples were 1.5 x 1.5 x 40 mm in size. The volume fractions of retained austenite and transformed martensite were calculated using Rietveld analysis.

In situ observation of the ferrous martensitic transformation has also been reported using a laboratory X-ray diffractometer for isothermal transformations. Xu et al. [58] measured the room temperature strain induced martensitic transformation of a AISI 304 stainless steel using a Bruker D8 diffractometer. The authors calculated the volume of transformed martensite based on the measured peak heights. Because of the much lower X-ray intensity of laboratory diffractometers, it would not be possible to use such a method with the fast cooling rates that are achievable using a synchrotron source, making such an approach unsuitable for the many alloys that have fast critical cooling rates.

Christien et al. [51] used neutron diffraction to study the transformation of 17-4PH stainless steel from martensite to austenite during heating and back to martensite during cooling. Phase fractions were calculated using Rietveld analysis. They generally found good agreement with the results from neutron diffraction and dilatometry, with the exception of the A_{C3} temperature. The dilatometric data indicated that the martensite had fully transformed to austenite by 810°C, whereas the neutron diffraction data suggested that the transformation was not complete until 950°C. The authors' explanation for the discrepancy was that due to the similar densities of austenite and martensite at temperatures above 850°C, dilatometry is unable to differentiate between austenite and martensite at these temperatures.

2.6.8 Measurement variability

To assess the variability in determining phase transformation temperatures between laboratories, Nitsche and Mayr [59] sent ASTM A335 M P91 steel samples to several[1] laboratories (one of which was based in the authors' university) to determine the start and finish temperatures of both the α' → γ and γ → α' transformations. The laboratories were asked to measure the transformation temperatures during a slow heat treatment (28°C/h through AC1 and AC3 to 1000°C and 10°C/s quenching) and a fast heat treatment (100°C/s heating to 1300°C and 20°C/s cooling). All but two of the laboratories used dilatometry, with the other two using thermal methods. The laboratories were asked to determine the transition temperatures from their data using their standard methods.

Table 2.1 – Summary of Nitsche and Mayr's [59] results of the phase transformation start and end temperatures as measured by several different laboratories for an ASTM A335 M P91 steel.

	Slow heating and cooling				**Fast heating and cooling**			
	A_{C1}	**A_{C3}**	**M_s**	**M_f**	**A_{C1}**	**A_{C3}**	**M_s**	**M_f**
Min	768	828	362	204	821	904	349	197
Max	825	924	427	311	909	1064	406	336
Range	57	96	65	107	88	160	57	139
Mean	812	882	385	243	882	965	380	248
Std Dev	18.1	28.3	16.1	30.6	26.1	43.0	16.3	40.0

---

[1] It is unclear exactly how many laboratories were involved in this study. Ten laboratories are acknowledged (including one at the authors' institution). There are twelve data points for the first task (slow heating and cooling), and eleven data points for the other two tasks.

Table 2.1 shows a summary of Nitsche and Mayr's results. It can be seen from their results that there is a significant spread in the results for all of the transformation temperatures. It can also be seen that the variance is greater in measuring the transformation end temperatures, and with the exception of M_S, greater during fast heating and cooling. The authors also provided the laboratories with the dilatometric data for the heating and quenching of a 9Cr martensitic heat resistant steel, and asked the laboratories to use their standard methods to calculate the transformation start and end temperatures from the data; the results of which are reproduced in Table 2.2. Comparison of the results in Table 2.1 and Table 2.2 indicates that whilst a significant part of the variance in the transformation temperatures comes from the experimental method, there is also a significant contribution to the results variance from the different data analysis methods employed. As noted by the authors, the determination of the transformation end temperatures is more difficult to calculate; it is for this reason that variance remains so significant for these temperatures even when the influence of the experimental method is removed.

Table 2.2 – Summary of Nitsche and Mayr's [59] results of the phase transformation start and end temperatures as calculated by several different laboratories from identical dilatometry data.

	Analysis of standard data			
	A_{C1}	A_{C3}	M_s	M_f
Min	895	945	385	270
Max	914	1005	400	345
Range	19	60	15	75
Mean	905	977	391	294
Std Dev	6.2	20.7	4.6	29.0

It should also be noted that the difference in the measured values for the martensitic transformation temperatures may be due to a change in the prior austenite grain size. The material was delivered to the participants as seamless tube, which the individual laboratories were responsible for preparing into the necessary sample shapes and sizes. It is entirely possible that the tube may have been thermo-mechanically processed to produce sheet, and that any such processing may have caused a change in the microstructure.

2.7 Summary

Research into martensite dates back to ancient times, but it was not until the invention of the X-ray diffractometer and the electron microscope that the nature of martensite could be properly investigated. Early researchers investigated crystallographic relationships between austenite and martensite, and comprehensive phenomenological theories were developed to describe the transformation. Because of the extremely rapid rate at which the martensite grows, the nucleation of martensite has been more difficult to study and is less well understood than for diffusional transformations.

During the twentieth century a wide range of techniques were used by researchers to investigate the kinetics of the martensitic transformation. The early innovation in measurement techniques seems to have somewhat disappeared from the more recent literature, no doubt in large part to the easy availability of commercial instruments that the researcher can employ with little effort. However, despite the scarcity of recent work to improve the measurement techniques for observing martensitic kinetics, the problems with currently used measurement techniques are not difficult to find. As highlighted by Nitsche and Mayr, consistency in measurement between different laboratories is still a significant problem despite many of the laboratories using identical instruments.

3 Instrument design

3.1 Instrument requirements

3.1.1 Heating and cooling rates

The instrument was initially designed to study press hardened steels and as such there was a requirement to be able to heat at a rate at least equal to that used industrially. For an Al-Si coated 22MnB5 steel, a heating rate of 12°C/s is recommended [60], so this would be the absolute minimum heating rate required. However, to increase the flexibility of the machine it was felt that a minimum heating rate closer to 50°C/s would be a more appropriate objective.

The cooling rates used in the industrial press hardening process are dependent on the stamping pressure, but will cool from 700°C to 400°C in approximately 0.5 s [61], which gives an average cooling rate of 600°C/s. However, it should be noted that the critical cooling rate to achieve a fully martensitic transformation in a 22MnB5 steel is approximately 27°C/s [60] to 30°C/s [61].

3.1.2 Measurement of the start temperature of the martensitic transformation

An introduction to some of the different methods of measuring the start temperature of the martensitic transformation in steels is presented in section 2.5. In this section, the three main reasons for selecting resistance measurement as the technique to measure the transformation start temperature will be explained.

3.1.2.1 Measurement region of nearly constant temperature

The most significant advantage of the electrical resistance measurement technique is the degree to which the measurement can be constrained to a region of nearly uniform temperature. In initial experiments that were undertaken at the start of this project to measure M_S using a Bähr DIL 805A/D high-speed horizontal dilatometer, samples of 3 mm thick low carbon steel were cut into pieces 10 mm long and 4 mm wide. Two type S (Pt-Pt/Rh) thermocouples were spot welded in a helium atmosphere to each sample, one in the centre of the samples and one at the edge of the samples. In each experiment the central thermocouple acted as the feedback sensor for the closed-loop control of the sample temperature. The samples were supported and measured by hollow silica rods. During heating and holding the temperature as measured by the edge thermocouple was not significantly lower than the temperature measured in the centre. However, during helium quenching large temperature differences were observed, with the edge temperature being measured as much as 188°C cooler than the centre. The dilatometer measures the bulk dilatation, but as there is a significant thermal gradient through the bulk, transformations will be measured as starting at artificially raised temperatures during rapid cooling, as the regions that are contributing to the dilatation that is interpreted as the start of the transformation will be cooler than the (centrally) measured temperature. Assuming that the thermal gradient itself cannot be eliminated, the two solutions would be either to apply a correction based on the thermal gradient, or to constrain the measurement to a region with a small thermal gradient. Applying a correction based on the thermal gradient is somewhat impractical as this would require both an accurate knowledge of the temperature distribution, as well as the way that the property that is being measured varies with temperature[2].

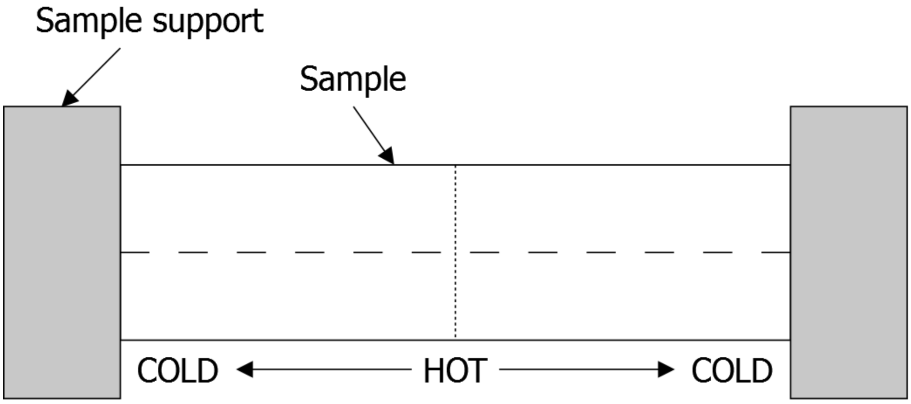

Figure 3.8 – The significant thermal gradient in the sample is from the sample centre to the edges in contact with the sample supports due to heat loss through conduction. Properties measured along the dashed line will be an average value from regions of different temperature. Properties measured along the dotted line will be almost isothermal.

---

[2] If it is already known how the property being measured varies with temperature, it is unclear what would be the purpose of performing the experiment.

If the main temperature gradient is from the centre towards the sample supports, which is due to heat loss by conduction, then by measuring a suitable material property in a direction normal to this direction (dotted line in Figure 3.8), the effect of the temperature gradient can be negated. The thermal expansion of a hot region will be constrained by an adjacent cooler region, which means that even if the measurement direction is normal to the direction that has the maximum temperature gradient, the measured thermal expansion will still be less than the value that would be measured for a sample at uniform temperature. Conversely, the electrical resistivity of a region of a sample should not be affected by adjacent regions of differing resistivity.

If the electrical resistivity of the sample along the dotted line in Figure 3.8 only depends on the temperature and microstructure along that line, then the question is how well can the electrical resistivity measurement be constrained to that isothermal region? To answer this question a finite element model was created in COMSOL Multiphysics 4.2 to find the measured resistance for different sample lengths. The length ranged from 1 to 150 mm using a parametric study, and the resistance was calculated as if using a four wire technique by applying a point current of 502 mA to a point on the dotted line of Figure 3.8 that was 1 mm from the long edge (the edge that connects the two sample holders) of the sample, and a point current of opposite polarity was applied to the point that was 1 mm from the other long edge. The voltage difference was measured between the two points on the dotted line of Figure 3.8 that were 3 mm from the two long edges, and the resistance was calculated by dividing the voltage difference by the measurement current. The numerical results are presented in Appendix 1, for a sample bulk resistivity of 10.7 µΩ / cm. Figure 3.9 shows how the measured resistance (normalized to the resistance of the sample when 150 mm long) varies with sample length. The results of the FE model show that the sample length does not significantly affect the measured electrical resistance until the length is reduced below 20 mm: this demonstrates that the region that contributes to the measured resistance is largely constrained to the volume that is close to the dotted line of Figure 3.8.

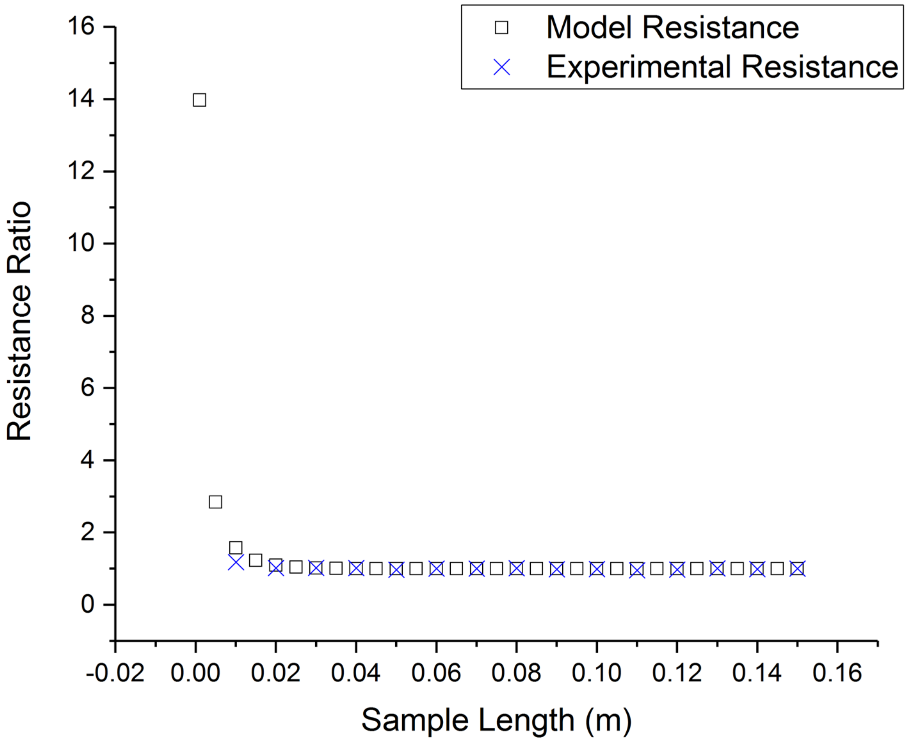

Figure 3.9 – The electrical resistance, measured using a four-wire method with probes connected along the length centre line, does not significantly increase from the value measured with a 150 mm long sample until the length is reduced below 20 mm.

To validate the results of the finite element model, a 3 mm thick piece of Armco pure iron was cut to be 150 mm long by 20 mm wide. One of the two large faces of the sample was marked with a series of lines in the width direction that were spaced 5 mm apart. Four nichrome wires were spot welded on to the central line, with an outside pair of wires being 1 mm from the long edges, and an inside pair that was 3 mm from the long edges. The electrical resistivity of the sample was measured using a calibrated Agilent 34420A with offset correction enabled; the outside pair of wires were connected to the current supply terminals, and the inside pair were connected to the voltage sense terminals (see Figure 3.10). After the initial measurement of the 150 mm sample, the sample was reduced to 140 mm long by cutting 5 mm from the two ends using the markings. The resistance measurement was repeated, and the sample length reduced by another 10 mm. This was continued until a final measurement was taken with the sample being 10 mm long. The numeric values can be found in Appendix 2, and the normalized measurements can be seen plotted with the results from the FE model in Figure 3.9. The experimental results agree with the model that the region of the sample that significantly contributes to the measured electrical resistivity is less than 10 mm away from the measurement direction (dotted line in Figure 3.8).

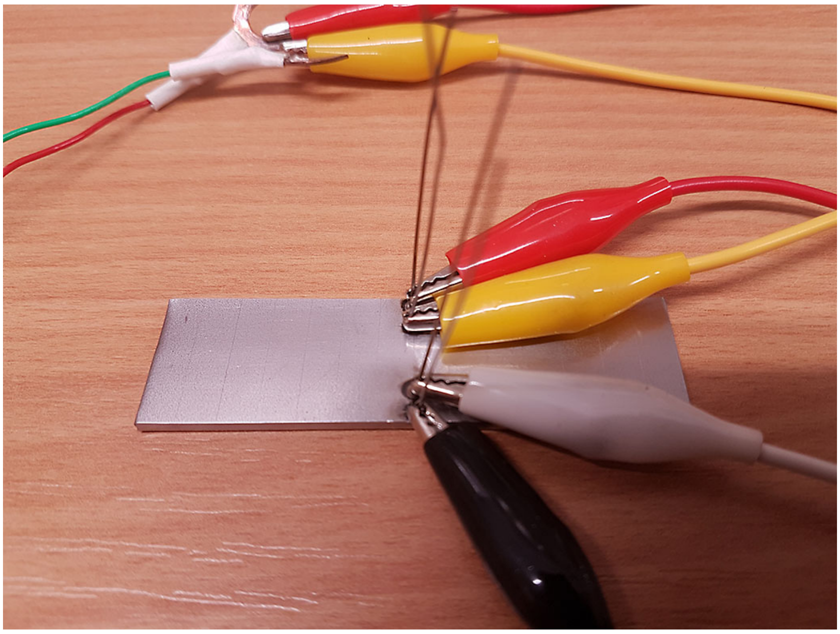

Figure 3.10 – The investigation of the effect of sample length on the measured electrical resistance.

3.1.2.2 Measurement of a wide range of transformations

Electrical resistivity measurements can be used to measure the start and finish temperatures of the ferrite to austenite, austenite to ferrite, as well as the austenite to martensite. Many of the magnetic techniques can only detect the ferrite to austenite transformation when this occurs below the Curie temperature. As mentioned in section 2.5.7, the low count rate of laboratory X-ray sources would make standard X-ray diffraction an unsuitable technique for use with fast heating and cooling rates. Dilatometry does not suffer from any of the problems described in this section, but electrical resistivity measurements have the advantage that they can also be used to detect precipitation, both in ferrous [46] and non-ferrous [62] alloys.

3.1.2.3 Ease of implementation

The final advantage of using electrical resistance measurements is the ease of implementation compared to many of the other methods. Contact dilatometry requires the use of precise mechanical transducers, and would present many difficulties with resistance heating. The magnetic techniques would be relatively straightforward to implement, but the limitations outlined above preclude their consideration. X-ray diffraction is not a suitable technique due to the speed restriction, but in any case would be significantly more involved than electrical resistance measurements. Neutron diffraction would be an excellent technique for measuring the transformation temperatures, but would be almost impossible to implement in a small laboratory.

3.1.3 Thermal etching and vacuum requirements

The prior austenite grain size is an important material property that can affect the start temperature of the martensitic transformation[30, 32-34], and these changes in the transformation start temperature can affect the final material properties[35]. Thermal etching removes many of the complexities[63] of either trying to directly observe the austenite grain structure at elevated temperatures, or using chemical etchants that are very sensitive to the alloy chemistry. Stéphan Joly at ArcelorMittal developed a procedure for use in a Bahr DIL805A/D quenching dilatometer that was found to consistently thermally etch samples for revealing the prior austenite grain structure of quenched steels. The method developed by Joly [prefix64suffix] is to grind and polish one face of the sample, as one would for optical microscopy, to a finish of 1µm, which is placed in the dilatometer without chemical etching. The chamber is then evacuated until the pressure is less than or equal to 9×10^{-5} mbar, before backfilling with high-purity helium gas to a pressure of 0.8 bar. The chamber is then evacuated a second time, but this time to the lower pressure of less than or equal to 5×10^{-5} mbar, and then finally backfilled to a pressure of 0.8 bar with helium. This procedure of twice evacuating the chamber to a high vacuum, before backfilling with a high-purity inert gas, is designed to remove any impurities from the atmosphere that may interfere with the thermal etching.

The desire to be able to use thermal etching according to Joly's method in the quenching simulator, leads to the requirement that the samples should be heated and cooled in a chamber that can be evacuated to a vacuum of at least 5x10^{-5} mbar, before being filled with an inert gas.

3.1.4 Tensile testing and sample dimensions

The workflow of this project's industrial sponsor has been to use dilatometry to investigate the transformation kinetics, and then when tensile tests have been required, to prepare suitable samples in a Gleeble deformation simulator. There are two problems with this approach: firstly, the different heat transfer characteristics of the two machines means that the heat treatments as seen by the samples will differ; and secondly, that the sponsor has had problems with tensile samples prepared using the Gleeble failing near the jaws. The first problem can be solved be designing the quenching simulator to perform the heat treatments on samples that are sufficiently large to enable the machining of tensile test specimens from the samples, so that the same sample that has had its martensitic start temperature measured is then subjected to the mechanical testing. The second problem has been attributed to the Gleeble prepared samples being insufficiently heated at the ends, and therefore not being fully austenitized before quenching, which has caused the ends of the sample to have significantly lower ultimate tensile strength than the test piece parallel region. This second problem can be mitigated by minimizing the thermal gradient in the parallel region of the tensile specimen.

A problem that any resistance heating system will encounter is that if the sample is to be heated to a temperature that approaches the melting point of the alloy used to construct the sample clamps, then the sample clamps will require cooling, which in turn will cause a significant thermal gradient across the sample. The thermal gradient will be greatest towards the clamps and will reduce in the central region (see 3.2.1.4). ISO 6892-1:2009 [65] specifies in Annex B three sample types for the room temperature testing of sheet metal between 0.1 and 3 mm thick: the recommended parallel length for a type 1 test piece is 75 mm with a width of 12.5 ± 1 mm. The maximum width that this project's sponsor can produce on their pilot mill is 150 mm, if this length is used for the quenching simulator samples then this gives 37.5 mm at both ends of the parallel region of the tensile specimen, which should contain the significant part of the temperature difference (see3.2.1.4).

3.1.5 Unconstrained thermal expansion of the samples

The standard sample dimensions for use in the quenching simulator will be 150 x 20 x 1-3 mm. If the material has an average linear thermal co-efficient of expansion from 20°C to 700°C of 13.0×10^{-6}°C^{-1}, then the longest dimension of an unconstrained sample will expand by 1.33 mm. If the same sample is now rigidly constrained at the two smallest faces, the sample will have an internal elastic strain that is given by the product of the Young's modulus, the linear co-efficient of thermal expansion and the temperature increase. If the Young's modulus for the material is 200×10^9 N / m^2 the internal elastic stress will be 1.77×10^9 N/m^2 – the material will fail before such an internal stress could be supported, given that the ultimate tensile strength (UTS) of an advanced high strength steel (AHSS) may only be 1.5×10^9 N/m^2[4]. What these calculations do demonstrate is the scale of effect that constraining the sample during heating will have on the samples.

Nishiyama [66] calculated that an applied stress would increase the martensitic start temperature at a rate of 1.6°C / kg / mm^2 or 0.163°C / MPa. Applying Nishiyama's result to the previously calculated stress would give an increase in M_s of 288.5°C at 700°C. Nishiyama's calculation was based on data of strains up to approximately 420 MPa, so it is unreasonable to expect the results to accurately extrapolate to strains of 200×10^9 N / m^2, but this result does give some useful information about the magnitude of effect that constraining the sample during heating would have on the measurement of M_s. A more valid application of Nishiyama's calculation is to calculate the maximum applied strain that can be tolerated for a given change in M_s: if an increase of 3°C in M_s is acceptable, then this equates to a maximum applied stress of:

$$\sigma = \frac{\Delta M_s}{\frac{dM_s}{d\sigma}} = \frac{3℃}{0.163℃ \cdot \mathrm{MPa}^{-1}} = 18.4\ \mathrm{MPa}. \qquad 3.1$$

Then for M_s to be affected by no more than 3°C in a sample of 1 mm thickness, the sample must be able to thermally expand with a force acting against the two smallest faces of no more than:

$$F_{TE} = \sigma A = 18.4 \times 10^{6} \times 20 \times 10^{-3} \times 1 \times 10^{-3} = 368\ \mathrm{N}. \qquad 3.2$$

3.2 Sample heating and quenching systems

3.2.1 Heating system

3.2.1.1 Heating voltage and lossless heating rates

A decision, based largely on initially selected components that were never utilized, was made to use a maximum mains supply current of 40 A, which for single phase electricity in the UK gives an input power of 9.6 kW. Given the low electrical resistance of metallic samples of the geometry outlined in section 3.1.4, it is necessary to reduce the voltage from the 240 V mains voltage to a value of a few volts. The simplest way of achieving this is to make use of a transformer. Given the input limits of 240 V and 40 A, the voltage to give the quickest heating rate will depend upon the sample resistance. Combining Ohm’s law with the equation for the power dissipated in a resistor leads to equation 3.3, which can be used to calculate the optimum secondary voltage for a given sample resistance:

$$V = R\sqrt{\frac{P}{R}} \tag{3.3}$$

Appendix 6A lists the resistances of samples of some metals that may be used with the quenching simulator. It can be seen from this appendix that the resistances of the test pieces fall between 10^{-5} and 10^{-2} Ω, with steels being in the middle of that range. Figure 3.11 plots the optimum transformer secondary voltage for maximum sample heating rate for various sample resistances. A heating voltage of 4.8 V was selected (sample resistance of 2.4 x 10^{-3} Ω), as this is close to the optimum value for steels at a range of temperatures, but also allows operation with reduced heating for alloys on either side of the conductivity scale, such as aluminium and titanium. For a maximum input power of 9.6 kW, a secondary output voltage of 4.8 V corresponds to a maximum secondary current of 2000 A.

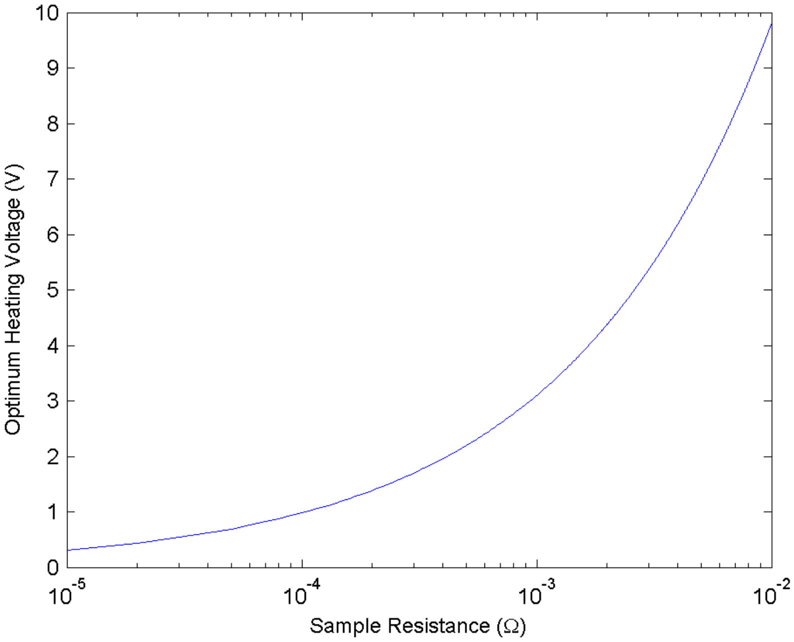

Figure 3.11 – The optimum sample heating voltages for an input power of 9.6 kW calculated according to equation 3.3.

In order to enable the heating of samples with electrical resistance less than 2.4 mΩ it is necessary to be able to reduce the secondary output voltage, otherwise the main input current will exceed the specified value of 40 A. A frequently encountered method that can be used to provide additional control of the RMS output voltage for an AC supply is phase angle control. In phase angle control a semiconductor switch is closed only for a certain part of each half cycle of the supply voltage sine wave (see Figure 3.12). As shown in Figure 3.13, by adjusting the turn-on angle of the semiconductor switch the RMS value of the load voltage is altered [67].

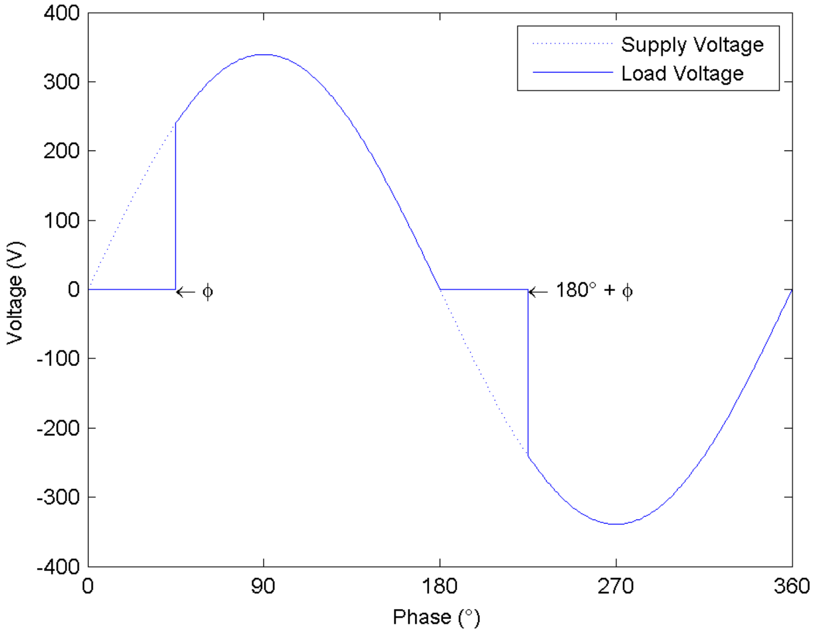

Figure 3.12 – Supply and load voltages for phase angle control with turn-on angle ϕ.

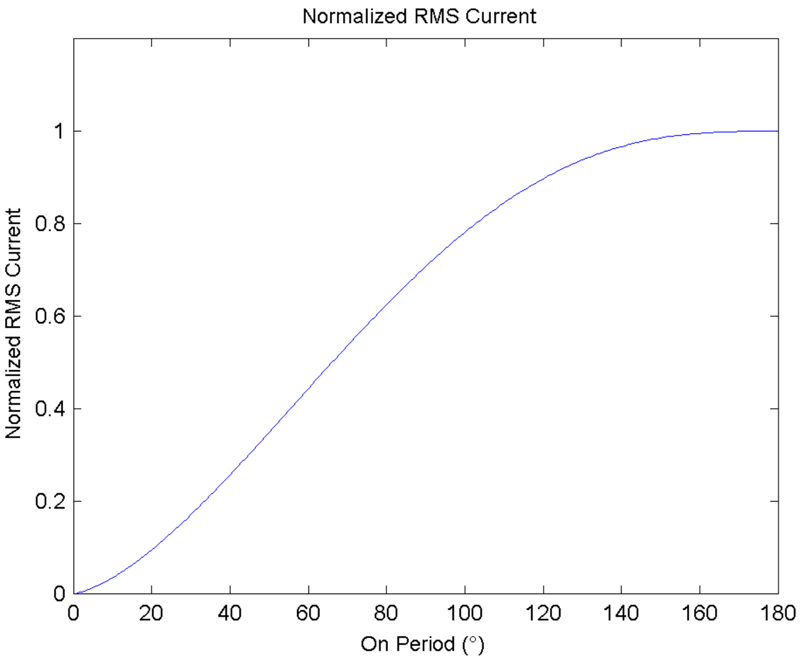

Figure 3.13 – Normalized RMS value of a phase angle controlled signal. For conventional phase angle control the turn-on angle ϕ is equal to 180° less the on period.

3.2.1.2 *Zero voltage turn-on phase angle control*

In addition to sample resistance, Appendix 6A also shows the calculated heating rate for each sample type in the absence of any heat loss, and with the assumption that if the sample resistance is less than 2.4 mΩ, that the voltage can be accurately reduced to achieve a heating current of 2000 A_{RMS}. However, to achieve the precise voltage control that is assumed in Appendix 6A, it would be necessary to precisely know the sample resistance versus temperature in advance. An alternative approach that does not require knowledge of the sample resistivity is to modify the method of phase angle so that turn-on is at 0° and turn-off is at ϕ (see Figure 3.14). The instantaneous current can then be continuously monitored, and if the measured value reaches a specified limit, the semiconductor switches can be opened to prevent the current exceeding the limit (see Figure 3.15).

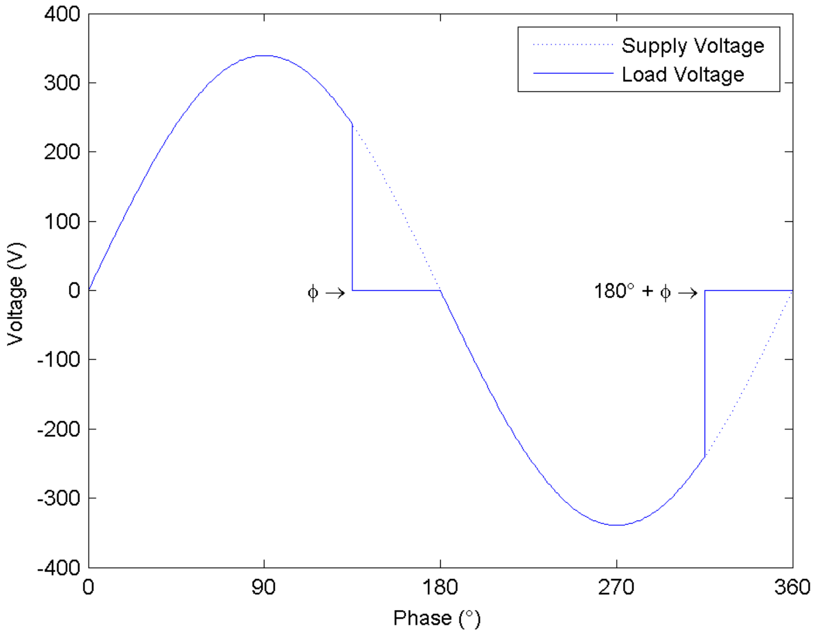

Figure 3.14 – Supply and load voltages for modified phase angle control with turn-off angle ϕ.

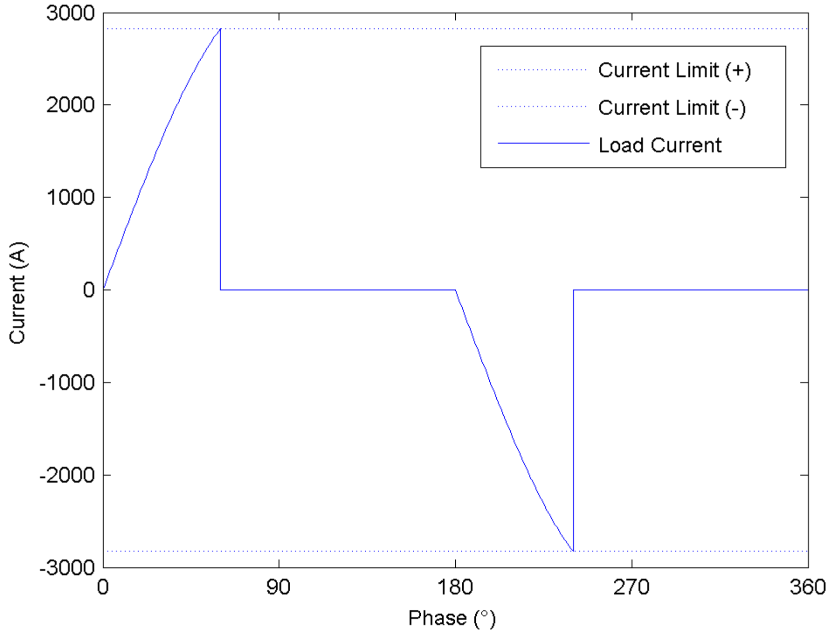

Figure 3.15 – Modified phase angle control with instantaneous current monitoring.

The peak value of a pure sinusoidal signal can be calculated by multiplying the RMS value by $\sqrt{2}$. If the instantaneous current limit is chosen by calculating the peak value of the 2000 A_{RMS} input sinusoid (2828 A), the heating RMS current will always be less than the limit of 2000 A_{RMS}, whereas any value greater than this would allow values greater than 2000 A_{RMS}. However, a significant downside of using this method of instantaneous current monitoring is that for any sample that is current limited, which will be any sample with a resistance less than 2.4 mΩ, will have a turn-off angle less than 90°. As shown in Figure 3.13, when the semiconductor switch is only open for 90° or less, the RMS value of the resulting waveform will be a maximum 0.707 times the RMS value of the complete sinusoid. Figure 3.16 plots the maximum RMS current versus sample resistance when using such an approach. In the case of the sample resistance exceeding 2.4 mΩ, the instantaneous current limiting will not be activated, and the maximum RMS current can simply be calculated using Ohm's law.

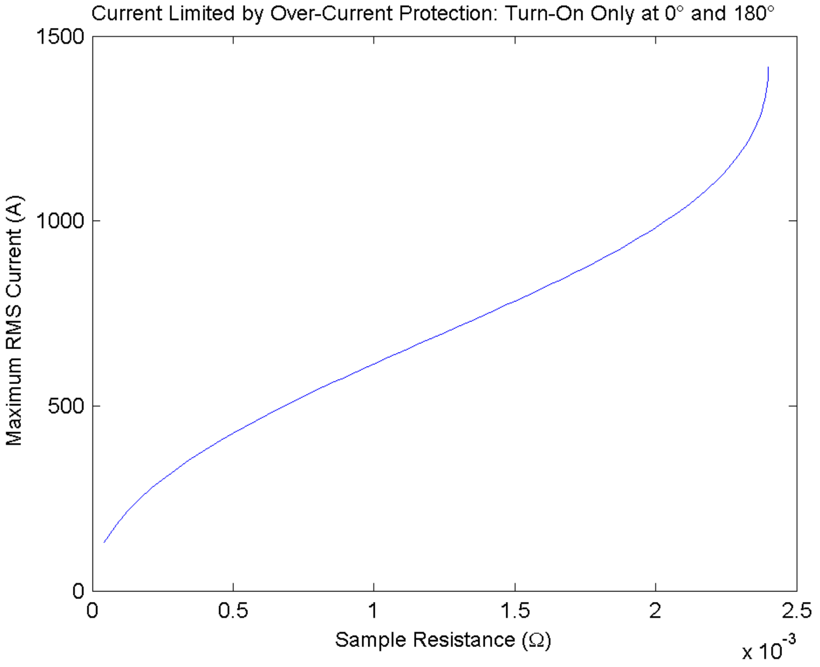

Figure 3.16 – The maximum RMS current when using an instantaneous current limit of 2828 A vs. sample resistance.

The maximum RMS current for a sample with electrical resistance below 2.4 mΩ can be increased by further modifying the phase angle control approach to include a second on period within each 180° half cycle, which is symmetric about 90° (see Figure 3.17).

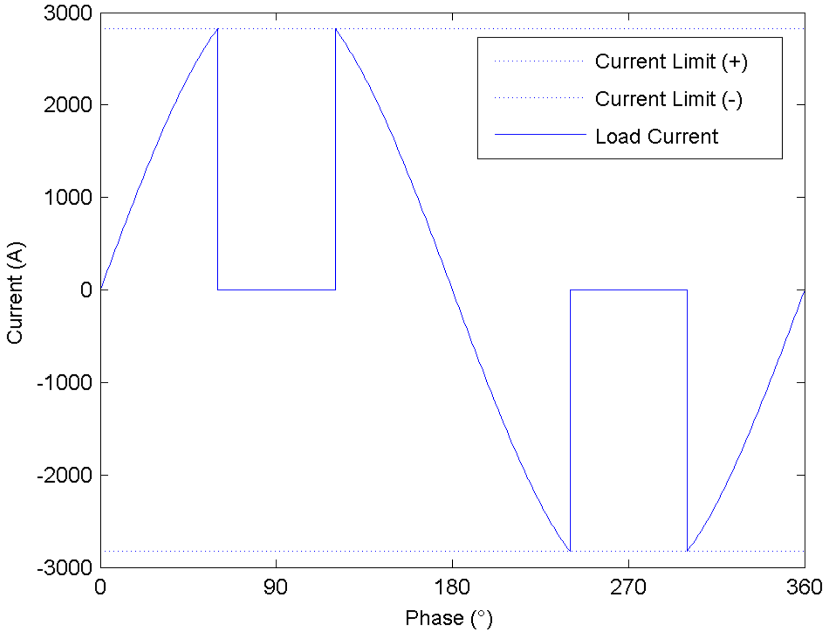

Figure 3.17 – Modified phase angle control with instantaneous current monitoring and a second on period per half cycle that is symmetric about 90°.

Figure 3.18 shows the calculated maximum RMS current for samples with resistance less 2.4 mΩ when using a second on period per half cycle. It can be seen that the maximum achievable RMS current now approaches 2000 A as the sample resistance approaches 2.4 mΩ, which is a significant improvement on the case for a single on period as shown in Figure 3.20.

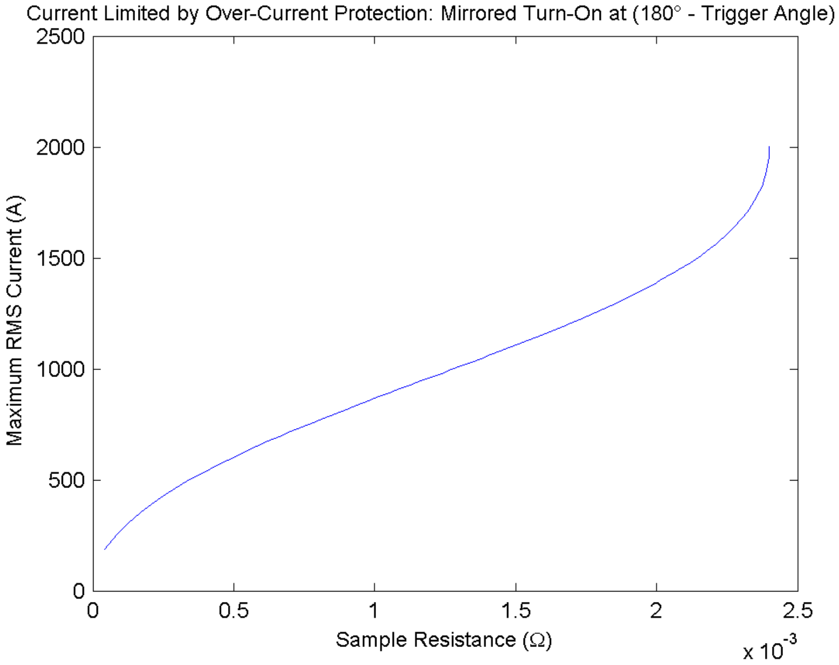

Figure 3.18 – The maximum RMS current with a second turn-on phase per half cycle when using an instantaneous current limit of 2828 A vs. sample resistance.

Although the use of symmetric turn-on angles with instantaneous current monitoring offers a significant benefit, it should be noted that there is a problem with such an approach, namely, that the resulting RMS value of the two symmetric on periods may be greater than the RMS value of the requested turn-off angle. For example, if a turn-off angle of 80° has been requested, but the instantaneous current monitoring opens the semiconductor switch at 79°, and subsequently turns-on at the symmetric angle of 101°, the resulting RMS value will clearly be greater than was requested. This problem can be overcome by using an asymmetric turn-on angle, where the second on period in the half cycle is equal to or less than the first on period. For each pair of requested turn-off angle and actual turn-off angle due to over current monitoring, an asymmetric turn-on angle was calculated so that the RMS value of the resulting waveform is as close to the RMS value of the requested turn-off angle as possible. The calculated asymmetric turn-on angles were calculated using a Matlab script by rounding down to the nearest integer, and are presented graphically in Figure 3.19. Figure 3.20 shows the ratio of requested RMS to delivered RMS using this approach.

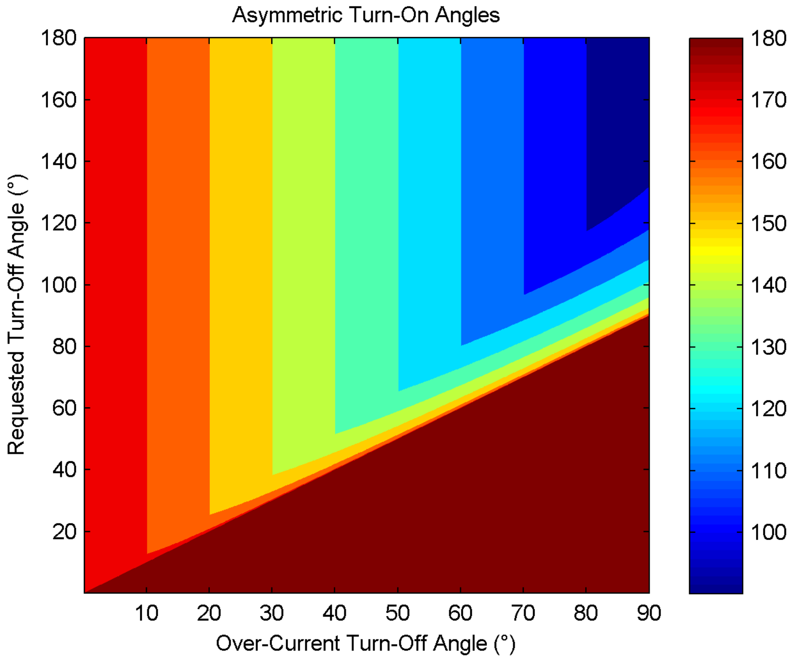

Figure 3.19 – The calculated asymmetric turn-on angle to optimize RMS current using instantaneous current limiting.

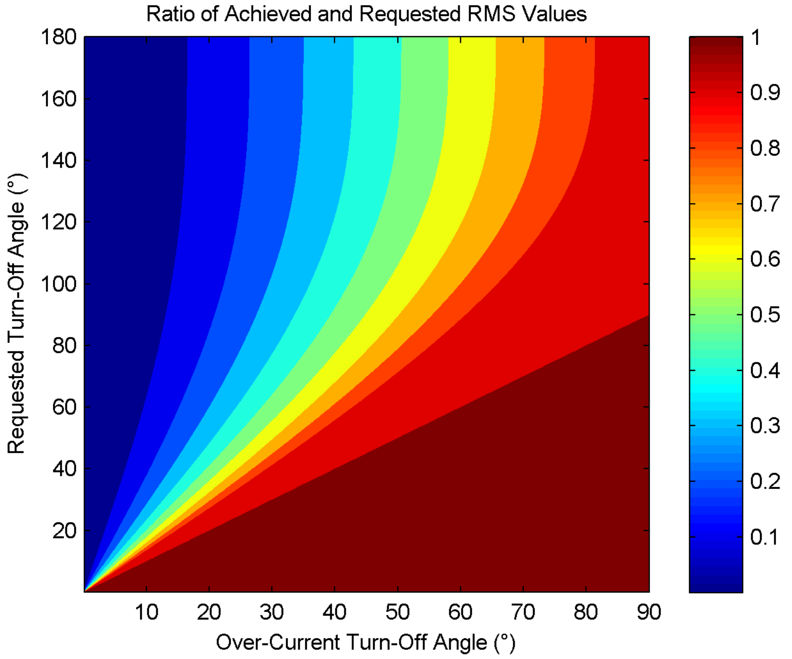

Figure 3.20 – The ratio of achieved to requested RMS current using instantaneous current monitoring and the asymmetric turn-on angles from Figure 3.19.

3.2.1.3 Zero voltage turn-off phase angle control

Although the approach of zero voltage turn-on phase angle control as presented in the previous section has the significant benefit of not requiring the sample resistance as a function of temperature to be know in advance, there is also a significant disadvantage over the conventional phase angle approach of zero-voltage turn-off: namely, the need to dissipate large amounts of energy when turning off the semiconductor switch. The need to dissipate energy comes from the switch having both current flowing through it and a voltage across it during turn-off. The electronics that were used to attempt zero-voltage turn-on phase angle control (see section 3.4.4) were unable to reliably dissipate the energy in the switch at turn-off, leading to both significant electromagnetic emission and very poor reliability. It is for these reasons that it was decided to move to a more conventional approach to phase angle control.

As previously mentioned the main problem with using a zero voltage turn-off approach is that it is necessary to know the sample resistance before the experiment, so that the applied power will not exceed the instrument's safe working limit of 2000 A RMS heating current. One possible approach would be to require the user to measure and input the sample resistance, but any error in either of those steps could lead to machine failure. The instrument avoids the necessity for the user to measure the sample resistance by prior to the heat treatment turning on a small amount of current (turn-on at 162°) that would not cause failure even with a 1 mm thick aluminium sample, and then using the instantaneous current sensor to measure the current at a specific phase angle (170°) (see Appendix 27). As both the voltage and current are known at the measurement angle, the sample resistance as seen by the heating circuit can be calculated from Ohm's law. If the apparent sample resistance is greater than or equal to 2.4 mΩ, no turn-on angle can exceed the instruments power limit; but for sample resistances lower than 2.4 mΩ, the control software calculates the maximum permissible conduction angle (minimum turn-on angle) to limit the RMS heating current to 2000 A.

3.2.1.4 Heat loss

To gain an understanding of the heat loss and sample temperature gradient during heating, a finite element model was created in COMSOL Multiphysics 4.2. The model simulated the heating due to a constant 2000 A current through a 150 x 20 x 2 mm steel sample, connected to an initial design for the sample clamps made of 316L stainless steel. The electrical resistivity of the steel sample was calculated within COMSOL by using liner interpolation based on the assumed resistivities of 24.8 x 10^{-8} Ω·m at 20°C (default value from COMSOL materials library) and 120 x 10^{-8} Ω·m at 900°C (taken from [42]). A value of 0.5 was used for the emissivity of the sample. All other material properties used the COMSOL default values.

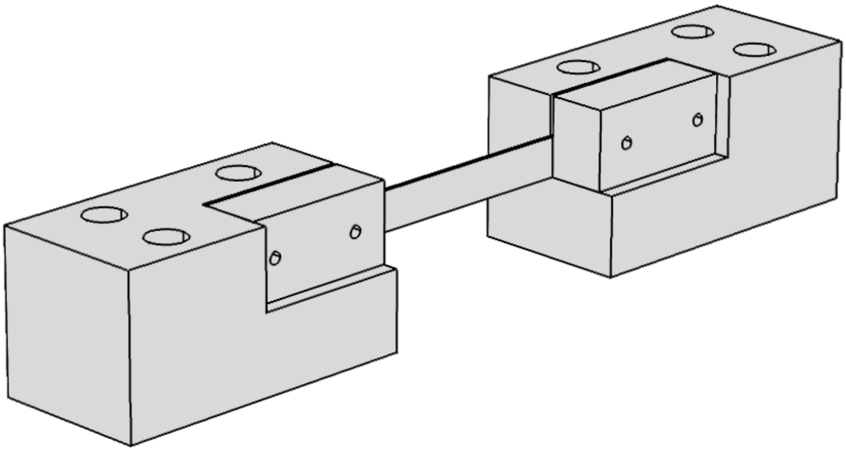

Figure 3.21 – Geometry of the heat loss finite element model.

The model accounted for conductive losses by assuming that the square ends of the sample clamps were held at 20°C. The losses due to radiation and convection heat transfer were modelled only for the sample region, as these were assumed to be much more significant than any losses from the much cooler sample clamps. The convective losses were modelled by instructing COMSOL to calculate an effective heat transfer coefficient for the top sample surface, another for the bottom surface, and a third coefficient to be used for the two large vertical faces.

The simplification of assuming a constant heating current of 2000 A, even when the sample resistance is greater than 2.4 mΩ, means that the Joule heating in the sample is over-estimated at higher temperatures. With this over-estimation of the Joule heating power the model calculated a maximum sample temperature of 1612.3°C after 2 s. The heat loss due to conduction, convection, and radiation, as well as the total heat loss are plotted against the maximum sample temperature in Figure 3.22.

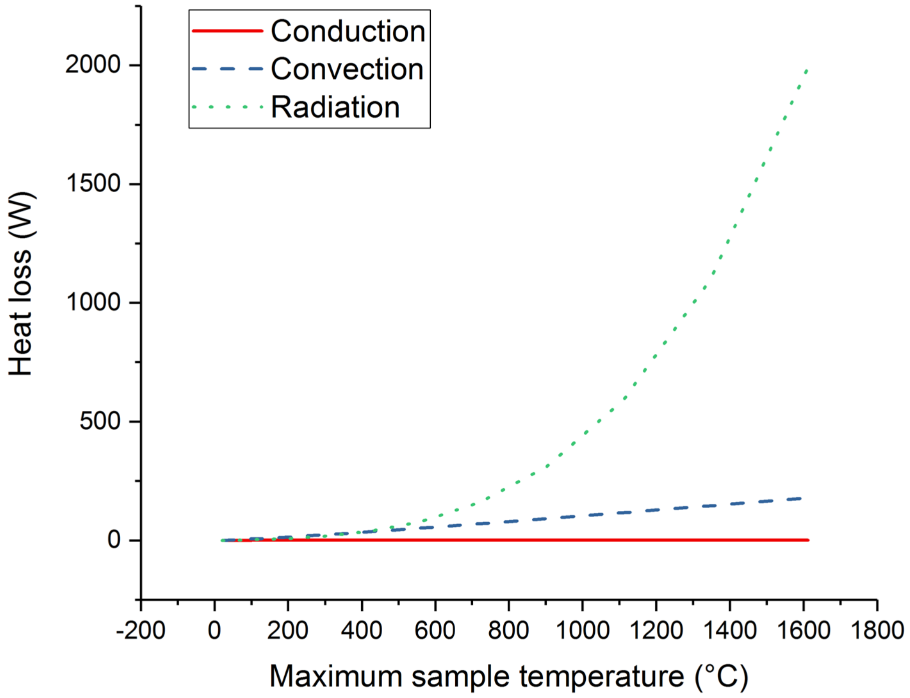

Figure 3.22 – Heat loss vs temperature during an 800°C/s heat of 2 mm thick steel.

It is desirable to have the sample temperature as uniform as possible, so that any subsequent analysis or mechanical testing of the heat treated sample is of a homogeneous test piece. A primary objective for the heat loss model was to gain an indication of the sample temperature distribution.

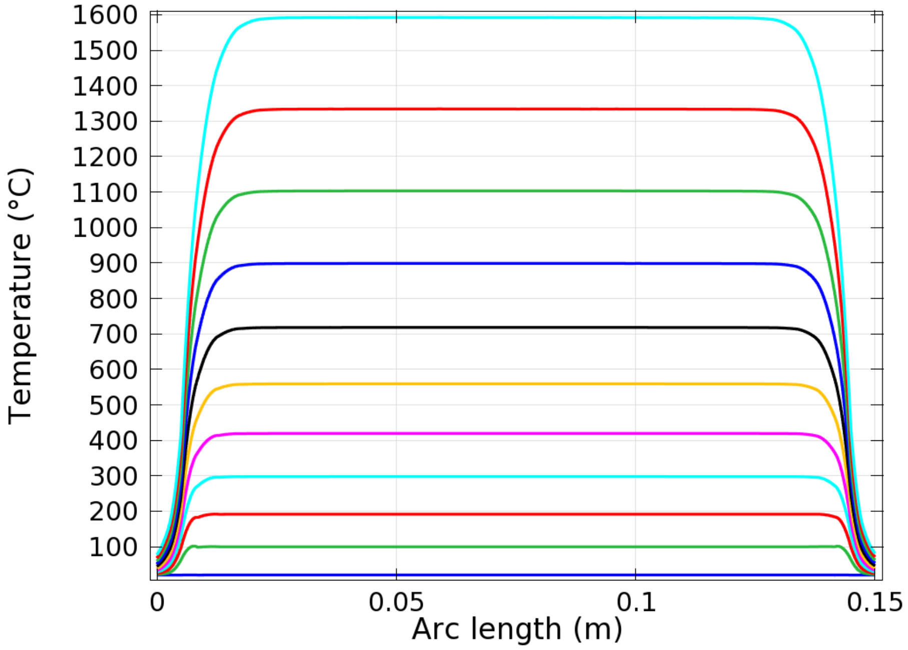

Figure 3.23 – The temperature distribution along one of the top edges of the sample at 0.2s intervals.

Figure 3.23 shows the temperature along one of the top edges of the sample at 0.2 s intervals. It can be seen from this figure that during heating the temperature gradient is largely constrained to the ends of the sample. As per section 3.1.4, only the central 75 mm would be required to produce a tensile test specimen in compliance with ISO 6892-1:2009[65]. This means that according to the results of this heat loss model it should be possible to produce tensile test specimens that have been uniformly heated, and should therefore have uniform microstructures.

As previously explained the model over-estimates the heat input from Joule heating at elevated temperatures. To more accurately estimate the maximum instrument heating rates, the average sample resistance as calculated by COMSOL was used to calculate the sample resistance at each time step. If the sample resistance was less than or equal to 2.4 mΩ, the heat input was calculated by multiplying the square of the current (2000 A) by the sample resistance. If the sample resistance was greater than 2.4 mΩ, the heat input was calculated by dividing the square of the voltage (4.8 V) by the sample resistance. Assuming a specific heat capacity for steel of 475 J/kg/°C, the heat capacity of a 47.1 mg sample is 22.4 J/°C. Subtracting the total heat loss as calculated in the model from the heat input calculated as described above, gives the net heat flux, which when divided by the heat capacity gives the heating rate. The heating rate is plotted against temperature in Figure 3.24 and the calculated results, along with the FE model results, are presented numerically in Appendix 7. At room temperature the sample resistance is below 2.4 mΩ, and the voltage must be reduced (by phase angle control) to below 4.8 V to limit the current to 2000 A. As the sample temperature increases, so does the sample resistance. As the Joule heat input is the product of the resistance with the square of the current, the heating rate increases. Once the sample temperature has increased such that the electrical resistance has increased to 2.4 mΩ, the heating rate reaches a maximum, as this is the greatest sample resistance for which a heating current of 2000 A can still be delivered. As the sample temperature increases further, and the sample resistance become larger, the voltage cannot be further increased beyond 4.8 V, and the heating current decreases. The decrease in heat input along the increase in heat loss leads to the rapid decrease in heating rate with increasing temperature.

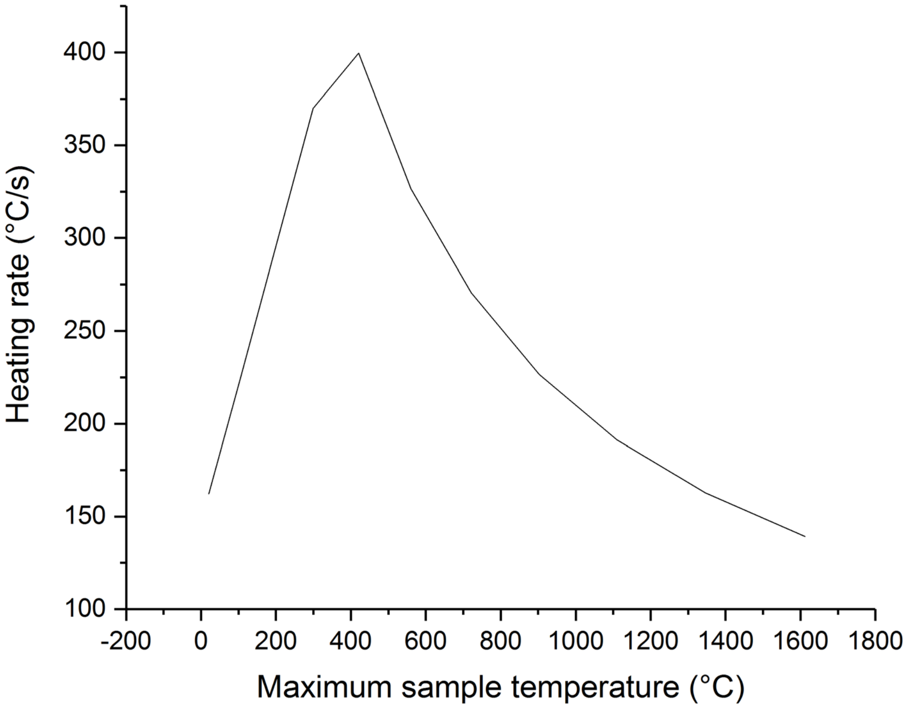

Figure 3.24 – The maximum predicted heating rate for a 2 mm thick steel sample vs temperature.

3.2.1.5 Electrical power feedthroughs (sliding contact system)

The resistance heating system uses a maximum current of 2000 A passing through the sample to heat by Joule heating (see 3.2.1.1). Electrical power feedthroughs are required that enable this level of current to enter the vacuum chamber and form a good electrical connection with the sample clamps and in turn with the sample itself. The sample must be allowed to expand freely upon heating, otherwise the internal stress will affect M_s (see 3.1.5). To enable free expansion of the samples it is necessary to either allow the samples to move relative to the clamps or to allow the clamps to move relative to the feedthroughs / vacuum chamber walls.

The simplest form of flexible coupling between the feedthroughs and sample clamps would be a loop of cable. However, the cross sectional area of cable that is capable of carrying 2000 A is so large that the size of the cable loop would be much bigger than the entire vacuum chamber and would require a force greater than the 368 N calculated in section 3.1.5 to deflect by the thermal expansion of the sample.

To overcome the inflexibility of ordinary cable, a second possibility would have been a bus bar made from copper braid, as such assemblies are designed to enable flexible electrical connections. However, the exposed surface area of copper braid could cause a significant increase in the time taken to evacuate the chamber if used with water quenching due to the adsorption of water molecules. Several manufacturers of copper braid were contacted about the possibility of manufacturing a braid that was encapsulated in PTFE to reduce the adsorption, but none of the manufacturers were able to produce a product to the necessary specifications.

The third idea for producing the flexible electrical coupling was to make use of a sliding contact. A problem with an electrical contact is that due to the surface roughness of the mating faces of the contact is that the cross sectional area will be greatly reduced at the interface [68], increasing the current density, which can cause excessive localized heating when the current is large. By compressing together sufficiently smooth contact faces it is possible to significantly increase the contact area by elastic deformation, and thereby reduce the contact electrical resistance[68, 69]. A perfectly round spherical electrode that is in contact with a perfectly flat electrode will make a point contact, but as the two are compressed together the elastic deformation of the components will lead to an increased area of contact.

The electrical power feedthroughs for the quenching simulator were designed using a form of the third idea. The flat electrode is a cuboidal electrode that penetrates the chamber wall, with a series of 48 total electrodes compressed into the four largest faces of the cuboid. The initial idea was to change the geometry of the 48 electrodes from spheres to cylinders with spherical cap contact tips. The material of choice for the cuboidal electrode was 316L stainless steel for its low vacuum outgassing and resistance to sensitization (carbide precipitation) during welding. The choice of material for the 48 electrodes was oxygen free copper for low outgassing and excellent electrical conductivity. The small face of each cuboidal electrode that faces into the chamber was recessed, and an insulating block (Macor) was secured in the recess to prevent the end of the electrode shorting to the clamp body.

The greater the force with which the copper electrodes are compressed into the stainless steel cuboid, the better the region of contact will be. However, as the compression increases so will the resistance to sliding, which will constrain the sample to a greater degree as it tries to thermally expand. The limiting value for the constraint was calculated as F_{TE} = 368 N in section 3.1.5, which can be used to calculate the maximum force with which the electrodes can be compressed. The static friction force that resists movement of the clamp when there are *n* electrodes each compressed into the feedthrough with a force of F_N is given by:

$$F_s = \mu_s \cdot F_N \cdot n \tag{3.4}$$

where μ_S is the static co-efficient of friction, which is 0.23 between copper and (304) stainless steel [70]. By setting $F_s = F_{TE}$ the maximum force compressing the copper electrode into the stainless disc can be calculated as

$$F_N = \frac{F_{TE}}{\mu_s \cdot n} = \frac{368}{48 \times 0.23} = 33.3\ \mathrm{N}. \qquad 3.5$$

As the area of contact will increase as F_N increases, the contacts will be compressed using the maximum permissible force of 33.3 N.

3.2.1.6 Finite element modelling of electrodes

To model the mechanical behaviour of the sliding copper electrodes in compression, a finite element model was created using COMSOL Multiphysics 4.2. The model was 2D axisymmetric and used the *Solid Mechanics* module to model the elastic deformation between a single copper electrode and a flat 304 stainless steel electrode. A series of five different copper electrodes were modelled, with the curvature of the spherical cap contact region taking the values of 150, 300, 1000, 2000 and 4000 mm. In each case the two components were compressed together with a force of 33.3 N (see 3.2.1.5). The boundary regions between the two components were modelled with an extremely fine mesh size (modified to have a maximum element size of 50 µm) and a fine mesh size for the remainder of the objects.

The results of the COMSOL model of the sliding contacts compression are shown in Appendix 8. It can be seen from the results that when the contact region of the copper electrode is formed from a spherical cap of small diameter, that is to say that the contact region shows steep curvature, that the von Mises stress field is highly concentrated at the tip of the electrode to the extent that the copper would undergo plastic deformation in that region (the peak von Mises stress is 194 MPa for 150 mm, but the yield strength of copper is only 33.3 MPa [71]). The results show that as the diameter of the spherical cap increases and the curvature of the contact region lessens that the von Mises stress field becomes less concentrated at the tip of the electrode and that the peak stress decreases below the yield point of the material when the diameter of the spherical cap reaches 4000 mm. The model also shows that the contact area between the two parts increases as the diameter of the spherical cap increases, going from approximately 0.62 mm^2 at 150 mm to 4.83 mm^2 at 4000 mm.

3.2.1.7 Electrode compression and conduction tests

The results of the sliding contacts finite element modelling (see 3.2.1.6) show, that with a sufficiently gentle curvature on the contact area of the copper electrode, that the elastic deformation of the copper electrode as it is compressed into the stainless steel block creates a significant region of contact. In order to test the amount of current that such an electrode can handle, two test pieces were machined from oxygen free copper, one with a flat contact region and one with the gentlest curvature that the machine shop could achieve in the contact region. A disc of 304 stainless steel was machined to represent the vacuum feedthrough. A holder for the copper electrode, made from PTFE to allow electrical isolation of the copper electrode was also machined. Drawings of the four test parts are presented in Appendix 9.

A 200 A power supply was constructed by using a custom built Birmingham Transformers 9.6 kVA single phase transformer with 4.8 V output. The primary coil of the transformer was connected in series with a phase angle controller (PAC) constructed from a United Automation CSR104B power regulator chip to enable control of the output voltage and hence the output current. A high power 60 Ω electrical resistor was made by winding nichrome wire on a hollow cylinder (I.D. = 25 mm, O.D. = 32 mm) of vitreous silica and coating the assembly with Sheffield Refractories Jonsett TA high alumina cement; this high power resistor was placed into series with the transformer primary and PAC to limit the maximum secondary current to 200 A. The electrical circuit was completed by using 25 mm^2 copper cable to connect the power supply to the copper electrode and the stainless steel disc. Electrical current in the 25 mm^2 copper cable was measured using a UNI-T UT203 Hall effect clamp meter.

To compress the copper electrode into the stainless steel disc the initial approach was to use a Hounsfield H100KS tensile / compression test machine with a 1000 N load cell. However, the H100KS was unable to accurately maintain the 33.3 N force that was required. The experiment was then modified to make use of the closed loop feedback system in a CETR UMT-2 Micro Tribometer (see Figure 3.25), which was able to maintain the 33.3 N force between the samples accurately. Each electrode was tested at 10, 25, 50, 75 and 100 A by bringing the electrode and disc into contact, allowing the force to stabilize at 33.3 N, and then increasing the current from zero to the test current. An additional test was performed for the curved electrode at 125 A, but this was not repeated for the flat electrode. In each test the electrode conducted the test current for 120 s before reducing the current to zero and separating the two components. After each test the contact surfaces of the two components were visually inspected for any signs of damage.

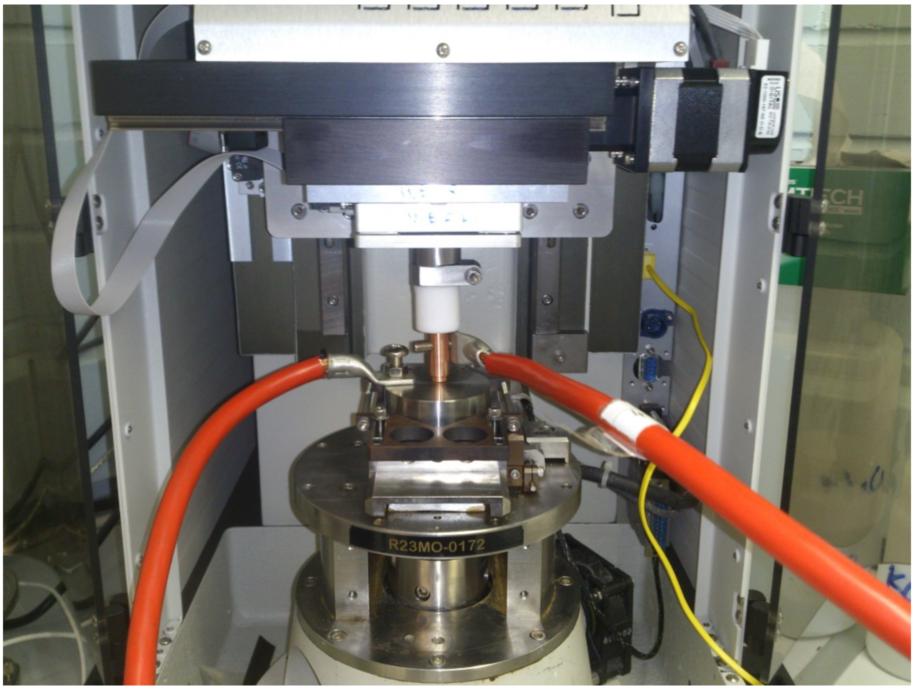

Figure 3.25 - Testing the electrical behaviour of a copper electrode compressed into a stainless steel disc using a CETR UMT-2 Micro Tribometer.

Both the electrode with the curved contact region and the electrode with the flat contact region showed no signs of damage from any of the currents up to and including conduction at 100 A. As can be seen from Figure 3.26, when the electrode with the curved contact region was tested at 125 A some damage did occur to the electrode. It should be highlighted that the damaged occurred at the edge of the contact tip (where the spherical cap intersects the cylinder) and not at the tip of the electrode: this can be explained by the difficulty that was found in trying to keep the copper electrode perfectly normal to the disc. It is likely that if the copper electrode could be kept perfectly normal to the disc that the maximum conduction current would be increased due to the increased stress field distribution / greater contact area.

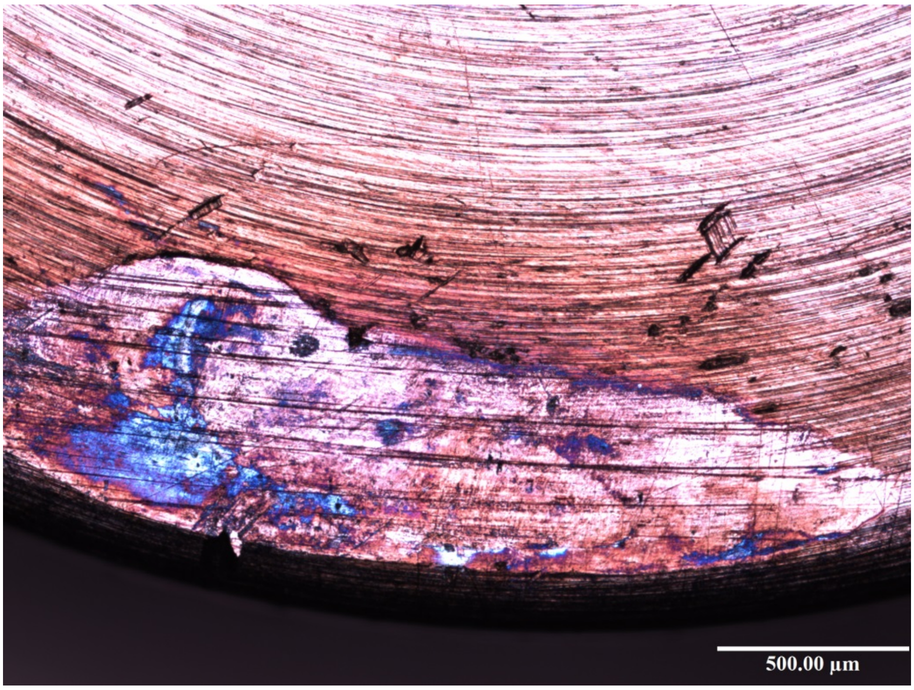

Figure 3.26 - Optical micrograph of the edge of the copper electrode with the curved contact region after conducting 125 A for 120 s.

As each feedthrough makes use of 48 copper electrodes, if the 2000 A current is distributed evenly between the electrodes this would mean each electrode carrying 41.7 A. Hence, a value of 100 A represents a safety margin of 140% to allow for uneven current distribution between the electrodes.

3.2.1.8 Sample clamp construction and cooling

The 48 copper electrodes for each feedthrough are supported in four electrically insulating holders that arrange the electrodes in an array of three by four. The holders are made from Macor, which is a machinable ceramic made by Corning. Macor was chosen for this role as it exhibits low outgassing, is an electrical insulator, can withstand temperatures up to 1000°C, can be machined using standard metalwork tools, and as it does not require firing after machining can be machined to a close tolerance.

A close fit of the copper electrodes into the Macor holders is desirable to keep the electrodes close to perpendicular to the surface of the stainless steel feedthroughs, but there needs to be some clearance to stop the electrodes from binding in the holes, and to allow for the greater thermal expansion of the copper than the Macor. As it is significantly easier to specify a non-standard external diameter for a turned part than it is for the internal diameter of a drilled hole, the holder diameter was first fixed at 9.1 mm. Assuming a maximum operating temperature of 100°C, a coefficient of thermal expansion of 90 x 10^{-7} / °C for Macor, a coefficient of thermal expansion for copper of 17.7x10^{-6} / °C, and a manufacturing tolerance for both the internal and external diameters of ±50 µm, the electrode body diameter can be calculated as follows. The diameter of the holder bore at 100°C can be calculated as:

$$\varnothing_H^{100°C} = 9.1 \times (1 + 90 \times 10^{-7} \times 75) = 9.106\,mm. \tag{3.6}$$

Summing the machining tolerance of both components enables the maximum electrode diameter at 100°C to be calculated as:

$$\varnothing_E^{100°C} = 9.106 - 0.05 = 9.006\,mm. \tag{3.7}$$

This gives an electrode body diameter at 25°C of:

$$\varnothing_E^{25°C} = 9.006 \times (1 - 17.7 \times 10^{-6} \times 75) = 8.994\,mm. \tag{3.8}$$

The final designs for the electrodes and electrode holders are shown in Appendix 10 and Appendix 11. The electrodes were manufactured by Shakespeare Engineering, South Woodham Ferrers, and the electrode holders were manufactured by Multi-Lab, Throckley. Inspection of the drawings shows that the electrode tip diameter was chosen to be 350 µm smaller than the matching hole in the holder, this is more than three times the clearance between the electrode body and the holder, as a close fit is not required to maintain electrode orientation. Given the electrode body length of 6.4 mm, the maximum angular deviation of the electrodes from perpendicular at 25°C, which will occur when the holder is oversize and the electrode body diameter and length are undersize, can be calculated as:

$$\theta = sin^{-1}\left(\frac{(9.1 + 0.050) - (8.994 - 0.050)}{(6.4 - 0.050)}\right) = 1.86°. \quad 3.9$$

To compress the copper electrodes into the stainless steel electrodes, a spring was placed between the copper electrode and a retaining cap with a series of wells to locate the springs. The free length of the springs is 8 mm, and as the distance between the rear shoulder of the electrodes and the bottom face of the retaining cap wells is only 7.6 mm, each spring is compressed by 0.4 mm upon assembly. With the clamp fully assembled, but without the stainless steel feedthrough inserted, the electrodes are pressed into the Macor holders, and the distance between the tips of two opposite copper electrodes is 36 mm. Appendix 12 shows the construction of the stainless steel feedthrough, from where it can be seen that the section width of the cuboidal insert is 37 mm. As the width of the insert is 1 mm greater than the space between the electrode tips, each pair of springs must be compressed by an additional 1 mm when the feedthrough is inserted, giving a total spring compression of 0.9 mm. The springs were custom made by Lee Spring Ltd, Wokingham to have a load of 33.3 N when compressed by 0.9 mm, which is the required force as calculated in section 3.2.1.5. The springs were constructed from beryllium copper wire with a diameter of 1.5 mm and were silver plated to reduce the electrical resistivity as the springs also fulfil the role of electrically connecting the copper electrodes to the clamp bodies through the retaining caps.

To reduce shear loading of the feedthrough from the weight of the assembled clamps, the clamp bodies are fitted with a dovetail clamp that fits on a matching dovetail bed made from PTFE. The bed is made from PTFE as it offers a very low coefficient of friction, which reduces the constraint on the sample during heating, has low outgassing in vacuum conditions, and electrically isolates the clamp bodies from the vacuum chamber.

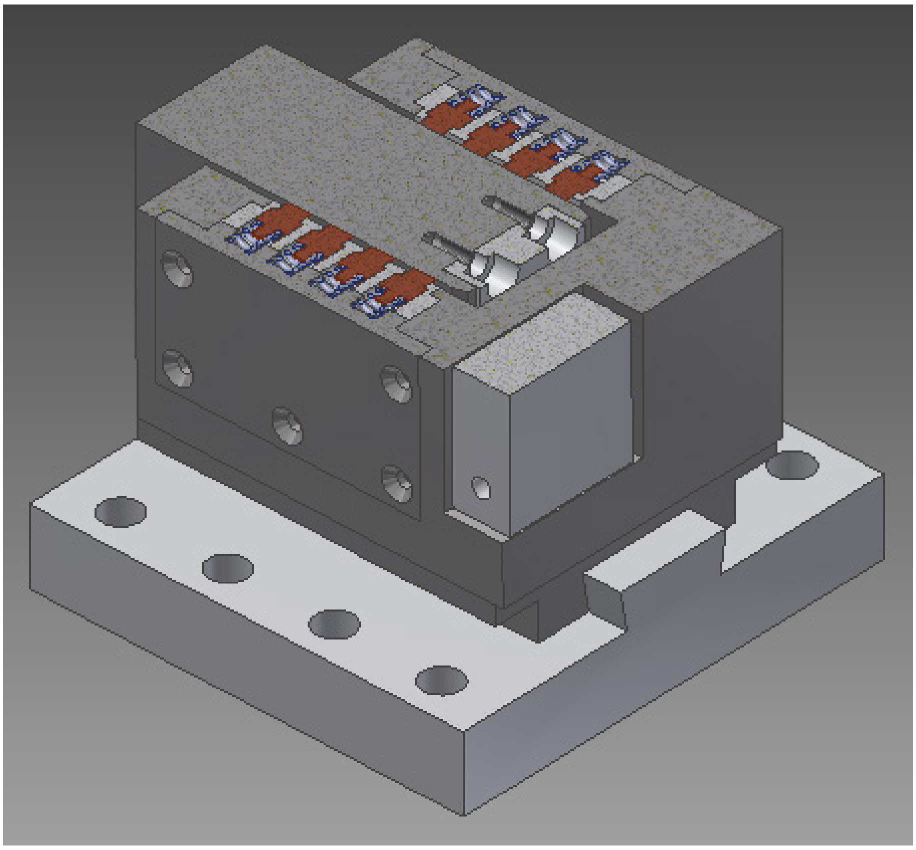

Figure 3.27 - Cutaway of a sample clamp with the feedthrough inserted.

Due to the direct thermal connection between the sample clamps and the heated sample it is important to have a means of cooling the clamps during operation. The initial plan was to manufacture the clamps using additive layer manufacture (ALM) to enable an internal cooling circuit to be placed within the clamp bodies that would cool the region both near the sample contact and the sliding electrodes. To test the suitability for vacuum service of ALM components, a cylinder closed at one end and with a KF25 vacuum flange at the other end were manufactured on my behalf from 316L stainless steel powder using a Renishaw SLM125 selective laser melter. The component was tested using an Edwards Spectron 300E leak detector by directly connecting the KF25 flange of the component to the detector. The leak rate of the component was shown to be in excess of 10^{-3} mbar·l·s^{-1}, which is several orders of magnitude greater than is normally specified for vacuum components. A second test component (Figure 3.28) was made using the SLM125, with a different build orientation in an aim to reduce porosity. The modified component was also checked with the Spectron 300E, but displayed similar leak rates. The second component was subsequently sintered for 2 hours at 1360°C in an attempt to further reduce porosity, but when tested using the Spectron 300E the leak rate remained greater than 10^{-3} mbar·l·s^{-1}.

Figure 3.28 – The second ALM test piece to investigate the possibility of using selective laser melting to manufacture vacuum leak tight components.

Due to the difficulty in creating a simple ALM component that is leak tight, the challenge in creating a component as complicated as the sample clamps that is leak tight was judged to be too great given the many other challenges in this project. Investment casting was briefly considered as an alternative manufacturing route that would enable a complex internal cooling path, but this was adjudged to have a low chance of success. The final manufacturing method to be considered for placing an internal cooling circuit within the clamp bodies was to create the paths by drilling a series of interconnected holes that would then be plugged and welded at the surface. However, the downside of this approach is the great difficulty in trying to drill the long thin holes that would be needed to carry the coolant near the feedthrough and electrical contacts.

To compare how the cooling capability of a reduced cooling circuit that is present only near the sample to the more complex cooling circuit originally envisaged, the two different cooling circuit layouts were modelled in ANSYS Fluent. Each geometry was modelled for a coolant input pressure of 2 bar, an input pressure of 4 bar, and an input flow rate of 1 m/s. In all six cases the temperature of the input coolant was 300 K. The only heat source was that the clamp face that makes contact with the sample was held at a constant temperature of 1273 K. The coolant was thermally coupled to the conduit walls, and the heat flux through all other faces was zero (perfect insulation). The clamp body used the default ANSYS Fluent parameters for steel, and for the coolant the default properties for water were used. In all models the coolant inlet is the bottom connection and gravity is assumed to be 9.8 m/s^2. It should be noted that the heating effect from current flow in the clamp body and across the electrical contacts was not modelled. The joule heating in the body can reasonably be assumed to be much smaller than the joule heating in the sample. However, the joule heating across the contact-feedthrough interface may have a more significant effect, nevertheless this was not included in the model as there was insufficient data to make reliable assumptions about the heat generated.

The numerical results from the six models are presented in Appendix 13, which show that the complex cooling circuit has a greater pressure drop between the input and outputs for a given flow rate than the drilled and filled cooling circuit. Both geometries show an increased cooling effect with increased coolant flow rate, but the increase in cooling effect is less than may have been expected (see Figure 3.29). Appendix 14 contains images showing the clamp body surface temperatures for the six modelled conditions.

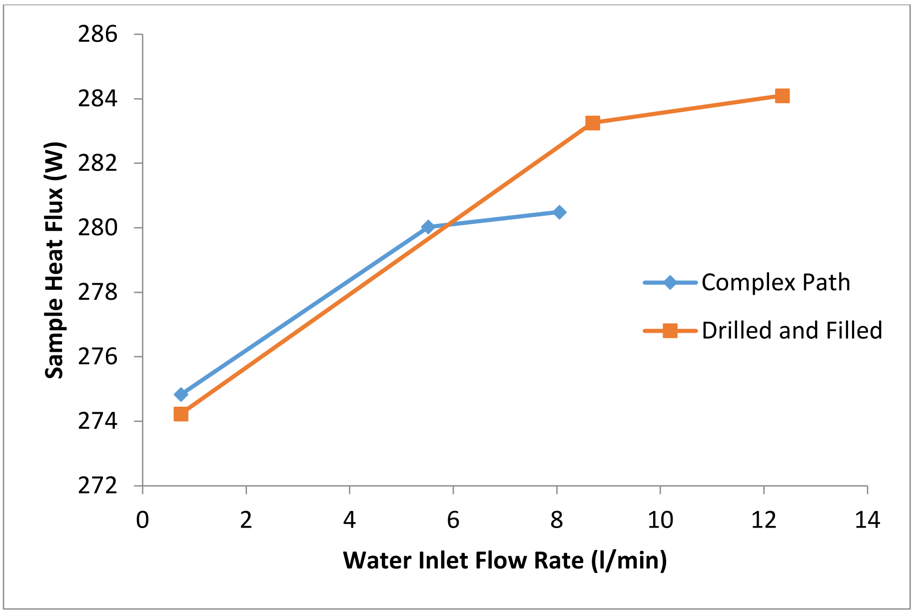

Figure 3.29 – The heat removal rate for the different clamp geometries vs. coolant flow rate.

The results of the ANSYS Fluent model on cooling performance were used to support the decision to manufacture the clamp bodies from a solid billet of 316L stainless steel. The clamps, along with the electrode retaining caps, were manufactured by Agemaspark Ltd, Doncaster. The cooling circuit was manufactured by drilling blind holes for the coolant flow paths, and then inserting a plug that was welded into place for all paths apart from the input and output ports. For connecting coolant pipes to the clamp bodies, Swagelok female VCO fittings (SS-4-VCO-3-4MTW) with connecting nuts already in place (SS-4-VCO-4) were welded to the input and output ports of both clamp bodies. The rectangular holes for the power feedthroughs were made by electro discharge machining (EDM). All other features were realized using conventional machining operations. The drawings for the clamp bodies and retaining caps are presented in Appendix 15 and Appendix 16.

3.2.1.9 High current cable

Standard electrical installations tables such as those found in BS EN 60204 [British Standards Institute72] are used to select a cable cross sectional area (CSA) that is appropriate for the installation type. However, the 2000 A heating current is significantly beyond the currents listed in such tables. For example, table 6 in BS EN 60204 specifies that cables of CSA from 0.75 to

120 mm^2 are suitable for maximum currents from 10 to 240 A when not enclosed. Extrapolating from table 6 in BS EN 60204 suggests a cable CSA of 2591 mm^2, which is a diameter of 101.8 mm. As the weight and cost of such a cable would be significant it was decided to look at the cable voltage drop as a starting point to determine a suitable cable CSA. If the maximum permissible voltage drop along the estimated 2 m of cable is chosen to be 0.1 V, then with a resistivity of 1.72x10^{-8} Ω·m, the minimum cable diameter should be 29.6 mm. The smallest standard cable size to meet this requirement is 1000 mm^2 cable, which has a diameter of 35.7 mm.

Cable selection tables such as those found in BS EN 60204 are based on the cable heating. To assess whether 1000 mm^2 cable would be an appropriate selection, an FEM model of the cable heating in COMSOL Multiphysics was created. To reduce the computational demands of trying to simultaneously model the convection and electromagnetic field in the cable, a first stage computational fluid dynamics (CFD) model was created to calculate an effective heat transfer coefficient for the convective heat loss. The model was a two dimensional model of an infinite length of 35.68 mm diameter copper wire, with 6.16 mm of XLPE insulation around the copper, and a further protective layer of 2.5 mm thick PVC (see Figure 3.30). The emissivity of the outer layer of PVC was assumed to be 0.91. The copper portion of the model was heated with a uniform heat source of 2.5 $°C \cdot s^{-1} \cdot \rho \cdot C_p$ in units of W/m^3, to give an approximate lossless heating rate of 2.5 °C/s. The value chosen for uniform heat source has no effect on the calculated value of the heat transfer coefficient, it only affects the rate at which the cable heats up and the time that must be simulated. For temperatures between 30 and 80°C the average effective heat transfer coefficient was found to be approximately 3.25 W/(m^2·K).

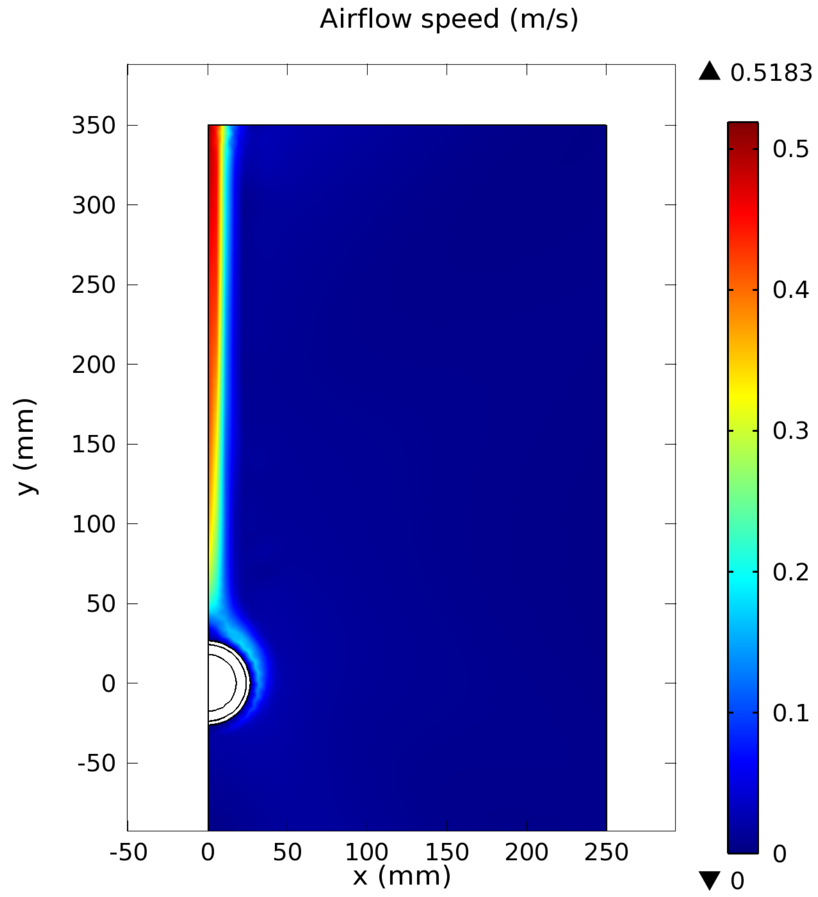

Figure 3.30 – The modelled airflow in m/s of a 1000 mm^2 copper cable with XLPE and PVC insulation after 150 s of heating with a uniform heat source.

A second 2D model of the same cable was then created using the same emissivity of 0.91, but with the convective heat loss now modelled using the effective heat transfer coefficient of 3.25 W/(m^2·K). This second model took an alternating current whose surface integral across the copper region summed to 2000 A and varied that current at 50 Hz to model the skin effect[3]. Figure 3.31 shows the how the current has been pushed to be outside of the conductor due to the skin effect.

---

[3] The skin effect is the tendency of large or high frequency currents to create a magnetic field toward the centre of a conductor that acts to push electrons towards the conductor surface, and cause a decrease in effective CSA.

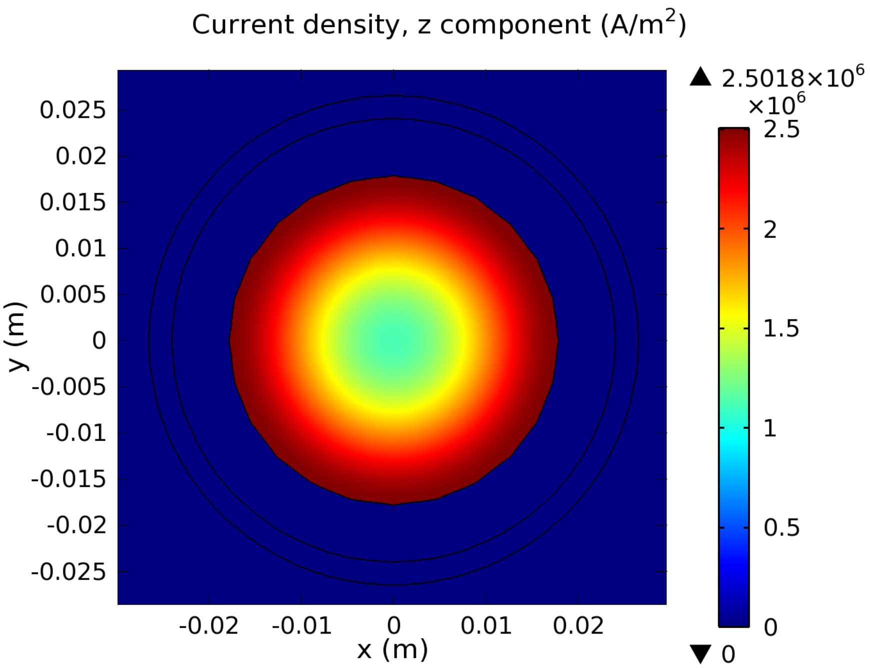

Figure 3.31 – The modelled current density in A/m² for a 1000 mm² copper cable with 2000 A 50 Hz alternating current.

Figure 3.32 shows the calculated steady state temperature distribution in the cable. The maximum conductor temperature is calculated as 125.6°C, which is significantly more than the 90°C permitted for XLPE in BS EN 60204.

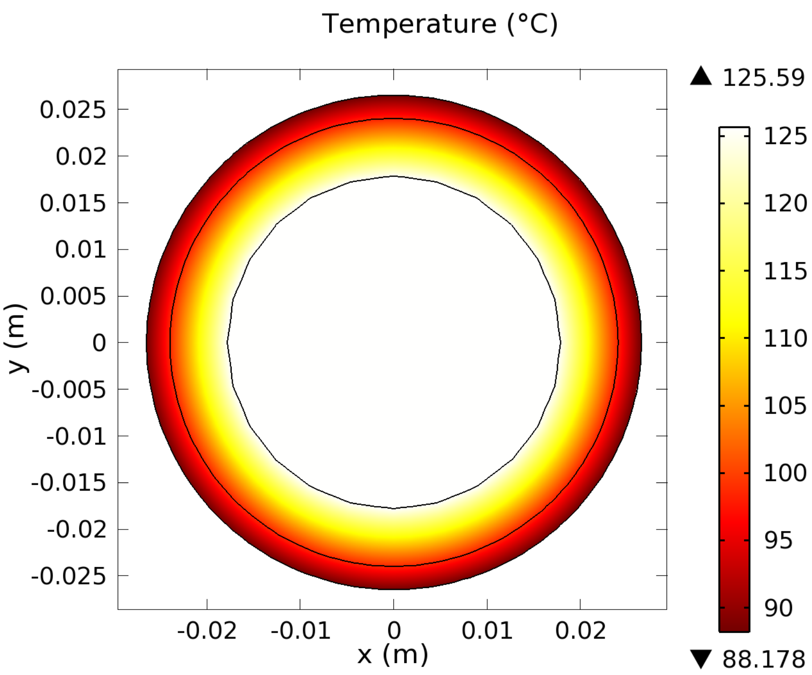

Figure 3.32 – The steady state temperature distribution in °C of a 1000 mm² copper cable with 2000 A 50 Hz alternating current.

As the same voltage drop can be achieved from two 500 mm^2 conductors as one 1000 mm^2 cable, it was decided to investigate whether the increased ratio of surface area to volume and reduced diameter of two cables carrying 1000 A would lead to a reduced temperature. As per the 1000 mm^2 cable, a first stage model was constructed to calculate the effective heat transfer coefficient to represent the convective heat loss. For this model the copper diameter was 25.2 mm, with a 4.63 mm thick layer of XLPE insulation, surrounded by a 1.5 mm thick protective layer of PVC. For the 500 mm^2 wire the average effective heat transfer coefficient was calculated to be approximately 4.0 W/(m^2·K). Using the calculated heat transfer coefficient in an electromagnetic model for the 500 mm^2 cable shows a much less pronounced skin effect (Figure 3.33) than for the 1000 mm^2 cable.

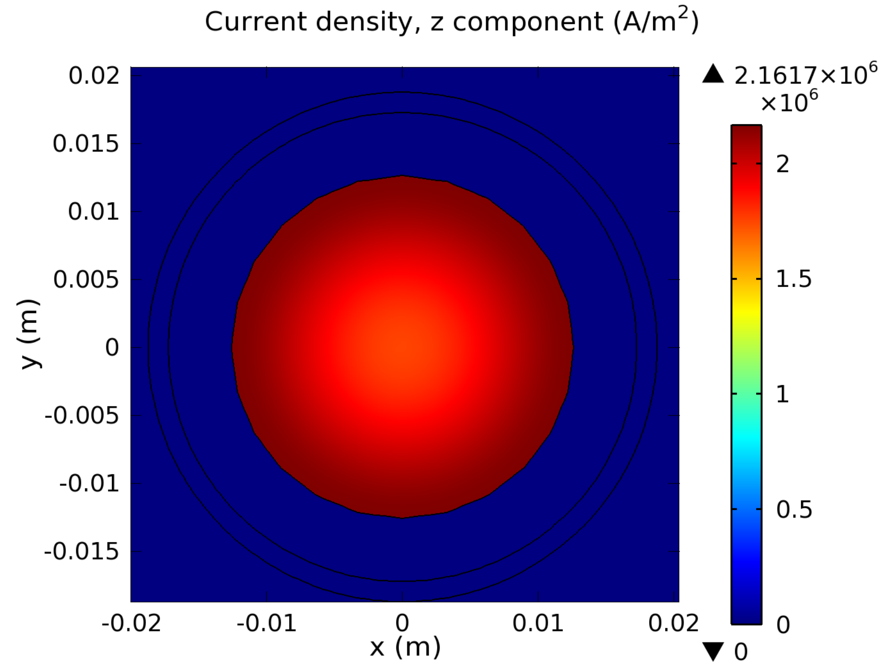

Figure 3.33 – The modelled current density in A/m^2 for a 500 mm^2 copper cable with 1000 A 50 Hz alternating current.

The reduced skin effect lessens the reduction in effective CSA, which in turn lessens the increase in resistance and joule heating. This reduction in joule heating, coupled with the increase in the ratio of surface to volume leads to the cooler temperature distribution of Figure 3.34. The maximum conductor temperature of the 500 mm^2 cable is now 69.9°C, which is easily within the 90° limit for XLPE insulated cable in BS EN 60204.

To implement this solution, 500 mm^2 1 kV XLPE cable was purchased from Cleveland Cable Company Ltd, Middlesbrough. To connect the cable to the feedthroughs and to the transformer secondary terminals, four Nexans C400-630x16 mechanical cable lugs were purchased; these mechanical cable lugs facilitate the fitting of crimp style connectors, without the necessity for large hydraulic crimpers, through the use of shear bolts that permanently secure the cable. Figure 3.35 shows two of the cables terminated with the mechanical cables lugs and connected to one of the power feedthroughs.

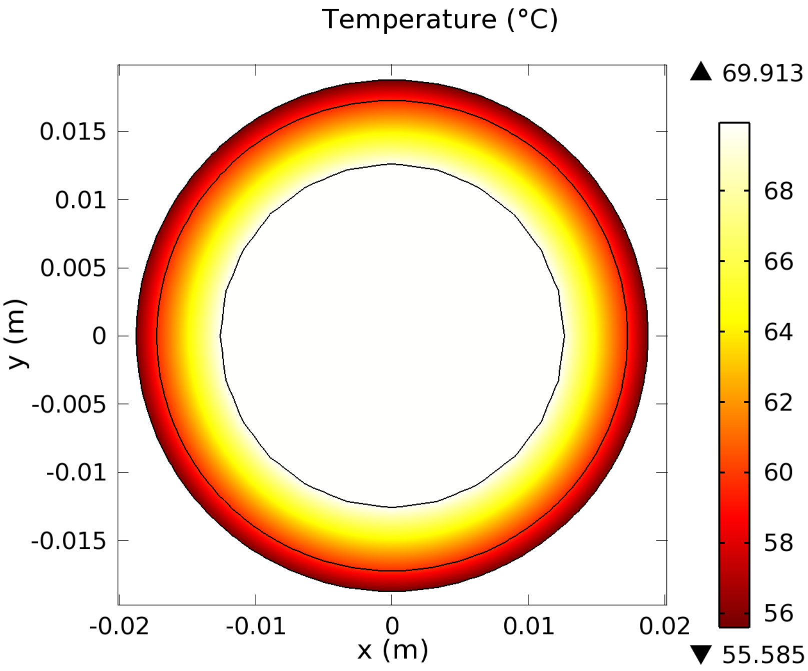

Figure 3.34 – The steady state temperature distribution in °C of a 500 mm^2 copper cable with 1000 A 50 Hz alternating current.

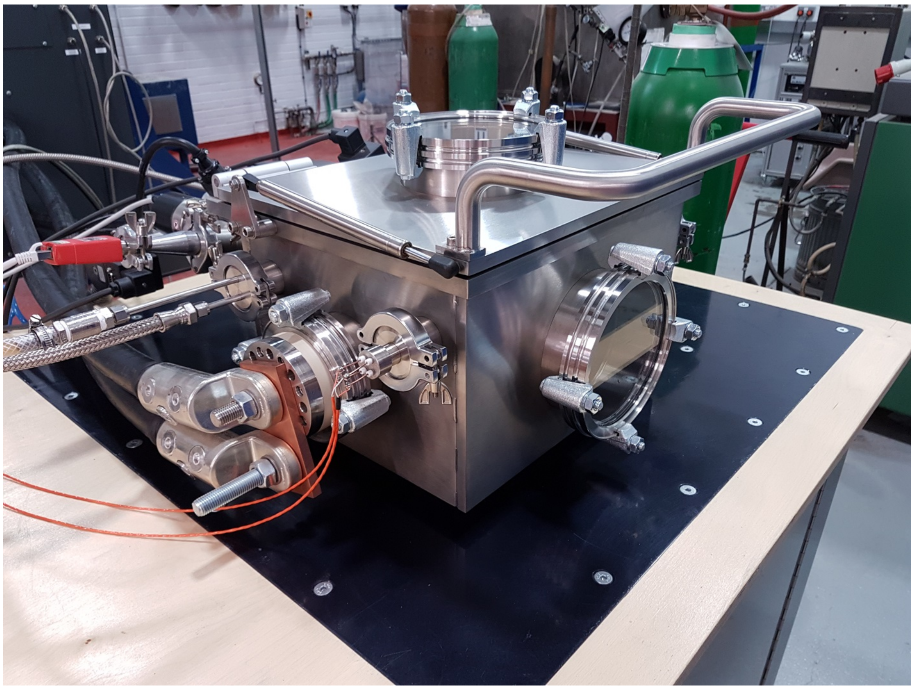

Figure 3.35 – The two 500 mm2 cables can be seen coming from one of the transformer secondary terminals to one of the power feedthroughs.

3.2.2 Quenching system

3.2.2.1 Experimental determination of cooling rates

Due to the increasing price and poor availability of helium [73] it was decided that the quenching simulator would need to make use of argon instead of helium for the inert atmosphere. However, given that the thermal conductivity of argon is only 12.4% of that of helium [71] it was felt necessary to assess the cooling rates that could be achieved using jets of argon gas to ensure that it would exceed the critical cooling rate for martensite formation in the alloys of interest.

A Delavan LF20-80° flat cone spray nozzle was used to form an argon jet and was also used with ordinary mains water for comparison. Cooling rates were also measured using a Delavan CCR2.0-80° flat cone Cool-Cast nozzle (designed for use in continuous casting applications) to atomize water with argon. A third nozzle was made from a section of 15 mm copper pipe that had a series of 14 x 1 mm holes on the surface whose centres were on a line parallel to the z-axis of the pipe: this nozzle was used with argon as the quenching fluid.

Table 3.3 - Chemical composition of the steel used to assess spray nozzle cooling rates.

Alloying Element	C	Mn	S	P	Si	Nb	Al	N
10^{-3} wt. %	252	2220	1	15	114	40	32	4.5

A steel alloy of composition shown in Table 3.3 was cast, homogenized, hot rolled and then cold rolled to 1mm thick 150 mm wide strip at ArcelorMittal Maizieres Research. A series of 150 x 20 x 1 mm samples were cut from the cold rolled strip, where the longest dimensions of the samples were parallel to the transverse direction (TD) of the sheet. A type K thermocouple was attached to the sample using nichrome wire such that the thermocouple junction made contact with the centre of one of the large faces of the sample being tested. The thermocouple temperature was recorded both during heating and cooling using a PicoScope TC-08 thermocouple data logger connected to a personal computer.

The samples were individually placed into the centre of a tube furnace set to 1100°C and left for the temperature to stabilize[4]; a constant flow of argon was maintained through the tube of the furnace during heating to reduce oxidation and decarburization of the samples. The samples were then removed from the tube furnace using heated tongs and placed into holders made from fire brick so that the 20 mm dimension (RD) was normal to the ground. As soon as the samples were placed into the holders, the cooling jet was activated so that it impinged onto the face of the sample opposite the face to which the thermocouple was attached (Figure 3.36). The cooling jet remained active until the temperature stabilized at a minimum. The experiments were repeated using new samples for the conditions listed in Appendix 3, with each condition being used three times. Argon pressure was controlled using a BOC 8500 two stage regulator, and water pressure was controlled using a gate valve and pressure gauge fitted to the faucet: in

---

[4] The heating time was not measured for each sample but was normally a few minutes. A single experiment was conducted on a sample that was heated for 1 hour, and there was no difference in the cooling rate measured for that sample and a sample heated for a few minutes when both were allowed to cool naturally.

both cases, pressure was set during flow prior to quenching and was not modified during the quench.

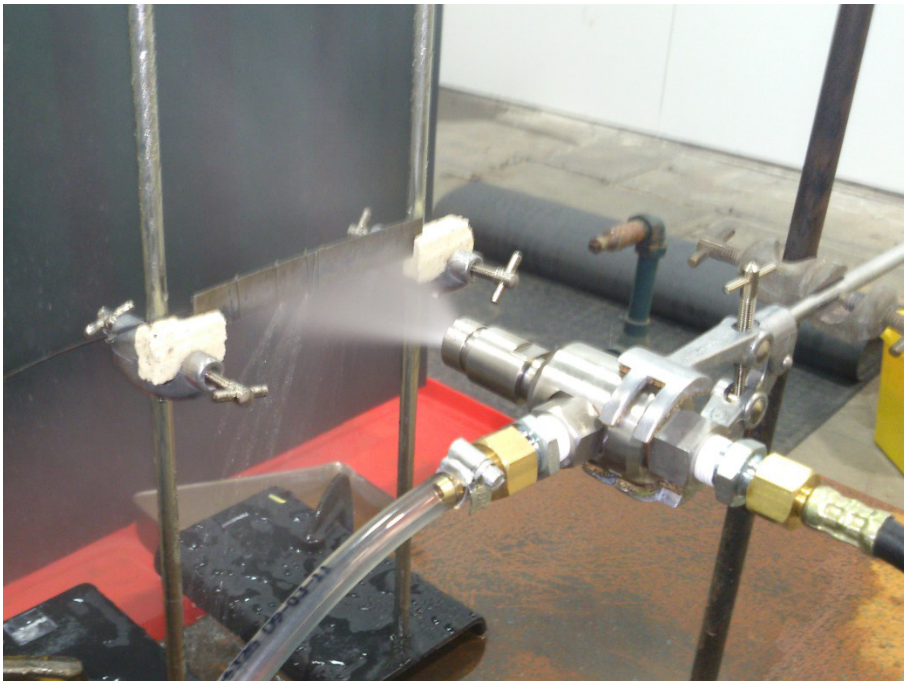

Figure 3.36 - Measuring the cooling performance of a Delevan CCR 2.0-80° Cool-Cast nozzle using argon to atomize mains water.

The cooling curves obtained from the various experimental conditions listed in Appendix 3 are presented in Appendix 4. Appendix 4A shows the cooling curves that were obtained for samples that were allowed to naturally cool: the curves showing an exponential type decay in temperature. The cooling curve for sample A3, which was austenitized for approximately 1 hour is also included in the Appendix 4A and it can be seen from inspection of the figure there is no apparent difference in cooling between that sample and the samples that were austenitized for a few minutes.

Appendix 4B and Appendix 4C contain the cooling curves for the water cooling and the argon atomized water cooling[5]. The curves in both of these sections can be broken down into the same constituent regions: there is an initial phase of natural cooling as the sample is removed from

---

[5] It should be noted that results from only two experiments using the Delavan LF20-80° flat cone spray nozzle using argon at a pressure of 6 bar are included in the results as the temperature data failed to record for one of the experiments.

the furnace and placed into the clamps; next there is a knee where the cooling spray gradually turns on; and finally there is a much steeper region of exponential temperature decay when the spray is fully operational. The initial region of natural cooling shows similar rates for all the different conditions, but there is some significant variation in the start temperature of the knee region, which can be attributed to the slight variations in time taken to remove the sample from the furnace, placed into the clamps and actuate the cooling jet. The knee regions show greater variation for the atomized water cooling, and it is suggested that this is because it was necessary to individually actuate the water and argon and that the relative timings of those actuations affected these transition cooling regions. Average cooling rates are presented in Appendix 5, where Appendix 5A shows the average cooling rate from 1050°C to 50°C. However, because of the experimental difficulties previously described, calculating a cooling rate over the region 1050°C to 50°C underestimates the nozzle cooling rates because it includes both the unforced and transition cooling regions that have much lower cooling rates. To ensure that only the cooling dominated by the spray nozzles is considered in the calculation of the average cooling rates, the cooling rates presented in Appendix 5B are for the interval 700°C to 400°C. It can be seen in Appendix 5B that all of the forced cooling methods exceed the minimum cooling rate of 27°C/s specified in section 3.1.1. A factor that has likely caused an under recording of cooling rates is due to the thermocouple position: as the thermocouple was placed on the face opposite to that being cooled by the fluid jet, the temperature being recorded was of the hottest face of the sample; indeed, during argon quenching it was possible to see the face with the thermocouple attached still red, whilst the face impinged by the fluid having already cooled to a dull grey.

Appendix 4D and Appendix 4E contain the cooling curves obtained using argon cooling with the Delavan LF20-80° flat cone spray nozzle and the nozzle manufactured from copper pipe. The curves in both these sections show initial unforced cooling regions, barely perceptible transition cooling regions, and regions where the cooling is dominated by the argon jets. Both sets of argon cooling curves show that the unforced cooling regions end at a much higher temperature than when using water cooling: this is because when using water cooling it was necessary to perform the quenching slightly away from the furnace for electrical safety, but when using argon quenching it was possible to place the clamps adjacent to the furnace to minimize the time between removing the sample from the furnace and commencing quenching. In Appendix 4E one can see an artefact in two of the cooling curves where the temperature appears to abruptly drop approximately 200°C, before increasing by a similar amount to re-join the previous slope of the curve: this was caused by electromagnetic interference between the furnace and the PicoScope TC-08 thermocouple data logger when the furnace elements switched on.

To assess whether the achieved cooling rates exceeded the critical cooling rate for a fully martensitic transformation, one sample quenched using a Delavan LF20-80° with 2.1 bar water (B16), another sample quenched using the nozzle made from copper tube with 8 bar argon (C36), and a third sample that was produced by quenching into a container of cold water (C38A) were analysed using X-Ray diffraction (XRD). The samples were prepared for XRD by cutting a 14 mm wide strip from one side of the centre of each sample. Any scale was removed using 400 grit silicon carbide paper to reveal the bare metal before cleaning in acetone. The XRD was performed using a Siemens D5000, using Cu Kα radiation with an average wavelength of 1.54178 Å. The aim of performing XRD was to enable calculation of the volume fraction of martensite by comparing the intensity of the (110) plane from the BCC ferrite with the intensities of the (101) and (110) planes for the BCT martensite [56]. However, as can be seen from the XRD data in Figure 3.37, Figure 3.38, and Figure 3.39 the resolution of the diffractometer was such that it was not possible to see the separation of the cubic (110) planes into the tetragonal (101) and (110) planes: the low carbon content of this alloy would cause a low degree of tetragonality [74], which makes it very difficult to resolve the (101) and (110) planes. Rietveld analysis [75] can be used to extract hidden peaks from diffraction data by refining the fit of computed data to fit the experimental results: Rietveld analysis was attempted using EXPGUI [76] / GSAS [77], but this technique was unable to extract any additional information.

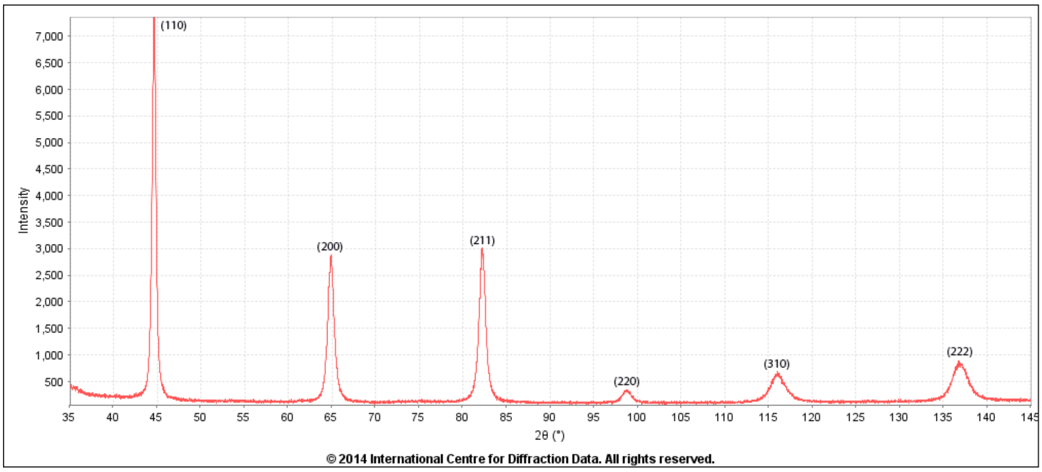

Figure 3.37 - XRD Diffraction data for a sample quenched using a Delavan LF20-80° with 2.1 bar water (B16).

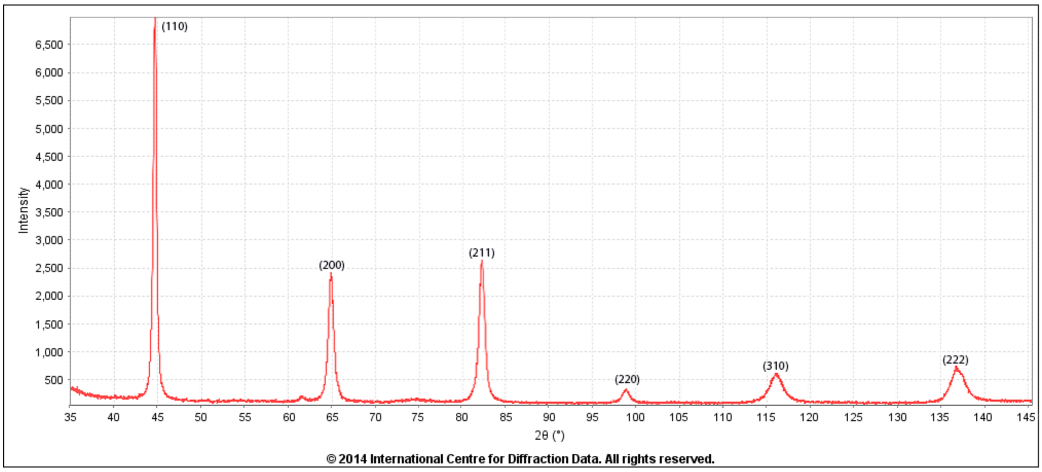

Figure 3.38 - XRD Diffraction data for a sample quenched using the nozzle made from copper tube with 8 bar argon (C36).

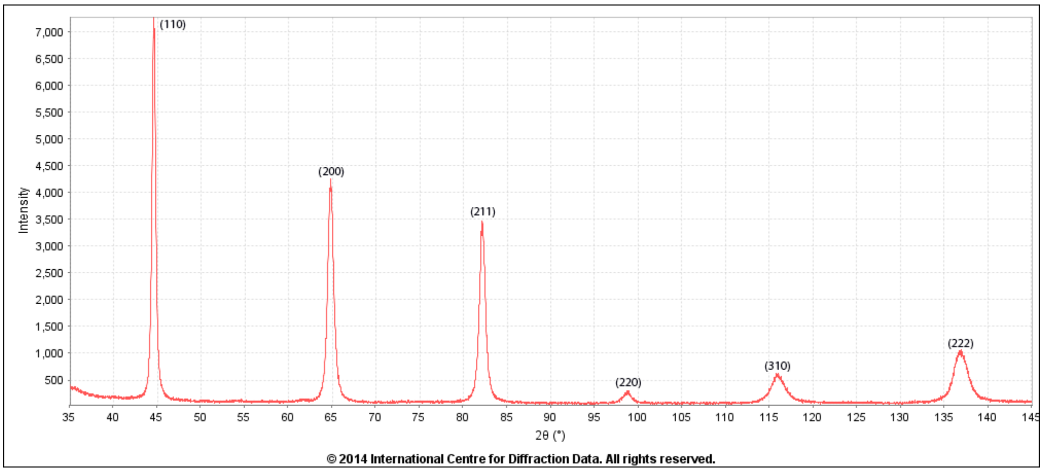

Figure 3.39 - XRD Diffraction data for the sample quenched by submersion into water (C38A).

As XRD proved unable to yield any quantitative information about the fraction of retained austenite, the three samples were mechanically ground and polished, etched using nital (methanol – 1% nitric acid) and microscopically examined using an FEI Inspect F field emission gun (FEG) scanning electron microscope (SEM). The micrographs for the three samples can be seen in Figure 3.40, Figure 3.41, and Figure 3.42. Comparison of the micrographs shows no obvious microstructural differences between the samples: assuming that the sample quenched by submersion in water had a fully martensitic microstructure, this would suggest that the cooling rate achieved for sample C36 of 51.9°C/s (calculated from 700°C to 400°C) is greater than the critical cooling rate to achieve a fully martensitic transformation in this alloy.

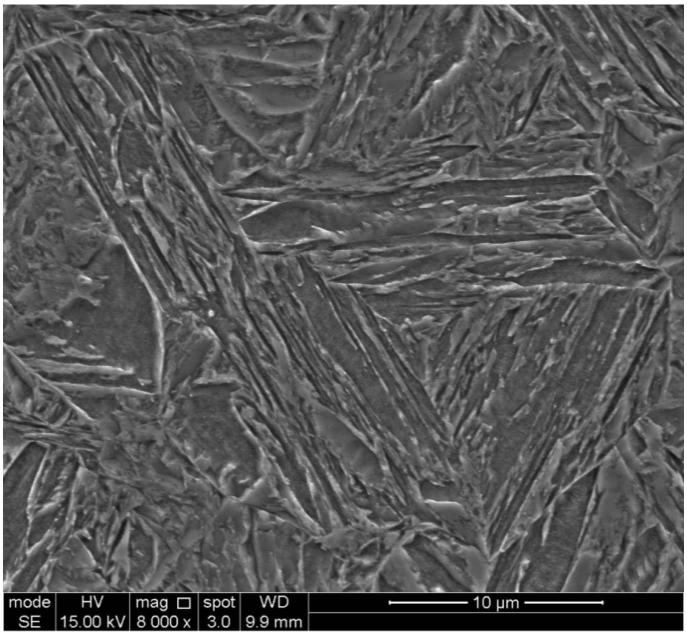

Figure 3.40 – SEM micrograph of a sample quenched using a Delavan LF20-80° with 2.1 bar water (B16).

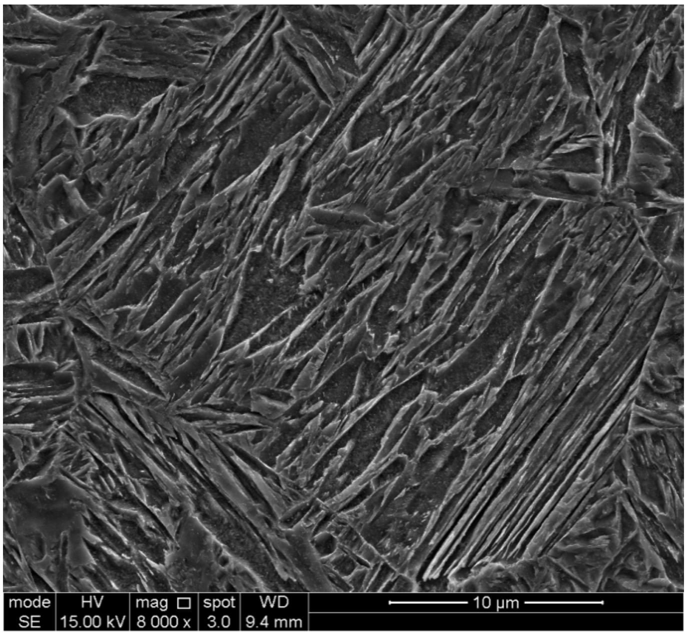

Figure 3.41 - SEM micrograph of a sample quenched using the nozzle made from copper tube with 8 bar argon (C36).

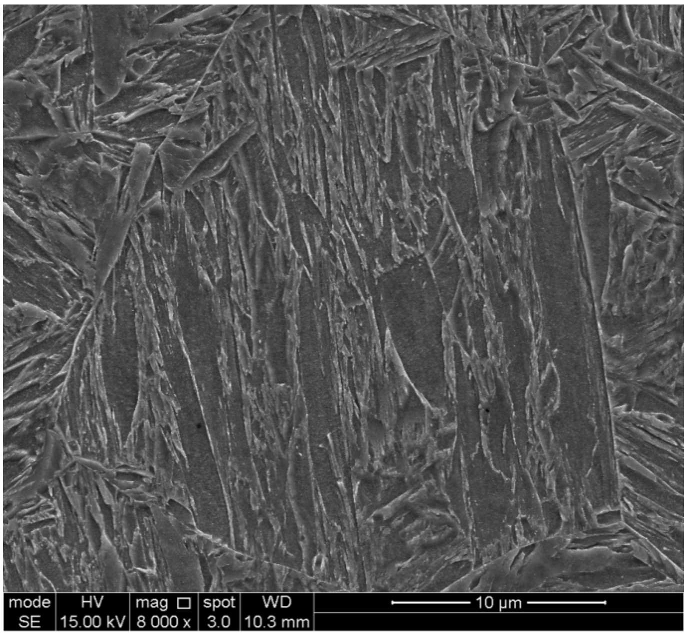

Figure 3.42 - SEM micrograph of the sample quenched by submersion into water (C38A).

3.2.2.2 Quenching system

The results of section 3.2.2.1 indicate that argon quenching is sufficient to quench certain steel alloys sufficiently fast to produce a fully martensitic structure. The quenching system has been designed to use primarily argon quenching; however, it was also reasoned that the system should be designed to enable the addition of water quenching should faster cooling rates prove necessary. The most obvious consequence of the choice to offer the potential of water quenching is the subsequent inclusion of a large gate valve on the bottom wall of the vacuum chamber to allow for the easy egress of water (see 3.3.2).

The instrument uses two Delevan LF nozzles that face each other, and when a sample is inserted into the instrument, which impinge on the two largest faces of the sample. To reduce the minimum nozzle distance, whilst still exposing the full length of the samples to the quench gas, the nozzle angles were increased to 110°, which gives a minimum nozzle distance from the sample of:

$$d_{\min} = \frac{150/2}{\tan^{-1}(110^{\circ}/2)} = 48.3mm \,. \tag{3.10}$$

As the cooling rate increases with the quenching fluid flow rate, it was decided to allow computer control of the cooling rate by the use of a proportional control solenoid valve to control the quenching fluid. As no high vacuum rated proportional control valves could be found, an Asco Series 203 valve (SCG203B001) that uses 300 Hz 24 V pulse width modulated (PWM) signal to control the valve opening was initially selected to act as the sole valve between the gas bottle regulator and the spray nozzle. The output side of the nozzle is open to the vacuum chamber, and must exhibit a low leak rate to enable the achievement of a high vacuum within the chamber. Initial testing and use of the Series 203 valve appeared to support its selection as a vacuum valve, but after less than 100 actuations the valve, either through wear or contamination, was unable to produce the necessary seal to achieve pressures below 1 mbar. As no proportional control valves designed for the required level of vacuum were commercially available, it was decided to place an additional on-off high vacuum rated valve between the proportion control valve and the quench nozzle. The secondary valve is fully closed during the vacuum pumping stage and is only opened during quenching. The selected valve was a Asco Series 030 valve (SCE030B013VH), which is rated for vacuums up to $1.33\text{x}10^{-6}$ mbar (10^{-6} Torr), and uses BSPP threads that are used elsewhere in the fluid connections. This combination of these two valves allows control of the fluid flow rate and achieves the low leak rates required for high vacuum.

3.3 Vacuum system

3.3.1 Vacuum pumps

Two common types of high vacuum pump that are capable of evacuating a chamber to the required pressure are the oil diffusion pump and the turbomolecular pump.

The diffusion pump contains a reservoir of oil that is heated. Upon heating, some of the oil will vaporize and rise up a central tower to be emitted downwards and outwards through a series of nozzles. Some of the momentum of the oil emitted from the nozzles is transferred to any gas particles from the vacuum chamber that collide with the oil jets, causing those gas particles to move towards an area of higher pressure that is lower in the diffusion pump [78]. The oil jets are contained by the cooled outer wall of the diffusion pump. As the oil is cooled it condenses and flows back to the reservoir to be reheated. A diffusion pump will contain additional nozzles below the uppermost layer nozzles that will then transfer additional downward momentum to any gas particles from the previous stage that collide with the oil jets. The maximum outlet pressure that a diffusion pump can tolerate ranges from 0.25 to 0.75 mbar [78], and as such must be used with a backing pump to provide the final link to atmosphere.

The turbomolecular pump also works on the principle of transferring kinetic energy to gas particles from the vacuum chamber to cause those particles to move towards a region of higher pressure. The turbomolecular pump does not make use of oil, but instead uses a series of turbine rotor-stator pairs that collide with the free gas particles, causing those particles to move towards the region of the pump with higher pressure. In normal operation the rotor blades rotate at tens of thousands of revolutions per minute by an electric motor, but if the pressure at the output end of the turbomolecular pump is too great these rear blades will be subject to viscous flow, which given a limited input torque from the electric motor, will cause the blades to slow and the pump to become ineffective [78]. Because of the limited output pressure of the turbomolecular pump, this pump must also be used with a backing pump to interface to atmospheric pressure.

The diffusion pump has much less mechanical complexity than the turbomolecular pump, which offers the advantages of reduced cost and the possibility of servicing by the user. Although the turbomolecular pump is much more complex than the diffusion pump, it does offer two significant advantages for this application. Firstly, the diffusion pump can contaminate the vacuum chamber with oil, which may affect the sample thermal etching. Secondly, the diffusion pump must be orientated vertically, as gravity must act to return the condensed oil to the reservoir, whereas the turbomolecular pump can be located in any orientation. This constraint on orientation has a direct effect on the potential pumping speed when used in the quenching simulator: the initial design was to use water quenching, which necessitated a large fluid outlet on the bottom side of the chamber. The diffusion pump would have needed to be attached to one of the chamber walls using a right angle, so as to maintain the vertical orientation. This would reduce the pumping speed as a high vacuum pump does not “suck out” gas from the chamber, but instead interacts with gas particles that have sufficient energy to desorb from the internal faces of the vacuum chamber, and whose random motion causes the particles to enter the inlet of the pump. The speed of a high vacuum pump is thus significantly affected both by the size of the opening to the chamber and the geometry of that opening. It is because of these two advantages of the turbomolecular pump that it was selected over the diffusion pump. The selected turbomolecular pump was an Oerlikon Turbovac 361 with Oerlikon Turbodrive TD20 Classic pump controller; the pump controller incorporates a DB25 PLC (programmable logic controller) connection for external electrical control.

An Oerlikon D25B rotary vane pump is the manufacturer recommended backing pump for the Turbovac 361, and was selected to serve as both the backing and roughing pump. The pump was fitted with a condensate trap to mitigate potential problems with water vapour, should water quenching be used in the future. The output of the rotary pump was connected to an exhaust filter to lessen any oil vapours emitted by the pump.

The vacuum pumping speed can be seen in Figure 3.43, which shows the chamber pressure against time for chamber evacuation of a titanium sample. It should be noted that the eight machine screws that secure the electrical connector brackets to the chamber were not vented, which caused a virtual leak in the chamber and significantly slowed down the chamber evacuation.

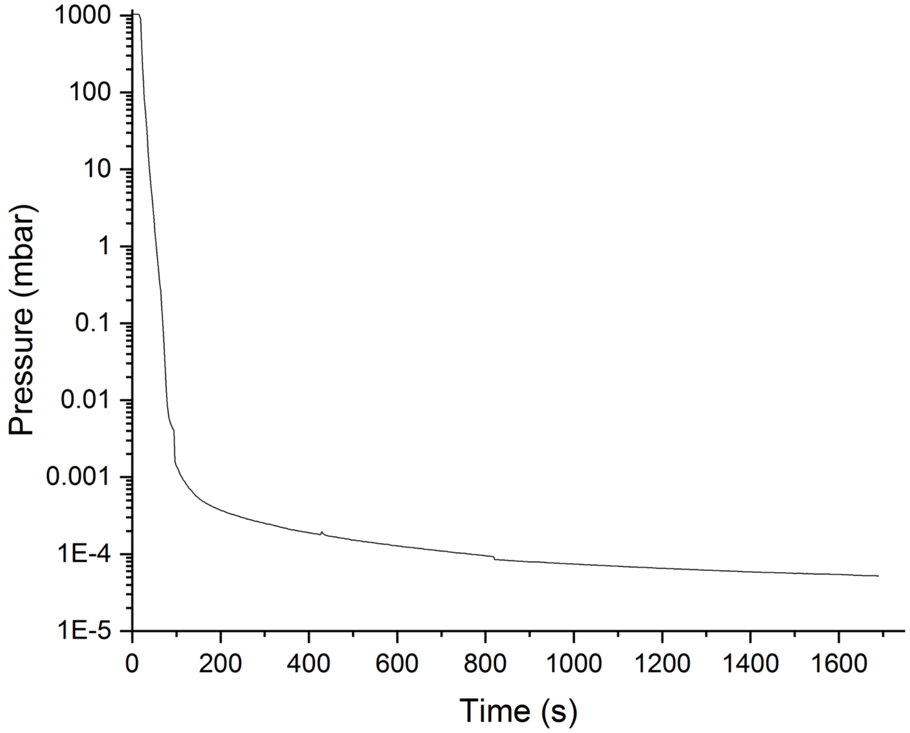

Figure 3.43 – The vacuum chamber pressure vs. time, when pumped down using the automatic pumping control.

3.3.2 Vacuum valves and feedthroughs

As described in section 3.3.1, the pumping speed of a high vacuum pump is affected by the size and geometry of the input connection to the vacuum chamber; for this reason, it was decided to select the largest vacuum port that the chamber could accommodate. The back wall of the chamber was designed to incorporate an ISO-K 160 vacuum flange, to which a 160 mm VAT Series 121 electro-pneumatic gate valve was mounted. Electro-pneumatic gate valves make use of compressed air to provide sufficient force to open and close a large valve, whilst making use of a low power solenoid to provide electrical control of the compressed air.

To offer the possibility of water quenching (see 3.2.2.2), the bottom wall of the chamber was designed with an ISO-K 100 flange. This bottom flange was also fitted with a VAT Series 121 electro-pneumatic gate valve, but with the correspondingly smaller diameter of 100 mm.

To enable the rotary vacuum pump to be used for both roughing and backing, valves are required to either connect the pump inlet directly to the chamber or to the output of the turbomolecular pump. An ISO-KF 25 vacuum port was placed on the back wall of the chamber for the roughing connection. A solenoid vacuum valve (Oerlikon Right-Angle Valve BAV 215064V01) was connected to the chamber roughing port, and another valve of the same type was connected to the output of the turbomolecular pump. Both right-angle valves were connected to the rotary pump by way of a tee junction.

For the connection of the clamp cooling circuit as well as the quench and venting gasses, two ISO-KF 40 feedthroughs were purchased, which each had a pair of ¼” stainless steel tubes passing through them (see Figure 3.44). One of the tubes of each of these feedthroughs was used for the cooling circuit, with the other two connections used for the quench and venting gasses. With the exception of the vacuum side connection for the venting gas, which needed no connection, Swagelok gaugeable tube fittings were fitted to the tube ends to enable the connection of the fluid pipes and hoses. As described in section 3.2.2.2, an Asco Series 203 valve was used in series with an Asco Series 030 valve to provide proportional control and vacuum tightness for the quenching fluid. A pair of the same valves was also used to control the admittance of the venting gas to the chamber.

The thermocouple feedthrough, purchased from Scanwel Ltd, was fabricated from type R / S thermocouple extension grade wire to provide a signal path for two type R or type S thermocouples through an ISO-40KF flange. Vacuum feedthroughs for type R / S thermocouples are typically made from extension grade wire to circumvent the use of costly platinum and rhodium, but this reduces the maximum temperature gradient that can be supported in the extension wire, in this case to 250°C.

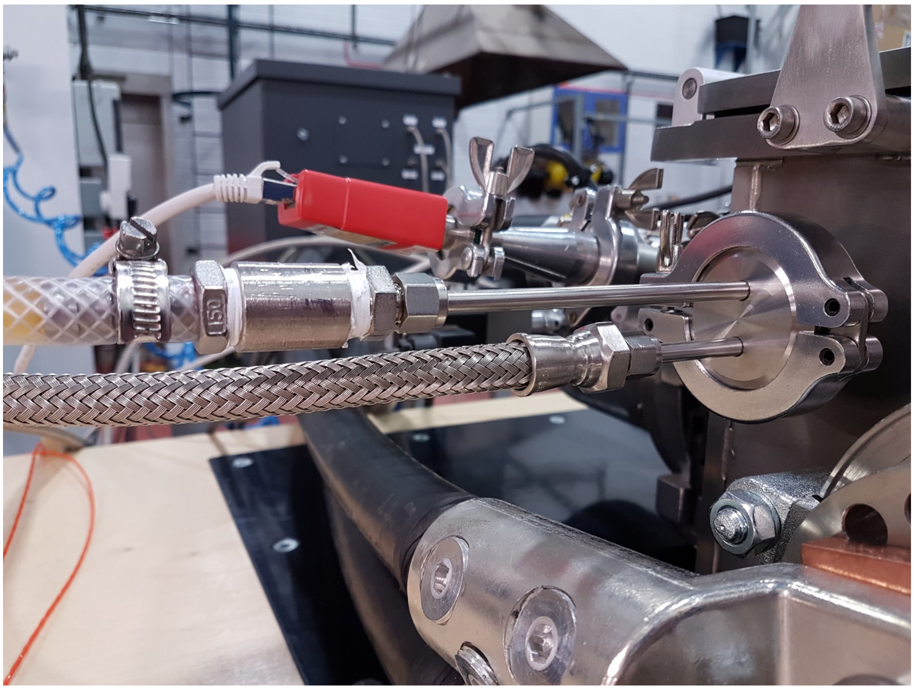

Figure 3.44 – One of the two fluid feedthroughs. The top connection is for the sample clamps coolant, and the bottom connection is for the inert gas.

To provide a signal path for the connections necessary for the electrical resistivity measurements, an ISO-40KF flange with a 25 pin Micro-D connector was purchased from MDC Vacuum Ltd, Uckfield, which is rated at 300 V and 5 A per pin. The decision to use the 25 pin connector was made when there was still the intention to implement spontaneous magnetic emission measurements. As only four of the twenty-five pins are required for the electrical resistivity measurements, the instrumentation module (see 3.5.6) provides a pass through to eight of the feedthrough spare pins on an externally accessible twenty-five pin Sub-D connector.

3.3.3 Vacuum measurement

Vacuum gauges that work on a wide variety of physical principles have been constructed, each of which will measure a slightly different range of pressures; however, inspection of the vacuum equipment manufacturers' catalogues shows that only a small subset of gauge types are readily available. The initial choice of vacuum gauge was an Oerlikon PTR 90 combined Pirani and cold cathode (Penning) gauge that is designed to measure from atmospheric pressure to 5×10^{-9} mbar. The gauge was connected directly to the vacuum control module (see 3.4.3).

The Pirani gauge works by heating a wire in the vacuum chamber and relating the pressure to the heat loss experienced by the element [78]. Pirani gauges can work on constant voltage, current, power, or temperature. A significant drawback to the Pirani gauge is that the heat loss is a function not only of the chamber pressure, but of the thermal conductivity of the gas in the chamber. If a gauge is calibrated for air, then when used to measure the pressure in a chamber containing a gas with thermal conductivity lower than air the gauge will indicate a pressure lower than correct. As the pressure is increased the gauge output may appear to almost remain static, greatly reducing the sensitivity. The situation when measuring gases with higher thermal conductivities can be worse, as the gauge output can saturate at relatively low pressures. Conversion charts such as in Figure 3.45 can be used to convert the gauge output value to the true pressure, but the conversion chart should be for the specific gauge as the gas dependency of the gauge is a function not only of the gas thermal conductivity, but also of the gauge construction [79].

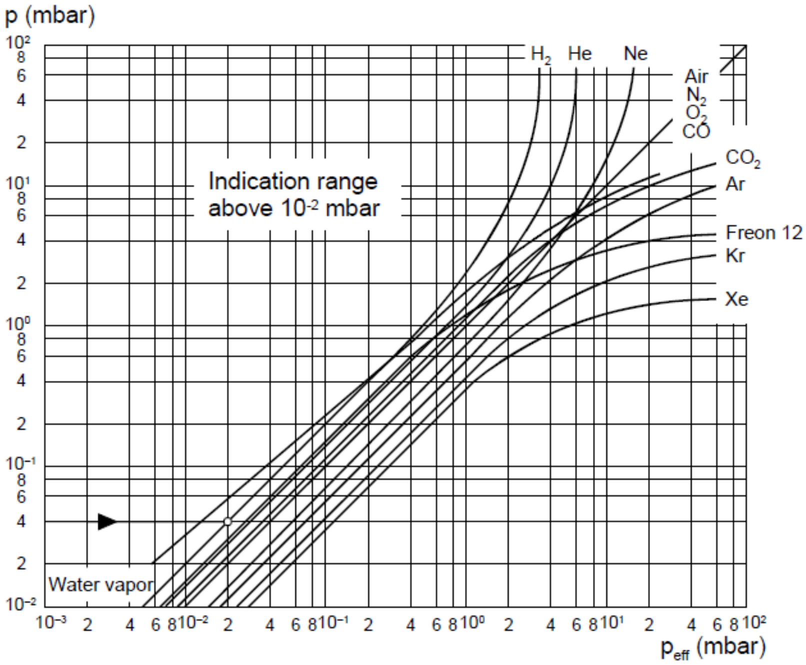

Figure 3.45 – The gas conversion chart to convert the gauge output to true pressure for gasses other than air as copied from the Oerlikon PTR90 vacuum gauge product manual.

The cold cathode gauge works by applying an electric field between two electrodes that is sufficient to cause emission of electrons from the cathode [78]. If any electron with sufficient energy collides with a gas molecule, the molecule may be ionized and will cause an increased current to flow between the electrodes. The output from a cold cathode ionization gauge can be increased by increasing the distance that the electrons travel, thereby increasing the number of ionized gas molecules: this is done by the addition of a magnet that causes the electrons to travel in a spiral path between the cathode and anode. As with other indirect vacuum measurement techniques, the cold cathode gauge shows a gas dependency, which is a function of the ionization probability of the gas molecules. The gas dependency of the cold cathode gauge is not as problematic as with the Pirani gauge as there is neither the loss of sensitivity nor the output saturation that is present with the Pirani gauge. Manufacturer provided pressure conversion charts can be used to convert the pressure measured by a cold cathode gauge when using with a gas other than for which it was calibrated.

During testing of the vacuum system, an unexpected problem was encountered with the Pirani part of the Oerlikon PTR 90 combined vacuum gauge. The gauge appeared to exhibit some kind of memory effect, whereby after the gauge was used with argon, the output signal of the gauge failed to give an output greater than 10 mbar, even when using air. The only solution would be to leave the gauge turned-off for an extended period of time (~10 hours). This memory effect did not appear to affect the cold cathode measurement. No explanation is offered for this behaviour, as all readily verifiable explanations have been discounted. The manufacturer was contacted and was also unable to offer any insight.

Given that the vacuum gauge was required to give readings from atmospheric pressure to 10^{-2} mbar for both air and argon, the optimum solution would have been to include a direct measurement vacuum gauge such as a capacitive gauge, which is gas independent. However, due to financial consideration, it was decided to make use of a freely available Edwards APG100-XM NW16 Pirani gauge, which despite showing significantly decreased sensitivity at pressures approaching atmospheric, did not exhibit any kind of memory effect. The vacuum control module was modified to enable simultaneous use of both the original and additional gauges (see 3.4.3).

3.3.4 Vacuum chamber

The vacuum chamber was fabricated from 12.7 mm thick 316L stainless steel by Scanwel Ltd according to the provided drawings and CAD model (see Figure 3.46). Abbreviated versions of the production drawings are included in Appendix 17.

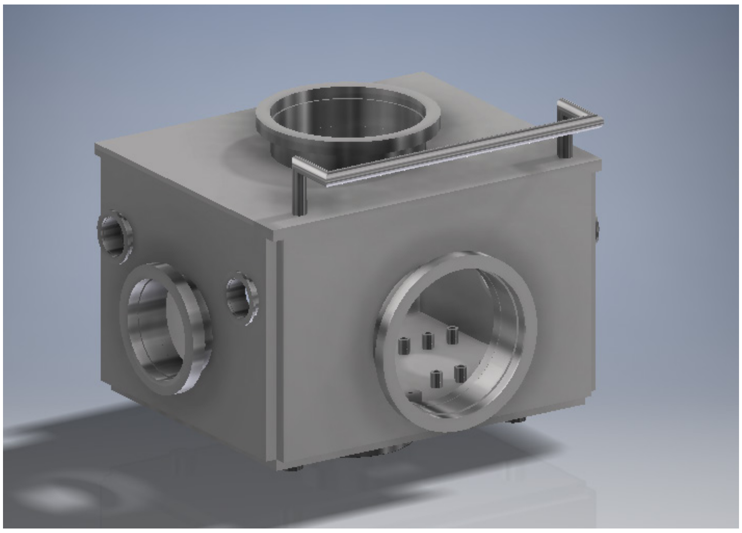

Figure 3.46 – Computer rendering of the vacuum chamber produced in Autodesk Inventor 2016 from the CAD model.

Appendix 17G shows the bosses that were welded to the inside bottom of the vacuum chamber for the mounting of the PTFE clamp beds (see 3.2.1.8) and the quench nozzle clamps.

3.4 Control system

3.4.1 Control system topology

The electronic control system is split into three parts: a personal computer that collects data and issues the commands necessary to implement the heat treatment; the electronic control modules that implement the commands issued by the PC; and, a bridge between the PC and electronic control modules. The electronic control modules make use of ARM SAM3X8E powered Arduino Due development boards.

The electronic control functions are split between four discreet modules that are linked together using a Controller Area Network (CAN). One of the modules, the bridge module, is connected to the PC using a full speed Universal Serial Bus (USB) connection. The bridge module acts as a link between the CAN network and the PC, allowing commands and data to pass in both directions.

The electronics used for the CAN communication, PCB temperature sensor, and LED status lights are described in the following section describing the bridge module electronics, but also apply to the vacuum system control modules, heating control module, and the gas control module.

3.4.2 Bridge module

The primary function of the bridge module is to act as a link between the PC and control modules. It was decided to connect the PC to the control modules using a USB connection because of the improved noise tolerance from differential signalling and the built-in hardware error checking of USB transfers. The use of differential signalling with twisted pair wires is an effective way to reduce low frequency magnetic interference [80], which is the type interference that one would expect from a 2000 A 60 Hz heating current.

USB transfers are always initiated by the host [81]. This means that for a device to be able to send transfers to a host, the host must periodically initiate IN transfers (transfers from device to host). The host will complete the transfer by returning any data that is available. If no data is ready, for transfer types other than isochronous, the device will respond with NAK (negative acknowledge). There is a constant processing overhead for the device in processing host initiated USB IN transfers even when there is no data to be sent[6]. For example, the minimum interval for a full speed interrupt transfer type is 1 ms, and for high speed devices this can be as low as 125 µs.

---

[6] Because of the strict timing requirements of the USB specification, USB transfer requests are serviced by a dedicated unit in the Arduino Due’s ARM processor. However, after each transfer request has been serviced a CPU interrupt is generated to preload any available data, which will be dispatched by the processor’s dedicated USB unit. It is this interrupt that generates a CPU overhead.

To reduce the processing overhead of the USB connection on the individual control modules it was decided that the bridge module should act as the single USB connection to the PC. The other control modules are then connected to the bridge module using a CAN network. CAN networks are multi-master networks, which means that all devices can initiate transfers. As any device can initiate a transfer, there is no need to submit any periodic requests for data. The CAN network makes use of a prioritized bus arbitration system for when two devices simultaneously attempt to initiate a message, whereby the message having the lower address is given priority. This enables the designer to ensure that high priority messages are less likely to be delayed due to timing issues by giving those messages low value addresses. The final, and perhaps most significant, reason for selecting a CAN network is that CAN was designed for use in noisy industrial environments.

To further improve the common mode noise immunity of the CAN network beyond that offered by the differential signalling, all modules used a Texas Instruments ISO1050 CAN isolator. Each module was also equipped with a dedicated switched mode power supply (SMPS) to enable a floating supply for the CAN side of the isolators. An additional benefit of isolating the CAN network was to break any ground loops that may have been formed between the modules. The CAN side connections of the ISO1050 isolator are protected from transient voltages by On Semiconductor NUP2105LT1G bidirectional transient voltage suppressor (TVS) diodes. The CAN side lines are then brought to a pair of external DE9 connectors for connecting to the other control modules. A pair of DE9 dongles, each containing a 120 Ω resistor, are used to terminate the CAN communication lines at the two ends of the network.

The original intent was to use a high speed USB connection between PC and bridge module, but when testing the phase angle control circuit that was made form discrete semiconductors, the USB connection demonstrated poor immunity to the switching noise. As it was anticipated that there could be some noise problems due to ground loops with the PC, the bridge module was manufactured to include an Analog Devices ADuM3160 full / low speed USB isolator. The decision to not use a USB isolator form the start was down to the unavailability of a commercial USB isolator chip that is capable of functioning with high speed USB. The combination of reducing the bus speed to full speed and isolating the BUS, did have some effect on reducing susceptibility to interference. As the isolation was not able to completely immunize the USB connection from noise, the approach was taken to have the bridge module monitor the health of the connection by monitoring the time since a transfer IN request was successfully received from the host. If a transfer IN request is not received for 14 ms the bridge module disconnects from and then reconnects to the USB. The PC program that is controlling the heat treatment is then notified of the disconnection and reconnection and resets the connection at the host side. The USB connection has to be monitored at the device side as the Microsoft Windows driver has been implemented using Microsoft WinUSB, which although able to monitor the status of the connection, is unable to reset the connection due to limitations in WinUSB.

To enable monitoring of the PCB temperature, the bridge module includes a Microchip TCN75AVOA temperature sensor IC. The Arduino Due uses the I2C serial interface to communicate with the TCN75AVOA.

In addition to USB, CAN, and I2C interfaces, the bridge module also includes a Maxim MAX3232 RS-232 transceiver, with a dedicated 3 V power supply, and electrical isolation form the Arduino microprocessor by a Texas Instruments ISO7421. The MAX3232 output pins, which are protected from transient voltages by the use of NXP PESD15VL2BT bidirectional TVS diodes, are brought to an externally accessible DE9 connector for future expandability.

The bridge module includes three LEDs that are mounted on the enclosure front panel to inform the user of the module status. There is a CPU active LED that flashes every 2 seconds to indicate that the module CPU is active. There are also a pair of LEDs, one for USB[7] and one for CAN, that activate if network communication is detected, and turn off after 2 to 4 s without

---

[7] For the vacuum system, heating, and gas control modules only the CPU and CAN status LEDs are present.

communication. The LEDs are switched by NXP BSS138AKA MOSFETs that are actuated directly by Arduino Due digital output pins. The MOSFET and other circuitry are protected from transient voltages on the wires that go to the module enclosure through the use of a pair of Panasonic EZJZ1V420FA varistors.

In addition to its communication functions, the bridge module is also responsible for controlling the 240 VAC cabinet cooling fans. The fans are switched using an NXP BT139-600 TRIAC, which is switched only at zero crossings to reduce noise by a Fairchild MOC3063M isolated TRIAC driver. To further reduce any switching noise the TRIAC has an RC snubber placed in parallel. To reduce any noise being brought into the bridge module by the power cable to the cooling fans there is a Schaffner 406-1-02 powerline filter placed between the TRAIC and cooling fans.

The bridge module circuit diagram can be found in Appendix 18.

3.4.3 Vacuum system control module

The vacuum system control module is responsible for monitoring the vacuum chamber pressure and actuating the vacuum valves, pumps, and TMP cooler. The vacuum system control module communicates with the other control modules and the control PC via the CAN network. The circuit diagram is presented in Appendix 19.

The right angle valves and gate valves described in section 3.3.2 were procured with 240 VAC solenoid coils. These valves are controlled through the use of NXP BT139-600 TRIACs, driven by Fairchild MOC3063M controllers as used by the bridge module for control of the cabinet cooling fans (see 3.4.2). The rotary vacuum pump (see 3.3.1) and TMP cooler are also actuated individually by using a MOC3063M and BT139-600 to switch the input power for each device. Because of the large current required for the rotary vacuum pump (up to 10 A) a separate powerline filter is used for the supply.

The turbomolecular pump is controlled via the TD20 controller (see 3.3.1). The vacuum system control module communicates with the TD20 using a 25 way PLC interface. The TD20 PLC interface uses 24 V switching voltages which are galvanically isolated from the Arduino Due. For communication from the control module to the TD20, the signals are isolated using Panasonic AQY210EH PhotoMOS relays that are switched using NXP BSS138AKA MOSFETs; the 24 V output voltage is provided by the TD20. For input communication the isolation is achieved using Avago ACPL-024L Digital CMOS Optocouplers. It should be noted there was a minor wiring error in the pinouts used for the 25 way PLC interface on the on the vacuum control module, which is visible in Appendix 19.

The chamber pressure is measured using an Oerlikon PTR 90 and an Edwards APG100-XM (see 3.3.3). Both gauges are supplied with 24 V DC power by the vacuum system control module. Both gauges output an analogue voltage that depending on value is used to indicate an error condition or a measured pressure. As explained in section 3.3.3, the control module was initially built to support one vacuum gauge. For this sole gauge the conversion of the analogue voltage was performed by using a voltage divider to reduce the amplitude by a gain of 0.194, which was then digitized using a Microchip MCP3421A0T ADC. The Arduino Due is able to request conversions from the MCP3421A0T using the I2C network. To support a second vacuum gauge an additional PCB was included in the module with a Microchip MCP3421A1T to perform the ADC. The MCP3421A1T is almost identical to the MCP3421A0T, the only difference being in the I2C address, which allows both ADCs to be connected to the same I2C network. As the pressure readings from the first vacuum gauge showed some small fluctuations, an active second order Sallen and Key low pass anti-aliasing filter with corner frequency of 5 Hz was added. The full circuit for the additional vacuum gauge can be found in Appendix 20.

To provide additional information to the user the vacuum system control module also includes a Midas MCCOG22005A6W-BNMLWI 20 x 2 character LCD. The Arduino Due communicates with the LCD using the I2C network. The information displayed is controlled by the module firmware.

The original intention had been for the vacuum control module to actuate the venting proportional control valve. However, it was found that pulsed current draw of the PCM control signal was leading to noise of the 24 V supply line. The same 24 V supply was used for both the PCM signal and the vacuum gauge, and this noise was leading to errors with the chamber pressure readings.

3.4.4 Heating control module

The heating control module provides the 240 VAC 40 A phase angle controlled input signal to the 50:1 9.6 kVA step down transformer (see 3.2.1.7) that delivers the 4.8 VAC 2000 A sample heating current. The full circuit diagram is included in Appendix 21.

As detailed in sections 3.2.1.2 and 3.2.1.3, the initial plan for the heating control had been to use a modified version of phase angle control with two conduction periods per half cycle. As such a scheme would require turn-off during current flow, neither the unidirectional thryristor, nor the bidirectional TRIAC would be applicable. An AC switch that can be switched at any time can be realized from a pair of either IGBTs or FETs and an opto-isolator [82]. In this approach when the transistors are turned-off, the AC current is blocked by one transistor during one polarity, and by the other transistor during the other polarity. When the transistors are switched on, the current is carried by the normal conduction path when the collector (drain) voltage is more positive than the emitter (source) terminal and by the integrated diode when the polarity is reversed. The opto-isolator is used to switch the transistors, as by attaching the negative output to the emitter (source) terminal and the positive output to the gate terminals, the opto-coupler output voltage will appear as the gate-emitter (gate-source) voltage regardless of the value of the emitter (source) voltage. The AC switch was implemented in the heating control module using an Avago ACPL-P340 opto-isolated gate driver to switch a pair of IXYS IXGN100N170 IGBTs (see Figure 3.47). As the IXGN100N170 does not include a reverse recovery diode, it was necessary to include a pair of discrete IXYS MDD95-16N1B diodes for conduction when the emitter voltage is more positive than the collector voltage. Because of the large power that is dissipated by the IGBTs and diode the module is fitted with a large heatsink and a pair of cooling fans.

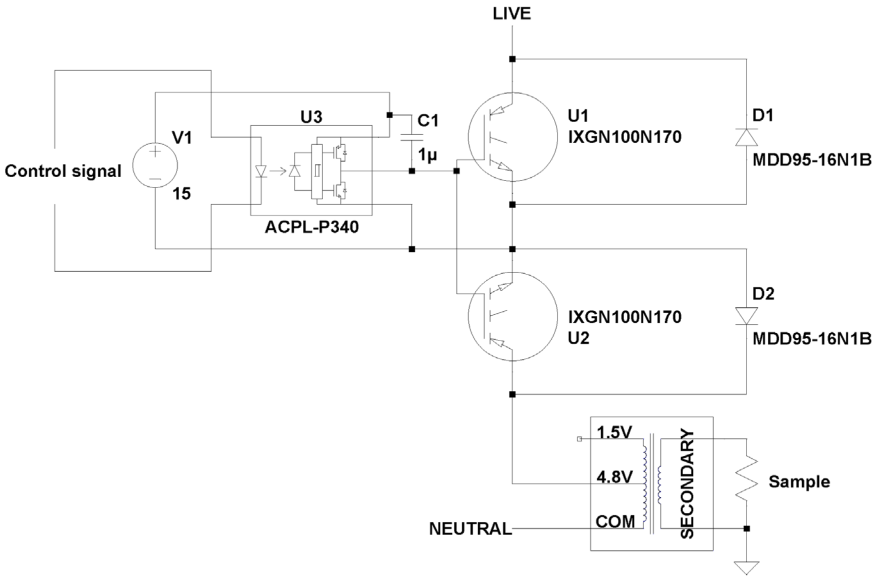

Figure 3.47 - AC Switch using a pair of IGBTs and diodes.

In order to perform phase angle control it is necessary to know the line voltage phase angle. The normal way to do this is to detect when the line voltage is zero using a zero-crossing detector. In the heating control module the zero-crossing detector was implemented using a pair of opto-couplers [83] (see Figure 3.48). In this circuit, as the live voltage increases from zero to the sum of the forward voltages of D1 and the top LED, the top photodiode will turn on. This photodiode will continue to be on until the line voltage drops below the sum of the forward voltages. Similarly, as the live voltage becomes more negative and is greater than the summed forward voltages of D2 and the bottom LED, the lower photodiode will turn on. Again, this photodiode will be on until the live voltage is less than the sum of the forward voltage drops. The zero-crossing time can be calculated by interpolating between the turn-off time of one photodiode and the turn-on time of the other photodiode. In the heating module the interpolation is performed using the Arduino Due’s microcontroller. Unfortunately, because of an error in the PCB artwork for the heating control module the bottom opto-coupler was rendered inactive. As the zero-crossing detector is an essential component for the module, it was necessary to adapt the interpolation strategy: by finding the midpoint in time between the photodiode turn-on and photodiode turn-off, the 90° cycle time could be calculated. The next zero-crossing time could then be calculated as being 5 ms after the 90° time.

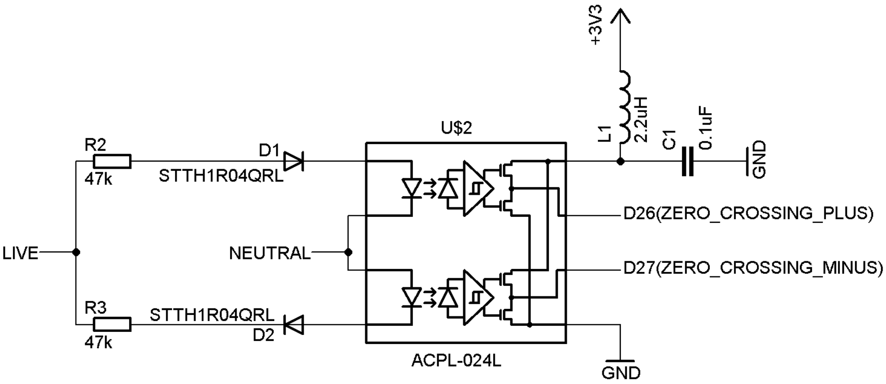

Figure 3.48 - Opto-isolator zero-crossing detector.

As explained in section 3.2.1.3, attempts to use phase angle control with non-zero turn-off proved unsuccessful due to the large amount of energy that needed to be dissipated. However, because the error with the zero-crossing detector described above was not immediately found, when it was attempted to use the AC switch made from the pair of transistors with zero voltage turn-off, the same problems continued to be present, as the turn-off was not occurring where it was thought to be. Due to the continued failure of the AC switch components, and the financial and time cost of continuing with that approach, it was decided to replace the discreet AC switch with a commercial phase angle control module. The selected module was a Celduc SG464120, which has an integrated zero-crossing detector and snubber circuit. The SG464120 turn-on angle is controlled by applying a DC voltage between 0 V (no conduction) and 5 V (full conduction). To provide the necessary analogue control voltage, an I2C controlled Microchip MCP4726A0T digital to analogue converter with second order anti-imaging filter (see Appendix 22 for the circuit diagram) was added as a supplementary PCB.

The heating module includes an LEM LF 310-S that was kindly provided by LEM UK for the instantaneous current monitoring that is described in 3.2.1.2. The LF 310-S is a non-contact current sensor that produces an output current that is equal to 1/2000th of the instantaneous input current. In the heating control module this output current is converted to a voltage by passing through a 20 Ω resistor and then biased to approximately 1.64 V so that the signal can be digitized. Prior to the ADC the signal is passed through an analogue opto-isolator of the type described in section 3.5.3. Intended for use when the IGBT AC switch was to be used, the output from the current sensor is also fed to a pair of comparators that can be compared to software defined limit voltages for the hardware turn-off of the switch when the instantaneous current exceeded a predetermined level. As the discrete component AC switch is no longer used, the main use of the current sensor is in determining the sample resistance and minimum turn-on angle to limit the sample current to 2000 A_{RMS} (see 3.2.1.3 and Appendix 27).

The heating control module also contains the electronics for controlling the quench gas proportional control valve. However, as with the control of the vent gas proportional control valves (3.4.3), this function has now been moved to within the gas control module (3.4.5).

3.4.5 Gas control module

The gas control module was not included in the initial design architecture as the admittance of venting gas was to be controlled by the vacuum system control module, and the admittance of the quenching gas was to be controlled by the heating control module. There are two reasons why it was necessary for these functions to be moved to a new module. Firstly, as described in section 3.2.2.2, it was necessary to include an additional vacuum valve in line with the proportional control valves. Secondly, as described in section 3.4.3, the proportional control valve actuation by the vacuum system control module was causing significant electrical noise to interfere with the chamber pressure readings. Given these two factors, it was decided that the best solution would be to move these functions to a dedicated module that would also be able to support the additional vacuum valves.

The Asco Series 203 proportional control valve opening is controlled by the duty cycle of a 24 V 300 Hz pulse width modulated supply voltage. The PWM signal for each proportional control valve is generated by Arduino Due's SAM3XE microprocessor PWM peripheral. This PWM signal then drives an NXP BSS138AKA MOSFET, which in turn switches the LED current through an Avago ACPL-P340 opto-isolated gate driver. The ACPL-P340 gate driver is used to provide galvanic isolation between the control module and proportional control valve. The proportional control valve is powered by a 24 V SMPS, with the return current of up to 0.5 A being pulse width modulated by an International Rectifier IRF1104 MOSFET that is driven by the ACPL-P340.

The Asco Series 030 vacuum valves are controlled by switching the 240 VAC supply voltage. As elsewhere in the control modules for the switching of line voltages, this is achieved by using a Fairchild MOC3063M to drive an NXP BT139-600 TRIAC. An additional pair of TRIACs and drivers are also included in the gas control module for future adaptability.

The full circuit diagram for the gas control module is in Appendix 23.

3.4.6 Control module power supplies

The control modules all include metal oxide varistors to act as transient suppressors. The bridge, vacuum, and gas control module all use a pair of Littelfuse TMOV20RP300M varistors that are connected between live and neutral, and live and protective earth. These devices include thermal fuses that disconnect the varistors in the event that they fail as a short circuit. There is a third terminal that is connected to the junction between the thermal fuse and the varistors, which can be used to monitor if the thermal fuse has failed and the varistors are no longer offering protection.

The circuit for monitoring the thermal fuse of each varistors has the varistor’s monitoring lead connected to a Fairchild H11AA1M AC input phototransistor optocoupler through an 18 kΩ current limiting resistor (peak current will be limited to 18.9 mA). Once the forward voltage drop across either of the input diodes is sufficient for conduction, there will be a voltage on the output emitter that will increase to 3.3 V as the diode forward voltage increases. The output from the H11AA1M is a 100 Hz pulse train with a duty cycle greater than 50%. This pulse train is fed into the set terminal of an SR latch, and the output is connected to the data input of a clocked D latch. The reset terminal of the SR latch is connected to an astable multivibrator (frequency of approximately 4.8 Hz), so that the SR latch will reset on the positive clock edge. The clock input of the D latch is connected to the same astable circuit, but such that the latch updates on the negative clock edge. The output from this circuit will be high as long as the H11AA1M emitter output is high (i.e. current is flowing through the thermal fuse) for any part of the time between the positive and negative clock edges. There is one of these circuits, sharing a common clock timer, for each of the two varistors.

The two 18 kΩ resistors in the bridge module varistor monitoring circuits each waste approximately 3.2 W of energy through Joule heating. To reduce the wasted energy the varistor monitoring circuits in the vacuum and gas control modules are modified by replacing the 18 kΩ resistors with a series combination of a 150 nF capacitor and a 500 mH inductor. The 150 nF capacitor has an impedance of 21.2 kΩ at 50 Hz, which by itself is sufficient for limiting the current in the optocoupler. The problem with using just the capacitor is that the impedance will decrease for high frequency noise, so the inductor is included to add some high frequency attenuation.

To cope with the increased load current, the heating module uses a pair of Littelfuse V321DA40 metal oxide varistors, which are also connected between live and neutral, and live and protective earth. These varistors do not include a thermal fuse. Both TMOV20RP300M and V321DA40 varistor types are manufactured with flame retardant coatings to reduce the chance of fire in the event of failure. All of the control modules incorporate replaceable wire fuses on both the live and neutral lines that should rupture in the event of the varistors conducting either due to failure or significant transient suppression.

The control modules all include a powerline filter for reducing noise that is emitted onto the powerlines and to attenuate any external noise that is present on the supply. The powerline filters are all off the shelf units that were chosen to match the individual module’s maximum operating currents. The powerline filters are connected downstream of the varistors. The heating control module uses two powerline filters: one filter is placed after the varistors and is used for the switched heating current; the second filter is to supply the PCB, and this is placed after an additional pair of lower rated fuses that are connected to the varistors.

The control module PCBs include Vigortronix VTX-214-010-109 fully encapsulated switched mode power supplies to provide a 9 V DC supply to the Arduino Dues. The Arduino Due boards incorporate a 3.3 V DC regulator that is used to power the processor and any other control module components that require 3.3 V. Reference to the control modules circuit diagrams (Appendix 18 to Appendix 23) will show the inclusion of additional encapsulated power supplies where other voltages, or voltages with different grounds, are required.

3.4.7 Control module firmware

The firmware for the bridge module, vacuum system control module, heating control module, and gas control module were written in C using Atmel Studio 6.2, and make use of the Atmel Software Framework v. 3.17 to access the SAM3XE’s peripherals.

The software for each module follows the same basic structure: configure the microcontroller, peripherals, and any connected devices; then enter an infinite loop, responding to hardware interrupts. The hardware interrupts are caused by the arrival of CAN messages, timers, and in the case of the bridge module the arrival of USB messages. The source code for the modules can be found in Appendix 41, Appendix 42, Appendix 43, and Appendix 44.

With the exception of the automatic mode on the vacuum control module, the control modules do not make decisions about the machine control, but instead act according to CAN messages sent from the control PC. The list of CAN commands is included in Appendix 40.

3.4.8 Control PC software

The main piece of software developed for controlling the instrument is the *Quenching Simulator Control Panel* (QSCP). QSCP was written using C++ and Microsoft Foundation Class (MFC) v. 11.0. MFC is an object-orientated abstraction of the Widows application programming interface (API), which simplifies the development of Windows based graphical user interface (GUI) programmes. In Windows terminology code written using MFC is native code, that is to say the code is compiled into machine code that runs directly on the microprocessor[8]. MFC has been frequently displaced by the more recent .NET framework for new GUI applications. However, the reason why .NET was not chosen for this project is that .NET code, like Java, generates managed code. Managed code is not machine code, but is code that is compiled to an intermediate language (IL) that must then be interpreted into machine code at runtime. Managed code has many advantages for both the programmer and the user, such as automatic memory management and enhanced security, but these come at the expense of runtime overheads. Due to the necessity for QSCP to perform real time control, it was judged that the extra burdens of running managed code should be avoided.

---

[8] Native code will not ordinarily have unrestricted access to the PC as the CPU will for general applications be in user mode, which has restrictions on the available CPU instructions, and hardware access being through calls to the operating system and drivers.

3.4.8.1 *User interface*

This section will give a brief overview of the QSCP software and the options available to the user for controlling the experiment. When the software is started the control panel is displayed (Figure 3.49), where the user can choose to specify the heat treatment, view the saved results from a previous heat treatment, or configure options. The option to run the heat treatment is disabled until a heat treatment has been specified.

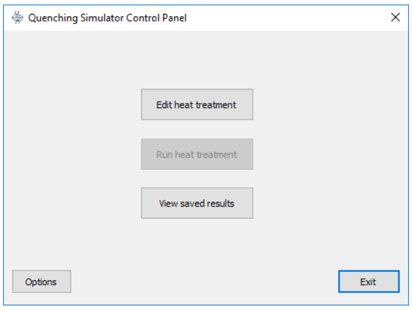

Figure 3.49 - The main screen when the QSCP software starts.

The edit heat treatment window (Figure 3.50) is where the user can either load an existing heat treatment or specify a new heat treatment. The temperature profile for the heat treatment is displayed in the large control. The heat treatment is specified as a series of steps, which are displayed in the bottom left of the window. For each step the user specifies the end temperature, the time taken to get to that temperature, and whether quenching can be used if required. The user can modify steps by clicking on the step, altering the parameters, and clicking the modify button. Heat treatments can be saved as a heating schedule data (.hsd) file for future use, exported to a comma separated variables file (.csv), or exported as an image file.

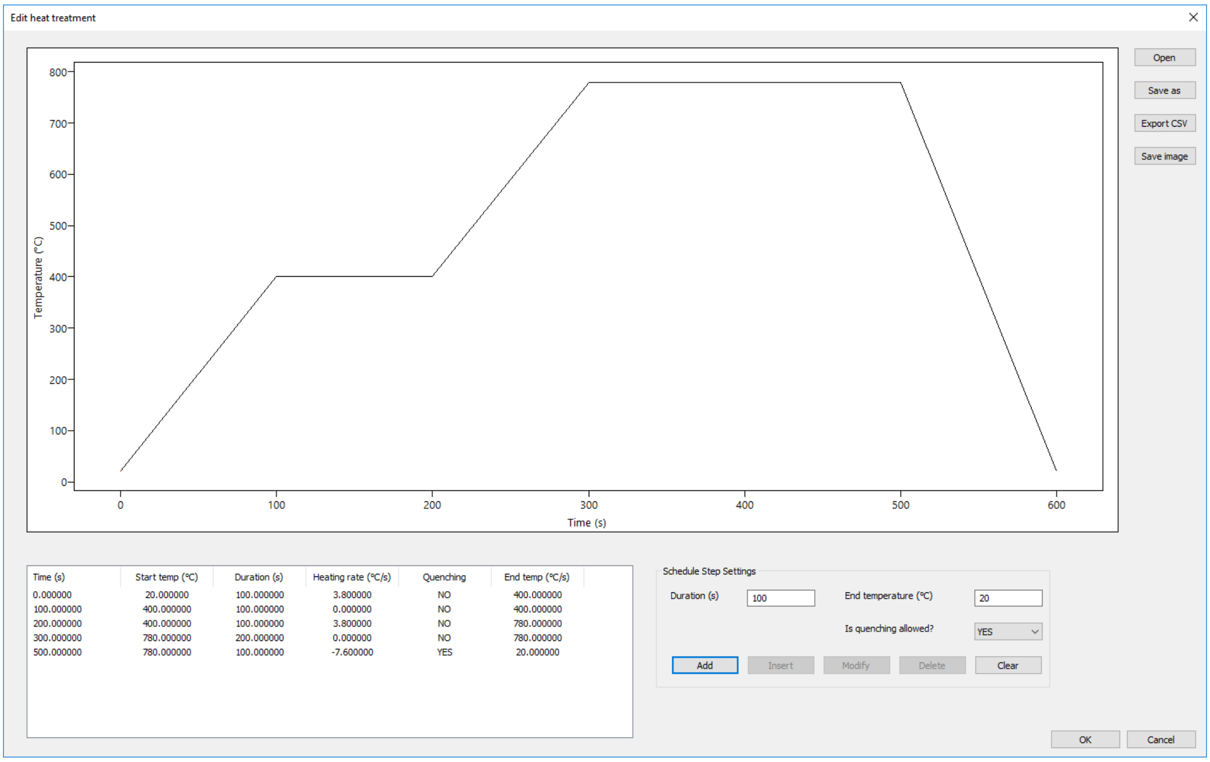

Time (s)	Start temp (°C)	Duration (s)	Heating rate (°C/s)	Quenching	End temp (°C/s)
0.000000	20.000000	100.000000	3.800000	NO	400.000000
100.000000	400.000000	100.000000	0.000000	NO	400.000000
200.000000	400.000000	100.000000	3.800000	NO	780.000000
300.000000	780.000000	200.000000	0.000000	NO	780.000000
500.000000	780.000000	100.000000	-7.600000	YES	20.000000

Schedule Step Settings

Duration (s) 100

End temperature (°C) 20

Is quenching allowed? YES

Figure 3.50 - The edit heat treatment window allows the user to load a heat treatment programme or to define a new programme.

The heat treatment will be executed from the run heat treatment window (Figure 3.51). The temperature profile will be displayed as a black line. Once the heat treatment is underway the sample measured temperature will be displayed in red. If selected in the user options a second variable will be displayed as a blue line and the right hand vertical axis will be changed to the appropriate units for measurements other than temperature. During operation, the temperature of the three thermocouples and the cold junction RTD will be displayed at the top of the window. If heating is enabled, as opposed to just taking measurements, the vacuum chamber pressure will also be displayed.

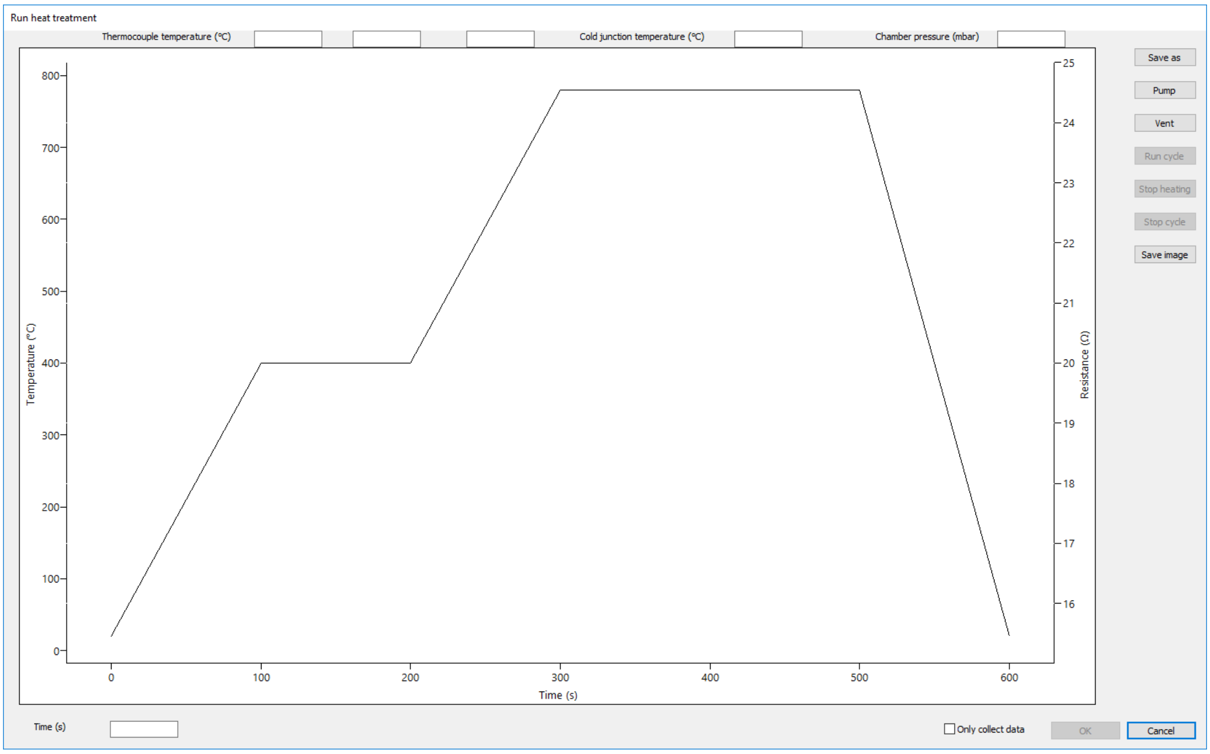

Figure 3.51 - The run heat treatment window.

Before the user can run the heat treatment he must first select the file name for saving the data: the user will always be required to specify the filename for a comma separated variable file containing the processed data, and will also be asked to specify the filename for a binary file if he has selected to save the raw unprocessed data. The only collect data check box allows the user to specify that no heating or quenching should take place, but that data should be recorded; this option is useful to check the sample connections before performing the actual heat treatment. The buttons labelled pump and vent send commands to the vacuum control module to either automatically pump or vent the chamber to a user specified pressure. The run cycle button will start the heat treatment (or measurement). The stop heating button will immediately stop all heating for the current heat treatment, but continue to record data until the end of the programme. The stop cycle button immediately ceases heating and quenching, and stops the recording of data. The save image button is used to export the displayed curves as an image file.

The view saved results window (Figure 3.51) is a simple viewer to allow the user to quickly view the results of previous heat treatments. The user can select the x and y variables independently from time, target temperature, phase angle, thermocouples 1 to 3, resistance measurement voltage, resistance measurement current, resistance, and either of the two external channels. The user can export the displayed data as an image file.

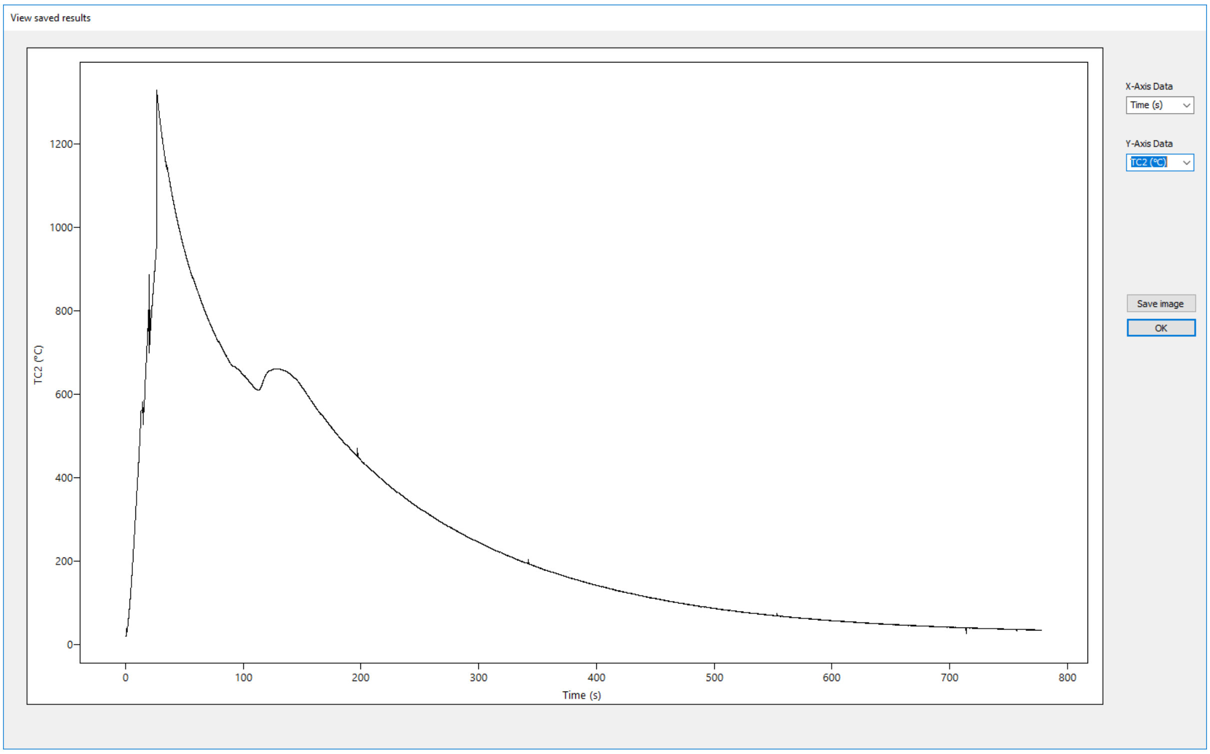

X-Axis Data: Time (s)

Y-Axis Data: TC2 (°C)

Figure 3.52 - The view saved results window enables the user to view the data from previous experiments.

The options dialogue (Figure 3.53) allows the user to enable and disable channels for data acquisition, select the thermocouple types for the individual channels, select the instrumentation amplifier gain (see section 3.5.1), and specify the second channel to display when running the heat treatment. It is from the options screen that the user can also open the following three dialogues.

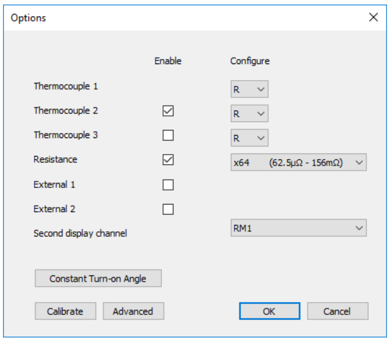

	Enable	Configure
Thermocouple 1		R
Thermocouple 2	☑	R
Thermocouple 3	☐	R
Resistance	☑	x64 (62.5µΩ - 156mΩ)
External 1	☐	
External 2	☐	
Second display channel		RM1

Figure 3.53 - The options dialogue.

The constant turn-on angle heating dialogue (Figure 3.54) lets the user specify that a heat treatment should be performed by heating a sample to a specified temperature with a specified phase control angle. Once the specified temperature, or the user specified time limit, has been reached the heating will be turned off. The user can also specify in this dialogue whether quenching should be used when the heating is terminated, and if so the quench gas proportional control valve opening. The length of time for which data will be recorded will be determined by the length of the programme specified in the edit heat treatment window, although the programme itself will be disregarded if the constant turn-on angle option is enabled.

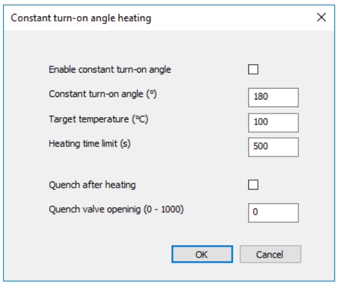

Enable constant turn-on angle ☐
Constant turn-on angle (°) 180
Target temperature (°C) 100
Heating time limit (s) 500

Quench after heating ☐
Quench valve openinig (0 - 1000) 0

Figure 3.54 - The constant turn-on angle heating dialogue.

The calibrate input channels dialogue (Figure 3.55) is where the polynomial coefficients are entered for the calibration corrections. The default coefficients loaded on starting QSCP are those calculated in sections 4.2, 4.3, and 4.4. Coefficients entered here will remain so until the programme is closed. The user has the option to save the current coefficients to file, or to load a set from file. The record voltage check box will disable heating and cause the run heat treatment window to record the filtered, but uncorrected, voltages instead of the measured quantity (i.e. the thermocouple voltage rather than calculated temperature); this option is for use when performing a calibration.

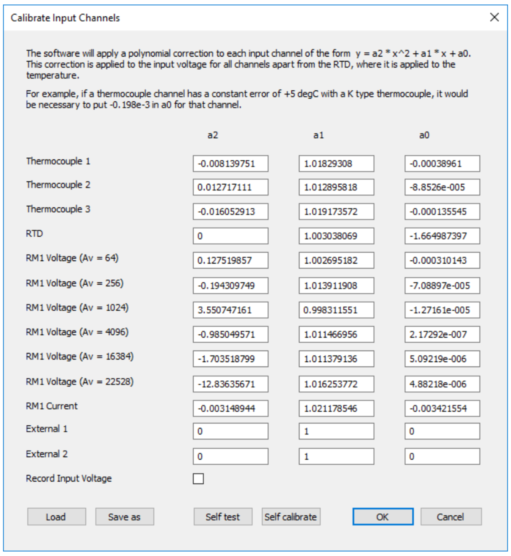

The software will apply a polynomial correction to each input channel of the form y = a2 * x^2 + a1 * x + a0. This correction is applied to the input voltage for all channels apart from the RTD, where it is applied to the temperature.

For example, if a thermocouple channel has a constant error of +5 degC with a K type thermocouple, it would be necessary to put -0.198e-3 in a0 for that channel.

	a2	a1	a0
Thermocouple 1	-0.008139751	1.01829308	-0.00038961
Thermocouple 2	0.012717111	1.012895818	-8.8526e-005
Thermocouple 3	-0.016052913	1.019173572	-0.000135545
RTD	0	1.003038069	-1.664987397
RM1 Voltage (Av = 64)	0.127519857	1.002695182	-0.000310143
RM1 Voltage (Av = 256)	-0.194309749	1.013911908	-7.08897e-005
RM1 Voltage (Av = 1024)	3.550747161	0.998311551	-1.27161e-005
RM1 Voltage (Av = 4096)	-0.985049571	1.011466956	2.17292e-007
RM1 Voltage (Av = 16384)	-1.703518799	1.011379136	5.09219e-006
RM1 Voltage (Av = 22528)	-12.83635671	1.016253772	4.88218e-006
RM1 Current	-0.003148944	1.021178546	-0.003421554
External 1	0	1	0
External 2	0	1	0
Record Input Voltage	☐		

Figure 3.55 - The calibrate input channels dialogue.

The advanced options dialogue is used to enable the recording of raw unprocessed data; this option is for the recording of the raw unprocessed data from the data acquisition card at a rate of 200,000 samples per second. This option was included for development purposes and should not normally be required, but has been retained as an option in case it is suspected that there are future data artefacts caused by the digital signal processing. Because of the rate at which the raw data needs to be saved to disk, it is not possible to parse the data as human readable files at run time. Any raw data files will need to be subsequently converted to CSV files using the standalone application QS Raw Data Converter.

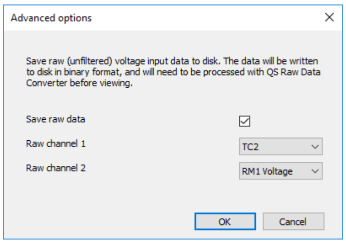

Save raw (unfiltered) voltage input data to disk. The data will be written to disk in binary format, and will need to be processed with QS Raw Data Converter before viewing.

Save raw data ☑

Raw channel 1 TC2

Raw channel 2 RM1 Voltage

Figure 3.56 - The advanced options dialogue.

3.4.8.2 Code structure

The code is implemented as an MFC dialog application, where each window described in section 3.4.8.1 is a class derived from CDialogEX. The windows other than the run heat treatment window are essential elements of the user interface and represent a considerable amount of work, but as they do not directly influence the machine performance, the detail of their operation will be omitted.

The run heat treatment window is the critical piece of code that is essential for the machine operation and a full copy of the header and source files can be found in Appendix 45 and Appendix 46. As these files are of considerable length and the operation not immediately obvious, a series of UML activity diagrams are included in Appendix 26 to Appendix 31 to provide an overview of the core functionality. The basic GUI handling of this window is encapsulated within the CRunHeatTreatment class, but the data processing and graphic data display is handled in a non-object orientated manner.

As shown in Appendix 26, when the user clicks to start the heat treatment the various options are loaded, and if heating is enabled, the minimum turn-on angle will be found (Appendix 27). The data acquisition tasks will then be configured and started. The NI-DAQmx will call the EveryNCallbackHighSpeed() callback function (Appendix 28) when 500 samples have been received; this callback function will be executed NI-DAQmx thread.

A thread is a path of code execution, whose processor time is managed by the operating system. In a simple situation each application consists of a single thread running on a processor with a single core, with multiple applications open, the operating system will rapidly switch between the different threads, giving each thread processor time, and thereby enabling multiple applications to run apparently simultaneously. If the processor has multiple cores, then the operating system can use those multiple cores to have multiple threads executing at the same time. Furthermore, it is possible to construct individual applications that use multiple threads, to take advantage of the multiple cores found in modern processors. However, such an approach is only useful if there are sections of the application code that do not need to execute in a predetermined order: this does apply to the code that controls the heat treatment.

To take advantage of the four cores that are found in the control PC’s AMD A10 5800B microprocessor, the code for running the heat treatment creates an additional thread that co-ordinates the digital signal processing (Appendix 29) and performs the digital signal processing for the first thermocouple channel and RTD, and additional threads for processing the other six input channels (Appendix 30), and processing the output (Appendix 31). As the data samples need to flow through these threads in the correct order there is also the need for a significant amount of thread synchronization, which can be seen in the code (Appendix 46). To help the reader understand the flow of data through the various threads and functions when reading the code, a data flow diagram for the first thermocouple channel is provided in Appendix 32.

3.4.8.3 Quenching Simulator USB Terminal

Prior to the QSCP application, a second application, the Quenching Simulator USB Terminal (Figure 3.57) was developed. This application is not intended for the general user, but was constructed to help the instrument development. This programme allows CAN commands to be sent to the control modules via the USB link to the bridge module. This enables the manual control of all aspects of the instrument, but has no support for the data acquisition system described in section 3.5.8.

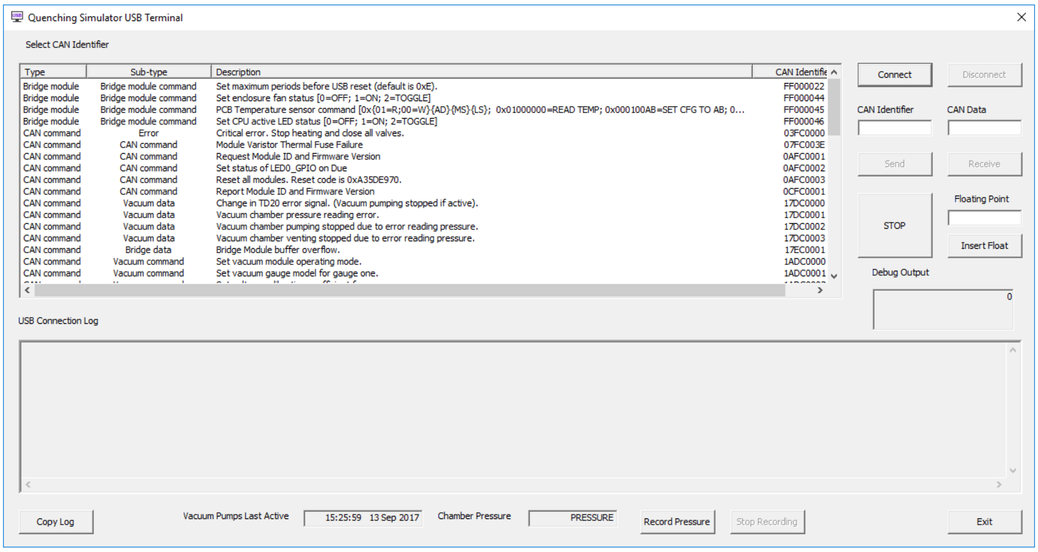

Type	Sub-type	Description	CAN Identifie
Bridge module	Bridge module command	Set maximum periods before USB reset (default is 0xE).	FF000022
Bridge module	Bridge module command	Set enclosure fan status [0=OFF; 1=ON; 2=TOGGLE]	FF000044
Bridge module	Bridge module command	PCB Temperature sensor command [0x{01=R;00=W}{AD}{MS}{LS}; 0x01000000=READ TEMP; 0x000100AB=SET CFG TO AB; 0...	FF000045
Bridge module	Bridge module command	Set CPU active LED status [0=OFF; 1=ON; 2=TOGGLE]	FF000046
CAN command	Error	Critical error. Stop heating and close all valves.	03FC0000
CAN command	CAN command	Module Varistor Thermal Fuse Failure	07FC003E
CAN command	CAN command	Request Module ID and Firmware Version	0AFC0001
CAN command	CAN command	Set status of LED0_GPIO on Due	0AFC0002
CAN command	CAN command	Reset all modules. Reset code is 0xA35DE970.	0AFC0003
CAN command	CAN command	Report Module ID and Firmware Version	0CFC0001
CAN command	Vacuum data	Change in TD20 error signal. (Vacuum pumping stopped if active).	17DC0000
CAN command	Vacuum data	Vacuum chamber pressure reading error.	17DC0001
CAN command	Vacuum data	Vacuum chamber pumping stopped due to error reading pressure.	17DC0002
CAN command	Vacuum data	Vacuum chamber venting stopped due to error reading pressure.	17DC0003
CAN command	Bridge data	Bridge Module buffer overflow.	17EC0001
CAN command	Vacuum command	Set vacuum module operating mode.	1ADC0000
CAN command	Vacuum command	Set vacuum gauge model for gauge one.	1ADC0001

Debug Output: 0

Vacuum Pumps Last Active: 15:25:59 13 Sep 2017

Chamber Pressure: PRESSURE

Figure 3.57 - The Quenching Simulator USB Terminal application.

3.5 Instrumentation

The instrumentation module is arguably the most critical piece of electronics in this project, as it is the instrumentation that records what has actually happened, and produces the scientific data. The instrumentation module contains three thermocouple channels, a platinum RTD for thermocouple cold junction compensation, a current source and voltage measurement circuit for electrical resistance measurements, and two external inputs for future expansion.

All channels make use of differential signalling, and where possible twisted pair cabling, to reduce interference from common mode and low frequency magnetic interference [80], which is the type that will be produced by the high current heating circuit.

The instrumentation module also contains optocouplers to electrically isolate the inputs from the PC data acquisition system (DAQ), and antialiasing filters to condition the signals for sampling. The circuit diagram for the instrumentation module is in Appendix 24.

3.5.1 Resistance measurement

The electrical resistance measurement is made using four wire Kelvin connections. In this arrangement a pair of wires is used to pass a known electrical current through the specimen being measured. Another pair of wires is used to measure the voltage drop across the sample. The voltage measurement pair is connected to a high input impedance amplifier, such that negligible current flows through this pair. This avoids any potential error in the measurement due to the voltage drop in the current carrying pair.

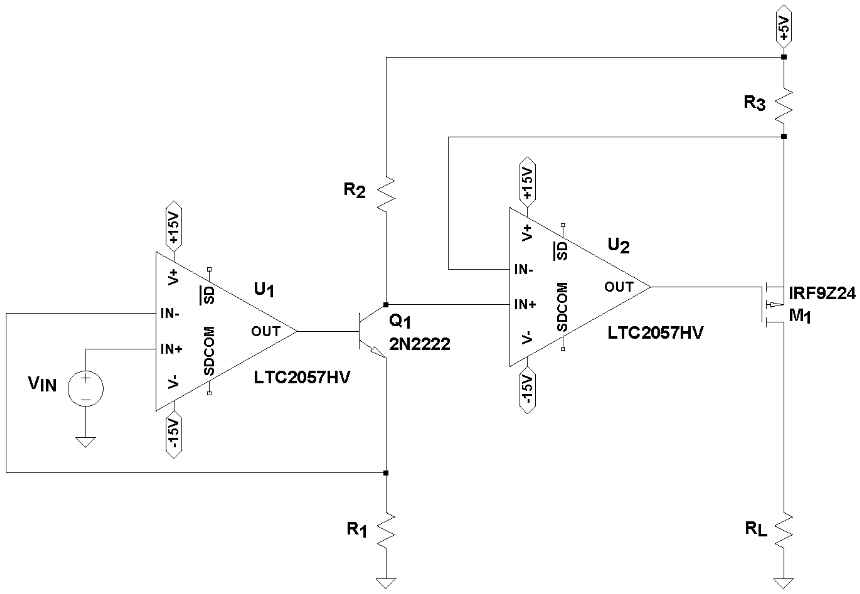

Figure 3.58 - Voltage controlled current source used for electrical resistance measurements.

The known electrical current is produced by a voltage controlled current source, taken from Horowitz and Hill[84], which is shown in Figure 3.58. As the operational amplifiers in this circuit make use of negative feedback, this circuit can readily be understood by making use of the op-amp *golden rules*, which can be stated as "I. The output attempts to do whatever is necessary to make the voltage difference between the inputs zero. … II. The inputs draw no current." Using the first op-amp *golden rule*, we can assume that the voltage at the inverting input of U_1 (and the emitter voltage of Q_1) is V_{IN}, which allows the current through R_1 to be calculated as:

$$I_{R1} = \frac{V_{IN}}{R_1} \tag{3.11}$$

If we assume that Q_1 has a very large current gain, then the collector current will be approximately equal to the emitter current, which making use of the second *golden rule* gives the current through R_2 as:

$$I_{R2} \simeq I_{R1} = \frac{V_{IN}}{R_1} \tag{3.12}$$

The collector voltage of Q_1 is equal to 5V less the voltage drop across R_2:

$$V_C = 5 - R_2 \frac{V_{IN}}{R_1} \qquad 3.13$$

The source voltage of the P-channel MOSFET M_1 is equal to 5V less the voltage drop across R_3. As the second *golden rule* states that no current flows into the op-amp inputs of U_2, the current through R_3 must equal that through the load (R_L). This allows the source voltage to be expressed in terms of the load current as:

$$V_S = 5 - R_3 I_L \qquad 3.14$$

Applying the first *golden rule* to U_2, which yields $V_S = V_C$, enables the load current to be calculated as a function of V_{IN} by combining equations 3.13 and 3.14 to give:

$$I_L = V_{IN} \frac{R_2}{R_1 R_2} \qquad 3.15$$

For the resistance measurement circuit V_{IN} is provided by an Intersil ISL21010-10 bandgap voltage reference as a constant value of 1.024 V. The resistor values were chosen as R_1 = 2 kΩ, R_2 = 1 kΩ, and R_3 = 1 Ω. This combination of input voltage and resistor values gives a nominal output of 512 mA. At a current of 512 mA, there will be a voltage drop of 512 mV across R_3 and a voltage drop of approximately 89.6 mV across M_1 (assuming $R_{DS\ (on)}$ = 175 mΩ), which means that the maximum load resistance for which the specified current can be delivered is 8.59 Ω. To accurately measure the actual output of this current source, the high impedance inputs of Texas Instruments PGA281 instrumentation amplifiers are connected across R_3, which after signal processing is connected to the data acquisition card.

To measure the voltage drop across the sample the inputs of a second PGA281 instrumentation amplifier are connected to the sample. Because of the very small voltages that are generated from the 0.5 A current source, the outputs of this voltage measurement PGA281 are fed into a third PGA281 for a second stage of gain. As the resistance measurement voltage will be proportional to the sample resistivity, which may vary by as much as almost two orders of magnitude (2.83×10^{-8} Ω·m for aluminium to 1.35×10^{-6} Ω·m for titanium) for potential alloys of interest, the gain of these two stages can be controlled by software. Two of the gain setting pins[9] on each of the PGA 281s are fixed, but the remaining three pins on each of the amplifiers are set by the digital outputs from the NI PCI-6143 data acquisition card. Of the 64 possible combinations, the user is able to select in the software one of the six gains listed in Table 3.4.

Table 3.4 – The user selectable gains for the voltage measurement part of the resistance measurement circuit. V_{MAX} indicates the maximum input voltage before the amplifier output will saturate. R_{MAX} is the resistance that will generate V_{MAX} when 0.5 A is flowing through the sample.

Stage 1 (U7)						***Stage 2 (U9)***						***Combined***		
G4	**G3**	**G2**	**G1**	**G0**	**A_{V1}**	**G4**	**G3**	**G2**	**G1**	**G0**	**A_{V2}**	**A_V**	**V_{MAX}**	**R_{MAX}**
0	1	0	0	0	32	0	0	1	0	0	2	64	$78.1\text{x}10^{-3}$	$156\text{x}10^{-3}$
0	1	0	1	0	128	0	0	1	0	0	2	256	$19.5\text{x}10^{-3}$	$39.1\text{x}10^{-3}$
0	1	0	1	0	128	0	0	1	1	0	8	1024	$4.88\text{x}10^{-3}$	$9.77\text{x}10^{-3}$
0	1	0	1	0	128	0	1	0	0	0	32	4096	$1.22\text{x}10^{-3}$	$2.44\text{x}10^{-3}$
0	1	0	1	0	128	0	1	0	1	0	128	16384	$305\text{x}10^{-6}$	$610\text{x}10^{-6}$
1	1	0	1	0	176	0	1	0	1	0	128	22528	$222\text{x}10^{-6}$	$444\text{x}10^{-6}$

3.5.2 Temperature measurement

The sample temperature measurement is achieved by spot welding thermocouples directly to the sample surface. The thermocouple voltage is a function of the temperature at the two dissimilar metal junctions. As the voltage is a function of the temperature at both the hot and cold metal junctions, to measure the absolute temperature of the hot junction using the thermocouple it is necessary to know the absolute temperature of the cold junction. Historic practice was to hold the thermocouple cold junction at 0°C using an ice bath, and although this method or the use of an electronic ice bath is still sometimes used, a more common approach is to directly measure the cold junction temperature. A voltage equal to the thermocouple voltage for the cold junction temperature is then added to the measured voltage. The temperature of the hot junction can then be calculated from this compensated voltage using

---

[9] On the first stage amplifier (U7) G2 is hard wired to 0V and G3 is hard wired to 5 V. On the second stage amplifier both G0 and G4 are hard wired to 0 V.

published data on the relationship between thermocouple voltage and temperatures such as found in ITS-90 [85] or available form thermocouple manufacturers.

In this instrument the thermocouple cold junction is formed when the thermocouple connector of the extension wire meets the copper thermocouple socket The law of intermediate metals tells us that the insertion of a third alloy (in this case copper) into the thermocouple circuit will not affect the thermal voltage if both ends of the third metal are at the same temperature [86]. The three thermocouple sockets are encapsulated by an isothermal copper block, whose temperature is measured using a platinum resistive temperature device (RTD). In the ITS-90 temperature scale [85] the ratio of the RTD resistance at a given temperature is defined as in equation 3.16[10]:

$$W(T_{90}) = \frac{R(T_{90})}{R(0.01\,°C)} \tag{3.16}$$

For temperatures between 0°C and 961.78°C W(T_{90}) can be calculated by equation 3.17, using the coefficients in Table 3.5.

$$W_r(T_{90}) = C_0 + \sum_{i=1}^{9} C_i \left[\frac{T_{90} - 481}{481}\right]^i \tag{3.17}$$

Table 3.5 – RTD coefficients for use in equation 3.17.

i	C_i	*i*	C_i
0	2.78157254	5	0.00511868
1	1.64650916	6	0.00187982
2	-0.13714390	7	-0.00204472
3	-0.00649767	8	-0.00046122
4	-0.00234444	9	0.00045724

As the cold junction RTD will only be subjected to small variations in temperature, the device is placed in a quarter Whetstone bridge to amplify the voltage due to the small changes in

---

[10] It should be noted that in this document T_{90} is the temperature expressed in °C, whereas in ITS-90 T_{90} is the temperature in units of K and t_{90} is the symbol for temperature in °C.

resistance. As the quarter bridge output voltage is not a perfectly linear function of the RTD resistance, the bridge output voltage was calculated numerically in Matlab for the selected excitation voltage of 1.024 V over the temperature range 0 to 40°C.

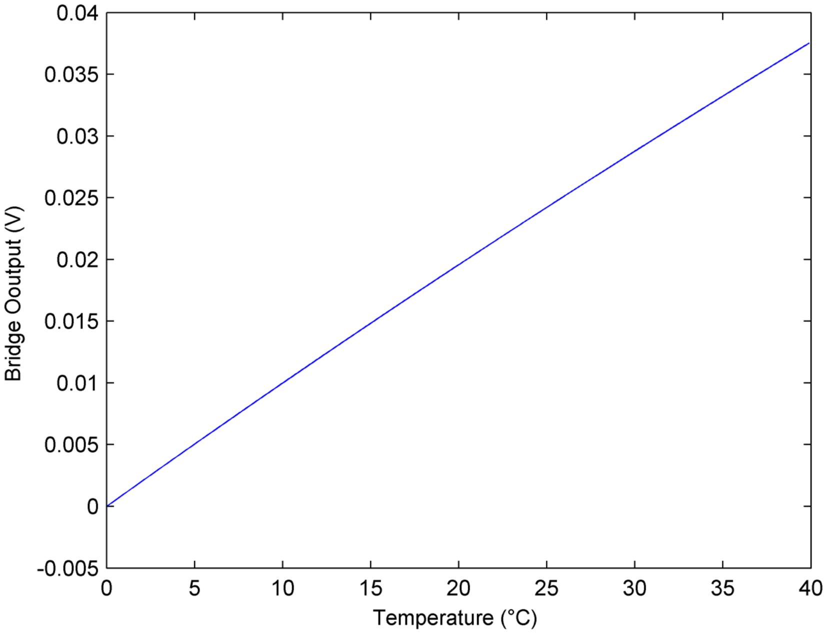

Figure 3.59 - The quarter Whetstone bride output voltage for a platinum RTD according to ITS-90 between 0 and 40°C.

The Matlab function polyfit() was then used to find a 5th order polynomial to find the RTD temperature as a function of the bridge output voltage. The 5th order polynomial is given in equation 3.18, and gives calculated errors of less than 1 x 10^{-6}°C from 0 to 40°C.

$$\begin{aligned} T = 2.505443552953665 \times 10^{4} \cdot V^{5} + 8.953607709845817 \times 10^{3} \cdot V^{4} \\ + 4.338749739120925 \times 10^{3} \cdot V^{3} + 2.059492299630510 \\ \times 10^{3} \cdot V^{2} + 9.793714010429769 \times 10^{2} \cdot V \\ - 10.0010060452900 \times 10^{-3} \end{aligned} \tag{3.18}$$

The bridge output is connected to the inputs of a Texas Instruments PGA281 instrumentation amplifier, with the gain set to 128. The master control software then uses the measured value (divided by the gain) in equation 3.18 to calculate the cold junction temperature. The compensation voltage is then calculated using the appropriate NIST thermocouple polynomial [87] and summed with the measured thermocouple voltage. The thermocouple hot junction temperature is then calculated by using the summed voltage with the NIST inverse thermocouple polynomial.

For measuring the thermocouple voltages, the three thermocouple sockets are also connected to the inputs of three PGA281 instrumentation amplifiers. As the instrument is primarily designed to be used with either type R or type S thermocouples, the thermocouple amplifiers are set to have a gain of 176. As the output voltage of the PGA281 is only guaranteed to go to 100 mV of the supply rails, this leaves only 4.8 V of output swing (split evenly about the 2.5 V common mode output voltage). This equates to a maximum thermocouple voltage of 27.27 mV, restricting the supported temperatures for type K and type N thermocouples. The maximum supported thermocouple temperatures are listed in Table 3.6.

Table 3.6 – Maximum supported thermocouple temperatures.

Thermocouple type	Maximum temperature (°C)
K	655
N	769
R	1768
S	1768

3.5.3 Analogue signal isolation

Electrical isolation is provided between all input signals and the PC data acquisition system. This isolation is provided for three main reasons: to improve the rejection of interference, to protect the PC from fault condition over voltages, and to allow the thermocouple input voltages to float. For the thermocouple temperature measurements one of the thermocouple wires is connected to the input amplifier ground to provide a path to ground for common mode voltages, but as the thermocouple is in electrical contact with the sample, this will attempt to pull the region where the two connect to ground (less the small voltage in the thermocouple lead). Without floating the thermocouple input stage ground, the system heating voltage would attempt, with up to 2000 A of current, to complete the circuit through the thermocouple instrumentation amplifier.

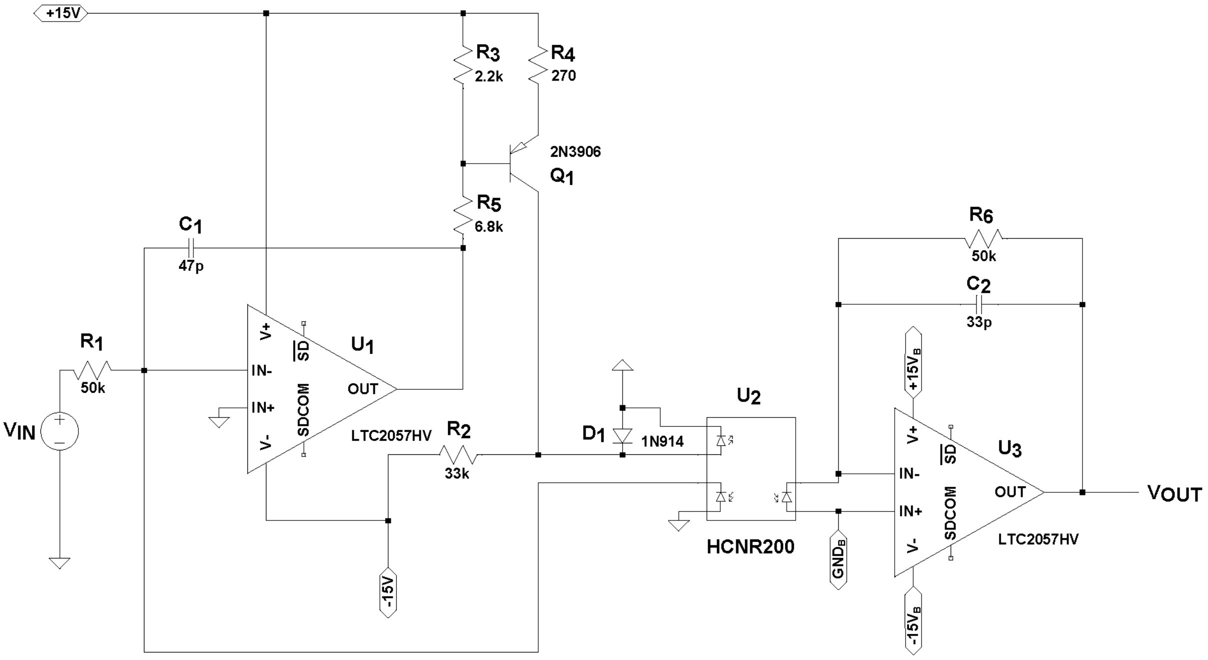

Figure 3.60 - Analogue isolator. This circuit uses feedback to linearize the output of the optocoupler.

Each half of the differential signal was isolated by the use of an Avago HCNR200 optocoupler. The isolation circuit is shown in Figure 3.60, which is taken from the HCNR200 datasheet. The HCNR200 consists of an LED and two photodiodes, one on the input side and one on the output side. The two photodiodes are well matched in the output photocurrent that is generated by the light emitted from the diode. The photodiode on the input side is used to linearize the photocurrent of the LED on the input side, which is converted to a voltage by a transresistance amplifier. The resistors R_3, R_4, and R_5 are used to bias Q_1 such that the LED of U_2 is kept in the light emitting region, which would otherwise turn-off for small input voltages. The resistors C_1 and C_2 are used to improve the stability of U_1 and U_3 by increasing the negative feedback at high frequencies, thereby reducing the closed loop gain and preventing the oscillations that could otherwise occur due to the phase shifts caused by the output capacitances of the amplifiers. The sole function of D_1 is to limit the potential reverse bias to the LED of U_2. The gain of this isolation circuit is controlled only by the resistors R_1 and R_6.

$$\frac{V_{OUT}}{V_{IN}} = \frac{R_6}{R_1} \qquad 3.19$$

As the operation of this circuit is non-trivial, and there is only a limited explanation in the HCNR200 datasheet, a full circuit analysis is provided in Appendix 25.

3.5.4 *Analogue signal processing*

The main analogue signal processing is the low pass anti-alias filtering that takes place after the analogue signal isolation. The Shannon sampling theorem states that a signal must be sampled at twice the rate of the highest frequency component for the information to later be accurately reconstructed. A consequence of this is that any components of the signal whose frequency is greater than half the sampling frequency will cause distortion by aliasing (see Figure 3.61).

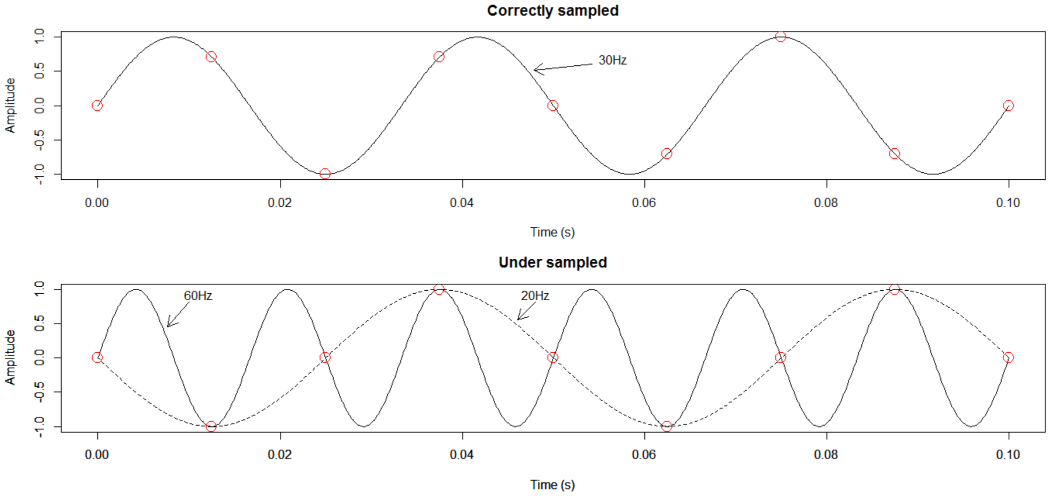

Figure 3.61 - Top: 30 Hz sine wave sampled at 80 Hz can be perfectly reconstructed. Bottom: 60 Hz sine wave sampled at 80 Hz cannot be reconstructed accurately as the sine wave cannot be distinguished from a 20 Hz sine wave: the 60 Hz frequency component has become aliased.

As real world signals contain broadband noise in addition to the signal of interest, it is not practical to sample at twice the rate of the highest frequency component. It is therefore common practice to include a low pass anti-aliasing filter to remove any frequencies above half the sampling rate. Converting the sampled signal from a continuous signal to a discrete signal introduces quantization noise, which is the noise due to the error between the actual signal value and the closest discrete value. A useful criterion for designing the anti-aliasing filter is that the noise of any remaining high frequency components should be less than the unavoidable quantization noise. If we assume that the quantization noise is evenly distributed, then for an n-bit digitizer the quantization noise to signal ratio is given by equation 3.20, which for a 16-bit ADC is -96.3 dB.

$$QNSR_{dB} = 20\log_{10}\left(\frac{1}{2^n}\right) \qquad 3.20$$

As the data acquisition card used in this instrument is 16-bit, the filter attenuation at frequencies above half the sampling frequency must be at least -96.3 dB to avoid introducing aliasing noise that is greater than the quantization noise. An ideal low pass filter would have a box like response in the frequency domain, showing no attenuation below the corner frequency and immediately transitioning to perfect attenuation at frequencies above the corner frequency. Real filters instead gradually transition from a region of low attenuation to a region of high attenuation; the transition from pass to attenuate is termed filter roll-off. Filter roll-off can be increased by increasing the order of the filter: a first order filter has a roll-off of -20 dB / decade, and a second order doubles this to -40 dB / decade, but as the filter order is further increased this will not only increase the complexity of the electronics, but will also introduce delays that can be problematic for real-time control systems (see Figure 3.63 and Figure 3.64). The analogue filter requirements can be lessened by sampling the signal at a very fast rate so that the there is a large region for the filter to transition from low attenuation at the signal frequencies to high (i.e. at least -96.3 dB) attenuation at half the sampling frequency – such an approach is referred to as oversampling. The signals of interest in this instrument will vary slowly and therefore have predominantly DC and low frequency components. If the NI PCI-6143 data acquisition card is configured to use a sampling frequency of 200 kHz, and a low pass corner frequency of 140 Hz is chosen, this will give approximately 2½ decades of spectrum for the filter response to roll-off. This means that the attenuation for a first order filter would be approximately -50 dB at half the sampling frequency, which is insufficient to meet the above criterion for keeping the aliasing noise below the quantization noise. However, the -40 dB / decade roll-off of a second order filter gives approximately -100 dB of attenuation at half the sampling frequency, which exceeds the -96.3 dB minimum requirement.

The Texas Instruments PGA281 instrumentation amplifiers that are used for the signal input have differential signal outputs, which offer a significant improvement in resilience to common mode noise. However, one disadvantage to the differential signal outputs is that commonly used analogue filter design software does not support active differential filter design. To circumvent this problem, Kuehl [88] has published a method for designing fully differential filters by using filter design software to first design a single ended multiple-feedback (MFB) topology filter. This is then easily converted to a differential filter by replacing the standard op-amp with a fully differential op-amp and *mirroring* the passive components. The filter design can then be verified in standard circuit simulation software if required. Kuehl's approach was used to design a single-ended 2nd order active Bessel filter[11] with a corner frequency of 140 Hz, which was then mirrored to yield a fully differential filter using the Texas Instruments OPA1632 fully differential operational amplifier. The filter circuit is shown in Figure 3.55, and the filter amplitude response and group delay are shown in Figure 3.63. This filter design is used as the anti-aliasing filter for the three thermocouple inputs, and both the voltage and current parts of the resistance measurement circuit.

---

[11] A Bessel filter is a filter with a response that has low phase distortion (uniform group delay).

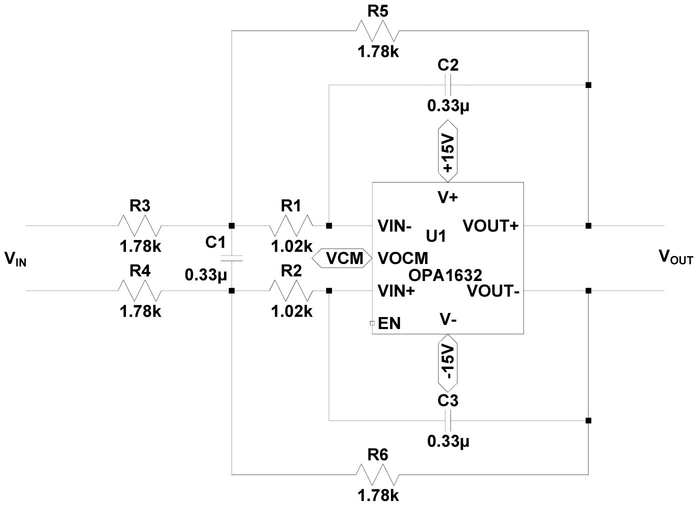

Figure 3.62 - A fully differential 2nd order low pass active filter.

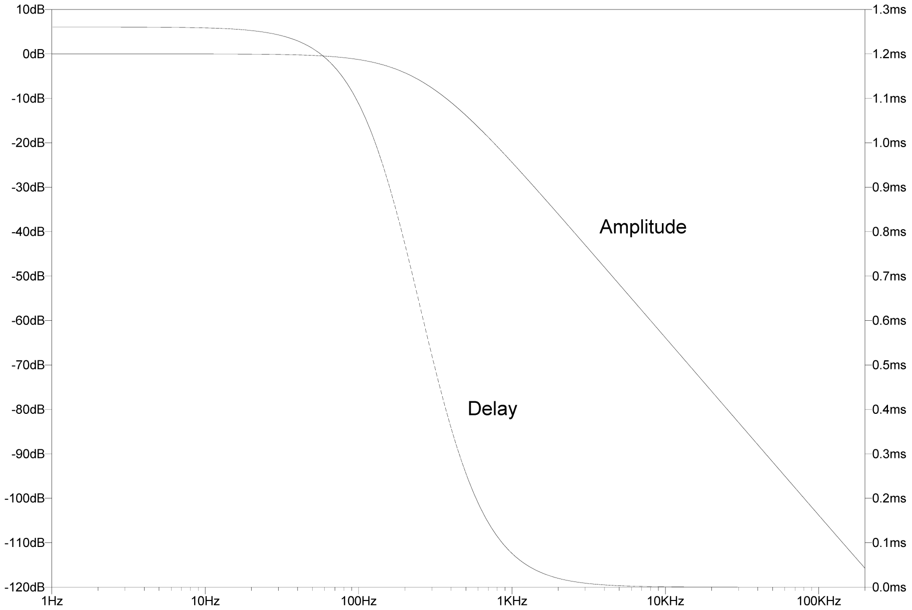

Figure 3.63 - The frequency response of the fully differential filter in Figure 3.55. Note the constant 1.26 ms delay at low frequencies.

Although oversampling has the advantages of reduced electronic complexity and potentially reduced delays, the main disadvantage is the computational requirement of digitally filtering and decimating the resulting signal (see 3.5.9). As the thermocouple cold junction temperature should be relatively stable, moderate delays introduced by filtering should be inconsequential. For this reason, the RTD bridge voltage signal is passed through an analogue 8th order active filter to reduce the digital processing load. The 8th order filter is designed using the method of Kuehl, and is effectively four filters of the type in Figure 3.55, with different values for the resistors and capacitor, cascaded together. The frequency response of the RTD anti-aliasing filter appears in Figure 3.64, and the circuit diagram can be found in the full instrumentation module circuit diagram in Appendix 24.

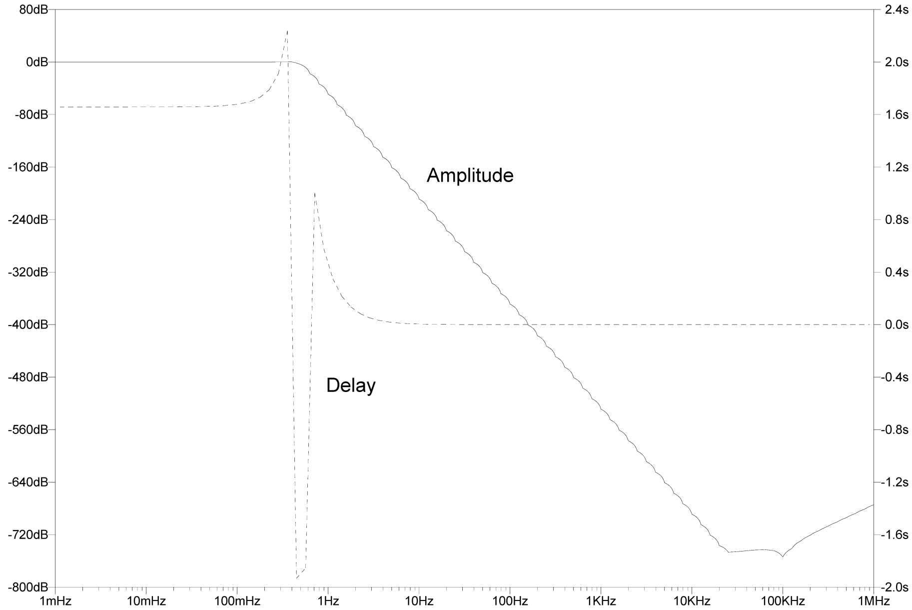

Figure 3.64 - The frequency response of the RTD 8th order fully differential active filter. The filter attenuation reaches -96.3 dB at approximately 2 Hz due to the -80 db / decade roll-off, but this comes at the expense of 1.67 s of delay at very low frequencies.

3.5.5 Digital signal isolation

Although, unlike the other electronics modules, the instrumentation module is not connected to the CAN bus, there is still digital communication with the control PC for the setting of amplifier gain (see 3.5.1). To provide protection from over voltages for the control PC and to improve noise rejection for the sensitive analogue electronics in the instrumentation module, the digital inputs from the PC DAQ card are electrically isolated using Avago ACPL-077L optocouplers. The ACPL-077L optocoupler encompasses an LED and CMOS driver along with a photodiode with CMOS output. The circuit implementation is straightforward, requiring only power supply connections and three bypass capacitors. The ACPL-077L has a very low input current because of the CMOS input, and according to the datasheet offers a CMRR of 35 kV / µs.

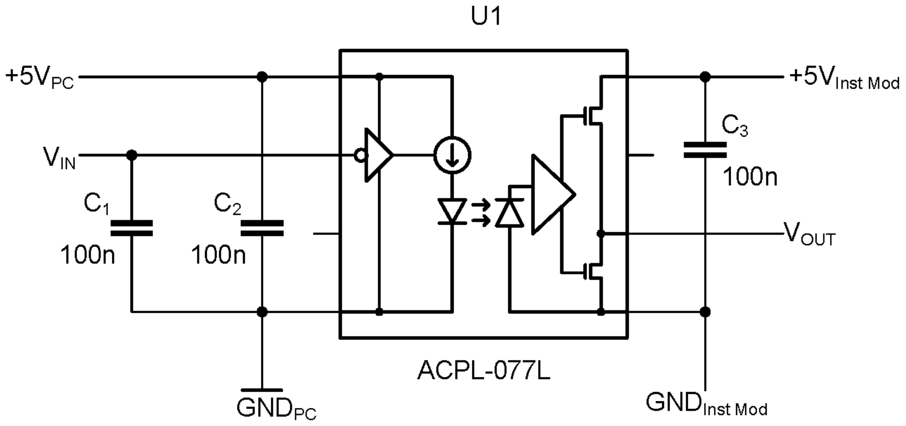

Figure 3.65 - The circuit used to provide electrical isolation for digital inputs to the instrumentation module.

3.5.6 Vacuum feedthrough unallocated conductors

The four wires required for the resistance measurement circuit enter the vacuum chamber through a twenty-five pin Micro-D connector (see 3.3.2). To facilitate the future use of additional measurement techniques, eight of the nineteen unused feedthrough conductors are made available on an externally accessible twenty-five pin Sub-D connector. The unavailability of the remaining thirteen connectors is due to the congestion of tracks in the connector region on the PCB. If future work requires more than 8 signal lines, or significant current or voltages, then additional feedthroughs can be added by using a tee on a suitable chamber port.

3.5.7 External inputs

The National Instruments PCI-6143 accepts the simultaneous sampling of up to eight differential analogue input channels (see 3.5.8). The three thermocouple channels and RTD combined with the resistance measurement circuit uses six channels, leaving two unused channels. These two unused differential channels are available for additional user inputs through a nine pin D-sub connector on the rear of the instrumentation module. With the exception of Zener diodes (1N4733A) to offer basic over-voltage protection, there is no analogue signal processing circuitry within the instrumentation module for the external channels. The external channels would require as a minimum a suitable anti-aliasing filter to reduce any significant frequency components above 100 kHz, and depending on the sensor type may also require electrical isolation. The external channels receive the same digital signal processing (see section Data acquisition system) as the thermocouple and resistance measurement channels, and can be enabled by the user in the control panel software for voltage recording. Conversion to measured parameter from sensor output voltage must be completed by the user in post-processing.

3.5.8 Data acquisition system

The data acquisition system consists of a National Instrument PCI-6143 data acquisition card installed in a personal computer (PC) running Microsoft Windows 10. The PCI-6143 offers simultaneous sampling of up to eight differential signals, with sampling rates of up to 250 kHz and 16-bit conversion. The common mode rejection ratio of the analogue input channels in differential mode is a relatively modest 75 dB at 50 Hz. Of the eight available channels three are used for the thermocouple inputs, one for the RTD bridge voltage, one for the resistance measurement voltage, one for the resistance measurement current monitoring, and two are made available as external input for future adaptability.

In addition to the eight analogue input channels the PCI-6143 has eight digital channels that can be used as either inputs or outputs. Six of these channels are used as outputs to control the instrumentation amplifier gains for the resistance measurement voltage sensing circuit (see 3.5.1). The PCI-6143 also contains two 24-bit counter / timers that are unused.

The PCI-6143 is controlled by the Quenching Simulator Control Panel software (see 3.4.8) which is written in C++ / MFC. The PCI-6143 functionality is accessed through the NI-DAQmx application programming interface.

3.5.9 *Digital signal processing*

Figure 3.59 shows the output[12] from the data acquisition card for the thermocouple channel prior to any digital signal processing. The data is from a sample of cobalt being heated to 550°C with a constant turn-on angle of 135°, before being allowed to cool naturally. It appears from the raw data that the noise is significant only when the heating current is applied.

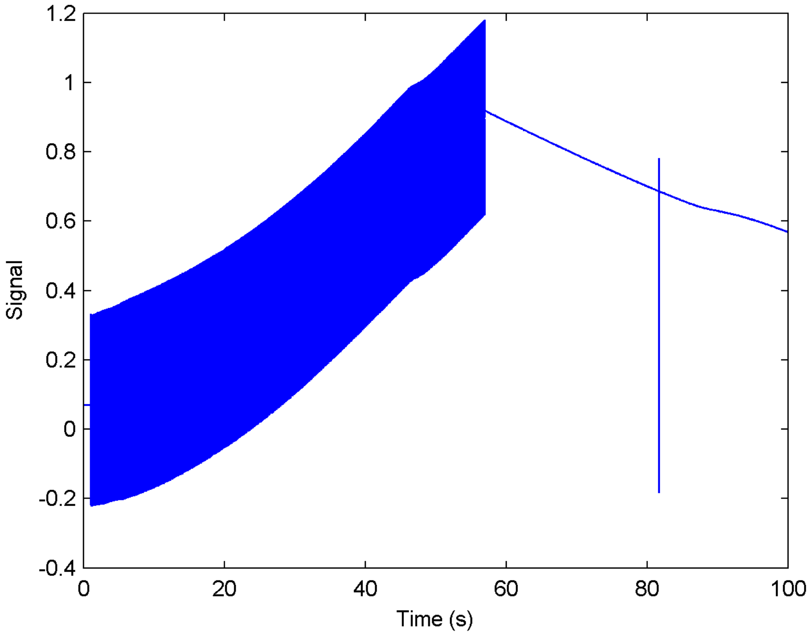

Figure 3.66 - The unprocessed thermocouple signal at 200,000 samples per second.

It is difficult to determine the source of the noise in the fast Fourier transform (FFT) when the x-axis shows the full spectrum (Figure 3.60). However, if the FFT is enlarged in the low frequency region (Figure 3.61), it can clearly be seen that the noise is 50 Hz harmonic noise; this confirms that the noise is due to the large 50 Hz chopped heating current.

---

[12] The signals displayed in this section have been multiplied by -1 for clarity, so that the signal becomes more positive as the temperature increases: the actual input sample becomes more negative as the temperature increases.

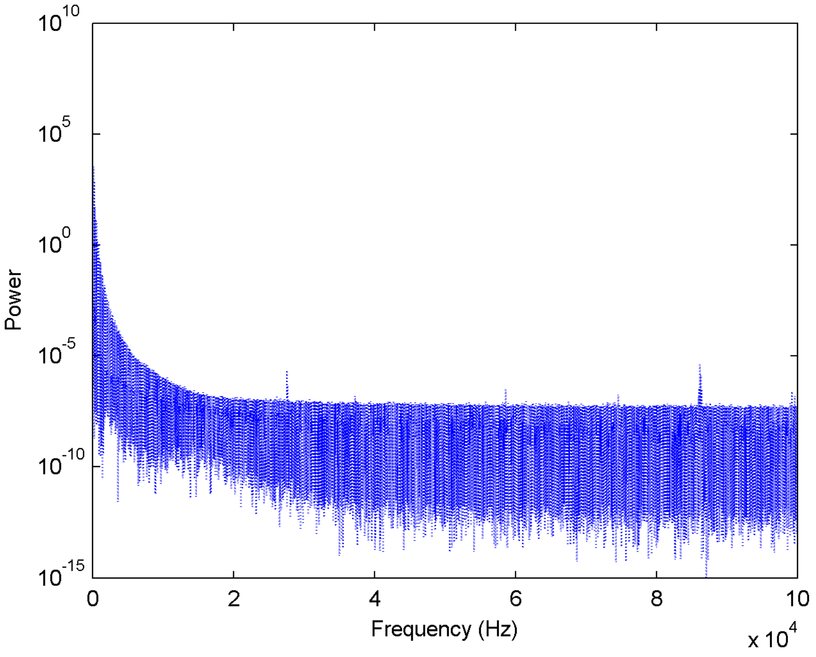

Figure 3.67 - The FFT of the raw input samples.

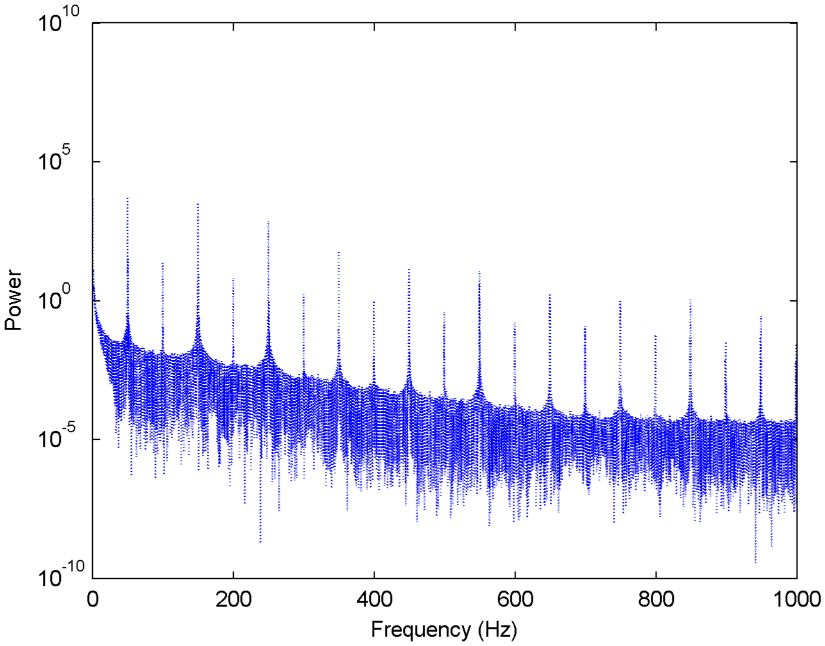

Figure 3.68 - The raw input samples FFT, enlarged to clearly show values between DC and 1 kHz.

Once the signal noise spectrum is known, the remaining question before a filter can be designed is what is the signal spectrum? All of the input signals will be slowly varying DC signals: for example the thermocouple voltage is a function of temperature and will only change as quickly as the temperature changes. If the sample is quenched at the critical cooling rate for a 22MnB5 steel of 27°C/s, then it would be necessary to take 27 readings per second to have readings at 1°C intervals. Given that the error of class 1 type R thermocouple wire will be at least 1°C, reading at 1°C intervals would seem to be a reasonable target. With this in mind, it was decided that the input samples should be decimated to 50 samples per second, which to avoid aliasing would first require low pass filtering with an attenuation of at least -96.3 dB (see 3.5.4) at frequencies above half the sampling frequency (0.5 f_s = 25 Hz).

There are two main types of common digital filters: finite impulse response (FIR) filters, and infinite impulse response (IIR) filters. Equation 3.21 shows the general form of the z-domain[13] digital filter transfer function; FIR filters have B(z) = 1. FIR filters are the more commonly implemented type of digital filter because of the inherent stability, good availability of design tools, and can be designed to have a linear phase response.

$$H(z) = \frac{B(z)}{A(z)} \tag{3.21}$$

Ichige et al. [89] published an algorithm that can be used to estimate the required order of an FIR filter to meet design criteria. The required criteria are the passband ripple (δ_p), the stopband attenuation (δ_s), the passband edge frequency (f_p), and the stopband edge frequency (f_s). For a single stage antialiasing filter, if the design criteria are defined as δ_p = 0.05 dB, δ_s = 98 dB, f_s = 25 Hz, and f_p = 20 Hz to allow for the filter roll-off, then Ichige's algorithm estimates a filter order of 154,651. This filter would require 154,651 storage elements, 3.09×10^{10} multiplications per second, and most significantly have a delay of 387 ms. Such a filter is clearly impractical, not only because of the onerous processing requirements, but also because of the control error caused by the delay: if the sample is being heated or cooled at just 27°C/s, the feedback value for the control system would be inaccurate by 10.4°C.

---

[13] The z-domain is the discreet signal equivalent of the Fourier domain for continuous signals.

The processing and memory requirements of a filtration and decimation system can be reduced by performing the filtering and decimating in multiple stages: this is termed multirate signal processing. The total decimation factor needed to get from 200,000 samples per second to 50 samples per second is 4000. To calculate the processing and memory requirements for a multirate scheme, the 23 integer factors of 4000 greater than 1 were calculated. The values of the overall decimation factor of 4000 divided by these factors were calculated, and the integer factors greater than one of these numbers were found. The first stage decimation factors were then divided by these new factors only if they were less than or equal to the first stage decimation factors. This process was repeated until no factors were left. Including the original single stage filter and decimator, this gave a total of 97 different ways to achieve the overall decimation of 4000 when the decimation factor was less than or equal to the factor of the previous stage. Using the method of Ichige, the order of filter for each stage was calculated with the same values of δ_p = 0.05 dB and δ_s = 98 dB, but with stopband edge frequency that would be equal to half of the sampling frequency of the following stage. The passband frequency was increased to 25 Hz for all stages apart from the final stage, where it remained at 20 Hz. The decimation factors, estimated filter orders, total multiplications per second, total storage requirements, and delays for the different factor combinations are tabulated in Appendix 33. It can be seen in Appendix 33 that the use of multirate signal processing can significantly reduce the processing requirements for filtering, but worsens the delay. The processing requirements are reduced as it is the filter order at high sampling frequencies that makes the significant contribution to the total multiplications per second. The majority of the delay comes from the final stage, which must transition from passband to stopband in just 5 Hz; this can be seen from the column in Appendix 33, which indicates the total delay excluding the last stage.

It was decided to investigate performing multirate decimation as calculated in Appendix 33, but with the final stage replaced with a filter of much lower order for the real-time control, and to use a post-processing filter for the final recorded data. From the calculated multirate schemes, a three stage process of decimating by 20, then by 20, and finally by 10 was chose as having a good combination of reduced processing requirements, low delay excluding the final stage, whilst keeping the number of stages manageable.

The first stage linear phase filter was designed using the Matlab function firgr() for 156th order filter with $f_p = 25$ Hz and $f_s = 5000$ Hz for a sampling frequency of 200,000 Hz. Figure 3.62 shows the magnitude response of the calculated filter. It can be seen from the magnitude response of the filter that it does not completely satisfy the requirement to attenuate the signal by at least -96.3 dB above 5000 Hz. However, it is necessary to consider the prior attenuation by the analogue anti-aliasing filter (see 3.5.4). For example, the first peak in the stopband ripple is where the filter attenuation degrades to -84.6 dB at a frequency of 5.2 kHz, at which point the analogue filter attenuation is approximately -52.6 dB, which gives a total attenuation of -137.2 dB at 5.2 kHz. As the analogue filter attenuation continues to improve with increasing frequency, this will be the poorest region of stopband attenuation.

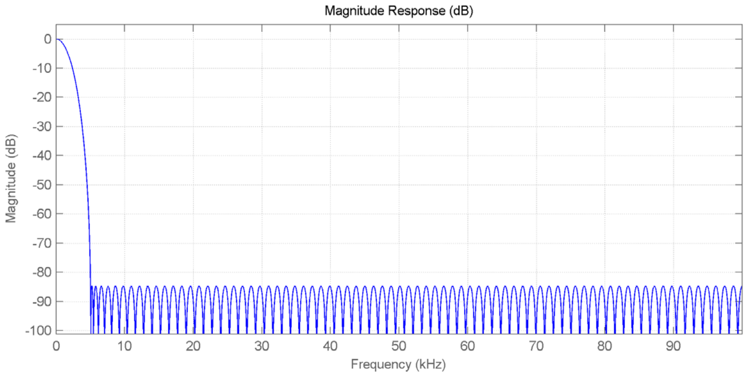

Figure 3.69 - The magnitude response of the first stage FIR filter.

Figure 3.63 shows the thermocouple signal and FFT after applying the first stage filter in Matlab and then decimating by a factor of 20. It should be highlighted that the Matlab filter does not apply the filter initialization that is used in the QSCP code, and as such a small region of startup transient can be seen.

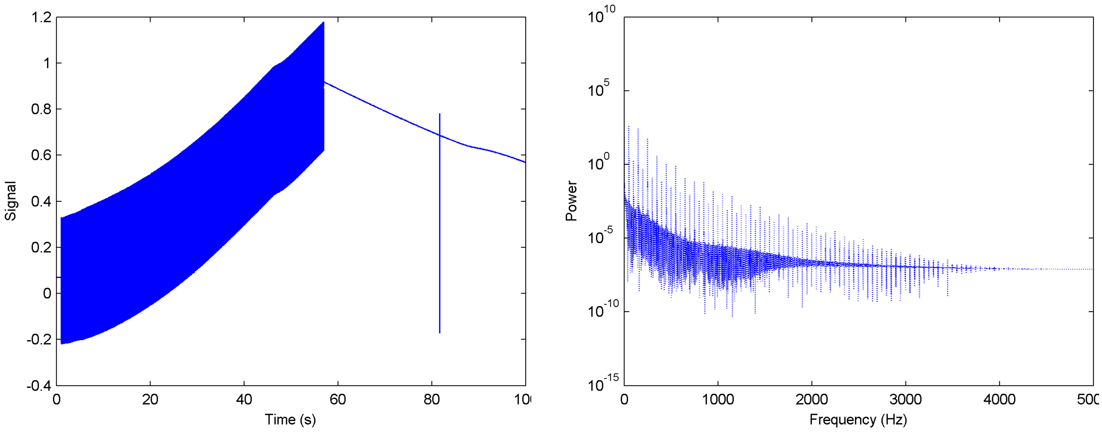

Figure 3.70 - The thermocouple signal (left) and FFT (right) after the first stage filter and decimator.

The second stage filter was also designed using the Matlab function firgr(), but with the parameters N = 174, f_p = 25 Hz and f_s = 250 Hz for a sampling frequency of 10,000 Hz. Figure 3.64 shows the magnitude response of the second stage filter.

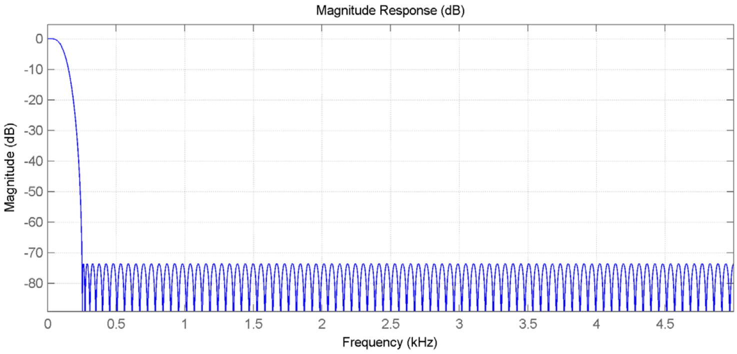

Figure 3.71 - The magnitude response of the second stage FIR filter.

The results of applying the second stage filter and decimating by a second factor of 20 are shown in Figure 3.65.

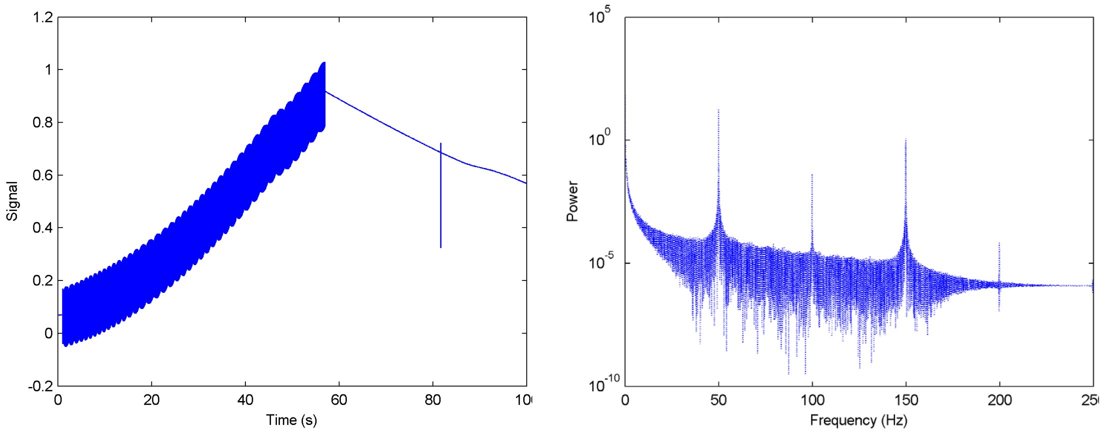

Figure 3.72 - The thermocouple signal (left) and FFT (right) after the second stage filter and decimator

Efforts to design a FIR filter with low delay and good noise attenuation proved to be unsuccessful. As the noise has clearly defined peaks it was decided to try designing an IIR filter for the third stage by using the Matlab fdatool to manually place the filter zeros (see Figure 3.66).

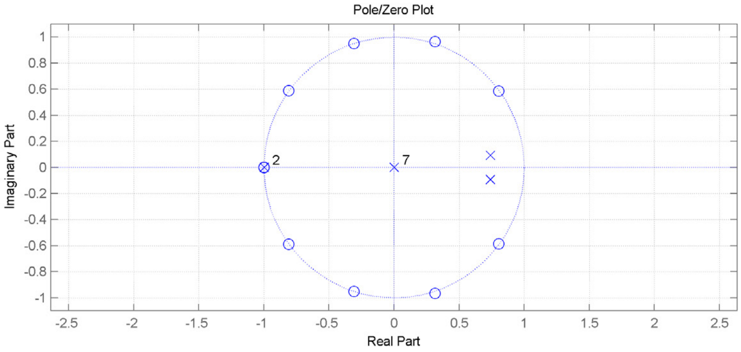

Figure 3.73 - The pole zero plot for the third stage IIR filter.

The IIR filter was designed to be 10th order to limit the group delay to 10 samples at 500 samples per second, which leads to a delay of 1 output samples (20 ms). Figure 3.67 illustrates how the manual pole zero placement enables the IIR filter response to be accurately tuned to the 50 Hz harmonic noise.

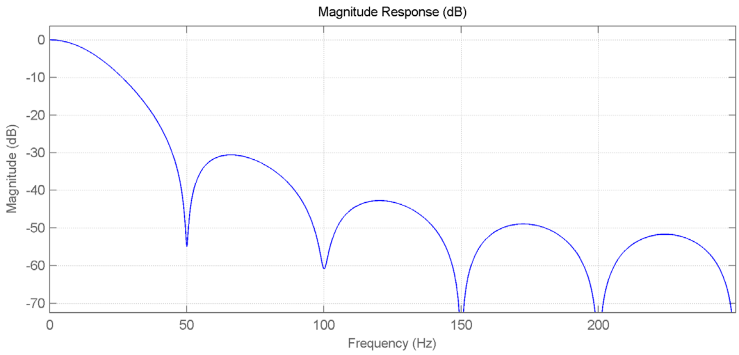

Figure 3.74 - The magnitude response of the third stage IIR filter.

Figure 3.68 shows the signal and FFT after applying the third stage IIR filter and decimation. This figure also shows the signal after being filtered with the 388th order filter that Ichige's algorithm predicted would be necessary. It can be seen that for the noise present in this instrument that there is no obvious difference in performance between the two filters. As such it was assessed that there would be no benefit to using a separate filter to post process the saved data after the second stage, and the same data from the IIR filter would be used both for control and measurement.

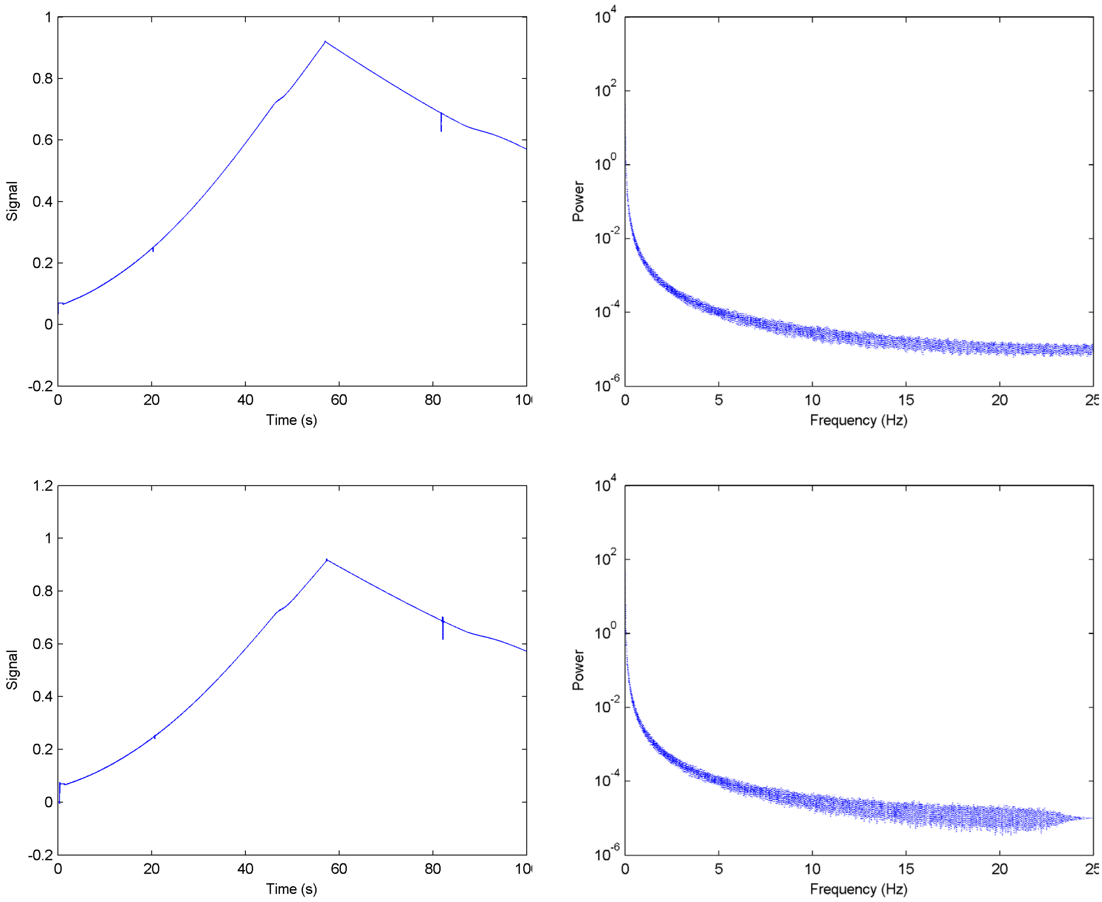

Figure 3.75 - The thermocouple signals and FFTs for the 10th order IIR filter (top row) and the 388th order FIR filter (bottom row).

3.5.10 Instrument enclosure

An enclosure for the main components of the instrument was designed in Autodesk Inventor. The enclosure was designed to mount the vacuum chamber on the top of a three section cabinet. The left hand cabinet section is for the control PC, the central section is for the electronics modules, and the right hand section is for the rotary vacuum pump. The chamber consists of a steel box section frame with a sheet steel skin to offer limited dust ingress protection as well as some additional electromagnetic shielding. Figure 3.69 shows the completed instrument enclosure as fabricated by Premier Engineering Ltd, Doncaster.

Figure 3.76 - The quenching simulator instrument enclosure.

3.5.11 Module enclosures

The four control modules and the instrumentation module were installed in Schroff Multipac Pro rack mountable cases. The case front panels were machined by Schaeffer AG, Berlin. Figure 3.70 shows the module enclosures installed in the centre section of the main instrument enclosure.

Figure 3.77 - The individual module enclosures installed in the main instrument enclosure.

3.5.12 Transformer framework

Figure 3.71 shows the transformer framework that was constructed by MIG welding steel box section, which was then spray coated. The transformer framework was necessary to raise the transformer to approximately the same level as the vacuum chamber power feedthroughs (see 3.3.2) because of the inflexibility of the high current cable (see 3.2.1.9).

Figure 3.78 - The power transformer and support frame.

4 Calibration

This chapter outlines the procedures used to calibrate the different measurement systems used in the quenching simulator. Prior to any calibration procedures the quenching simulator electronics, control PC, and any external instruments were switched-on to warm-up for at least two hours[14] before any measurements were taken. Once warmed-up, and after every few hours, the data acquisition card self-calibration procedure (see 4.5) was activated.

The measurements were conducted at times when there were as few sources of electrical interference being used as was possible. Indeed for the resistance measurement voltage calibrations (4.4), the signal levels were so low that the LED lighting that was close to the instrument was switched-off as there appeared to be electromagnetic interference.

4.1 Vacuum gauge calibration

The vacuum gauge calibration can be broken down into three parts: the calibration of the vacuum module data acquisition system, the gauge adjustment, and the calibration for argon.

The vacuum module data acquisition system consists of a signal conditioner and analogue to digital converter. For gauge one the signal conditioner is an attenuator made from two resistors, and for gauge two this is followed by a 2nd order anti-aliasing filter (see 3.4.3). Any errors in the data acquisition system would primarily be expected to arise from the component tolerances in the signal conditioners. For example, the attenuator has a nominal gain of 0.1948, but even using precision resistors with a tolerance of ±1% the actual gain will be between 0.1917 (-1.59%) and 0.1980 (+1.64%). To correct for this error a variable voltage laboratory power supply was connected to pins 3 and 4 on the vacuum gauge socket on the control module for gauge one. The voltage output from the laboratory power supply was measured using a Keithely 2000 6½

---

[14] The two hour warm-up period was specified in the manual for the nanovoltmeter.

digit digital multimeter (DMM). The output from the power supply was adjusted from 0 V to 10 V in 1 V steps, and both the voltages measured by the multimeter and the vacuum control module ADC were recorded. This process was then repeated for the gauge two input. The results of both sets of measurements appear in Table 4.7.

Table 4.7 – Vacuum module gauge input calibration data.

Gauge one input			Gauge two input	
Input (V)	**ADC reading (V)**		**Input (V)**	**ADC reading (V)**
0.000000	0.015080		0.000000	0.015080
0.998870	0.996240		0.999518	0.992711
2.000350	1.995368		2.002850	1.989271
3.000250	2.993212		3.004180	2.983907
4.002770	3.993302		4.003620	3.976618
5.002250	4.990825		5.003700	4.969970
6.000680	5.986744		6.003010	5.962360
7.002320	6.985872		7.004580	6.957637
8.001100	7.982433		8.004400	7.950669
9.002510	8.981561		9.003250	8.942738
10.000330	9.979726		10.004420	9.937373

Two first order polynomials of the form in equation 4.22 were fitted to the data in Table 4.7 using Microsoft Excel to express the true input voltage in terms of the ADC reading. The calculated coefficients are $a_1 = 1.0029$ and $a_0 = -0.0043$ for gauge one input, and input $a_1 = 1.0074$ and $a_0 = -0.0047$ for gauge two input. For both the gauge inputs the coefficient of determination (R^2) for the polynomial fits was very close to 1.0. This polynomial correction is applied to both gauge inputs in the vacuum control module firmware (see 3.4.7).

$$V_{IN} = a_1 \cdot V_{ADC} + a_0 \tag{4.22}$$

Both the Oerlikon PTR 90 and the Edwards APG100-XM vacuum gauges have options to calibrate the gauge outputs. The PTR 90 gauge adjustment was performed by allowing the gauge to warm-up for thirty minutes before evacuating the chamber to a pressure of approximately 2×10^{-5} mbar. The HV potentiometer was then adjusted until the reading from the calibrated gauge one ADC indicated a voltage of 4.20 V, before turning the potentiometer 1/3 turn anticlockwise. The chamber was next vented to atmospheric pressure and allowed to stabilize for around 20 minutes. The ATM potentiometer was then adjusted until the gauge voltage was 8.60 V.

The APG100-XM gauge was adjusted by allowing the gauge to warm-up for 30 minutes at atmospheric pressure. The CAL button was pressed to automatically calibrate the gauge for atmospheric pressure. The chamber was evacuated to a pressure of approximately 2 x 10^{-5} mbar, before pressing the CAL button to adjust for vacuum. As the output from both gauges can drift due to contamination and ageing, it is recommended that the calibration be performed periodically.

As explained in section 3.3.3 the vacuum gauge output is affected by the gas type. Oerlikon provide charts for the PTR 90 that enable the user to convert the gauge output to a true pressure reading for a range of commonly used industrial gasses. To enable the vacuum control module to make the conversion automatically, 11 values of the indicated pressure were read from the conversion chart for 11 values of true argon pressure from 2.5 x 10^{-6} mbar to 4 x 10^{-3} mbar. As detailed in section 3.3.3, the PTR 90 is only used for pressure readings below 4 x 10^{-3} mbar, and the vacuum system is not designed to achieve ultra-high vacuums. The fifth order polynomial in equation 4.23 was fitted to the data using Microsoft Excel. The data points and conversion polynomial are plotted in Figure 4.1.

$$P_{TRUE} = 1.4743 \times 10^{10} \cdot P_{IND}^{5} - 1.4632 \times 10^{8} \cdot P_{IND}^{4} + 5.7034 \times 10^{5} \cdot P_{IND}^{3} - 8.2478 \times 10^{2} \cdot P_{IND}^{2} + 7.6410 \times 10^{-1} \cdot P_{IND} \qquad 4.23$$

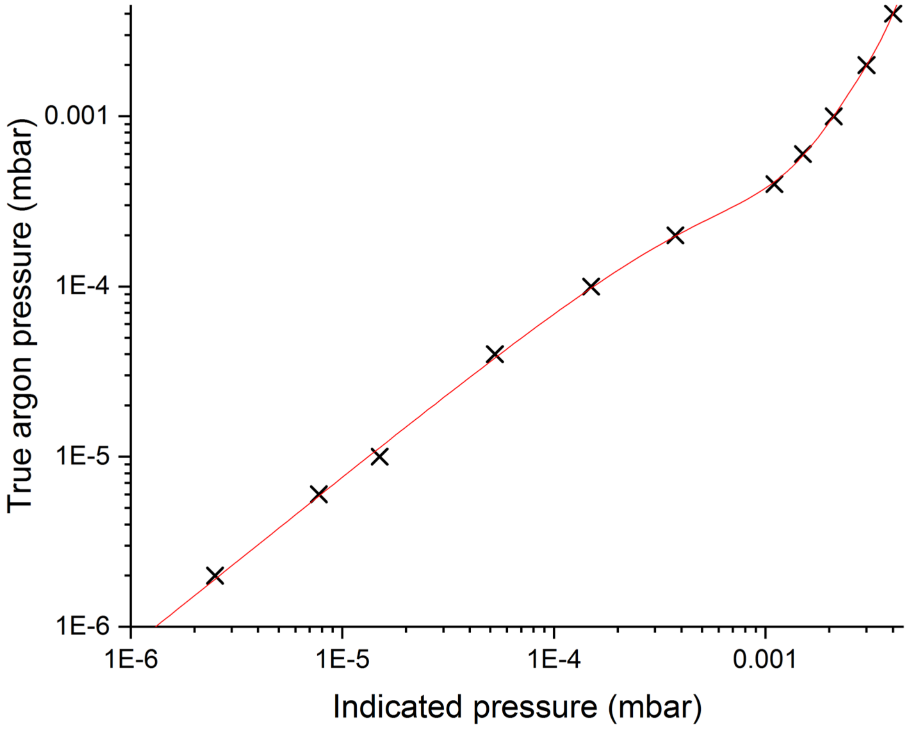

Figure 4.1 - The function to convert the indicated pressure to true pressure for the Oerlikon PTR 90 vacuum gauge when used with argon.

To create the conversion function for the APG100-XM gauge when used with argon, the indicated pressure was read from the Edwards APG100-XM conversion chart for 7 true pressures below 30 mbar. For pressure above 30 mbar a Bourdon mechanical vacuum gauge was connected to one of the chamber feedthroughs. The vacuum chamber was evacuated, and then vented with argon. The venting was halted a number of times, and both the true pressure as indicated on the Bourdon gauge and the pressure as indicated by the APG100-XM gauge were recorded. This process of evacuating and intermittently venting was repeated twice more to give a total of 59 measured data points. Different fitted curves were investigated using Microsoft Excel, where it was found that the best fit was achieved using the piecewise function in equation 4.24.

$$P_{TRUE} = \begin{cases} 0.007e^{0.9299P_{IND}}, & P_{IND} \geq 8.760098898 \\ 2.585P_{IND}^{1.0296}, & P_{IND} < 8.760098898 \end{cases} \quad 4.24$$

Figure 4.2 is a plot of the piecewise conversion function along with the data points taken from the data sheet and measured experimentally.

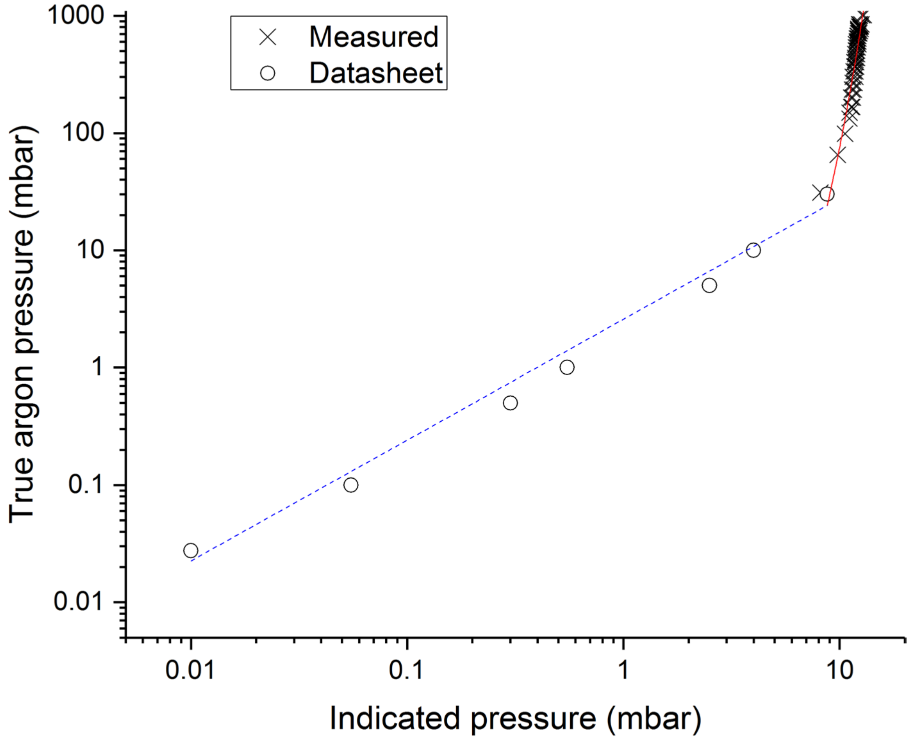

Figure 4.2 - The piecewise function to convert the indicated pressure to true pressure for the Edwards APG100-XM vacuum gauge when used with argon.

The argon gas conversion functions are included in the vacuum control module firmware, and are automatically applied to the adjusted pressure readings if the module has been told that argon is in the chamber.

4.2 Thermocouple calibration

The ideal method for calibrating a thermocouple is to calibrate the thermocouple and reader as a combined system. This involves using the thermocouple and reader with a series of fixed point temperature references. Fixed point references are a series of very high purity materials that undergo phase transformations at temperatures defined in ITS-90 [85]. The thermocouple and reader can then be calibrated to pass through these points. However, in this instrument the thermocouple is formed by spot welding thermocouple wire to the sample surface. The thermocouple is used for one experiment, the ends welded to the sample are cut-off, and a new thermocouple will be made from the remaining wire for the next experiment. As each experiment is performed with a new single use thermocouple, it is not possible to include the thermocouple itself in the calibration.

If the actual thermocouple cannot be calibrated, then there is no choice but to accept the manufactured tolerance. The instrument is currently being used with class 1 type R thermocouple wire, which has a manufactured tolerance of ±1°C between 0 and 1100°C. What this means is that the thermal voltage generated by the thermocouple due to the temperature at the hot and cold junctions will be a voltage that when converted to temperature will be within ±1°C of the actual hot junction temperature plus any errors in measuring the thermocouple voltage and the cold junction temperature.

As detailed in section 3.5.2 the thermocouple is connected to an instrumentation amplifier, which then goes through an analogue differential signal isolator, then an anti-aliasing filter, before being digitized by the ADC. The measured voltage will be distorted by any gain errors in the amplifier, gain errors and offset caused by passive components tolerances in the isolator and filter, by any conversion errors in the ADC, and by any gain errors in the digital filters.

To reduce the voltage measurement errors a Time Electronics 404N millivolt source was connected in turn to each thermocouple input socket using copper wire with a copper-copper thermocouple plug. The indicated output voltage from the 404N was varied from 1 µV to 26 mV. The actual output voltage was measured using a calibrated Agilent 34420A nanovoltmeter, which has the one year accuracies listed in Table 4.8, and this was recorded along with the voltage measured by the quenching simulator instrumentation (see Appendix 34, Appendix 35, and Appendix 36).

Range	Accuracy
1.0000000 mV	± (20 nV + 0.0050 % of reading)
10.000000 mV	± (30 nV + 0.0050 % of reading)
100.00000 mV	± (400 nV + 0.0040 % of reading)

Table 4.8 – One year voltage measurement accuracies of the Agilent 34420A nanovoltmeter.

A second order correction polynomial of the form in equation 4.25 was calculated for each thermocouple input to relate the true thermocouple voltage to the voltage output from the data acquisition system. The calculated polynomial coefficients appear in Table 4.9.

$$V_{TC} = a_2 \cdot V_{DAQ}^2 + a_1 \cdot V_{DAQ} + a_0 \qquad 4.25$$

	a_2	a_1	a_0
TC1	-0.008139751	1.018293080	-0.00038961
TC2	0.012717111	1.012895818	-8.8526×10^{-5}
TC3	-0.016052913	1.019173572	-0.000135545

Table 4.9 – The coefficients for the polynomial correction function for the thermocouple input channels.

The true voltages (as measured by the nanovoltmeter) are plotted against the voltages measured by the quenching simulator, along with the calibration correction function for thermocouple channel 1 in Figure 4.3, for channel two in Figure 4.4, and for channel three in Figure 4.5.

The polynomial correction functions are applied by the QSCP software after the final stage of filtering and decimation, immediately before the addition of the cold junction compensation voltage. The correction functions are not used when the option to record voltages has been selected.

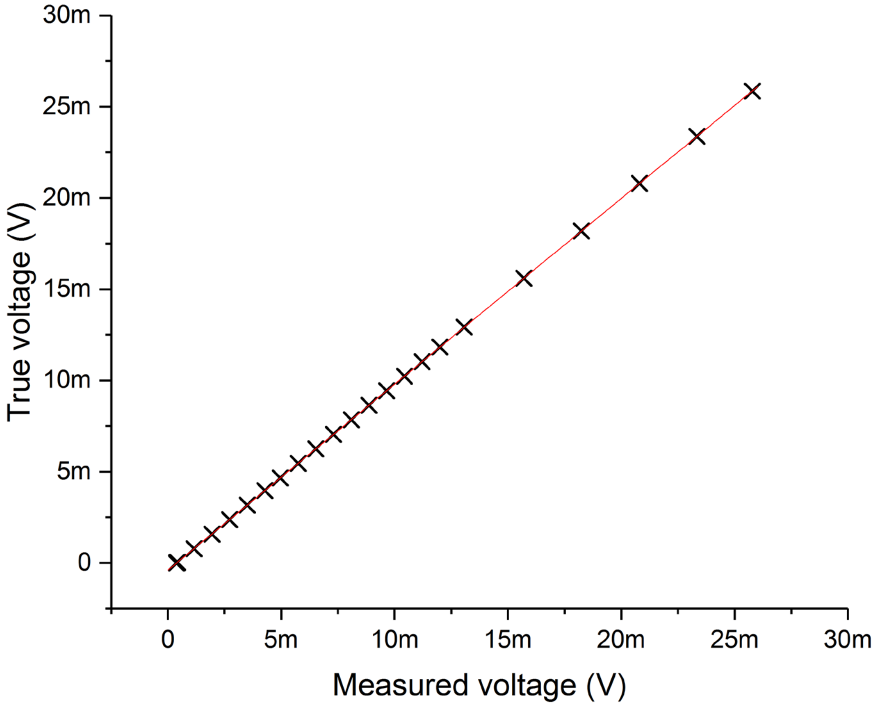

Figure 4.3 - The calibration data and correction function for thermocouple channel one (TC1).

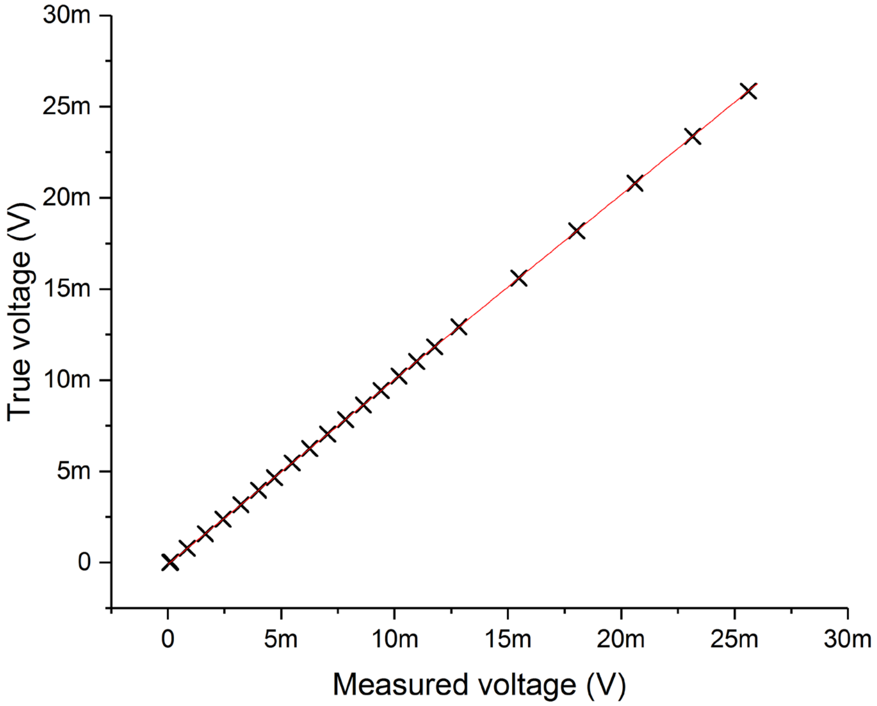

Figure 4.4 - The calibration data and correction function for thermocouple channel two (TC2).

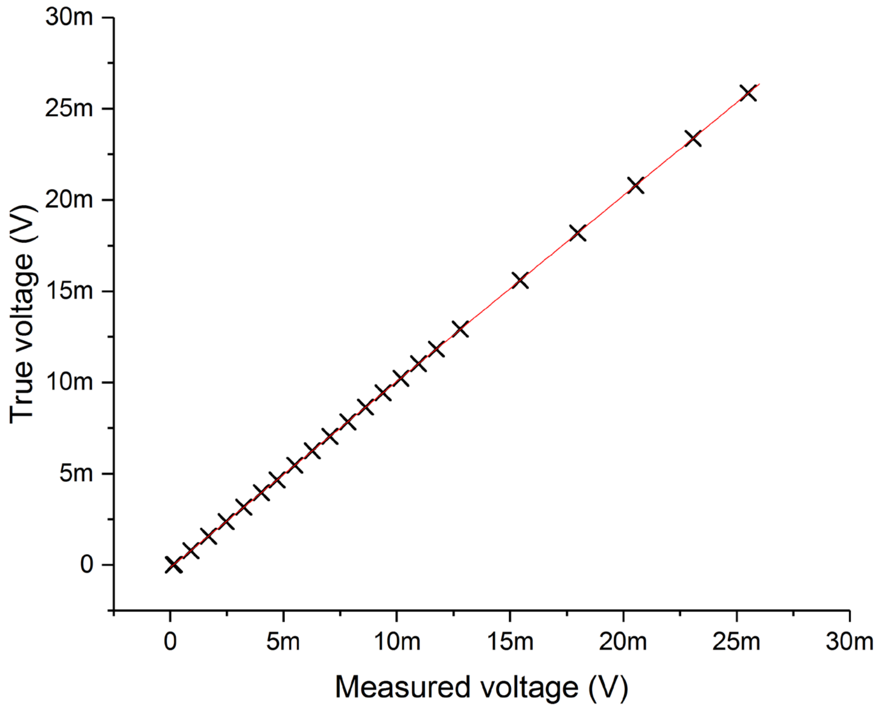

Figure 4.5 - The calibration data and correction function for thermocouple channel three (TC3).

4.3 Cold junction RTD calibration

To calibrate the thermocouple cold junction RTD, a calibrated semi-standard RTD connected to a calibrated Isotech milliK was placed into contact with the thermocouple cold junction isothermal block (Figure 4.6). The temperatures as measured by the calibrated RTD and as measured by the cold junction RTD were recorded 21 times at different ambient temperature over several days. The recorded data is included in Appendix 37.

The temperature as measured by the cold junction RTD and the calibrated RTD do not appear to have a relationship (Figure 4.7) as clear as found for the thermocouple inputs (4.2). Nevertheless, a first order polynomial calibration correction function was calculated (a_1 = 1.003038069 and a_0 = -1.664987397) with a correlation of determination (R^2) of 0.92, indicating a good fit. The polynomial correction function is applied by the QSCP application after decimation, and before the temperature is used to calculate the cold junction compensation voltages.

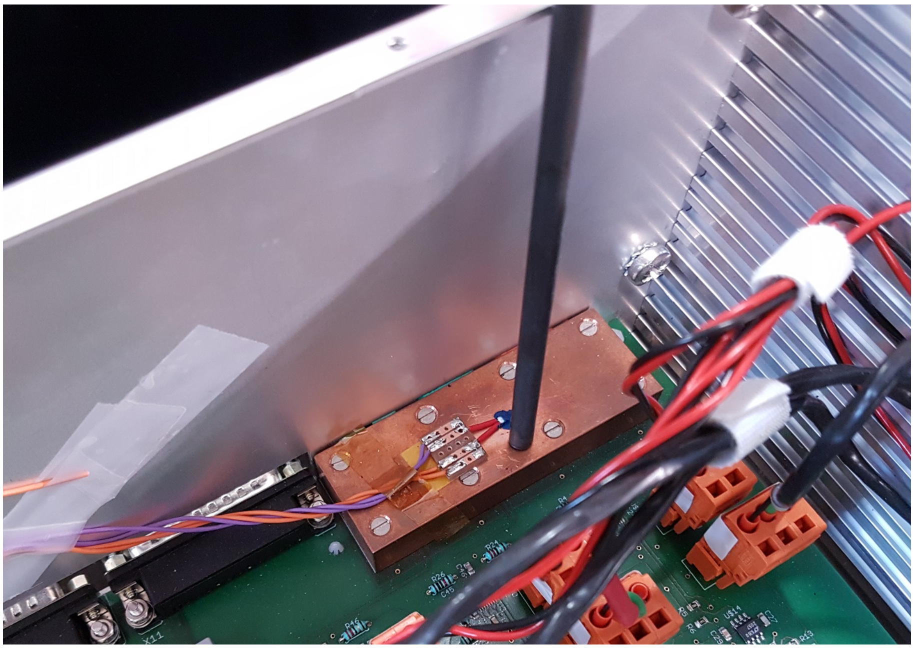

Figure 4.6 - A calibrated RTD (grey vertical rod) is placed into contact with the thermocouple socket isothermal block for calibrating the cold junction RTD (small white cuboid set in blue adhesive).

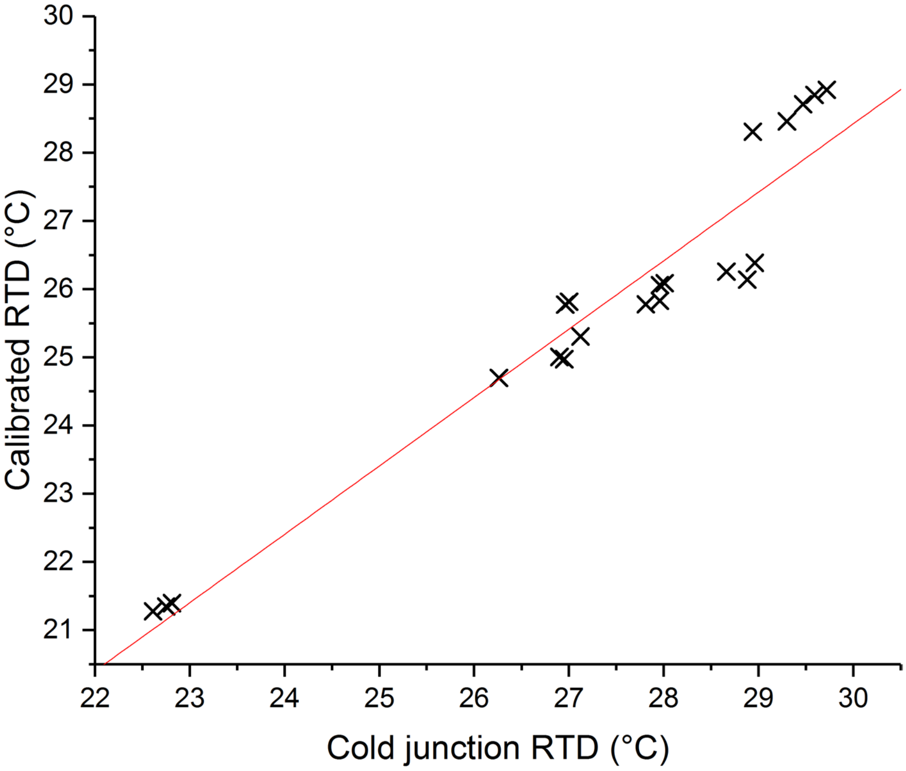

Figure 4.7 - The calibration data and correction function for the cold junction RTD.

4.4 *Resistance measurement calibration*

The resistance measurement is composed of the current source and voltage measurement parts (see 3.5.1). The current delivered by the current source is measured by passing that current through a 1 Ω resistor whose voltage drop is measured by an instrumentation amplifier. There is no facility in the current source implementation to calibrate the output, but the current measurement can be calibrated to ensure that the output is accurately measured.

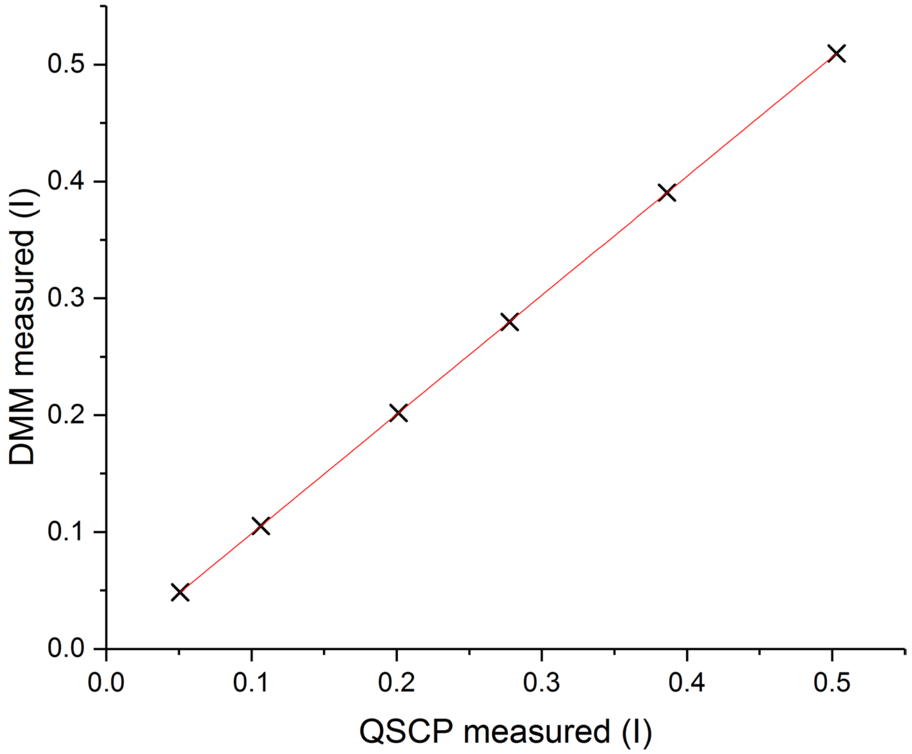

Figure 4.8 - The calibration data and correction function for the resistance measurement current source current measurement.

The current measurement was calibrated by connecting the current source outputs to a series connection of a calibrated Keysight 34465A DMM and a resistor. The current as measured by the DMM and by the quenching simulator instrumentation were recorded. The resistor was then changed to a resistor of a different value and another pair of readings were recorded. This process was repeated until a total of six data pairs were recorded (see Appendix 38). The second order polynomial coefficients a2 = -0.003148944, a1 = 1.021178546, and a0 = -0.003421554 were calculated to correct the measured values. The correction function and data points are plotted in Figure 4.8.

To calibrate the voltage measurement part of the resistance measurement circuit the same voltage source and nanovoltmeter as used for the thermocouple input channel calibration (see

4.2) were connected to the voltage measurement terminals. As the voltage measurement instrumentation amplifiers have a gain that can be set by the user (see 3.5.1), and the instrumentation amplifier gain error can be a source of the measurement error, the calibration was performed separately for each of the six user selectable gains. For each gain setting, eight voltages were measured (Appendix 39), and these were used to calculate the coefficients in Table 4.10 for second order polynomial correction functions.

A_v	a_2	a_1	a_0
64	0.127519857	1.002695182	-0.000310143
256	-0.194309749	1.013911908	-7.08897×10^{-5}
1024	3.550747161	0.998311551	-1.27161×10^{-5}
4096	-0.985049571	1.011466956	2.17292×10^{-7}
16384	-1.703518799	1.011379136	5.09219×10^{-6}
22528	-12.83635671	1.016253772	4.88218×10^{-6}

Table 4.10 – The coefficients for the polynomial correction functions for the resistance measurement voltage.

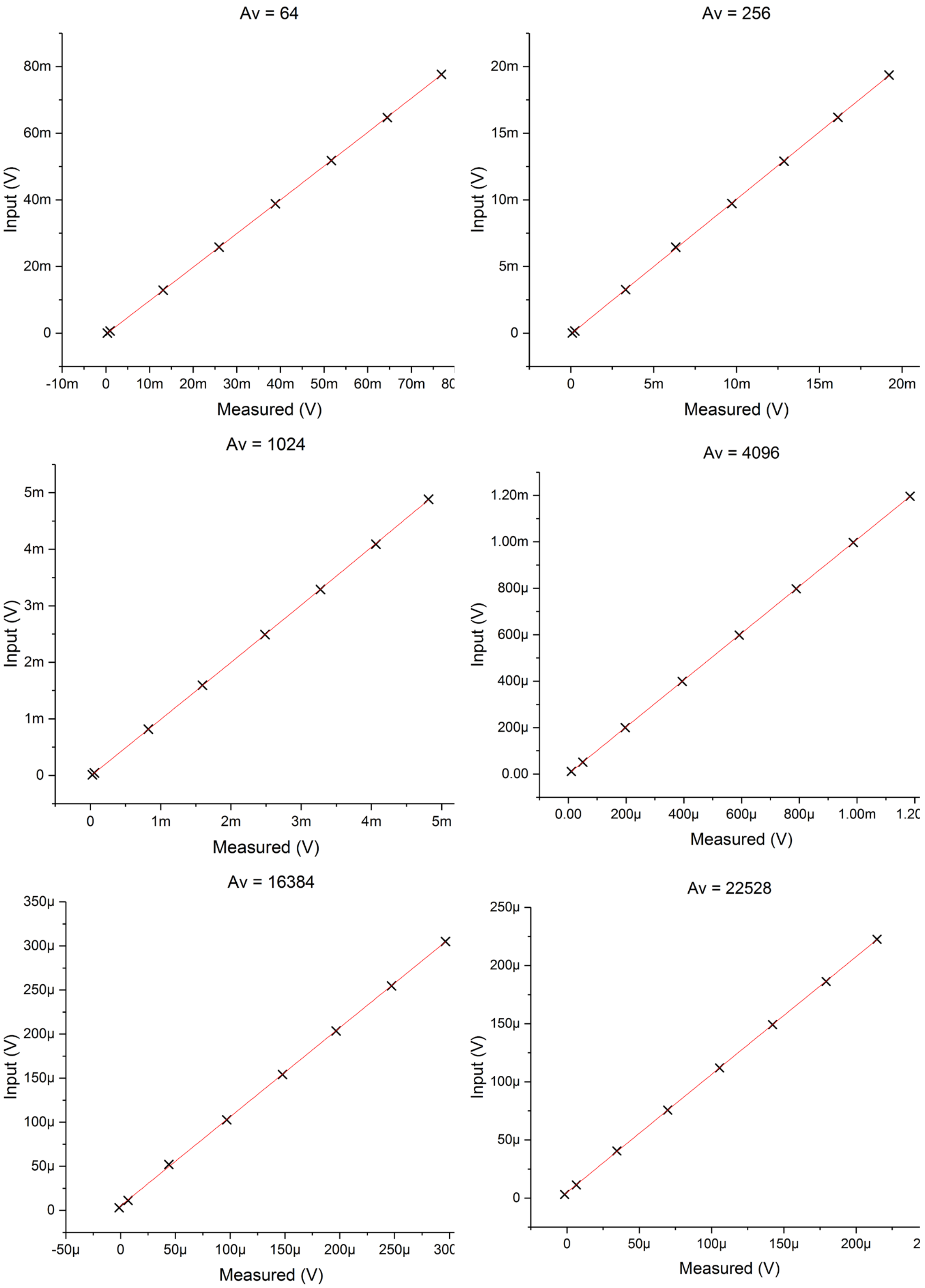

Figure 4.9 - The calibration data and correction functions for the resistance measurement voltage measurement for the six different instrumentation amplifier gains.

4.5 Data acquisition card calibration

The National Instruments PCI-6143 data acquisition card (see 3.5.8) was factory calibrated as part of the manufacturing process. The PCI-6143 has a self-calibration facility to compensate for changes in operating conditions. The user is able to activate the self-calibration procedure from the calibrate dialog in the QSCP software (see 3.4.8.1).

5 Results

5.1 Temperature measurement

To validate the calibrated temperature measurement system a semi-standard type R thermocouple was inserted into an isothermal block that had been placed in an Isotech Pegasus thermocouple calibration furnace. The thermocouple was allowed to reach thermal equilibrium with the furnace and isothermal block. The thermocouple was connected to a calibrated Isotech milliK reader and the temperature was recorded. The thermocouple was immediately disconnected from the milliK and connected to the first thermocouple input (TC1) on the instrumentation module, and the temperature was recorded for 10 seconds using the Quenching Simulator Control Panel (QSCP) application. The thermocouple was then immediately returned to the milliK and the temperature recorded. This procedure was then repeated for the second (TC2) and third (TC3) thermocouple inputs. The Pegasus furnace was then set to a temperature of approximately 100°C, allowed to stabilize, and the measurement procedure repeated. The temperature was then increased a further five times, and the measurements repeated, to give data for each thermocouple input channel at seven temperatures.

Table 5.11 – The temperature validation measurements for thermocouple channel one (TC1).

milliK Before (°C)	milliK After (°C)	milliK Mean (°C)	QSCP (°C)	Difference (°C)
20.39	20.16	20.28	18.39	-1.88
100.59	100.38	100.49	98.89	-1.59
194.50	194.18	194.34	193.29	-1.05
303.74	303.73	303.74	302.68	-1.05
378.04	378.01	378.03	377.01	-1.02
582.45	582.12	582.29	582.11	-0.18
782.89	782.69	782.79	783.12	0.33

Table 5.12 – The temperature validation measurements for thermocouple channel two (TC2).

milliK Before (°C)	milliK After (°C)	milliK Mean (°C)	QSCP (°C)	Difference (°C)
20.20	20.15	20.18	18.55	-1.63
100.35	100.25	100.30	99.46	-0.84
194.18	193.92	194.05	192.48	-1.57
303.86	303.85	303.86	303.12	-0.74
378.17	378.13	378.15	377.59	-0.56
582.06	581.51	581.79	581.81	0.03
782.71	782.37	782.54	782.83	0.29

Table 5.13 – The temperature validation measurements for thermocouple channel three (TC3).

milliK Before (°C)	milliK After (°C)	milliK Mean (°C)	QSCP (°C)	Difference (°C)
20.18	20.08	20.13	18.27	-1.86
100.29	100.15	100.22	99.75	-0.47
193.95	193.71	193.83	193.81	-0.02
303.99	303.97	303.98	303.65	-0.33
378.25	378.17	378.21	378.10	-0.11
581.40	581.10	581.25	581.62	0.37
782.37	782.35	782.36	782.87	0.51

The data for the three thermocouple input channels are tabulated in Table 5.11, Table 5.12, and Table 5.13. Inspection of the data shows that all three channels exhibit the greatest difference from the milliK at room temperature, with a mean difference of -1.79°C. The milliK has a one year accuracy of ±4 µV, which for a type R thermocouple is approximately ±0.8°C. The errors of the semi-standard thermocouple are listed in Table 5.14. In the validation measurements the thermocouple error can be ignored for the milliK readings as calibration data was entered for that thermocouple, but the measurement error of ±0.8°C is still present. If we consider the largest measured difference, which was the room temperature measurement for TC1, the actual temperature could be 20.18 °C ± 0.8°C, which gives a range from 19.38°C to 20.98°C. There is no calibration data for the semi-standard thermocouple at room temperature, but the mean voltage error of the three lowest temperature measurements is -7.33 µV, which is an error of approximately -1.4°C. If the QSCP reading is corrected for the room temperature error, as the milliK was, then the temperature range becomes 18.39°C to 19.79°C. As these two temperature ranges overlap, it can be said that the temperature measured by the milliK and the instrumentation module agree within the uncertainty of the measurements. As the error is less for all the other thermocouple input channel measurements, the same will be true for those conditions.

Table 5.14 – The thermocouple voltage errors taken form the calibration certificate for the semi-standard thermocouple. The temperature error is approximate.

T (°C)	V_{error} (µV)	T_{error} (°C)
Initial 350.48	-9	-1.7
599.96	-5	-1
850.05	5	1
1099.88	12	2.2
Final 350.87	-8	-1.5

5.2 Thermal performance

To investigate the thermal performance of the quenching simulator a 2 mm thick sample of eutectoid steel was heated to approximately 950°C in an argon atmosphere with a constant heating turn-on angle of 100°. Figure 5.10 shows the plot of temperature versus time. The sample was heated from 25.17°C to 949.61°C in 39.94 s, which is an average heating rate of 23.1°C/s. A turn-on angle of 100° is a conduction angle of 80°, which gives a voltage that has an RMS value that is 62.5% that of full conduction (Figure 3.6). If this is squared to give an indication of the power ratio, this gives 39.1%. Hence, the 23.1°C/s heating rate was achieved with just under 4/10ths full power. The achieved heating rate is just over 46% of the 50°C/s in the instrument requirements (see 3.1.1), so with full power the instrument is likely to be close to the required heating rate. Unfortunately, there was insufficient time to assess the heating rates using higher power settings.

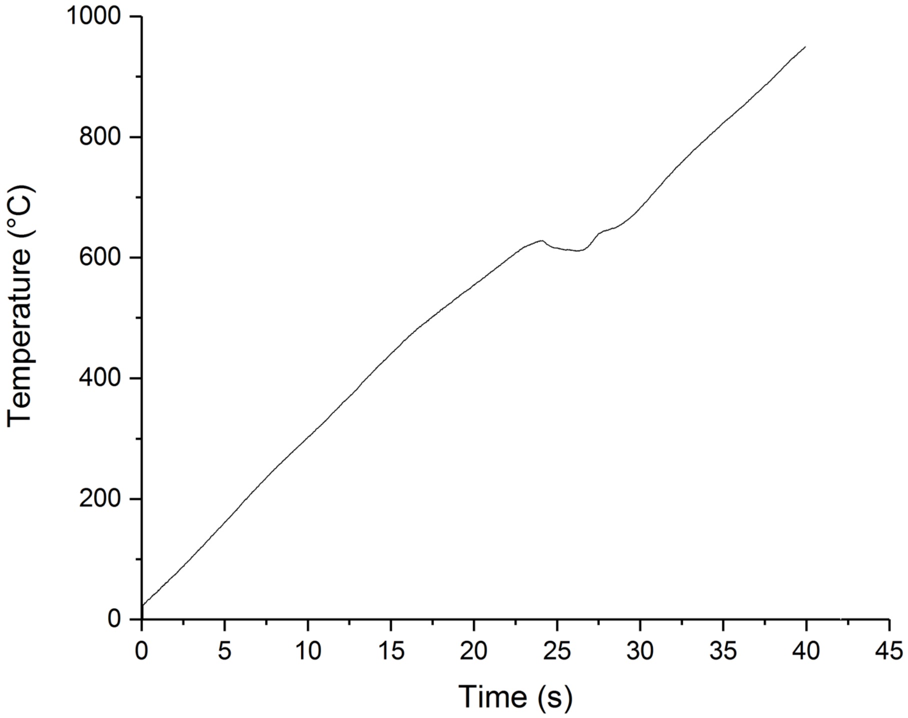

Figure 5.10 – The heating of a 2 mm thick sample of eutectoid steel with a constant turn-on angle of 100°.

To assess the cooling performance the same 2 mm thick eutectoid steel was quenched to room temperature with the maximum quenching gas proportional control valve opening (Figure 5.11). The sample was cooled from 947.89°C to 49.70°C in 85.12 s, which is an average cooling rate of 10.6°C/s. The time taken to go from 702.91°C to 400.04°C was 7.52 s, which is an average cooling rate of 40.3°C/s. The 40.3°C/s cooling rate is greater than the 27°C/s cooling rate that is required for 22MnB5 alloys over the same temperature range to achieve a fully martensitic microstructure [60].

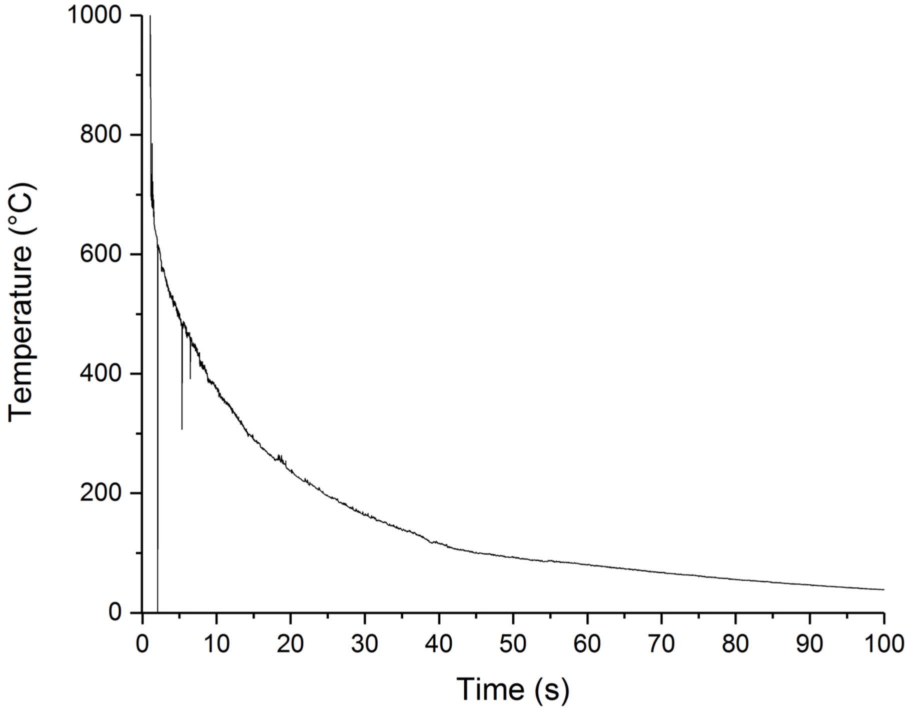

Figure 5.11 – The argon quenching of a 2 mm thick eutectoid steel sample.

5.3 Validation alloys

To assess the capability of this instrument to detect phase transformations using electrical resistance measurements, three metals with well-established phase transformation temperatures were chosen to validate the system. The metals chosen were high purity cobalt, high purity titanium, and a eutectoid steel. These metals were chosen due to a being readily available and to give a range of transformation temperatures from 442 to 882°C.

5.3.1 Cobalt

A 1 mm thick sample of 99.9% pure cobalt was placed in the quenching simulator and heated to approximately 550°C with a constant turn-on angle of 135° in an argon atmosphere. Once the target temperature had been achieved the heating was turned off and the sample was allowed to naturally cool. Figure 5.12 shows the thermal cycle, where there can be seen a subtle point of inflection during cooling around 406°C, which may represent a change in enthalpy due to a phase transformation.

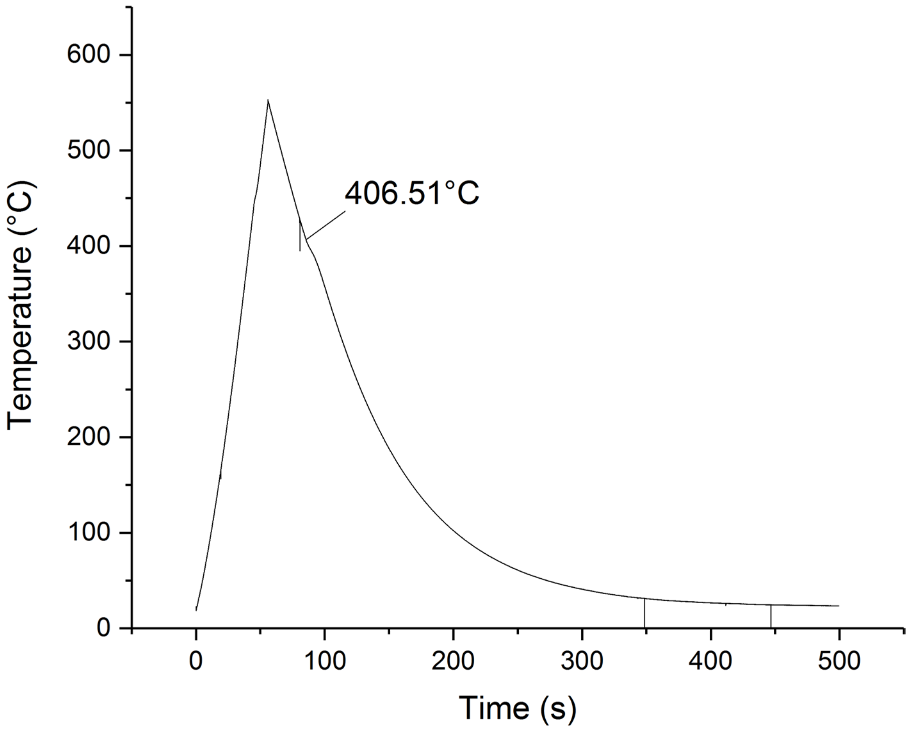

Figure 5.12 – The thermal history for cobalt sample A. A constant heating turn-on angle of 135° followed by natural cooling.

Figure 5.13 plots the change in resistance of the first sample during heating (in red) and cooling (in blue). During both heating and cooling there is an abrupt change in the measured resistance. During heating the abrupt change in resistance appears to commence at approximately 441°C, and during cooling the change starts around 417°C. Inspection of Figure 5.13 shows that there is a sharp discontinuity in the measured resistance that occurs shortly after heating is discontinued. The discontinuity is due to the electrical interference of the heating current with the resistance measurements (see 6.1).

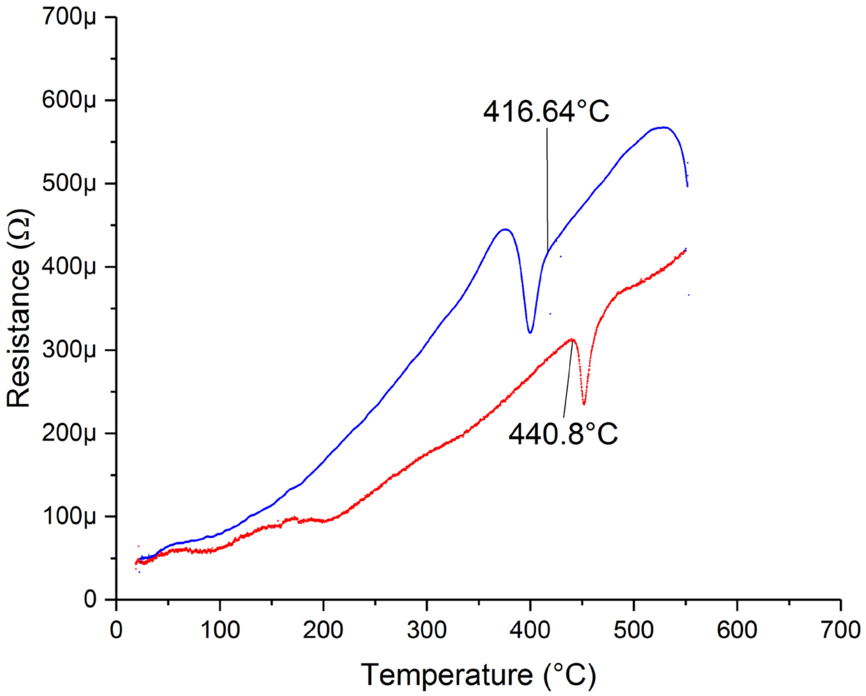

Figure 5.13 – The resistance vs. temperature curve for the cobalt sample A. The red curve is during heating. The blue curve is during cooling.

A second cobalt sample from the same sheet of material was then used to repeat the test three times to see both the repeatability between samples and the repeatability for the same sample. The resistance-temperature curves for the three runs are plotted in Figure 5.14, Figure 5.15, and Figure 5.16.

As with the first cobalt experiment, there is a discontinuity in the resistance measurement in all three experiments on sample B. Additionally, there is also a discontinuity in the temperature measurement, showing electrical interference of the heating current with the thermocouple. There is no clear evidence why there was a change in the susceptibility to electrical interference with the temperature measurement, but a possible explanation is due to the thermocouple spot welding (see 6.4).

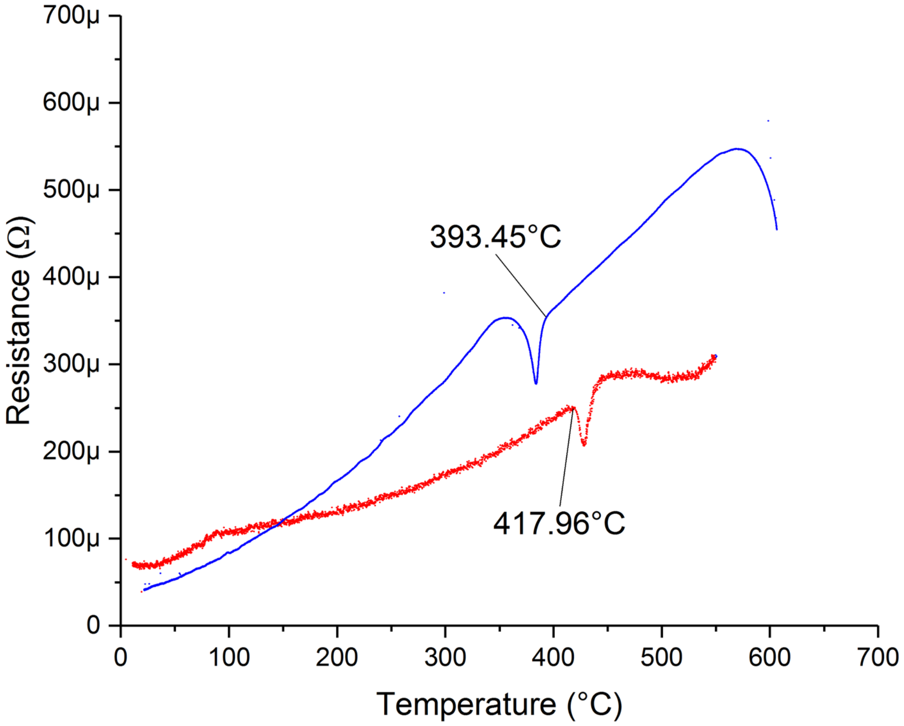

Figure 5.14 – The resistance vs. temperature curve for the cobalt sample B run 1. The red curve is during heating. The blue curve is during cooling.

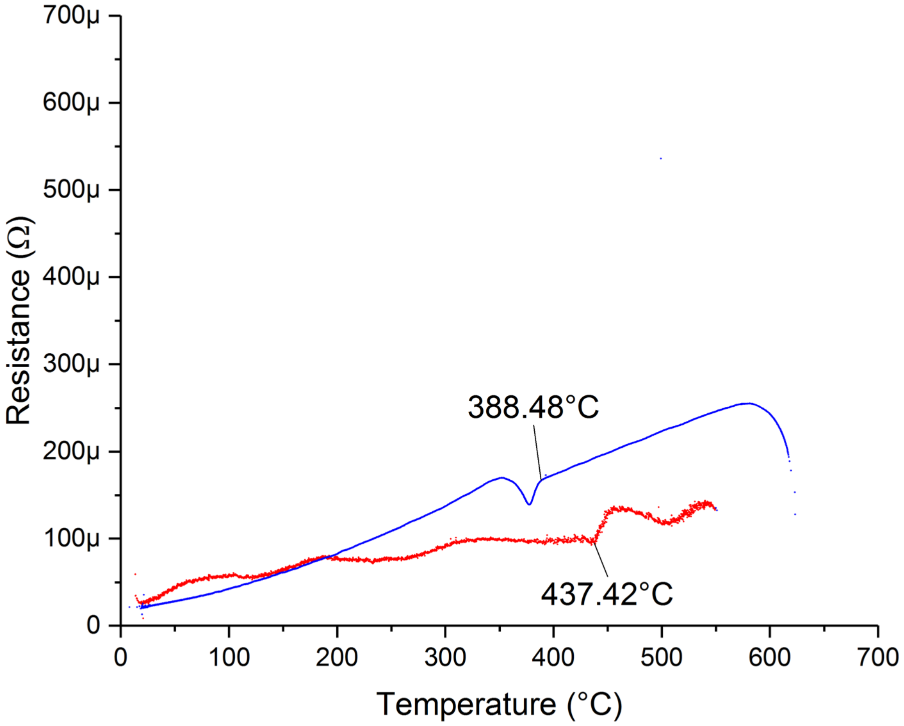

Figure 5.15 – The resistance vs. temperature curve for the cobalt sample B run 2. The red curve is during heating. The blue curve is during cooling.

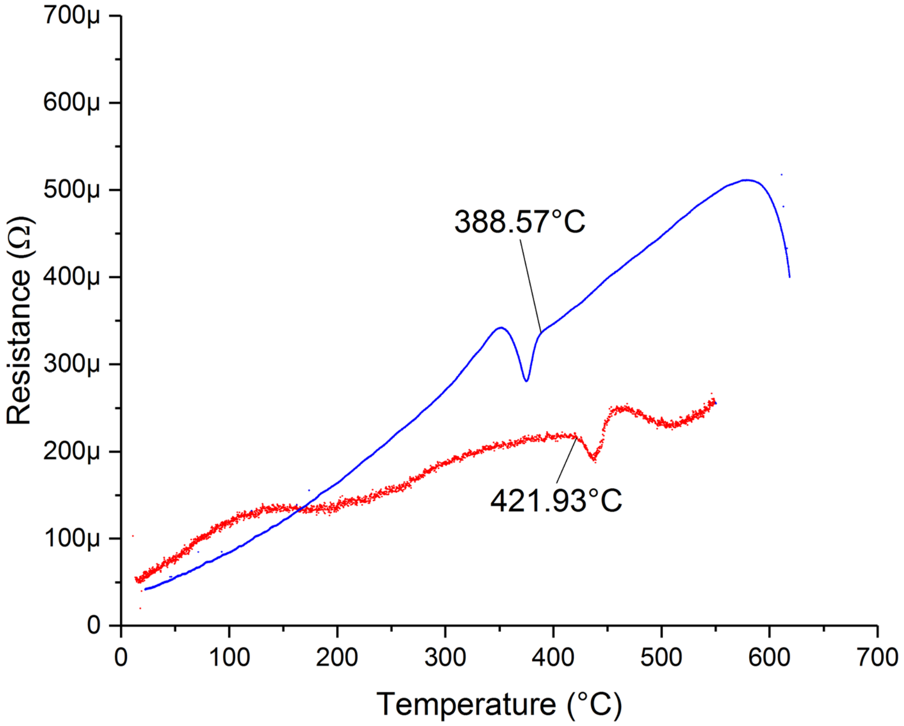

Figure 5.16 – The resistance vs. temperature curve for the cobalt sample B run 3. The red curve is during heating. The blue curve is during cooling.

The approximate temperatures at which the abrupt changes in resistance occur for the three runs of sample B, along with the figures for sample A, are listed in Table 5.15. Across the four experiments the mean value during heating is 430°C with a standard deviation of 9.7°C. For cooling the mean value is 397°C and the standard deviation is 11.8°C.

Experiment	Heating (°C)	Cooling (°C)
A	441	417
B1	418	393
B2	437	388
B3	422	389

Table 5.15 – The approximate temperatures at which the abrupt change in resistance starts for the four cobalt experiments.

Differential thermal analysis (DTA) was performed on my behalf on two samples cut from the same piece of cobalt as for the resistance measurements. The DTA was performed in a TA Instruments SDT Q600, using an alumina crucible and powder, a nitrogen atmosphere, and a heating rate of 10°C/min.

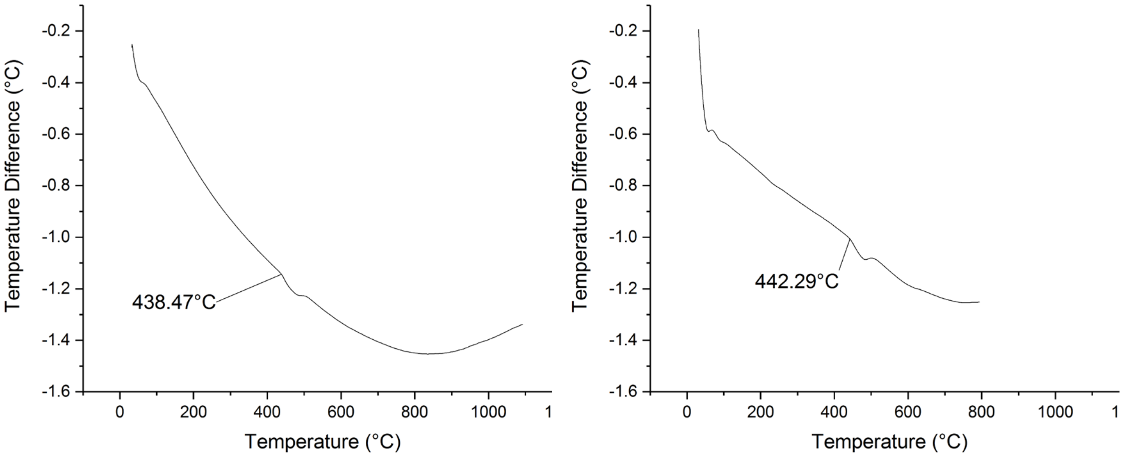

Figure 5.17 – The DTA curves for two samples of pure cobalt.

Figure 5.17 shows the DTA results for the two cobalt samples. Both samples show a minor change in the temperature difference between the sample and reference, in one sample this appears to start at around 438°C and in the other at 442°C. This is very close to the temperature of 442°C at which cobalt would be expected to transform from a hexagonal close packed (HCP) structure to face centred cubic (FCC) [71].

5.3.2 Titanium

A 1 mm thick sample of 99.6% pure titanium was heated in the quenching simulator to a temperature of 1000°C with a constant turn-on angle of 100° in an argon atmosphere. Once the target temperature was reached, the heating current was turned off and the sample was allowed to cool naturally. Figure 5.18 shows the temperature profile of the heat treatment. The temperature profile shows two clear points of inflection, one during heating (864°C) and one during cooling (856°C). These more obvious points of inflection in the curve indicate that there is a phase change with a higher change in enthalpy than was observed for cobalt (see Figure 5.12).

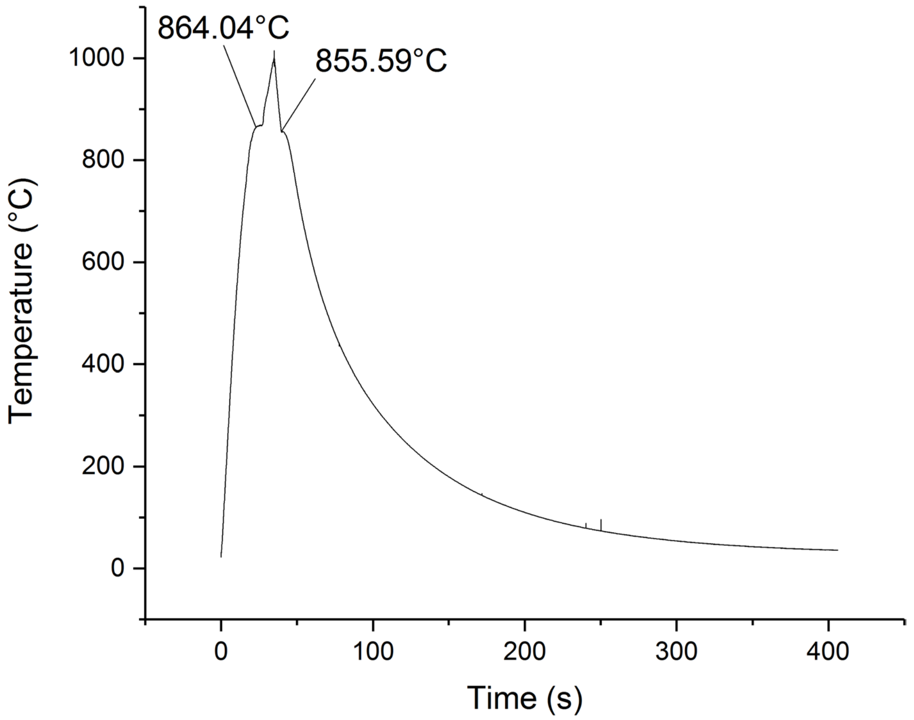

Figure 5.18 – The thermal history for the titanium sample. A constant heating turn-on angle of 100° followed by natural cooling.

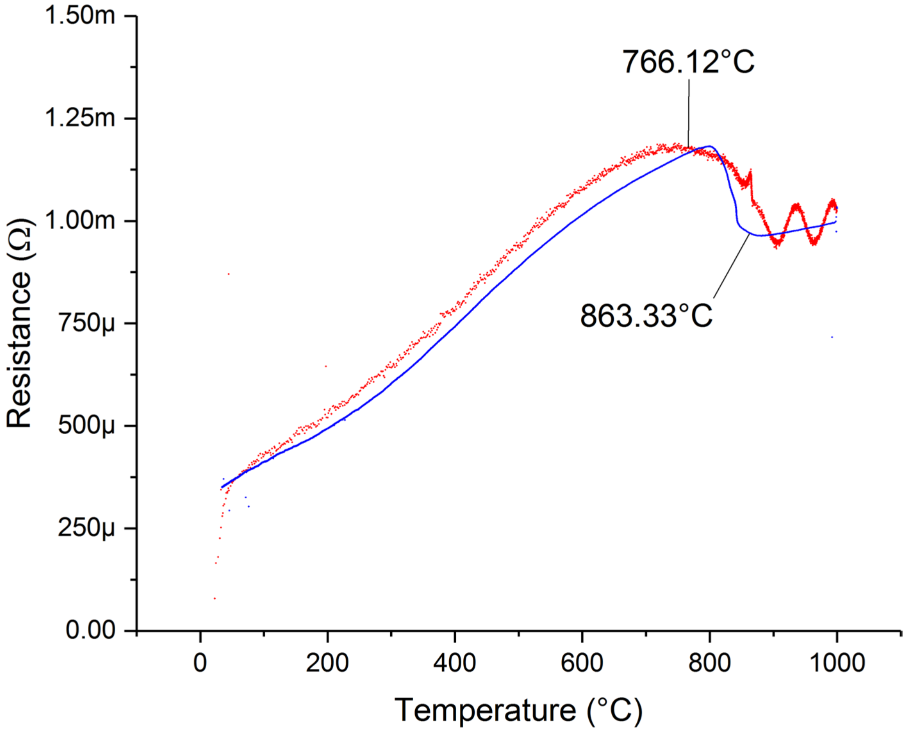

Figure 5.19 – The resistance vs. temperature curve for the titanium sample. The red curve is during heating. The blue curve is during cooling.

Figure 5.19 plots the resistance-temperature curve of the sample during heating and cooling. It appears that during heating the change in resistance that accompanies a phase transformation begins at around 766°C. The final part of the curve during heating appears to be sinusoidal, which also appears on the time resistance curve (Figure 5.20), but disappears during cooling. This would suggest that this sinusoid is interference from the heating current, which given the very low frequency, has most likely been aliased from a higher frequency (see 6.1).

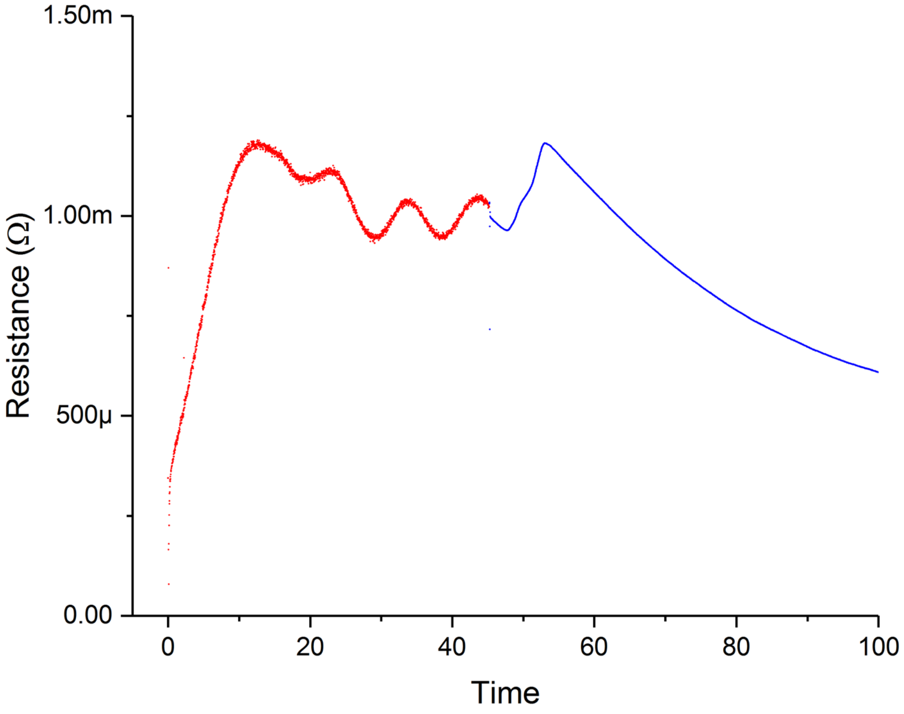

Figure 5.20 – The resistance vs. time curve for the titanium sample during heating (red) and the first part of cooling (blue).

The resistance-temperature curve (Figure 5.19) during cooling demonstrates a much clearer change in resistance, which appears to commence at around 863°C. Figure 5.21 shows the results for DTA on two pieces of the pure titanium, performed as for the cobalt (see 0). As with the temperature vs time curves, the DTA results for the titanium appear to show a phase transformation with a greater change in enthalpy than for cobalt. For the two titanium samples the transformation appears to start at 876°C and 878°C. The expected phase transformation temperature for titanium from HCP to body centred cubic (BCC) is 882°C [71].

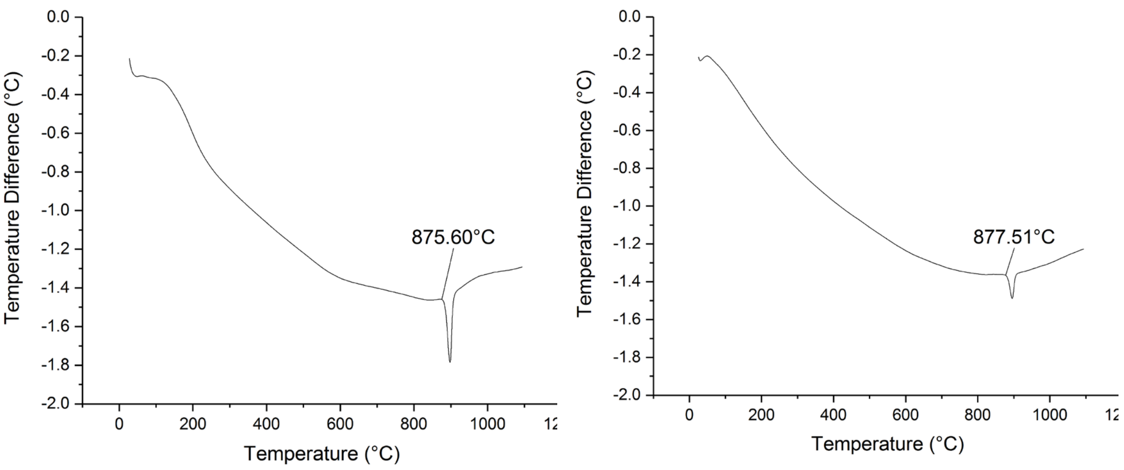

Figure 5.21 – The DTA curves for two samples of pure titanium.

5.3.3 Eutectoid steel

A 2 mm thick sample of eutectoid steel, with the composition as listed in Table 5.16, was heated in the quenching simulator with an argon atmosphere to a temperature of 950°C, using a constant turn-on angle of 100°. Once the target temperature was reached, the sample was allowed to naturally cool.

	Mn	C	Si	P	N	S
wt%	0.98	0.79	0.21	0.01	0.005	0.003

Table 5.16 – The alloying elements in the eutectoid steel.

Due to an operator error the data for cooling was not fully recorded, and the experiment was repeated. Figure 5.22 shows the heat treatment for the second heating and cooling of the eutectoid steel sample. During heating there appears to be a slight inflection in the temperature curve starting at around 578°C. During cooling there appears to be a pronounced evolution of heat that starts at around 496°C.

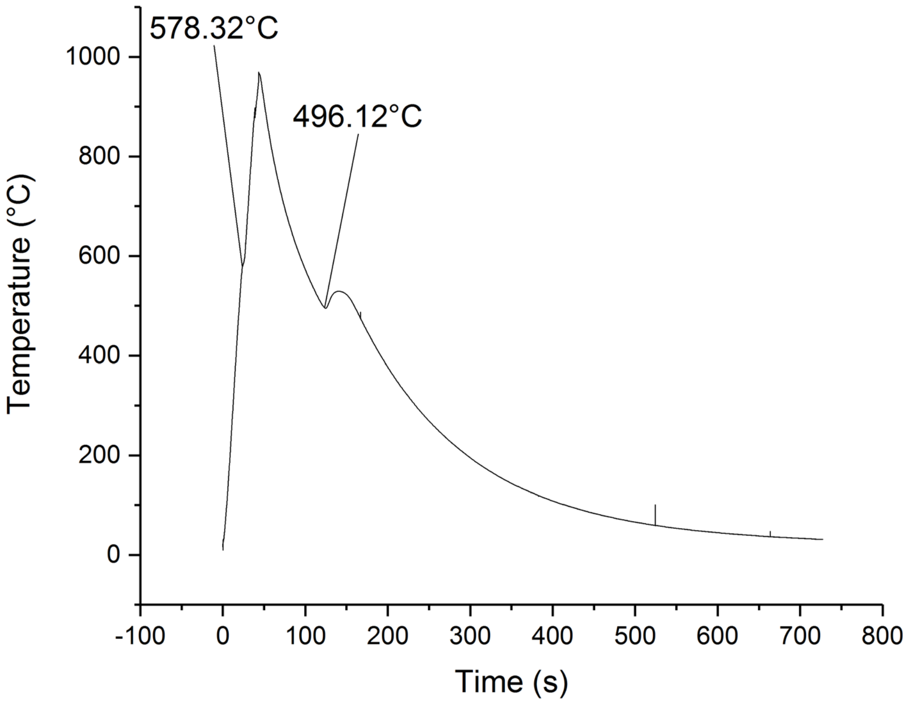

Figure 5.22 – The second heat treatment on the eutectoid steel sample. A constant heating turn-on angle of 100° followed by natural cooling.

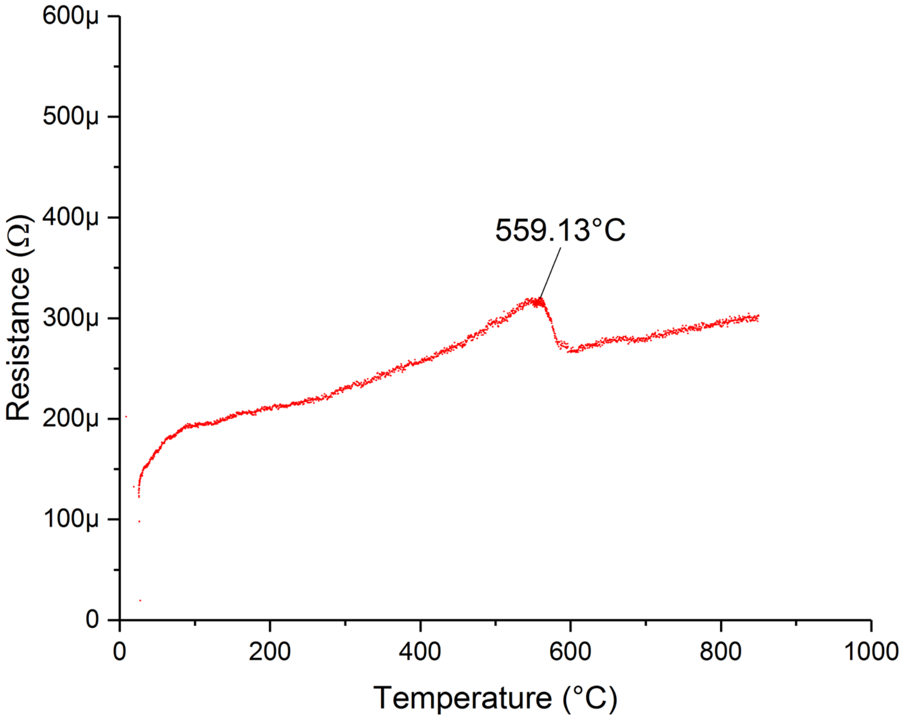

Figure 5.23 – The resistance vs. temperature curve for the eutectoid steel sample run 1. The data during cooling was not fully recorded and is omitted.

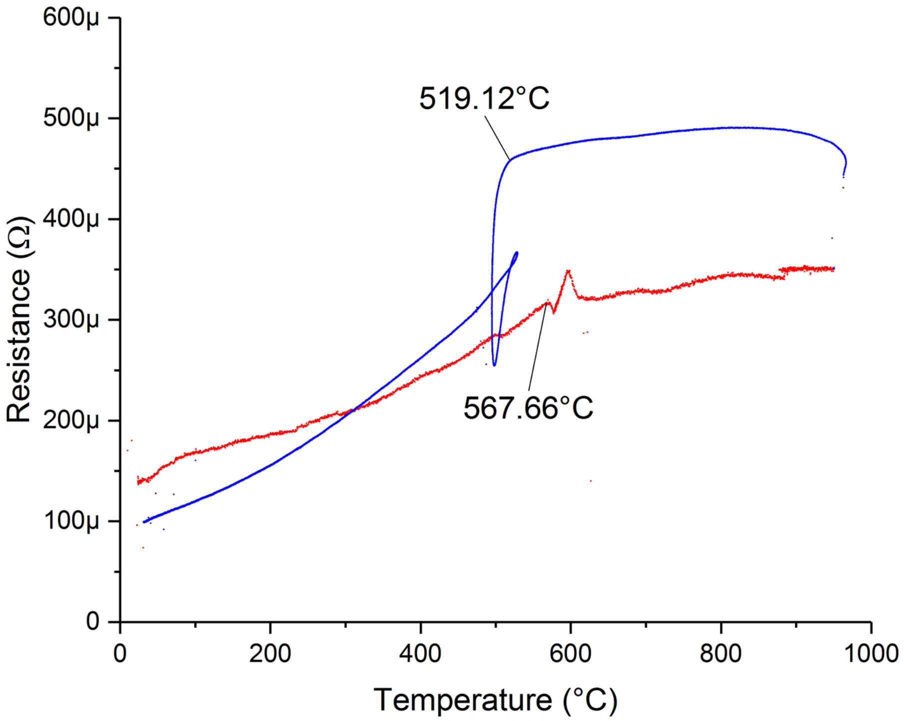

Figure 5.24 – The resistance vs. temperature curve for the eutectoid steel sample run 2. The red curve is during heating. The blue curve is during cooling.

Figure 5.23 plots the resistance against temperature for the first heat treatment, and Figure 5.24 plots the same quantities for the second heat treatment. During the first heat treatment there is a marked change in measured resistance that starts at approximately 559°C. During the second heat treatment the changes in resistance during heating are much less abrupt, although there appears to be a change that starts around 568°C. During cooling there is a large change in resistance that starts at approximately 519°C. The curve crosses over itself during heating as the heat evolved from the phase transformation momentarily raises the temperature (Figure 5.22). The start temperatures during heating and cooling are both significantly lower than the expected transformation to austenite at the eutectoid temperature of 727°C [71]. To verify these results the heating and cooling was performed on the same sample for a third time (Figure 5.25). During this third run the sudden change in resistivity during heating starts at around 558°C, and at around 526°C during cooling.

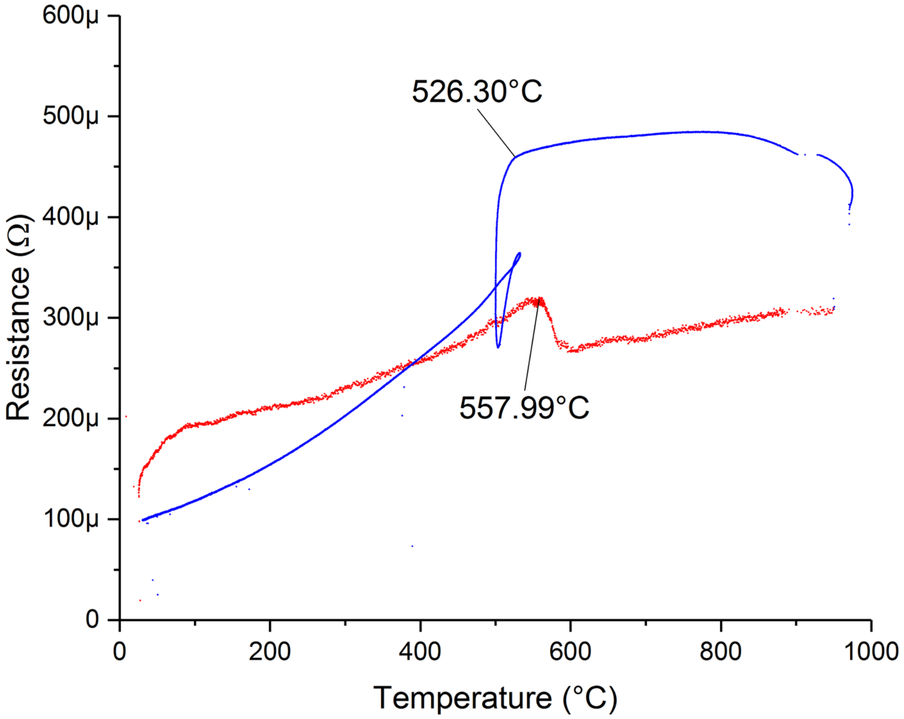

Figure 5.25 – The resistance vs. temperature curve for the eutectoid steel sample run 3. The red curve is during heating. The blue curve is during cooling.

DTA was also performed on two samples of the eutectoid steel (Figure 5.26), using the same conditions as for the cobalt and titanium samples. The two DTA experiments indicated transformation start temperatures of 725°C and 726°C, which are in very good agreement with the expected value of 727°C.

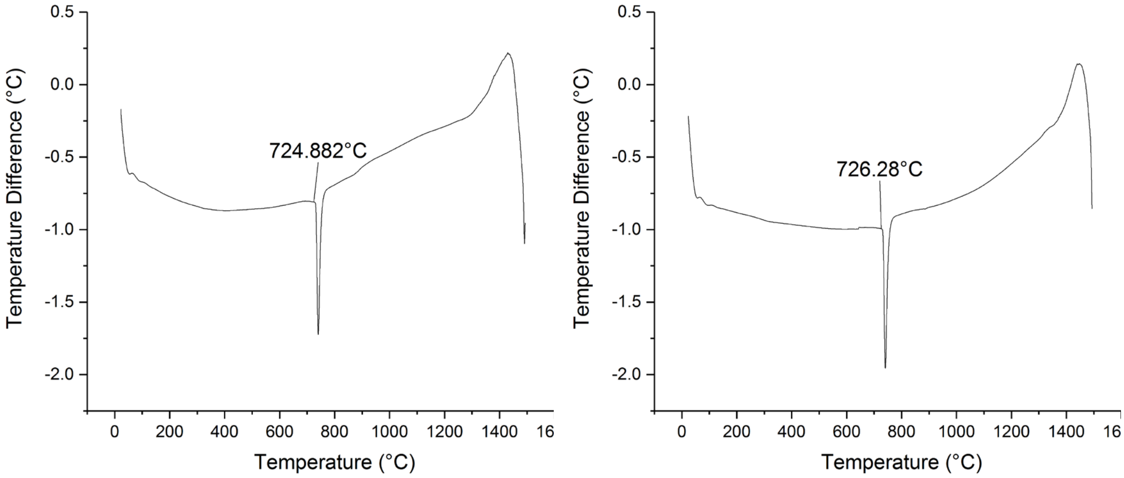

Figure 5.26 – The DTA curves for two samples of eutectoid steel.

6 Discussion

6.1 Common mode noise

The most significant challenge in this project has been how to accurately measure the small voltages generated by the thermocouples and resistance measurement current in the presence of a very large heating current.

The potential difference in the sample should be along the sample length, so in the absence of any additional currents the potential difference between any two points at the same distance along the sample length should be zero. Although the potential difference between two points should be zero, the potential difference between those points and a reference point (such as the amplifier power supply) will vary as the instantaneous voltage applied to the sample varies. The output of an ideal instrumentation amplifier whose inputs were connected to the two points would be zero, as the output would only be a function of the difference between the inputs. The voltage that appears at the inputs with respect to some reference point is called the common mode voltage, as it is common to both inputs. The ideal amplifier has an infinite common mode rejection ratio (CMRR) as the ratio of the output to the common mode input is infinite.

All real instrumentation amplifiers have a finite CMRR, which is to say that some fraction of any common mode input voltage will appear at the output as a differential signal. Increasing the differential gain will improve the CMRR, as this will improve the ratio of the two gains. The instrumentation amplifier used throughout the instrumentation module is the Texas Instruments PGA281, which has a minimum[15] DC CMRR of 110 dB for a gain of 1, and a minimum CMRR of 121 dB when the gain is increased to 128.

---

[15] The typical values are specified as 130 dB for a voltage gain of 1, and 142 dB for a gain of 128.

The thermocouple instrumentation amplifiers have a gain of 176 (see 3.5.2), the CMRR for a gain of 176 is not specified, but as the CMRR will improve with differential gain it is safe to assume a minimum CMRR of 121 dB. The resistance measurements take place in the middle of the sample, where the maximum voltage will be half the maximum instantaneous voltage. For the example in section 3.5.9, which had a constant turn-on angle of 135°, the peak common mode voltage will be $\sqrt{2} \times 2.4 \times \sin(135°) = 2.4\,V$. The CMMR is the ratio of the differential gain to the common mode gain, so if the common mode gain is 176 and this is divided by the CMRR then we get a common mode gain of 1.57×10^{-4} (-76.1 dB). So for the peak common mode voltage of 2.4 V the expected peak noise would be 360 µV (which for a type R thermocouple would be a temperature error of approximately 59°). However, looking at raw input data for the thermocouple channel in Figure 3.59, the peak noise appears to be more like 250 mV, which would indicate a CMRR closer to 65 dB.

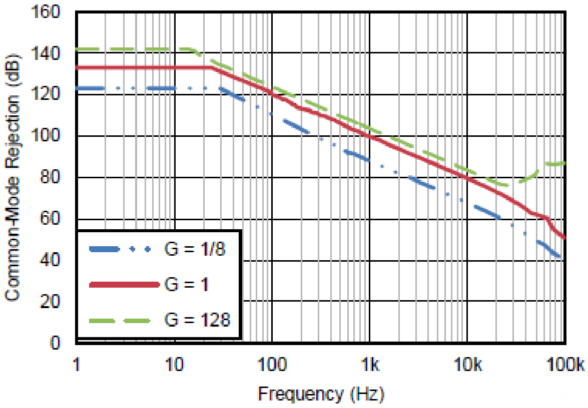

Figure 6.1 – The CMRR of the Texas Instruments PGA281 instrumentation amplifier vs frequency. Figure is reproduced from the product datasheet.

One possible explanation is that there are two factors that combine to degrade the apparent CMRR [90]. Firstly, the CMRR for all instrumentation amplifiers reduces with increasing frequency. Figure 6.1 shows that for the PGA281 the CMRR decreases by 20 dB/decade above frequencies around 15 Hz. Looking at the plot for a gain of 1/8, which starts at a CMRR that is close to the assumed minimum CMRR of 121 dB for gains of 176, it can be seen that the CMRR has fallen to just 60 dB by 20 kHz.

However, despite the CMRR being just 60 dB by 20 kHz, the second order anti-aliasing filter (see 3.5.4) has a differential signal attenuation of 76 dB. The attenuation of the anti-aliasing filter will continue to roll-off at 40 dB/decade, which should more than compensate for the CMRR roll-off of the instrumentation amplifier. However, this does not appear to be the case. This discrepancy is explained by the second contributing factor, which is that the instrumentation amplifier does not just convert the higher frequency signals to differential mode, but rectifies those components [90]. The drain current in a field effect transistor (like used for the PGA281 inputs) is proportional to the square of the gate-source voltage. If an input signal is the sum of two cosines, then the output will be the square of the sum of the two cosines.

$$(\cos A + \cos B)^2 = \cos^2 A + \cos^2 B + 2\cos A \cos B \qquad 6.26$$

$$\Rightarrow \frac{\cos(2A) + 1}{2} + \frac{\cos(2B) + 1}{2} + \cos(A + B) + \cos(A - B) \qquad 6.27$$

Equation 6.27 shows that the results of squaring the two input sinusoids are a component at twice of each of the input frequencies, a component at the sum of the input frequencies, another at the difference between the input frequencies, and a constant value. The two components of double the input frequency and the sum of the input frequencies are of no concern as they will be shifted into a region where the anti-aliasing filter has greater attenuation. However, the component that is due to the difference in frequencies will cause two high frequency components to create low frequency noise. For example, the 50 Hz harmonic noise components at 20,050 Hz and 20,000 Hz will produce noise at 50 Hz, which will not be attenuated by the anti-aliasing filter. The constant term is also a significant problem, as this will cause a DC offset in the output.

To avoid amplifier rectification it is necessary to include some element of high frequency common mode attenuation before the amplifier inputs. Common mode attenuation can be introduced by the inclusion of a common mode choke [90], which will filter only common mode voltages. An alternative approach is to include a passive differential filter [91], which will introduce both common mode and differential voltage attenuation.

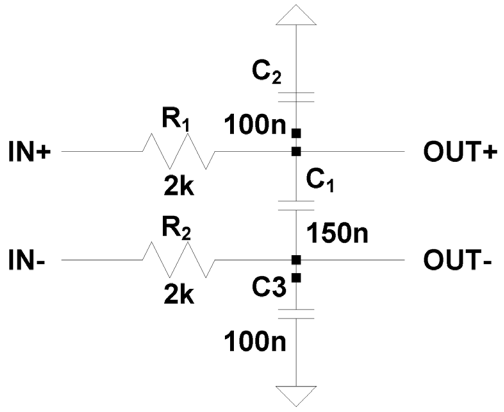

Figure 6.2 – A low pass differential filter to reduce instrumentation amplifier rectification [91].

Figure 6.2 shows a differential input filter of the type suggested by Kitchin et al. [91] to reduce amplifier rectification errors. Figure 6.3 shows the frequency response of this filter to common mode voltages.

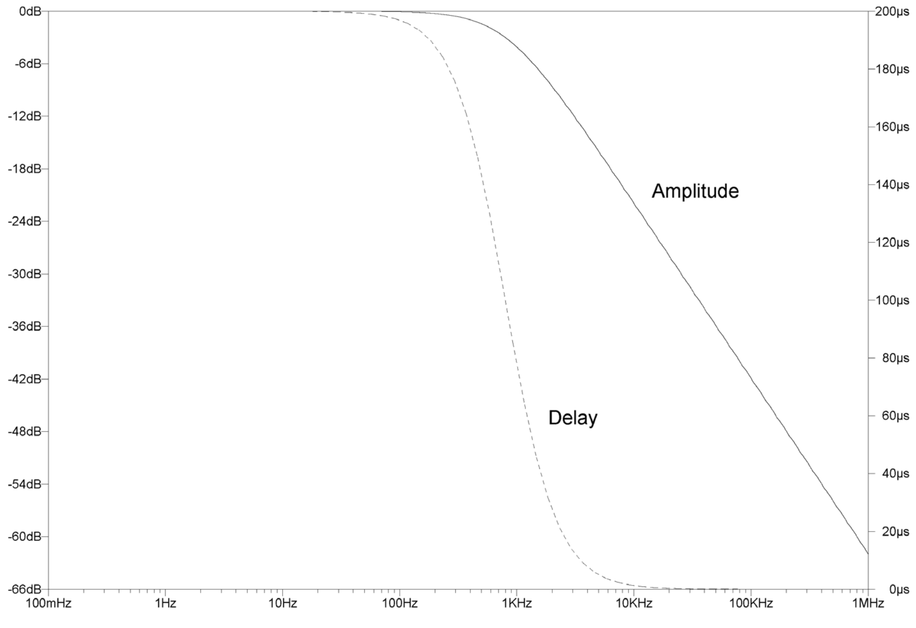

Figure 6.3 – The frequency response of the filter in Figure 6.2 to common mode signals.

It can be seen from Figure 6.3 that this filter introduces an additional common mode attenuation of 20 dB/decade, with a corner frequency of 795 Hz. So at a frequency of 20 kHZ, this should improve the CMRR of the PGA 281 to something closer to 90 dB. To investigate whether such a filter could significantly reduce the noise, a sample of 2 mm thick Armco pure iron was heated in an argon atmosphere in the quenching simulator to a temperature of 400°C. A constant turn-on angle of 140° was used. The selected amplifier gain for the resistance voltage measurement was 1024, which meant the first stage gain was 128 (see 3.5.1). The experiment was then repeated with the differential input filter of Figure 6.2 included for the resistance voltage measurement circuit. Figure 6.4 shows the first ten seconds of the raw input data, both with, and without the input filter.

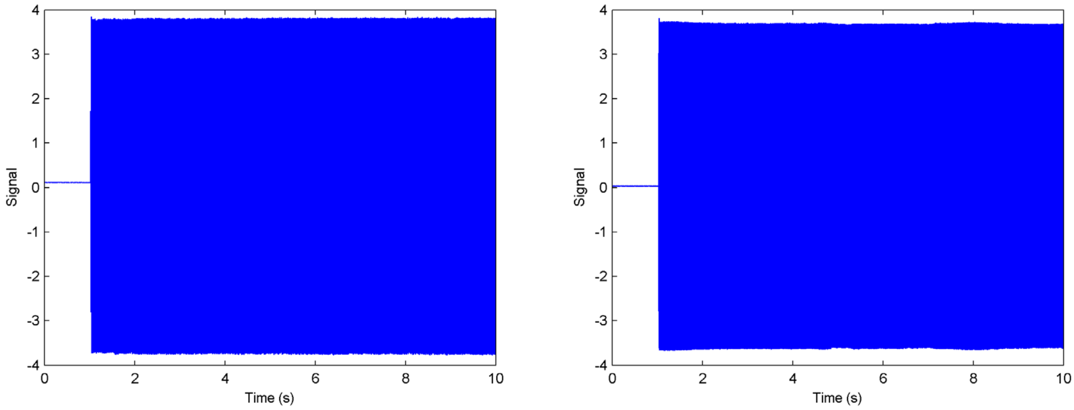

Figure 6.4 – The raw input data for the resistance voltage measurement for the first ten seconds of heating a sample of Armco pure iron with a constant turn-on angle of 140°. Left shows the raw data without differential input filter, and right shows the raw input data when used with a differential input filter.

Looking at Figure 6.4 there appears to have been relatively little reduction in the amount of noise. However, inspection of Figure 6.5, which shows the resistance measurement voltage data after digital signal processing, demonstrates that there was a significant improvement both in terms of the DC offset and the AC noise that arose from the heating current.

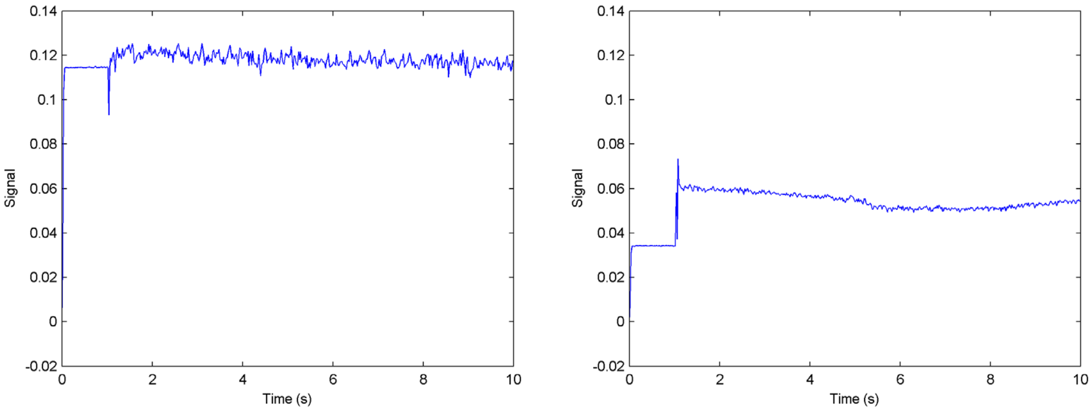

Figure 6.5 – The first ten seconds of output data after digital signal processing for the resistance measurement voltage without the input filter (left) and with the input filter (right).

The common mode frequency characteristics of the PGA 281 were not comprehensively understood until the scale of the noise problems became apparent when taking the resistance measurements during heating. It was not possible to take the resistance measurements during heating until the instrumentation module was completed, which was the final module. The thermocouple noise during heating became apparent much earlier in the project, and due to the thermocouple voltages being of much greater magnitude than the resistance measurement voltages, the noise appeared to have been sufficiently removed by the processes detailed in sections 3.5.4 and 3.5.9. Once the benefits of using a differential input filter were understood, a temporary filter was included for the resistance voltage measurement circuit. This filter was not in place for any of the calibration procedures, but was used for all of the experiments described in section 5.3.

The minimum CMRR of the PGA 281 will continue to roll-off at 20 dB/decade from 15 Hz. It is not until frequencies above 795 Hz that the input filter will start to compensate for the CMRR roll-off. By around 1 kHz the CMRR will be slightly below 90 dB and the filter attenuation will be around -4 dB. At 10 kHz these will be approximately 70 dB and -21 dB, and at 100 kHz they will be 50 dB and -41 dB. So the effect of the input filter is that the CMRR of the filter and PGA 281 combined will reach a minimum value of approximately 91 dB at around 1 kHz, and will not fall below that value.

The reason why there appears to be relatively little difference in the raw input data is that the power in the harmonic noise will decrease with increasing frequency. As the CMRR of the instrumentation amplifier starts to degrade from above 15 Hz and the input amplifier does not start to compensate until above 795 Hz, the region that will contain much of the noise power is at the mercy of the degradation in CMRR. Although much of the noise power remains, the filter does appear to make a significant difference to the amount of noise that is rectified and shifted to low frequency noise that cannot be removed by subsequent filtering.

The question may be asked, why not use an input filter with a lower corner frequency? This is a valid question, but as Figure 6.6 shows, the frequency response to the filter in Figure 6.2 for differential signals has a much lower corner frequency. So if the filter is tuned to fully compensate for the instrumentation amplifier CMRR roll-off, there will also be some attenuation to the differential signal of interest. An alternative approach would be to use a common mode choke, in addition to or instead of the filter, as this would only introduce common mode attenuation.

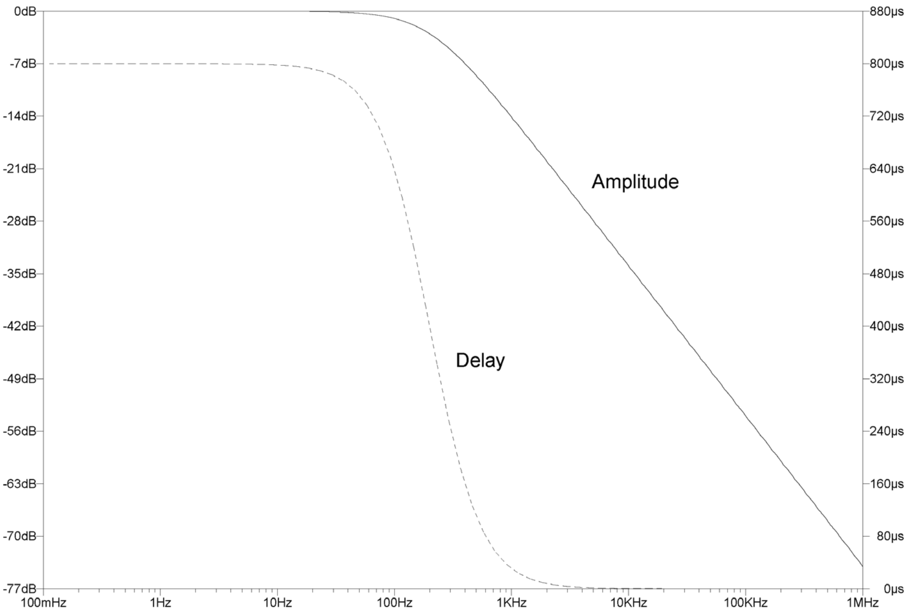

Figure 6.6 – The frequency response of the filter in Figure 6.2 to differential mode signals.

6.2 Digital signal processing

The digital filters (3.5.9) admirably perform their task of retrieving very small measurement signals from a background of significant noise. However, there are some issues that should be highlighted.

The filter order was estimated using Ichige's [89] algorithm, but as was highlighted for the first stage digital filter, the estimated filter order failed to meet the design criteria. For the first stage digital filter this did not matter as the attenuation deficit was more than made up for by the anti-aliasing filter. For the second stage digital filter, it can be seen by reference to Figure 3.64, that the stop band ripples only have an attenuation of -73.5 dB. This is supplemented by an attenuation at 250 Hz of -5.8 dB from the anti-aliasing filter (see Figure 3.56), and -0.1 dB from the first stage digital filter (see Figure 3.62). This gives a total minimum stop band attenuation from the three stages of just -79.4 dB, which is someway short of the required minimum of -96.3 dB (see 3.5.9). It was found that a filter order closer to 250th (from the estimated order of 174th) would be needed to meet the -96.3 dB target. A selection of the recorded data was reanalysed using a 250th order filter, but there was no discernible improvement. However, given the ease with which the second stage filter could be changed in the QSCP software, it would be prudent to rectify this issue.

In section 3.5.9 it was stated that there was no need for the use of a third stage post processing filter, as there was no observable improvement in signal quality over the real time IIR filter. In general, that statement holds to be true, but there are circumstances in which the IIR performance is insufficient. The frequency response of the third stage IIR filter (see Figure 3.67) is a series of notches, which have good attenuation only over a narrow bandwidth. Figure 6.7 shows the frequency response of the IIR filter around the first notch, and illustrates how small changes to the frequency can have a significant effect on the attenuation.

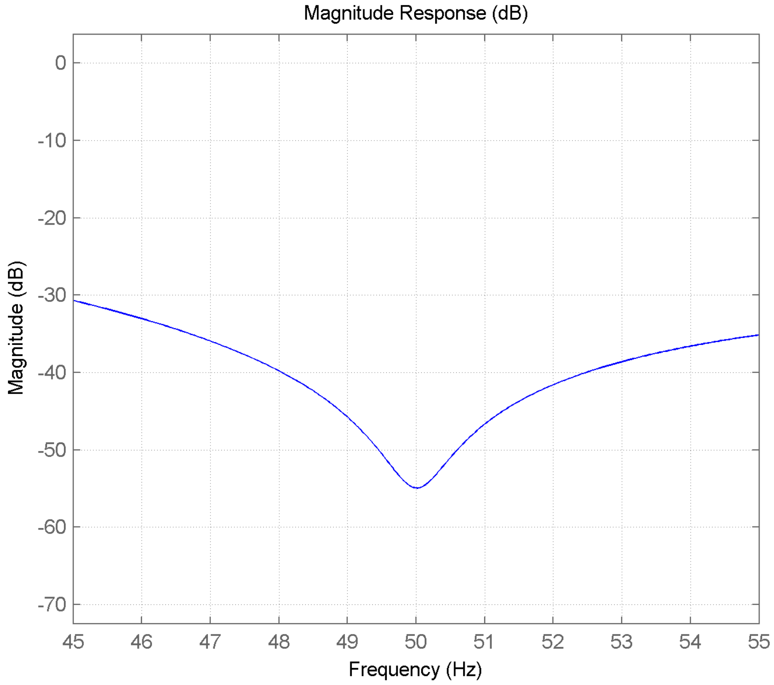

Figure 6.7 – The frequency response of the third stage digital filter. Enlarged to show the frequency response between 45 Hz and 50 Hz.

Figure 6.8 shows the FFT for the unprocessed thermocouple data from the experiment on cobalt sample A (0) and the titanium experiment (5.3.2), which have both been enlarged to more clearly show the region around the harmonic noise peak at 250 Hz[16]. It can be seen that there is a slight shift in frequency of the noise.

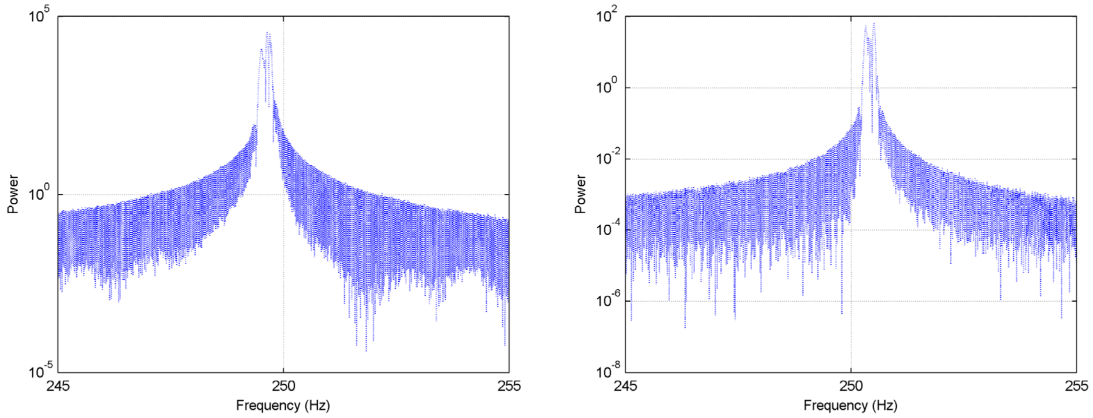

---

[16] All the harmonic noise peaks from 50 Hz onwards are shifted, but the shift becomes more obvious as the frequency increases. 250 Hz was chosen to display as it is the highest frequency peak that would remain after the second stage filter, but is more clearly visible than the earlier peaks.

Figure 6.8 – The FFT of the raw thermocouple data for the cobalt sample A (left) and the titanium sample (right). Both are enlarged to show the 250 Hz harmonic noise peak.

The shift in the FFT peak may be due to a shift in the mains frequency; the mains frequency voltage in the UK is specified as being 50 Hz ± 1% [92], but as can be seen from Figure 6.9 tends to be much more tightly controlled than that. The other explanation for the apparent frequency shift is a slight shift in the sampling frequency. Irrespective of the cause of the apparent frequency shift, this will cause a mismatch between the filter and the signal, shifting the noise peaks slightly out of the attenuation notches.

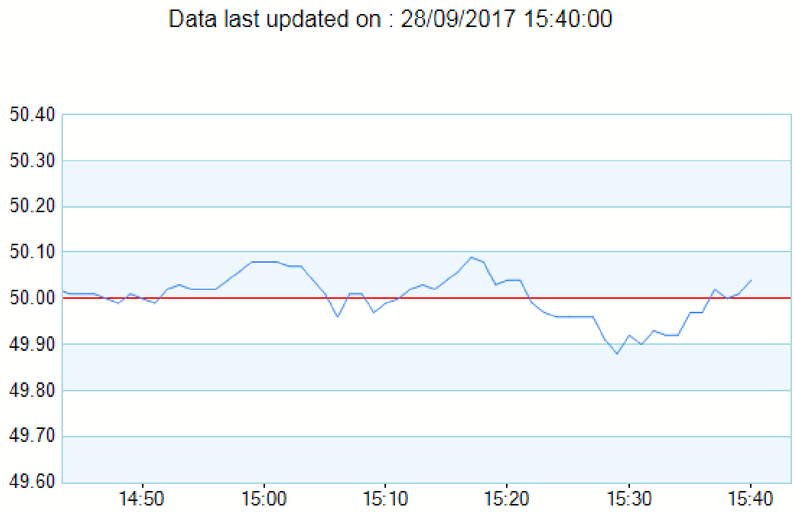

Figure 6.9 – Real time frequency data from the National Grid.

It is this relative shifting of filter and signal that allows a small amount of noise to pass through before the final stage of decimation for the titanium experiment. This noise is then aliased to an almost DC frequency, appearing as the very slowly varying sinusoidal noise in Figure 5.11. Figure 6.10 shows the (manually scaled) resistance vs time curve for the titanium experiment when used with a third stage FIR filter, which does not have the narrow bands of attenuation that characterise the real time IIR filter.

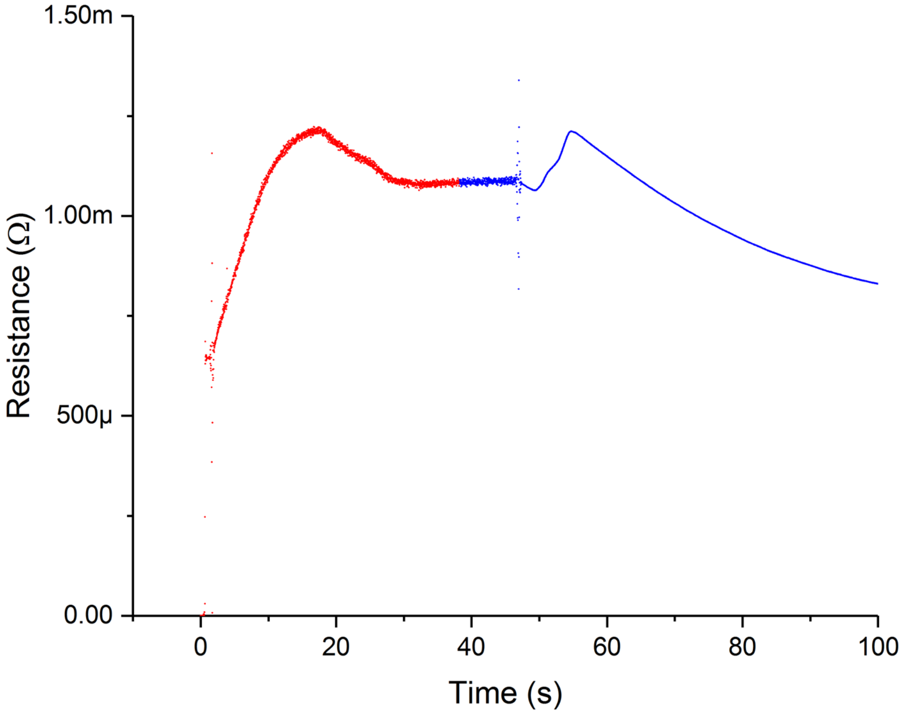

Figure 6.10 – The resistance vs. time curve for the titanium sample during heating (red) and the first part of cooling (blue) when filtered with a final stage FIR filter.

6.3 Phase transformation measurement

The resistance-temperature curves for the cobalt tests clearly show the phase transformations. The difference in the transformation temperatures during heating and cooling is due to kinetics. If the temperature of the sample could be held perfectly isothermally at the ideal transformation temperature then the transformation would take place at that temperature, although the transformation kinetics would be slow. However, as both during heating and cooling the transition through the ideal transformation temperature is rapid there is not sufficient time for the transformation to take place at that temperature with the available change in energy.

The difference between the transformation temperatures as measured by electrical resistance and DTA is relatively small, but still significant. It is clear that there remains some interference between the heating current and the instrumentation. It is suggested that the low temperature measured during cooling is due to the phase transformation kinetics, but that the low temperature during heating is due to a noise offset caused by the heating current. It can be seen from the resistance-temperature curves for the second cobalt sample (Figure 5.5, Figure 5.6, and Figure 5.7) that the heating current is supressing the temperature measurement, as once the heating current subsides the measured temperature suddenly increases. Without this offset, the measured temperature of the phase transformation would be above the ideal transformation temperature due to the kinetics.

The resistance-temperature curve for the titanium sample (Figure 5.10) appears to show similar results to the cobalt measurements. The phase transformation during cooling is measured at below the ideal temperature of 882°C, and the temperature during heating is artificially low due to electrical noise from the heating current.

For the phase transformation measurements on the eutectoid steel, the transformation temperatures during heating and cooling are again both lower than the ideal transformation temperature. However, whereas for the cobalt and titanium the transformation temperature during cooling was around 30°C lower than the ideal temperature, for the eutectoid steel it is closer to 170°C lower. The lower temperature is again due to the transformation kinetics. For pure cobalt and pure titanium the phase transformation only requires the movement of atoms over the short distances required to take the new crystal form. However, for the eutectoid steel to transform from austenite to pearlite there must be diffusion of carbon atoms over larger distances. It is again argued that the suppression of the transformation temperature during heating is due to electrical noise.

6.4 Spot welding

Based on limited observations, it would appear that the spot welding of the thermocouple and resistance measurement wires to the sample surface can affect the measurements. The spot welds for the initial experiments were conducted in air, but the results from these early experiments were very poor. For example, Figure 6.11 shows that the measured electrical resistance of a sample of Armco Pure Iron initially decreased on heating when the measurement wires had been welded in air.

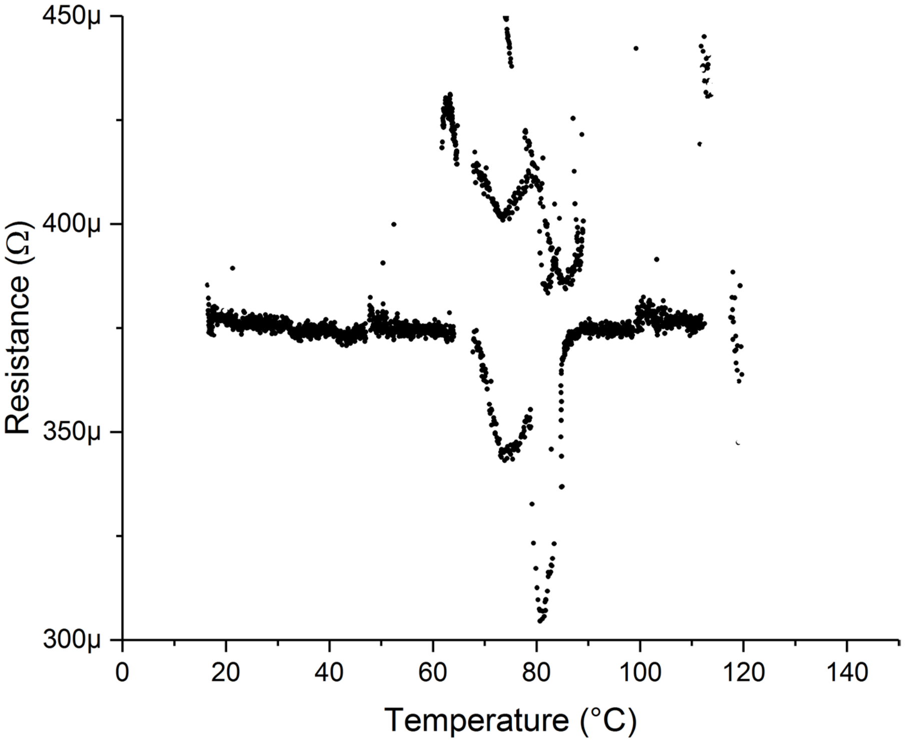

Figure 6.11 – The measured resistance for a sample of Armco Pure Iron initially decreased with heating.

It is believed that when welded in air there is a significantly greater likelihood that an oxide layer will be present in the weld, and that this metal oxide interface will form a diode. This diode will then rectify any AC noise that is present (see 6.1), creating significant DC offsets.

The introduction of argon seemed to vastly improve not only the appearance of the spot welds, but also the measurement results. Nevertheless, there still remains a large degree of variability in the appearance of the spot welds. It is suggested that the reason why there was much more significant temperature offset for all three measurements of cobalt sample B (0) than sample A, is the difference in weld quality between the two samples.

The effect of spot welding on the measurements is an area that deserves further investigation. Once the influence of weld quality has been established, a welding procedure should be developed to consistently produce suitable contacts.

6.5 Vacuum Measurement

The current vacuum measurement system (3.3.3) makes use of two gauges due to the issues that arose when using the combined Pirani and cold cathode gauge. The addition of the second Pirani gauge of a different model overcame the memory effect that appeared when using the combined gauge with argon, but is not an entirely satisfactory solution.

Reference to either Figure 3.38 or Figure 4.2 shows that as the argon pressure of a Pirani gauge approaches atmospheric pressure the gauge sensitivity is very low. This reduced sensitivity makes venting the chamber to an accurate pressure difficult, as the converted pressure reading tends to make large jumps in the measured pressure. Given that gas dependency of a Pirani gauge is a function not only of the gas, but also of the gauge construction [79], it is likely that as the gauge ages and become contaminated, the argon calibration performed in section 4.1, will decrease in validity.

The solution to both of the aforementioned problems would be the use of a direct pressure vacuum gauge. An indirect gauge such as a Pirani gauge measures a property other pressure, which is measured and then converted to a pressure reading. A direct pressure gauge, such as a Bourdon gauge, responds to pressure directly, and is not reliant upon the relationship between pressure and some third property. The suggested direct pressure gauge is a capacitance manometer, which works by having the pressure control the separation between the two electrodes, and hence altering the electrical capacitance. The electrical capacitance depends only upon the electrode separation, which in turn only depends on the force due to the gas pressure.

6.6 Sample clamping system

The sample clamping system (3.2.1.5) proved to be a difficult challenge. A number of different approaches were considered, and the selected approach of a sliding contact system became complex and expensive to manufacture. It was not possible to fully assess the success of this approach until the end of the project when the machine was capable of performing heat treatments. As can be seen from Figure 6.12, the samples tend to bow to accommodate thermal expansion along the sample length, rather than maintaining a cuboidal shape and spreading the sample clamps. It should however be noted that the sample deformation appear to reduce at the centre, which is the region to where the resistivity measurements are constrained (see 3.1.2.1).

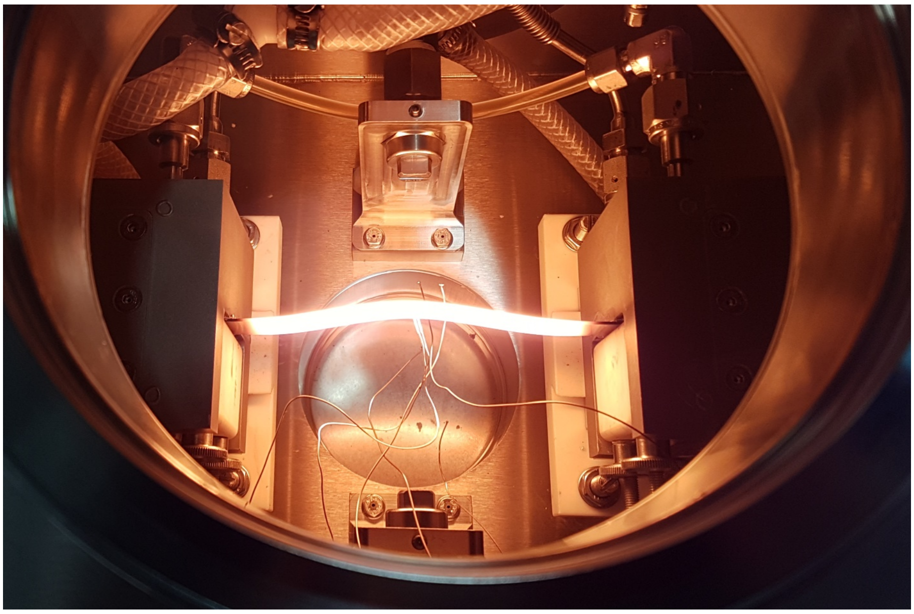

Figure 6.12 – A titanium sample can be seen to bow during heating. The nichrome wire used to measure resistance detached from the sample surface at approximately 1200°C.

In section 3.1.5 the maximum force with which the sample could be constrained whilst limiting the effect on M_S was calculated as 368 N. The force required to move the clamp bodies on their guide rails has not been measured, but based on the experience of machine assembly, there is no reason to question that the required force is around that level. However, even if the clamps can be moved with 368 N of force, this does not mean that this is how the samples will actually expand.

With hindsight, it would have been beneficial to create a FEM model to study the sample deformation during heating. There would still be a significant benefit to creating such a model, to verify the level of internal stress in the sample, so that this can be related back to the effect on M_S. If it were found that the internal stress within the sample did not affect MS, then as the sample clamps do not appear to move, they could in any future such machines be replaced with immovable clamps. If it were found that the internal stress does affect M_S, then it may be as wise to revisit the idea of using copper braid to form the flexible link, as to persevere with the sliding contact system.

6.7 Heating and quenching control

During initial testing of the quenching simulator it has been found that the strategy used to control the heating has a significant effect on the instrumentation. For example, it was observed that allowing large changes in the phase control turn-on angle produced packets of noise during the periods of rapid change. Large conduction angles were not intrinsically problematic, if the control angle was ramped to a new value. However, the best signal integrity was delivered by using a constant turn-on angle until the target temperature was reached, and this is the approach that was used for measuring all of the validation alloys (see 5.3).

One of the most problematic manifestations of the noise due to the control strategy was a change in the resistance measurement voltage offset that accompanied a change in turn-on angle. To a lesser degree this also affected the temperature measurement offset, but because of the smaller signal voltages had a significantly more pronounced effect of the resistance measurement voltage. It is likely that these offsets were caused by amplifier rectification (see 6.1), and as such it would seem prudent that any future efforts should first be directed towards improving the measurement fidelity before tackling the control.

Figure 6.13 shows the recorded temperature of a 2 mm thick sample of Armco pure iron being heated in the quenching simulator with an argon atmosphere. The quenching simulator attempted to follow the temperature profile that is shown by the black line by turning the current off when the temperature was too hot, and turning on (at 140°) when too cold. The red line shows the sample temperature as recorded by the thermocouple. The regions where the measured temperature appears noisy correspond to the regions where the heating current was switched.

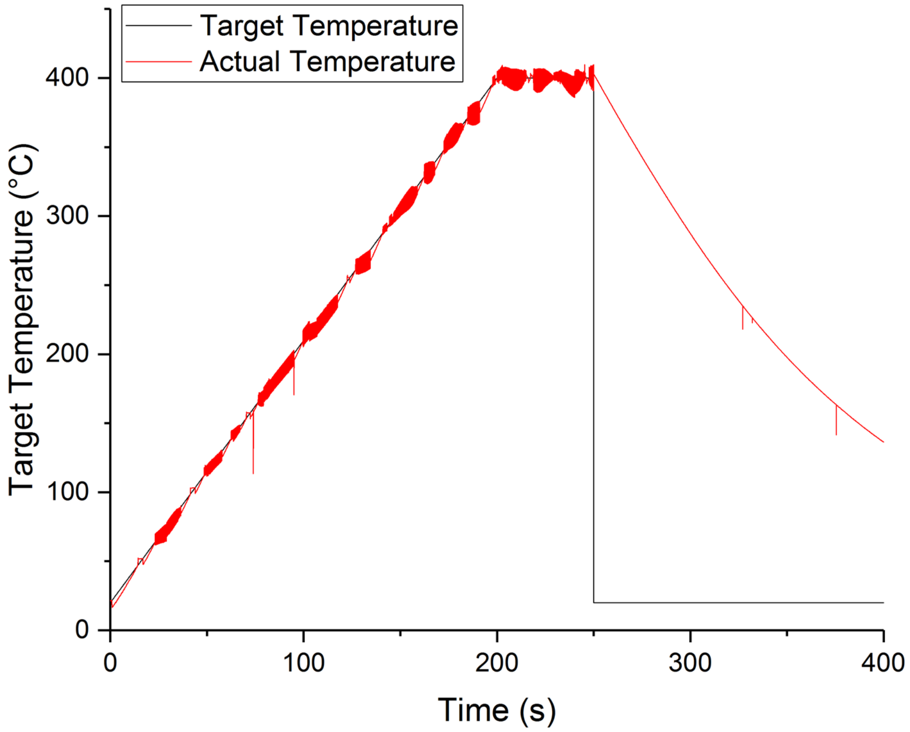

Figure 6.13 – A 2 mm thick sample of Armco pure iron being heated according to a specified profile using on-off control of the heating current. The black line shows the target temperature, and the red line shows the thermocouple reading.

Due to time constraints there has been very little development of the quenching control. The QSCP software currently has the option to specify the quench valve opening when used with a constant turn-on angle. When used in the normal temperature profile mode, the user specifies whether quenching may be used during each step. Then if the temperature is too high during a step where quenching is allowed, the quench valve will be slowly opened if the temperature is too hot, and slowly closed if the temperature is too cool. The effectiveness of this control strategy has not yet been investigated.

6.8 Cold junction calibration

The results of the cold junction calibration procedure (see 4.3) did not lead to a correction function with as high a coefficient of determination as for the other channels. The most obvious explanation for the results being less accurate is that the cold junction RTD and the semi-standard RTD were not fully in thermal equilibrium. As there were minor changes to the temperature of the isothermal block, the two RTDs responded to the change in stimulus at different rates, meaning that the RTD with the slower response would read lower than the other RTD as the temperature of the isothermal block was increasing and vice versa.

Given that the cold junction RTD is of class A accuracy and has an error of only ±0.15°C at 0°C and only ±0.3°C at 100°C, better calibration results may have been achieved by not attempting to calibrate the RTD and DAQ as a system, but to have calibrated only the DAQ using a voltage input as was done for the thermocouple channels.

7 Conclusions

After the introduction, this thesis commenced with a brief overview of press hardened and other modern automotive steels. The literature review then gave a description of the martensitic transformation in steels, before looking in more detail at factors that influence the transformation start temperature and kinetics. A detailed summary of the methods that have been used by various researchers to study the martensitic transformation and kinetics then followed, which concluded by looking at the difficulty faced by researchers in making measurements that are consistent across different laboratories.

The instrument design chapter started by setting out the design requirements for the quenching simulator, along with a justification for some of the strategic design decisions. The first part of the instrument design to be covered was the sample heating and quenching systems, where a proposed method of phase angle control using asymmetric turn-on angles was presented. Unfortunately, due to what was an unknown error with the zero-crossing detector along with the problem of dissipating large amounts of energy during the non-zero current turn-off, the proposed method of phase angle control could not be successfully implemented. Finite element method models were presented to model the heat loss during sample heating, and additional finite element method models to calculate the correct cable size to carry a 2000 A alternating current were detailed. Due to the difficulty in accurately modelling quenching using computer models, the quenching system design was supported by experimental evaluation.

The next part of the instrument design was for the high vacuum system. The vacuum system added a significant amount of cost and complexity to this project. The vacuum system was considered to be essential, so that thermal etching could be used to reliably reveal the prior austenite grain structure. However, the time taken design, source, manufacture, and snag the vacuum system added at least a year to this project. The details of the vacuum system are contained in the appendices, and should provide a useful shortcut for anyone designing a similar system.

The following part of the instrument design chapter looked at the hardware and software that was designed and built to control the quenching simulator. The basic design and common electronics of the modules were described, before the details of each of the four control modules were covered. Full circuit diagrams for each of the control modules appear in the appendices. The source code for the control modules was also included in the appendices. The structure of the Quenching Simulator Control Panel software was introduced, along with a series of UML activity diagrams to explain the software. The source code that relates to the execution of a heat treatment was included in the appendices. Because of the complexity of the software for the real-time digital signal processing of the analogue input channels, a data flow diagram was produced to aid the reader.

The final part of the instrument design looked at the instrumentation. This section included a detailed look at the electronics required for the four-wire electrical resistance measurement and the thermocouple measurements, before covering the general analogue signal processing electronics. A detailed description of the multi-rate digital signal processing was the concluding part of the instrument design chapter.

The fourth chapter introduced the methods used to calibrate the instrumentation. The calibration procedures covered the vacuum gauges, the thermocouple measurement electronics, the thermocouple cold junction, the resistance measurement circuit, and the data acquisition card. It is anticipated that the calibration procedures will be repeated periodically to maintain measurement accuracy, so this chapter should serve as a guide for future calibrations.

The two final major chapters present the results of the experiments to assess the instrument performance, and provide a discussion about those results. The temperature measurement system was shown to be in excellent agreement with a calibrated thermometer in the absence of electrical interference. Very good progress was achieved in retrieving the small measurement signals from a background of extensive electrical noise. There remain issues with the conversion of common mode noise to differential noise that cannot be subsequently separated, which in turn is affecting both the instrumentation and control. The digital signal processing is able to remove almost all of the converted noise in real time, but drifts in frequency between the mains power frequency and the sampling rate expose the limitations of the real time infinite impulse filter.

Despite these remaining issues, phase transformations were clearly observed using electrical resistance measurements. The remaining noise issues are only present during the application of heating current, and are not evident during cooling. It is unfortunate that due to a lack of time martensitic alloys have not yet been measured. Nevertheless, given the freedom from interference during cooling, this instrument should be well placed to serve its original purpose of measuring the martensitic phase transformation start temperature and kinetics.

8 Future Work

The main element of future work is to address the remaining common mode electrical noise in the temperature measurement instrumentation. As the suspected cause of the noise is the rectification and conversion to differential noise of the common mode noise in the instrumentation amplifier, the likely solution will be some type of additional filter placed between the sample and the instrumentation amplifier.

Once the remaining noise in the thermocouple measurement electronics has been addressed, the next step in the machine development will be to investigate alternative control strategies that will enable accurate control of heating and cooling. It remains unclear whether temperature control during cooling will be possible during quenching, or only during unforced cooling.

The remaining items of future work may be completed by future users of the quenching simulator, as they do not relate to machine development, and should be within the remit of the general metallurgist.

The thermal characteristics of the machine deserve more comprehensive characterization, particularly with regards to whether the region of the sample that contributes to the electrical resistance measurement is of nearly uniform temperature during heating, holding, and cooling.

The sample deformation during heating should be modelled to gain a quantitative understanding of the stress field within the sample and how this might affect the start temperature of the martensitic transformation.

The potential formation of metal-oxide diodes during spot welding is an issue that warrants further investigation. If it is found that a metal-oxide layer is being formed in the weld, then the spot welding procedure (including the atmosphere) should be optimized to resolve this.

References

[1] R. Kuziak, R. Kawalla, and S. Waengler, "Advanced high strength steels for automotive industry," *Archives of Civil and Mechanical Engineering,* vol. 8, no. 2, pp. 103-117, 2008.

[2] M. Takahashi, A. Uenishi, H. Yoshida, and H. Kuriyama, "Advanced High Strength Steels for Automobile Body Structures," *Materials Science Forum,* vol. 539-543, pp. 4386-4390, 2007.

[3] D. Cornette, P. Cugy, A. Hildenbrand, M. Bouzekri, and G. Lovato, "Ultra High Strength FeMn TWIP Steels for automotive safety parts," *Revue de Métallurgie,* vol. 102, no. 12, pp. 905-918, 2006.

[4] H. Karbasian and A. E. Tekkaya, "A review on hot stamping," *Journal of Materials Processing Technology,* vol. 210, no. 15, pp. 2103-2118, 2010.

[5] M. Nikravesh, M. Naderi, G. H. Akbari, and W. Bleck, "Phase transformations in a simulated hot stamping process of the boron bearing steel," *Materials & Design,* vol. 84, pp. 18-24, 2015.

[6] L. C. Kaufman, Morris, "The Martensite Transformation in the Iron-Nickel System," *Trans AIME,* vol. 206, pp. 1393-1401, 1956.

[7] R. F. Bunshah and R. F. Mehl, "Rate of propogation of martensite," *Trans AIME,* vol. 197, no. 9, pp. 1251-1258, 1953.

[8] E. C. Bain, "The nature of martensite," *Trans AIME,* vol. 70, pp. 25-46, 1924.

[9] G. Kurdjumow and G. Sachs, "ber den Mechanismus der Stahlhrtung," *Zeitschrift fr Physik,* vol. 64, no. 5-6, pp. 325-343, 1930.

[10] J. S. Bowles and C. S. Barrett, "Crystallography of transformations," *Progress in Metal Physics,* vol. 3, pp. 1-41, 1952.

[11] A. B. Greninger and A. R. Troiano, "Crystallography of austenite decomposition," *Trans AIME,* vol. 140, pp. 307-336, 1940.

[12] A. B. Greninger and A. R. Troiano, "The mechanism of Martensite formation," *Trans AIME,* vol. 185, pp. 590-598, 1949.

[13] J. S. Bowles and J. K. Mackenzie, "The crystallography of martensite transformations I," *Acta Metallurgica,* vol. 2, no. 1, pp. 129-137, 1954.

[14] E. R. Petty, "Introductory," in *Martensite: Fundamentals and Technology*, E. R. Petty, Ed. London: Longman, 1970.

[15] C. S. Roberts, "Effect of carbon on the volume fractions and lattice parameters of retained austenite and martensite," *Journal of Metals,* vol. 5, no. 2, pp. 203-204, 1953.

[16] T. Maki, S. Shimooka, and I. Tamura, "The Ms temperature and morphology of martensite in Fe-31 Pct Ni-0.23 Pct C alloy," *Metallurgical Transactions,* vol. 2, no. 10, pp. 2944-2945, 1971.

[17] T. Maki, "Microstructure and Mechanical Behaviour of Ferrous Martensite," *Materials Science Forum,* vol. 56-58, pp. 157-168, 1990.

[18] J. R. Strife, M. J. Carr, and G. S. Ansell, "The effect of austenite prestrain above the Md temperature on the martensitic transformation in Fe-Ni-Cr-C alloys," *Metallurgical Transactions A,* vol. 8, no. 9, pp. 1471-1484, 1977.

[19] P. J. Fisher and D. J. H. Corderoy, "The role of thermal stabilization in martensite transformations," *Metallurgical Transactions A,* vol. 10, no. 10, pp. 1421-1427, 1979.

[20] M. J. Roberts, "The strength of martensite," in *Martensite: Fundamentals and Technology*, E. R. Petty, Ed. London: Longman, 1970.

[21] G. Krauss, "Martensite in steel: strength and structure," *Materials Science and Engineering: A,* vol. 273-275, pp. 40-57, 1999.

[22] A. B. Greninger and A. R. Troiano, "Kinetics of the austenite to martensite transformation in steel," *Trans ASM,* pp. 537-574, 1940.

[23] L. Kaufman and M. Cohen, "Thermodynamics and kinetics of martensitic transformations," *Progress in Metal Physics,* vol. 7, pp. 165-246, 1958.

[24] M. R. Meyerson and S. J. Rosenberg, "The Influence of Heat Treating Variables on the Martensite Transformation in SAE 1050 Steel," *Trans ASM,* vol. 46, 1954.

[25] S. M. C. Van Bohemen, M. J. Santofimia, and J. Sietsma, "Experimental evidence for bainite formation below Ms in Fe–0.66C," *Scripta Materialia,* vol. 58, no. 6, pp. 488-491, 2008.

[26] B. N. P. Babu, M. S. Bhat, E. R. Parker, and V. F. Zackay, "A rapid magnetometric technique to plot isothermal transformation diagrams," *Metallurgical Transactions A,* vol. 7, no. 1, pp. 17-22, 1976.

[27] S. M. C. Van Bohemen and J. Sietsma, "Martensite Formation in Partially and Fully Austenitic Plain Carbon Steels," *Metallurgical and Materials Transactions A,* vol. 40, no. 5, pp. 1059-1068, 2009.

[28] B. Edmondson and T. Ko, "Spontaneous deformation of austenite during martensitic transformations," *Acta Metallurgica,* vol. 2, no. 2, pp. 235-241, 1954.

[29] D. P. Koistinen and R. E. Marburger, "A General Equation Prescribing the Extent of the Austenite-Martensite Transformation in Pure Iron-Carbon Alloys and Plain Carbon Steels," (in English), *Acta Metallurgica,* vol. 7, no. 1, pp. 59-60, 1959.

[30] E. M. Breinan and G. S. Ansell, "The influence of austenite strength upon the austenite-martensite transformation in alloy steels," *Metallurgical Transactions,* vol. 1, no. 6, pp. 1513-1520, 1970.

[31] T. G. Digges, "Influence of austenitic grain size on the critical cooling rate of high-purity iron-carbon alloys," *Journal of Research of the National Bureau of Standards,* vol. 24, no. 6, p. 723, 1940.

[32] M. Umemoto and W. S. Owen, "Effects of austenitizing temperature and austenite grain size on the formation of athermal martensite in an iron-nickel and an iron-nickel-carbon alloy," *Metallurgical Transactions,* vol. 5, no. 9, pp. 2041-2046, 1974.

[33] T. J. Nichol, G. Judd, and G. S. Ansell, "The relationship between austenite strength and the transformation to martensite in Fe-10 pct Ni-0.6 pct C alloys," *Metallurgical Transactions A,* vol. 8, no. 12, pp. 1877-1883, 1977.

[34] P. J. Brofman and G. S. Ansell, "On the effect of fine grain size on the Ms temperature in Fe-27Ni-0.025C alloys," *Metallurgical Transactions A,* vol. 14, no. 9, pp. 1929-1931, 1983.

[35] K. Maweja, W. Stumpf, and N. van der Berg, "Characteristics of martensite as a function of the Ms temperature in low-carbon armour steel plates," *Materials Science and Engineering: A,* vol. 519, no. 1-2, pp. 121-127, 2009.

[36] J. Burke, "The Methods of Measuring Reaction Velocities," in *The Kinetics of Phase Transformations in Metals*Oxford: Pergamon Press, 1965, pp. 37 - 38.

[37] F. B. Rote, W. C. Truckenmiller, and W. P. Wood, "Electrical Resistance Method for the Determination of Isothermal Austenite Transformations," *Trans ASM,* vol. 30, 1942.

[38] H.-S. Yang and H. K. D. H. Bhadeshia, "Uncertainties in dilatometric determination of martensite start temperature," *Materials Science and Technology,* vol. 23, no. 5, pp. 556-560, 2007.

[39] G. K. Burgess and I. N. Kellberg, "Electrical resistance and critical ranges of pure iron," *National Bureau of Standards Bulletin,* vol. 11, no. 236, pp. 457-470, 1915.

[40] A. W. McReynolds, "Electrical Observations of the Austenite-Martensite Transformation in Steel," *Journal of Applied Physics,* vol. 17, no. 10, p. 823, 1946.

[41] P. W. Brown and D. J. Mack, "Electrical resistivity and microstructural changes accompanying the isothermal decomposition of austenite in eutectoid steel," *Metallurgical Transactions,* vol. 4, no. 11, pp. 2639-2643, 1973.

[42] O. N. Mohanty and A. N. Bhagat, "Electrical Resistivity and Phase Transformation in Steels," *Materialwissenschaft und Werkstofftechnik,* vol. 34, no. 1, pp. 96-101, 2003.

[43] A. Amengual, V. Torra, A. Isalgue, and F. Marco, "Analysis of a martensitic transformation by optical microscopy, acoustic emission detection, resistance measurements and differential scanning calorimetry," *Thermochimica Acta,* vol. 155, pp. 115-134, 1989.

[44] W. Colner and O. Zmeskal, "An Electrical Resistance Apparatus for Studying Transformation in Stainless Steel," *Trans ASM,* vol. 44, p. 1158, 1952.

[45] F. G. Wilson and F. B. Pickering, "A study of zone formation in an austenitic steel containing 4% titanium," *Acta Metallurgica,* vol. 16, no. 1, pp. 115-131, 1968.

[46] F. G. Wilson and F. B. Pickering, "Resistance changes accompanying γ′ precipitation in austenitic steels," *Scripta Metallurgica,* vol. 2, no. 8, pp. 471-473, 1968.

[47] P. D. Garn and S. S. Flaschen, "Detection of Polymorphic Phase Transformations by Continuous Measurment of Electrical Resistance," *Analytical Chemistry,* vol. 29, no. 2, pp. 268-271, 1957.

[48] C. Nagler and W. Wood, "The Effect of Normal Elements and Alloy Elements on the Rate of Austenite Transformation in Cast Iron at Constant Temperature," *Trans ASM,* vol. 30, p. 491, 1942.

[49] E. Sharif, C. Bell, P. F. Morris, and A. J. Peyton, "Imaging the transformation of hot strip steel using magnetic techniques," *Journal of Electronic Imaging,* vol. 10, no. 3, p. 669, 2001.

[50] T. Kakeshita, K. Shimizu, T. Sakakibara, S. Funada, and M. Date, "Magnetic Field-Induced Martensitic Transformation in an Fe--31. 7 At.% Ni Alloy," *Trans. Jpn. Inst. Met.,* vol. 24, no. 11, pp. 748-753, 1983.

[51] F. Christien, M. T. F. Telling, and K. S. Knight, "A comparison of dilatometry and in-situ neutron diffraction in tracking bulk phase transformations in a martensitic stainless steel," *Materials Characterization,* vol. 82, pp. 50-57, 2013.

[52] H. Goldenstein, E. A. Huallpa, J. C. Sánchez, and L. R. Padovese, "Detecting martensitic transformations using spontaneous magnetic emission (SME)," *Journal of Alloys and Compounds,* vol. 577, pp. S736-S740, 2013.

[53] A. Bodin and P. D. Marchal, "The Use of Thermal-Analysis Techniques for the Validation of Phase-Transformation Models," (in English), *Steel Research,* vol. 65, no. 3, pp. 103-109, Mar 1994.

[54] G. R. Speich and A. J. Schwoeble, "Acoustic Emission During Martensite Formation," *ASTM STP 505,* pp. 140-151, 1972.

[55] S. M. C. Van Bohemen, M. J. M. Hermans, and G. Den Ouden, "Acoustic emission monitoring of bainitic and martensitic transformation in medium carbon steel during continuous cooling," *Materials Science and Technology,* vol. 18, no. 12, pp. 1524-1528, 2002.

[56] B. D. Cullity, *Elements of X-Ray Diffraction*, 2nd ed. Reading, Massachuesetts: Addison-Wesley, 1978.

[57] J. Epp, T. Hirsch, and C. Curfs, "In situ X-Ray Diffraction Analysis of Carbon Partitioning During Quenching of Low Carbon Steel," *Metallurgical and Materials Transactions A,* vol. 43, no. 7, pp. 2210-2217, 2012.

[58] Y. Xu, S. H. Zhang, M. Cheng, and H. W. Song, "In situ X-ray diffraction study of martensitic transformation in austenitic stainless steel during cyclic tensile loading and unloading," *Scripta Materialia,* vol. 67, no. 9, pp. 771-774, 2012.

[59] A. Nitsche and P. Mayr, "Round Robin test on measurement of phase transformation temperatures in 9Cr1Mo steel," *Welding in the World,* vol. 61, no. 1, pp. 81-90, 2017.

[60] R. Kolleck, R. Veit, M. Merklein, J. Lechler, and M. Geiger, "Investigation on induction heating for hot stamping of boron alloyed steels," *CIRP Annals - Manufacturing Technology,* vol. 58, no. 1, pp. 275-278, 2009.

[61] M. Geiger, M. Merklein, and C. Hoff, "Basic Investigations on the Hot Stamping Steel 22MnB5," *Advanced Materials Research,* vol. 6-8, pp. 795-804, 2005.

[62] B. Raeisinia, W. J. Poole, and D. J. Lloyd, "Examination of precipitation in the aluminum alloy AA6111 using electrical resistivity measurements," *Materials Science and Engineering: A,* vol. 420, no. 1-2, pp. 245-249, 2006.

[63] C. García de Andrés, M. J. Bartolomé, C. Capdevila, D. San Martín, F. G. Caballero, and V. López, "Metallographic techniques for the determination of the austenite grain size in medium-carbon microalloyed steels," *Materials Characterization,* vol. 46, no. 5, pp. 389-398, 2001.

[64] S. Joly, *Personal communication: A procedure for performing thermal etching on steels*. 2012.

[65] *ISO 6892-1: Metallic Materials - Tensile Testing - Method of Test at Room Temperature*, 2009.

[66] Z. Nishiyama, *Martensitic Transformation* (Materials Science and Technology). New York: Academic Press, 1978.

[67] F. F. Mazda, *Power electronics handbook*. London: Butterworth & Co, 1990.

[68] J. A. Greenwood and J. B. P. Williamson, "Contact of Nominally Flat Surfaces," *Proceedings of the Royal Society A: Mathematical, Physical and Engineering Sciences,* vol. 295, no. 1442, pp. 300-319, 1966.

[69] R. L. Jackson and I. Green, "A Finite Element Study of Elasto-Plastic Hemispherical Contact Against a Rigid Flat," *Journal of Tribology,* vol. 127, no. 2, p. 343, 2005.

[70] American Society for Metals, *ASM Handbook: Friction, Lubrication and Wear Technology v. 18* (ASM Handbook). Materials Park, Ohio: ASM International, 1992.

[71] F. Cardarelli, 2nd, Ed. *Materials Handbook: A Concise Desktop Reference*. London: Springer, 2008.

[72] *BS EN 60204-1:2006+A1:2009 Safety of machinery. Electrical equipment of machines. General requirements.*, 2006.

[73] S. Connor, "Why the world is running out of helium," in *The Independent*, ed. London, 23/08/2018.

[74] T. Bell, "Martensitic and Massive Transformations in Ferrous Alloys," in *Martensite: Fundamentals and Technology*, E. R. Petty, Ed. London: Longman, 1970.

[75] H. M. Rietveld, "A profile refinement method for nuclear and magnetic structures," *Journal of Applied Crystallography,* vol. 2, no. 2, pp. 65-71, 1969.

[76] B. H. Toby, "EXPGUI, a graphical user interface forGSAS," *Journal of Applied Crystallography,* vol. 34, no. 2, pp. 210-213, 2001.

[77] A. Larson and R. Von Dreele, "General Structure Analysis System (GSAS)," in "LAUR 86-748," Los Alamos National Laboratory, Los Alamos, New Mexico2000.

[78] J. F. O'Hanlon, *A User's Guide to Vacuum Technology*. Hoboken, NJ: Wiley-Interscience, 2003.

[79] K. Jousten, "On the gas species dependence of Pirani vacuum gauges," (in English), *Journal of Vacuum Science & Technology A,* Article vol. 26, no. 3, pp. 352-359, May 2008.

[80] T. Williams, *EMC for Product Designers*, 4th ed. Oxford, UK: Newnes, 2007.

[81] J. Axelson, *USB Complete: The Developers Guide*, 4th ed. Madison, US: Lakeview Research, 2009.

[82] D. A. Dapkus. (1994) Using MOS-gated power transistor in AC switch applications. *International Rectifier Design Tips*.

[83] R. W. Wall, "Simple methods for detecting zero crossing," presented at the Industrial Electronics Society, 2 - 6 November 2003, 2003.

[84] P. H. Horowitz, W., *The Art of Electronics*, 3rd ed. New York: Cambridge University Press, 2015.

[85] H. Preston-Thomas, "The International Temperature Scale of 1990 (ITS-90)," *Metrologia,* vol. 27, no. 1, pp. 3-10, 1990.

[86] G. W. Burns and M. G. Scroger, *The Calibration of Thermocouples and Thermocouple Materials*. Gaithersburg, MD: National Institute of Standards and Technology, 1989.

[87] National Institute of Standards and Technology. NIST ITS-90 Thermocouple Database [Online]. Available: http://srdata.nist.gov/its90/main/

[88] T. Kuehl, "Using the infinite-gain, MFB filter topology in fully differential active filters," *Analog Applications Journal,* no. 3Q, pp. 33-38, 2009.

[89] K. Ichige, M. Iwaki, and R. Ishii, "Accurate estimation of minimum filter length for optimum FIR digital filters," *IEEE Transactions on Circuits and Systems II: Analog and Digital Signal Processing,* vol. 47, no. 10, pp. 1008-1016, 2000.

[90] Analog Devices, "RFI Rectification Concepts," vol. MT-096, 1 ed: Analog Devices, 2009.

[91] C. Kitchin, L. Counts, and M. Gerstenhaber. (2003, 13th November) Input filter prevents instrumentation-amp RF-rectification errors. *EDN*. 101-102.

[92] P. Wilson, *The circuit designer's companion*, 3rd ed. Oxford: Newnes, 2012.

Appendix 1 – Modelled effect of sample length on apparent resistance

Length (m)	Electric potential (V) Point: 6	Electric potential (V) Point: 7	Voltage (V)	Resistance (Ω)	Resistance Ratio
150.0E-3	-9.19E-06	9.11E-06	1.83E-05	36.5E-6	1.00
145.0E-3	-9.24E-06	9.06E-06	1.83E-05	36.4E-6	1.00
140.0E-3	-9.25E-06	9.06E-06	1.83E-05	36.5E-6	1.00
135.0E-3	-9.05E-06	9.22E-06	1.83E-05	36.4E-6	1.00
130.0E-3	-9.13E-06	9.15E-06	1.83E-05	36.4E-6	1.00
125.0E-3	-9.06E-06	9.24E-06	1.83E-05	36.5E-6	1.00
120.0E-3	-9.15E-06	9.15E-06	1.83E-05	36.4E-6	1.00
115.0E-3	-9.04E-06	9.25E-06	1.83E-05	36.4E-6	1.00
110.0E-3	-9.00E-06	9.34E-06	1.83E-05	36.5E-6	1.00
105.0E-3	-9.00E-06	9.31E-06	1.83E-05	36.5E-6	1.00
100.0E-3	-9.17E-06	9.12E-06	1.83E-05	36.4E-6	1.00
95.0E-3	-9.16E-06	9.14E-06	1.83E-05	36.5E-6	1.00
90.0E-3	-9.20E-06	9.10E-06	1.83E-05	36.5E-6	1.00
85.0E-3	-9.09E-06	9.18E-06	1.83E-05	36.4E-6	1.00
80.0E-3	-9.28E-06	9.03E-06	1.83E-05	36.5E-6	1.00
75.0E-3	-8.96E-06	9.34E-06	1.83E-05	36.4E-6	1.00
70.0E-3	-9.09E-06	9.20E-06	1.83E-05	36.4E-6	1.00
65.0E-3	-9.10E-06	9.18E-06	1.83E-05	36.4E-6	1.00
60.0E-3	-9.22E-06	9.08E-06	1.83E-05	36.5E-6	1.00
55.0E-3	-8.90E-06	9.40E-06	1.83E-05	36.5E-6	1.00
50.0E-3	-9.07E-06	9.22E-06	1.83E-05	36.4E-6	1.00
45.0E-3	-9.16E-06	9.16E-06	1.83E-05	36.5E-6	1.00
40.0E-3	-9.18E-06	9.18E-06	1.84E-05	36.6E-6	1.00
35.0E-3	-9.18E-06	9.27E-06	1.84E-05	36.8E-6	1.01
30.0E-3	-9.41E-06	9.24E-06	1.86E-05	37.1E-6	1.02
25.0E-3	-9.45E-06	9.64E-06	1.91E-05	38.0E-6	1.04
20.0E-3	-1.00E-05	1.01E-05	2.01E-05	40.0E-6	1.10
15.0E-3	-1.13E-05	1.12E-05	2.25E-05	44.8E-6	1.23
10.0E-3	-1.42E-05	1.46E-05	2.88E-05	57.4E-6	1.58
5.0E-3	-2.60E-05	2.61E-05	5.21E-05	103.7E-6	2.85
1.0E-3	-1.15E-04	1.40E-04	2.56E-04	509.3E-6	13.97

The results of an FEM model in COMSOL Multiphysiscs 4.2 to investigate how the length of the sample affects the electrical resistance measured along the centre-line at right angle to the length. See section 3.1.2.1 for a full description.

Appendix 2 – Experimentally measured effect of sample length on apparent resistance

Length (m)	Resistance (Ω)	Resistance Ratio
150.0E-3	100.0E-6	1.00
140.0E-3	98.8E-6	0.99
130.0E-3	100.5E-6	1.01
120.0E-3	97.3E-6	0.97
110.0E-3	95.5E-6	0.96
100.0E-3	98.8E-6	0.99
90.0E-3	98.3E-6	0.98
80.0E-3	101.2E-6	1.01
70.0E-3	100.1E-6	1.00
60.0E-3	99.9E-6	1.00
50.0E-3	96.9E-6	0.97
40.0E-3	101.4E-6	1.01
30.0E-3	101.8E-6	1.02
20.0E-3	101.5E-6	1.02
10.0E-3	118.1E-6	1.18

The results of experimental measurements to investigate how the length of the sample affects the electrical resistance measured along the centre-line at right angle to the length. See section 3.1.2.1 for a full description.

Appendix 3 – Experimental parameters for determining spray nozzle cooling rates

Nozzle Type	Argon Pressure (bar)	Argon Flow Rate (l/min)	Water Pressure (bar)	Water Flow Rate[1] (l/min)	Nozzle to Sample Distance (mm)
Unforced Cooling	-	-	-	-	-
LF20-80°	-	-	6	11.2	90
LF20-80°	-	-	4	9.0	90
LF20-80°	-	-	2.1	6.5	90
CCR 2.0-80°	2.1	126[2]	1.2	2.2	90
CCR 2.0-80°	2.1	105[2]	4	5.7	90
CCR 2.0-80°	2.1	89[2]	6	7.7	90
LF20-80°	2.1	127[3]	-	-	165
LF20-80°	6	318	-	-	130
Drilled Copper Pipe	4	259	-	-	25
Drilled Copper Pipe	8	502	-	-	25

---

[1] The water flow rate is found by linearly interpolating the water flow rate data from the manufacturer data sheet.

[2] The argon flow rate is found by linearly interpolating the air flow rate data in the manufacturer data sheet. No correction is made for the fluid being argon.

[3] The argon flow rate was measured using a rotameter, and linearly interpolated where necessary.

Appendix 4 – Spray nozzle cooling curves

Appendix 4A – Unforced cooling

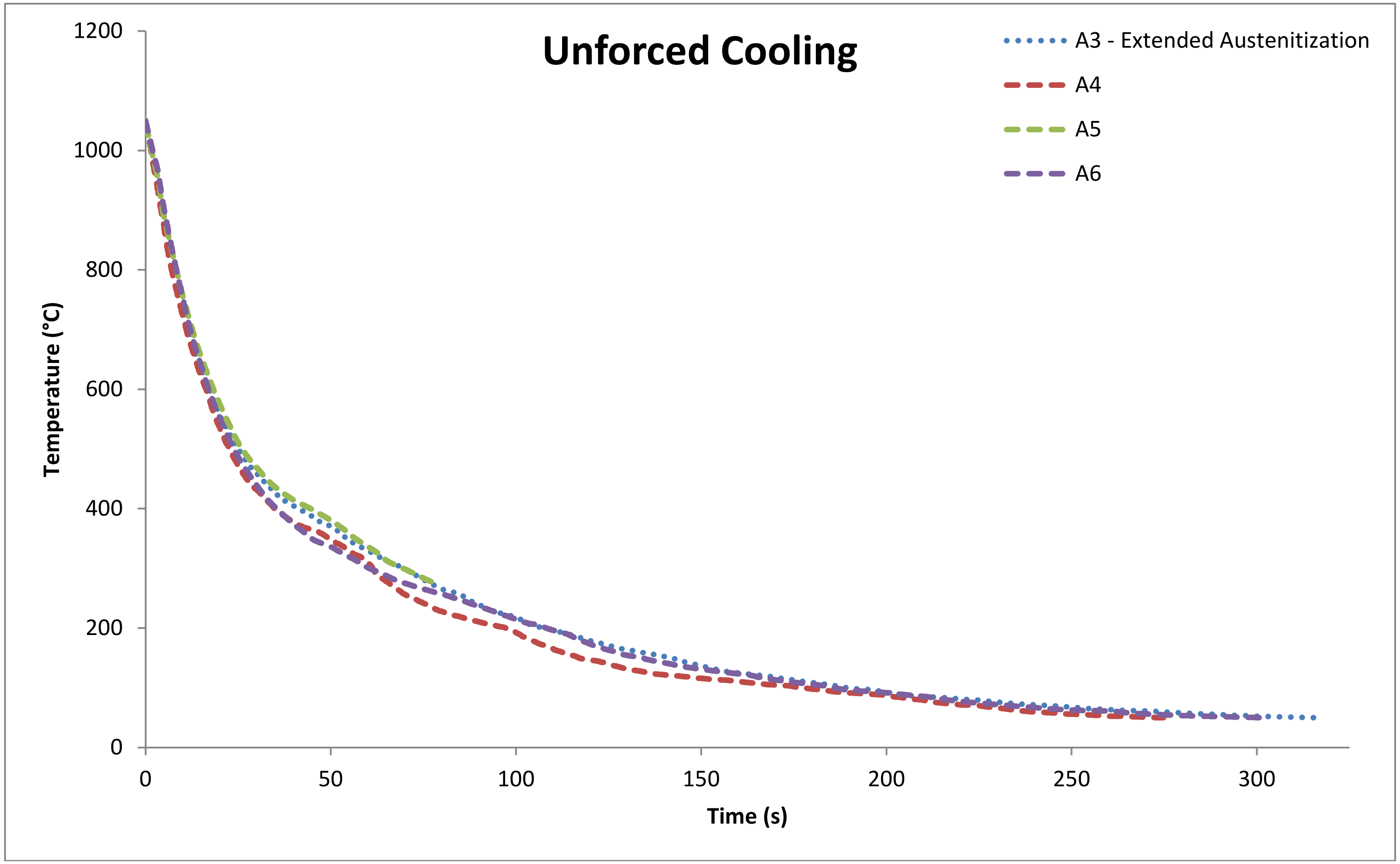

Appendix 4B – LF20-80° Water cooled

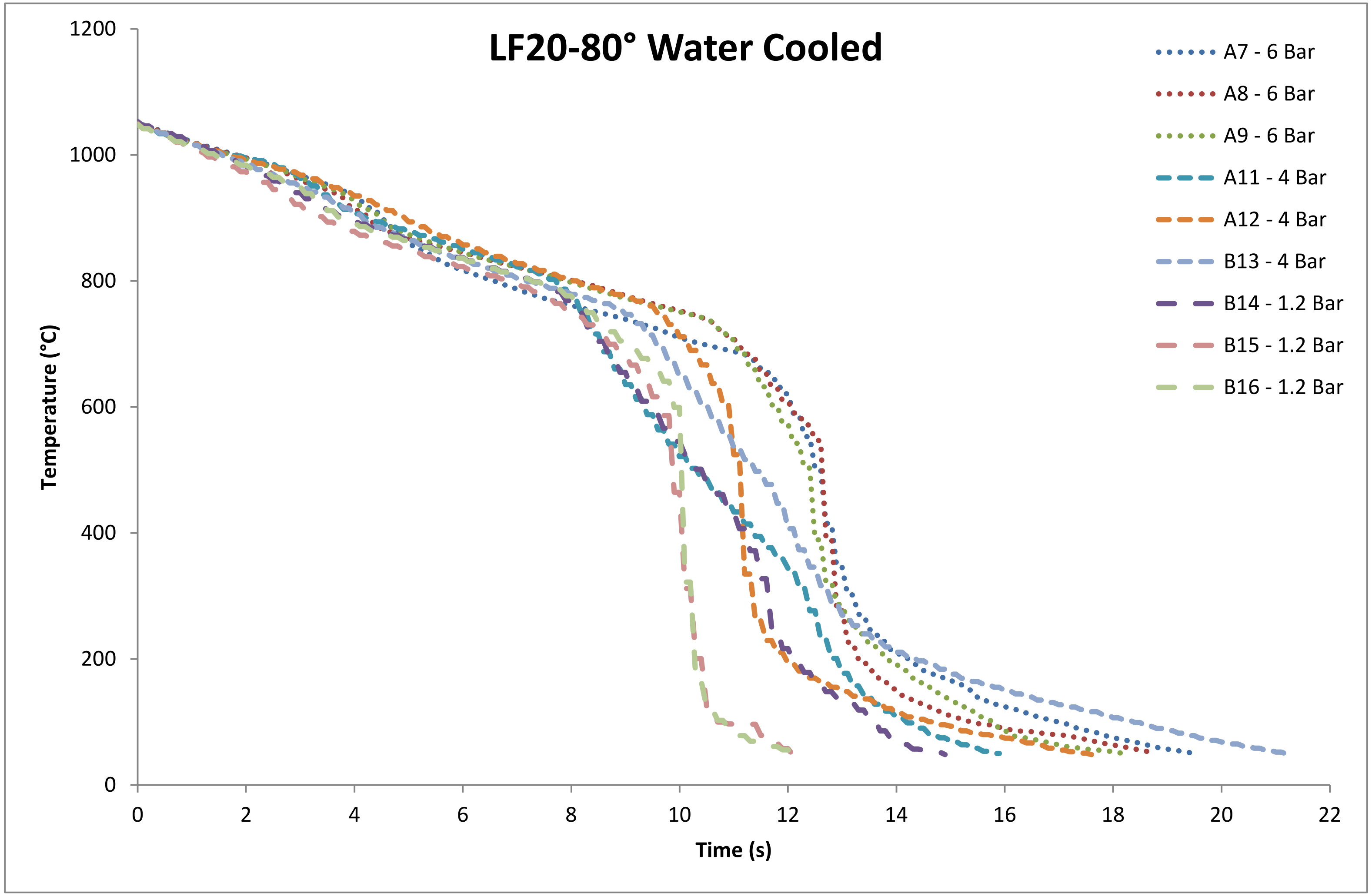

Appendix 4C – CCR 2.0-80° Atomized water cooled

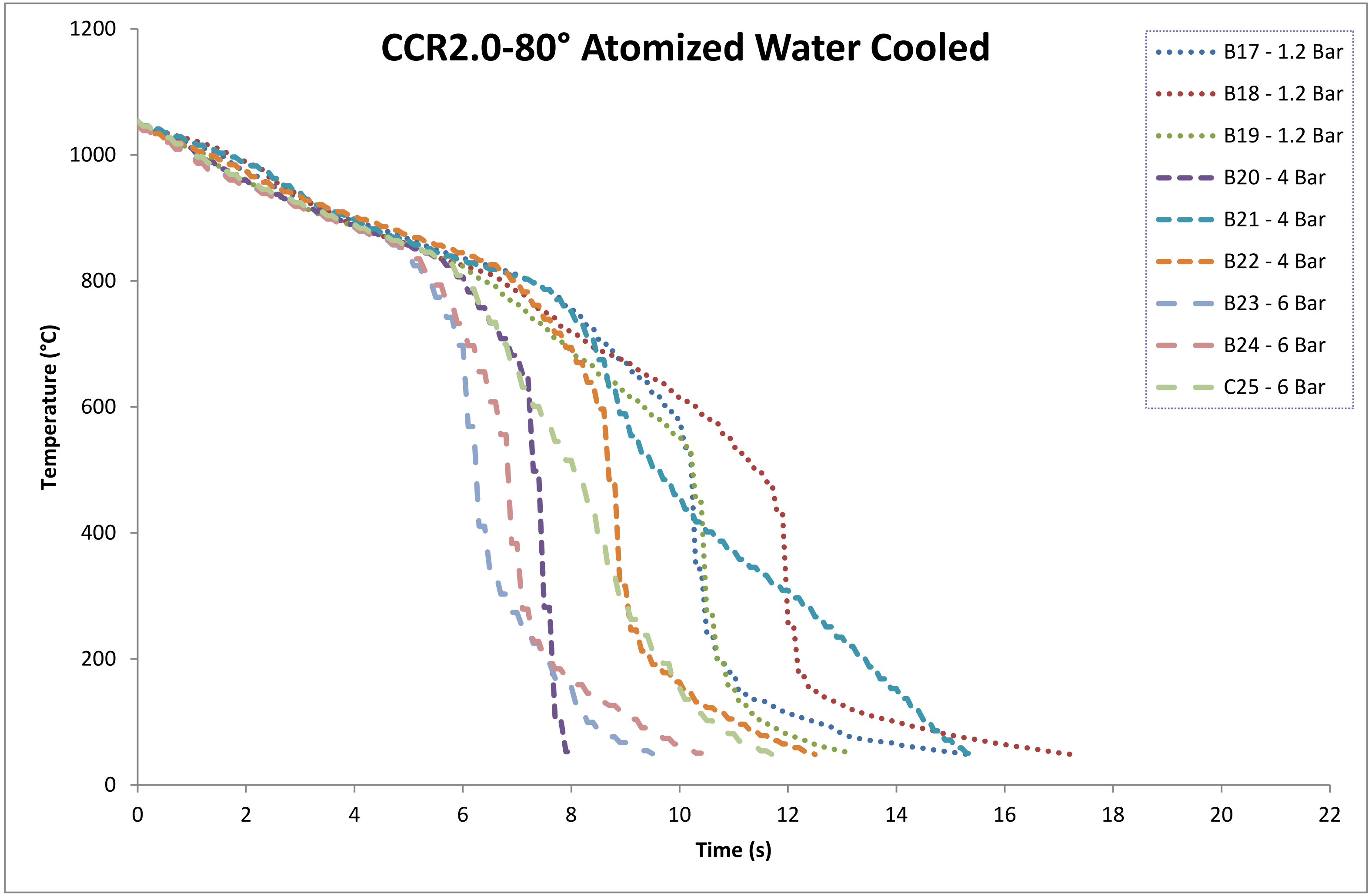

Appendix 4D – LF20-80° Argon cooled

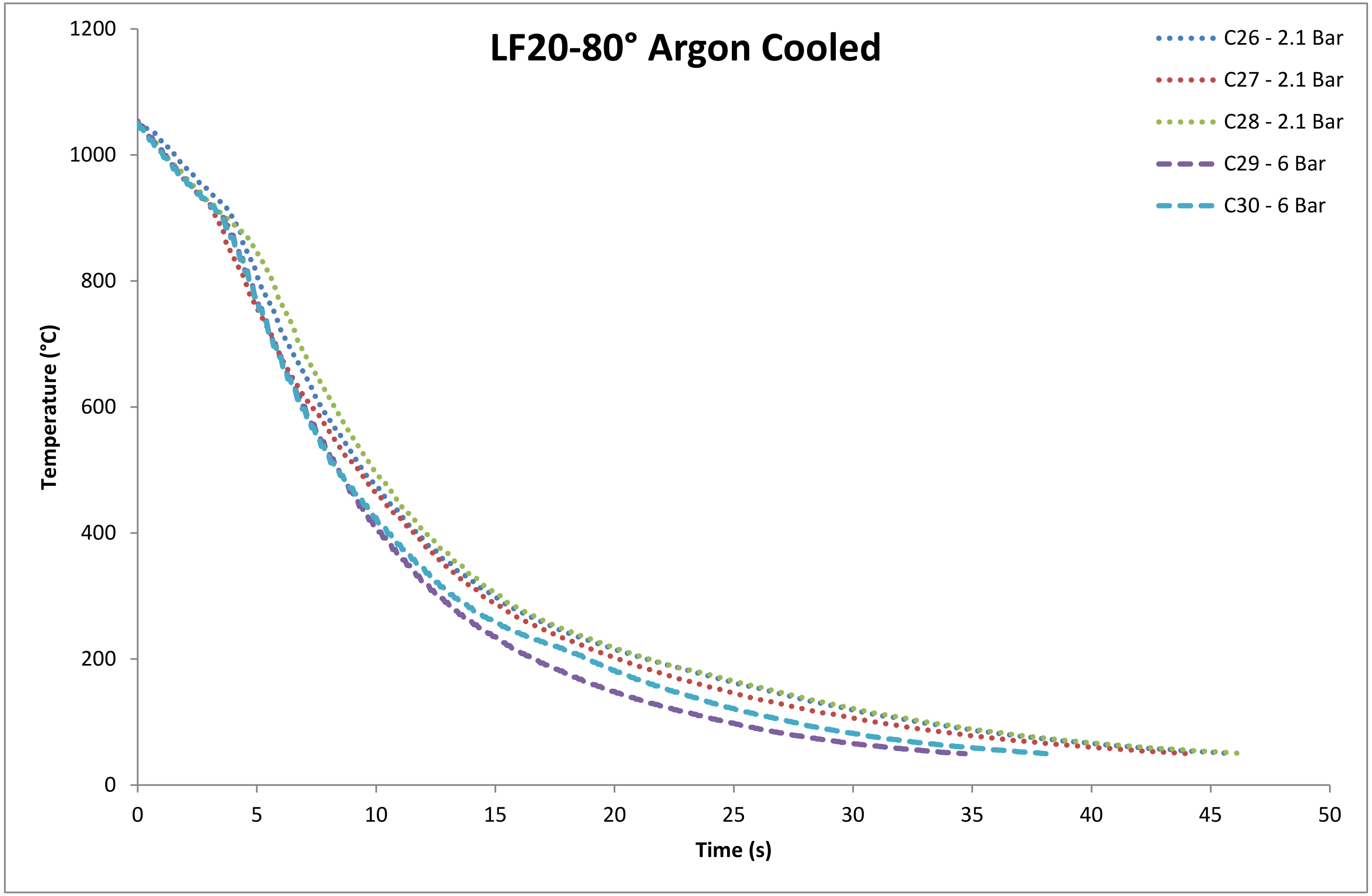

Appendix 4E – Drilled copper pipe argon cooled

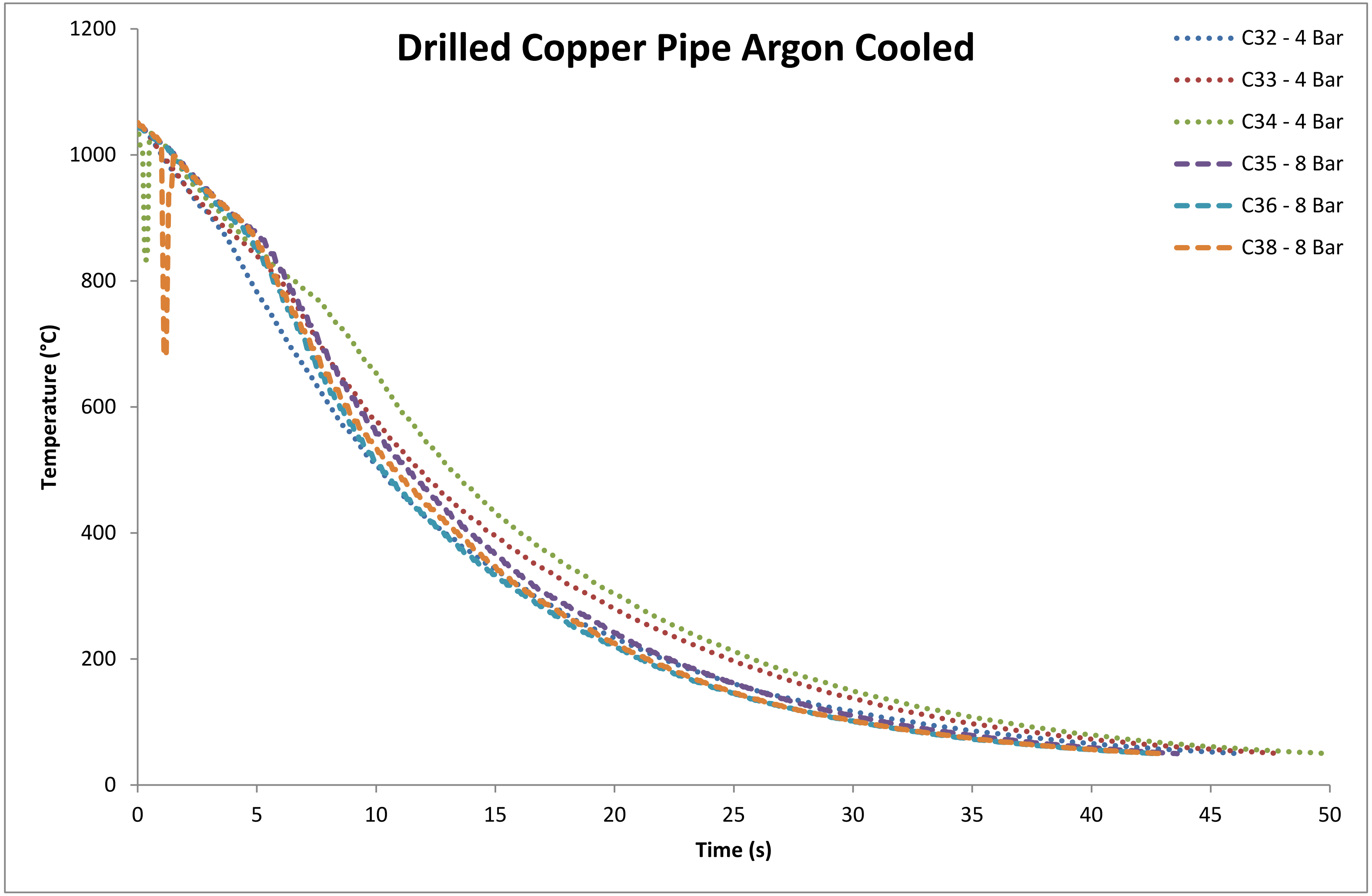

Appendix 5 – Spray nozzle cooling rates

Appendix 5A – Cooling rates from 1050°C to 50°C

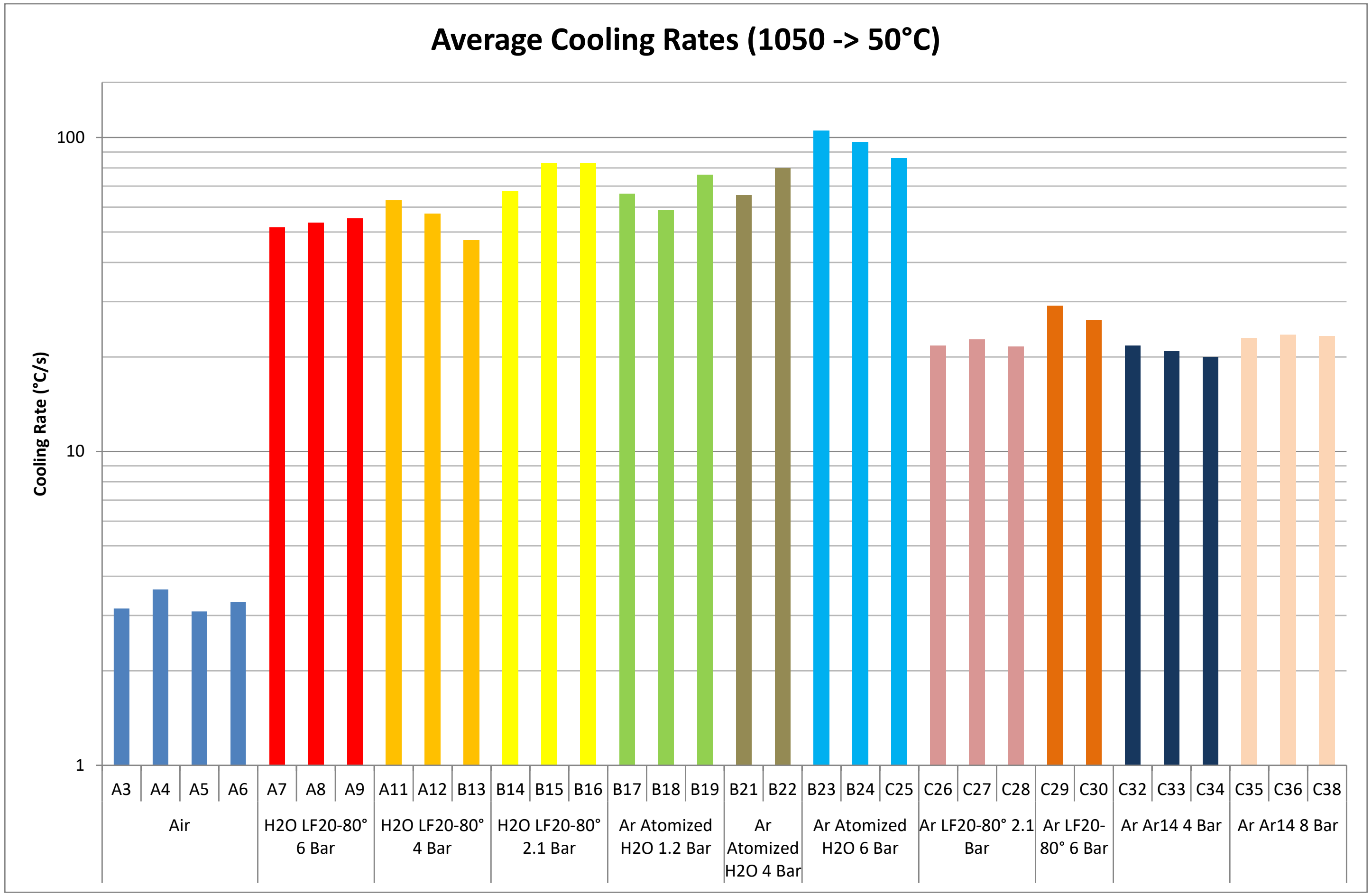

Appendix 5B – Cooling rates from 700°C to 400°C

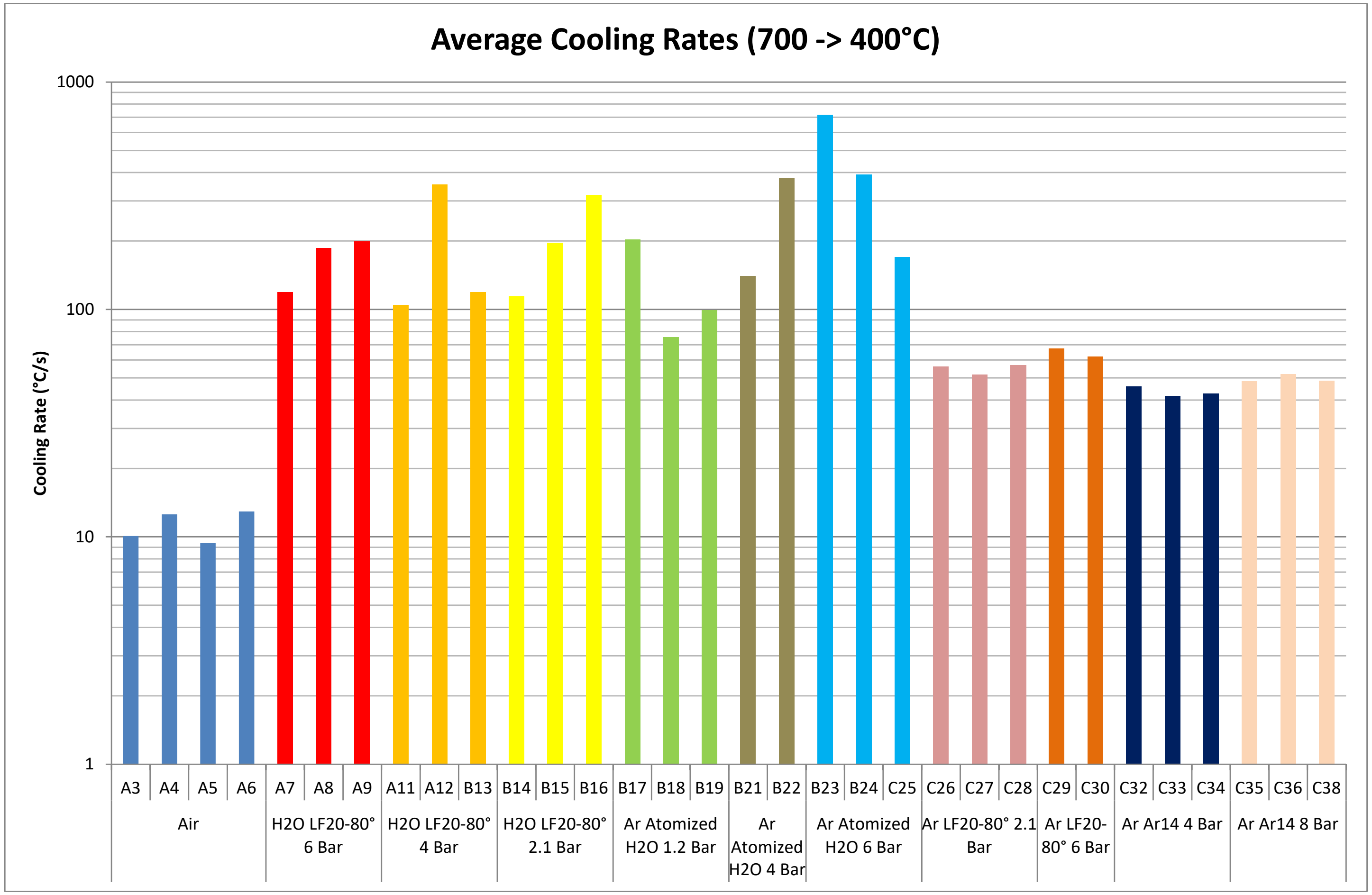

Appendix 6 – Lossless Joule heating rates

Appendix 6A – Lossless heating rates for 4.8 V_{RMS} and 2000 A_{RMS} limits

Alloy	Resistivity (Ω m)	Gauge (m)	Resistance (Ω)	Density (kg/m^3)	Cp (J/kg/°C)	Mass (kg)	C (J/°C)	Current (A)	Voltage (V)	Heating Rate (°C/s)
Steel (25°C)	2.48E-07	1.20E-03	1.55E-03	7.85E+03	4.75E+02	2.83E-02	1.34E+01	2000	3.10	461.88
Steel (900°C)	1.30E-06	1.20E-03	8.13E-03	7.85E+03	4.75E+02	2.83E-02	1.34E+01	591	4.80	211.25
Steel (25°C)	2.48E-07	2.00E-03	9.30E-04	7.85E+03	4.75E+02	4.71E-02	2.24E+01	2000	1.86	166.28
Steel (900°C)	1.30E-06	2.00E-03	4.88E-03	7.85E+03	4.75E+02	4.71E-02	2.24E+01	985	4.80	211.25
Steel (25°C)	2.48E-07	3.00E-03	6.20E-04	7.85E+03	4.75E+02	7.07E-02	3.36E+01	2000	1.24	73.90
Steel (900°C)	1.30E-06	3.00E-03	3.25E-03	7.85E+03	4.75E+02	7.07E-02	3.36E+01	1477	4.80	211.25
Aluminium	2.83E-08	2.00E-03	1.06E-04	2.70E+03	9.00E+02	1.62E-02	1.46E+01	2000	0.21	29.07
Nickel	6.93E-08	2.00E-03	2.60E-04	8.91E+03	4.40E+02	5.34E-02	2.35E+01	2000	0.52	44.20
Niobium	1.52E-07	2.00E-03	5.70E-04	8.57E+03	2.70E+02	5.14E-02	1.39E+01	2000	1.14	164.22
Titanium	1.35E-06	2.00E-03	5.06E-03	4.94E+03	7.10E+02	2.96E-02	2.10E+01	948	4.80	216.26
Lowest Resistance (Al)	2.83E-08	3.00E-03	7.07E-05	2.70E+03	9.00E+02	2.43E-02	2.19E+01	2000	0.14	12.92
Highest Resistance (Ti)	1.35E-06	1.00E-03	1.01E-02	4.94E+03	7.10E+02	1.48E-02	1.05E+01	474	4.80	216.26

Table showing the heating rates for different metals assuming perfect thermal insulation (no heat loss). All samples are 150 mm long and 20 mm wide, with thickness as listed in the table. The maximum output voltage is 4.8 V, but where this would result in a current greater than 2000 A_{RMS}, the voltage is reduced (highlighted cells) to give a current of 2000 A_{RMS}.

Appendix 6B – Lossless heating rates for 4.8 V_{RMS} and 2828 A_{PK} limited by phase angle control

Alloy	Resistivity (Ω m)	Gauge (m)	Resistance (Ω)	Density (kg/m^3)	Cp (J/kg/°C)	Mass (kg)	C (J/°C)	Current (A)	Voltage (V)	Heating Rate (°C/s)
Steel (25°C)	2.48E-07	1.20E-03	1.55E-03	7.85E+03	4.75E+02	2.83E-02	1.34E+01	1305	2.02	196.65
Steel (900°C)	1.30E-06	1.20E-03	8.13E-03	7.85E+03	4.75E+02	2.83E-02	1.34E+01	591	4.80	211.41
Steel (25°C)	2.48E-07	2.00E-03	9.30E-04	7.85E+03	4.75E+02	4.71E-02	2.24E+01	948	0.88	37.36
Steel (900°C)	1.30E-06	2.00E-03	4.88E-03	7.85E+03	4.75E+02	4.71E-02	2.24E+01	985	4.80	211.41
Steel (25°C)	2.48E-07	3.00E-03	6.20E-04	7.85E+03	4.75E+02	7.07E-02	3.36E+01	853	0.53	13.44
Steel (900°C)	1.30E-06	3.00E-03	3.25E-03	7.85E+03	4.75E+02	7.07E-02	3.36E+01	1477	4.80	211.27
Aluminium	2.83E-08	2.00E-03	1.06E-04	2.70E+03	9.00E+02	1.62E-02	1.46E+01	757	0.08	4.17
Nickel	6.93E-08	2.00E-03	2.60E-04	8.91E+03	4.40E+02	5.34E-02	2.35E+01	779	0.20	6.71
Niobium	1.52E-07	2.00E-03	5.70E-04	8.57E+03	2.70E+02	5.14E-02	1.39E+01	841	0.48	29.04
Titanium	1.35E-06	2.00E-03	5.06E-03	4.94E+03	7.10E+02	2.96E-02	2.10E+01	948	4.80	216.19
Lowest Resistance (Al)	2.83E-08	3.00E-03	7.07E-05	2.70E+03	9.00E+02	2.43E-02	2.19E+01	752	0.05	1.83
Highest Resistance (Ti)	1.35E-06	1.00E-03	1.01E-02	4.94E+03	7.10E+02	1.48E-02	1.05E+01	474	4.80	216.19

Table showing the heating rates for different metals assuming perfect thermal insulation (no heat loss). All samples are 150 mm long and 20 mm wide, with thickness as listed in the table. The maximum output voltage is 4.8 V, but where this would result in a peak instantaneous current greater than 2828 A (highlighted cells), the angle of conduction is reduced until the peak instantaneous current is limited to 2828 A. The current column displays the RMS value of this phase angle controlled type current.

Appendix 6C – Lossless heating rates for 4.8 V_{RMS} and 2828 A_{PK} with symmetric turn-on

Alloy	Resistivity (Ω m)	Gauge (m)	Resistance (Ω)	Density (kg/m^3)	Cp (J/kg/°C)	Mass (kg)	C (J/°C)	Current (A)	Voltage (V)	Heating Rate (°C/s)
Steel (25°C)	2.48E-07	1.20E-03	1.55E-03	7.85E+03	4.75E+02	2.83E-02	1.34E+01	1836	2.85	389.23
Steel (900°C)	1.30E-06	1.20E-03	8.13E-03	7.85E+03	4.75E+02	2.83E-02	1.34E+01	591	4.80	211.41
Steel (25°C)	2.48E-07	2.00E-03	9.30E-04	7.85E+03	4.75E+02	4.71E-02	2.24E+01	1409	1.31	82.53
Steel (900°C)	1.30E-06	2.00E-03	4.88E-03	7.85E+03	4.75E+02	4.71E-02	2.24E+01	985	4.80	211.41
Steel (25°C)	2.48E-07	3.00E-03	6.20E-04	7.85E+03	4.75E+02	7.07E-02	3.36E+01	1318	0.82	32.09
Steel (900°C)	1.30E-06	3.00E-03	3.25E-03	7.85E+03	4.75E+02	7.07E-02	3.36E+01	1477	4.80	211.27
Aluminium	2.83E-08	2.00E-03	1.06E-04	2.70E+03	9.00E+02	1.62E-02	1.46E+01	1271	0.13	11.74
Nickel	6.93E-08	2.00E-03	2.60E-04	8.91E+03	4.40E+02	5.34E-02	2.35E+01	1273	0.33	17.91
Niobium	1.52E-07	2.00E-03	5.70E-04	8.57E+03	2.70E+02	5.14E-02	1.39E+01	1308	0.75	70.24
Titanium	1.35E-06	2.00E-03	5.06E-03	4.94E+03	7.10E+02	2.96E-02	2.10E+01	948	4.80	216.19
Lowest Resistance (Al)	2.83E-08	3.00E-03	7.07E-05	2.70E+03	9.00E+02	2.43E-02	2.19E+01	1271	0.09	5.22
Highest Resistance (Ti)	1.35E-06	1.00E-03	1.01E-02	4.94E+03	7.10E+02	1.48E-02	1.05E+01	474	4.80	216.19

Table showing the heating rates for different metals assuming perfect thermal insulation (no heat loss). All samples are 150 mm long and 20 mm wide, with thickness as listed in the table. The maximum output voltage is 4.8 V, but where this would result in a peak instantaneous current greater than 2828 A (highlighted cells), the angle of conduction is reduced until the peak instantaneous current is limited to 2828 A. The current is then turned on at 180° less the turn-off angle, giving a waveform that is symmetric about 90°. The current column displays the RMS value of this phase angle controlled type current.

Appendix 7 – Modelled heat losses and calculated heating rates

Maximum temperature (°C)	Average temperature (°C)	Conductive heat loss (W)	Convective heat loss (W)	Radiative heat loss (W)	Total heat loss (W)	Average resistivity (Ω m)	Sample resistance (Ω)	Joule heating (W)	Heating rate (°C / s)
20.2E+0	20.1E+0	307.8E-6	1.9E-3	2.1E-3	4.3E-3	242.3E-9	908.7E-6	3.63E+03	162.3
102.5E+0	94.6E+0	183.4E-3	5.0E+0	2.1E+0	7.3E+0	331.7E-9	1.2E-3	4.98E+03	222.1
193.3E+0	180.2E+0	353.8E-3	12.9E+0	6.8E+0	20.0E+0	434.4E-9	1.6E-3	6.52E+03	290.9
299.0E+0	278.3E+0	514.8E-3	23.1E+0	16.9E+0	40.5E+0	552.2E-9	2.1E-3	8.28E+03	369.8
420.5E+0	390.2E+0	670.0E-3	35.8E+0	37.7E+0	74.2E+0	686.5E-9	2.6E-3	8.95E+03	399.6
560.8E+0	518.1E+0	818.2E-3	51.2E+0	79.3E+0	131.3E+0	839.9E-9	3.1E-3	7.32E+03	326.6
720.9E+0	663.0E+0	959.9E-3	69.5E+0	159.6E+0	230.1E+0	1.0E-6	3.8E-3	6.06E+03	270.5
903.1E+0	827.1E+0	1.1E+0	91.0E+0	310.8E+0	403.0E+0	1.2E-6	4.5E-3	5.07E+03	226.5
1.1E+3	1.0E+3	1.2E+0	116.2E+0	589.9E+0	707.3E+0	1.4E-6	5.4E-3	4.29E+03	191.3
1.3E+3	1.2E+3	1.4E+0	145.5E+0	1.1E+3	1.2E+3	1.7E-6	6.3E-3	3.64E+03	162.7
1.6E+3	1.5E+3	1.5E+0	179.5E+0	2.0E+3	2.2E+3	2.0E-6	7.4E-3	3.12E+03	139.3

The heat loss by conduction, convection, and radiation for a 2mm thick steel sample with emissivity of 0.5 as calculated using COMSOL Multiphysics. The heat capacity of the sample is assumed to be a constant 22.4 J/°C. The Joule heating rate is calculated assuming the electrical power is limited to a maximum current of 2000 A when the sample resistance is less than or equal to 2.4 mΩ, and is limited by a maximum voltage of 4.8 V when the sample resistance is greater than 2.4 mΩ.

Appendix 8 – Sliding contacts compression modelling

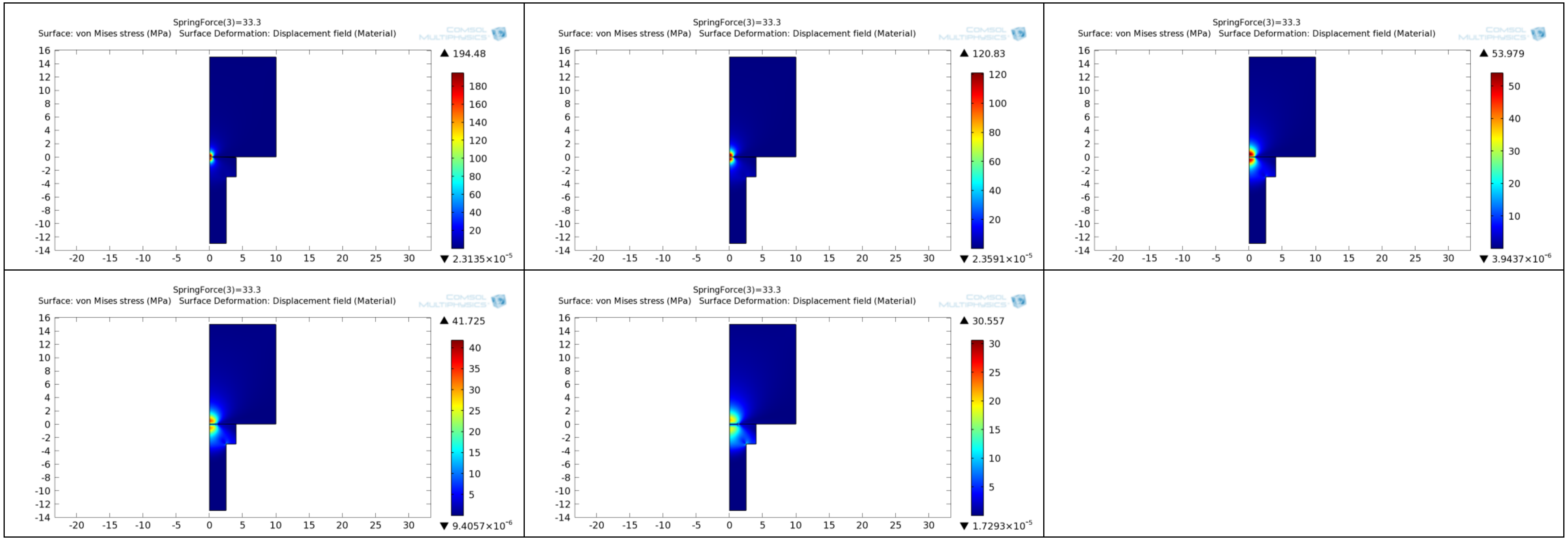

COMSOL Multiphysics 2D axisymmetric finite element model to show the elastic behaviour when a copper electrode with a contact area that is a spheric section is compressed into a 304 stainless steel block. The top row from left to right shows models for electrodes with spheric sections of diameter 150, 300, 1000 mm; the bottom row spheric sections have diameters 2000 mm (left) and 4000 mm (right).

Appendix 9 – Sliding contacts test pieces

Appendix 9A – Copper electrode with spheric section contact region

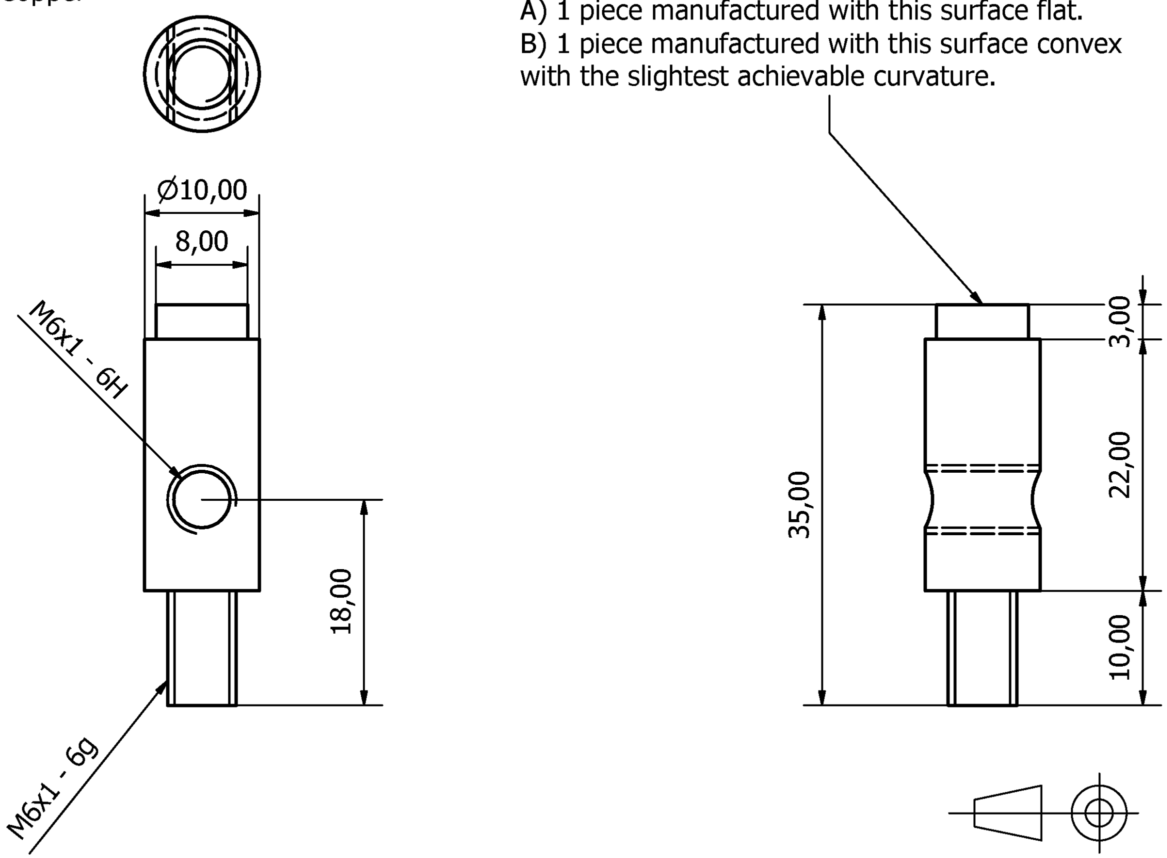

Oxygen Free Copper

A) 1 piece manufactured with this surface flat.
B) 1 piece manufactured with this surface convex with the slightest achievable curvature.

Appendix 9B – Stainless steel disc

304 Stainless Steel

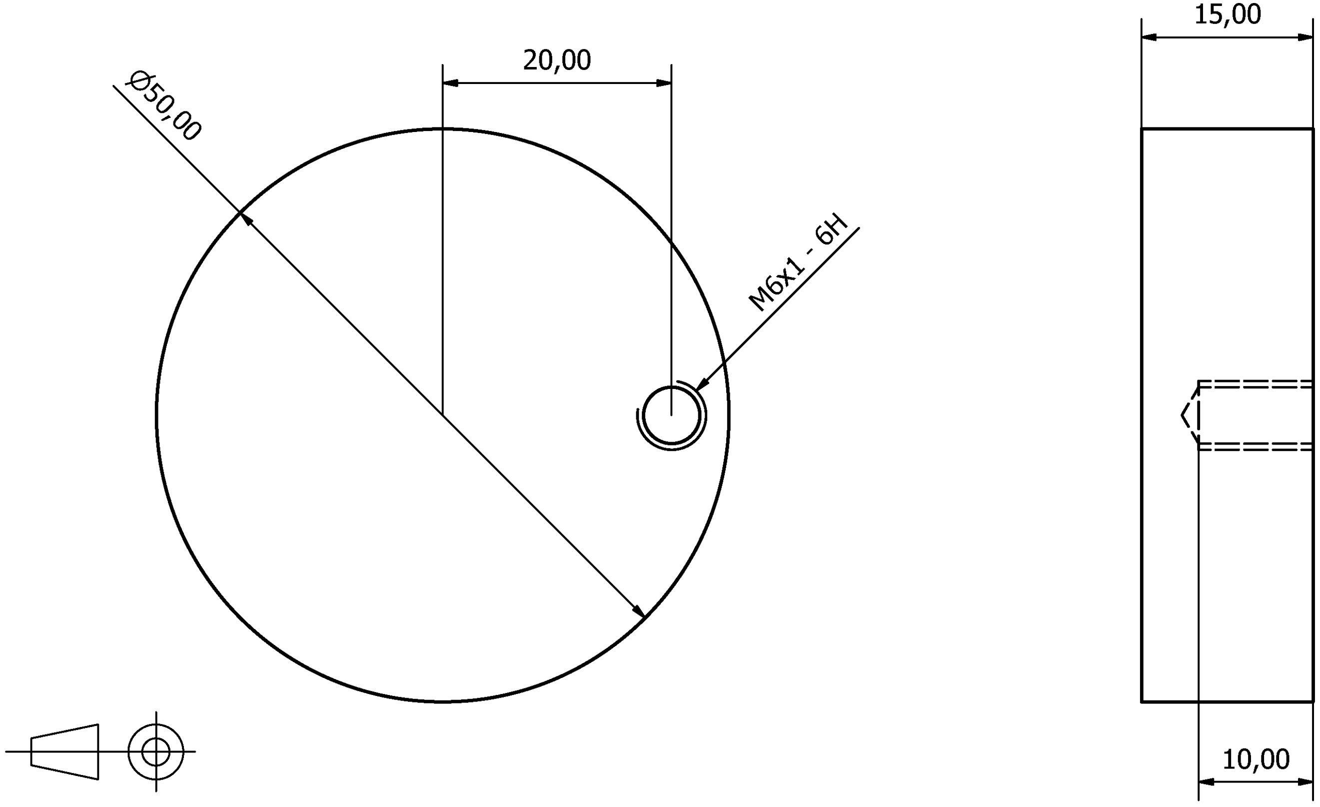

Appendix 9C – PTFE Electrode holder

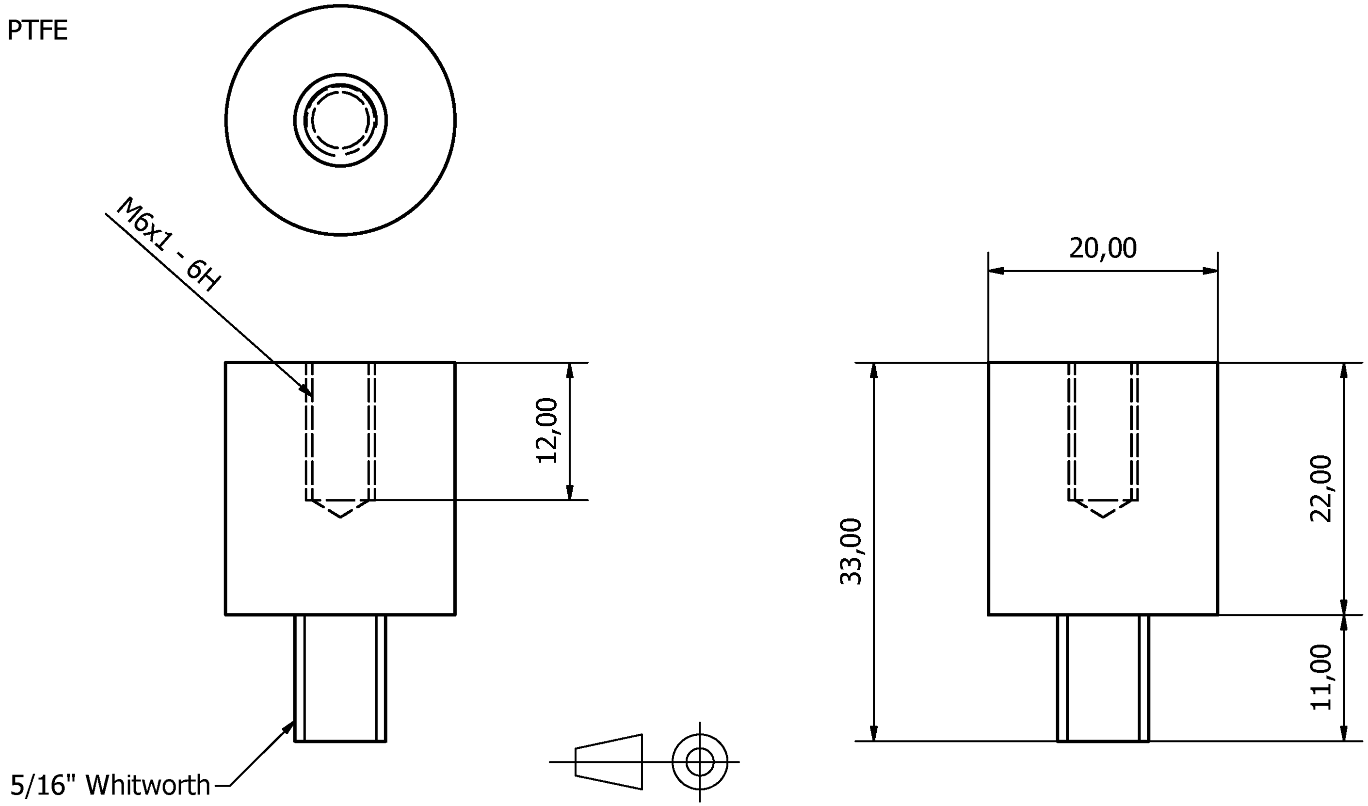

Appendix 10 – Electrodes

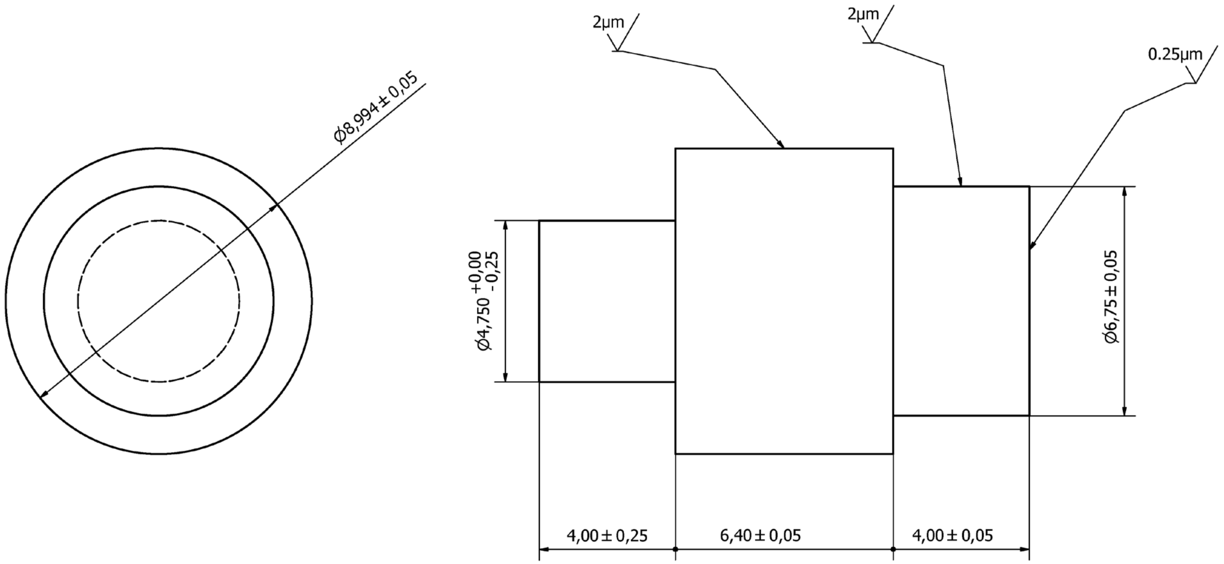

Appendix 11 – Electrode holders

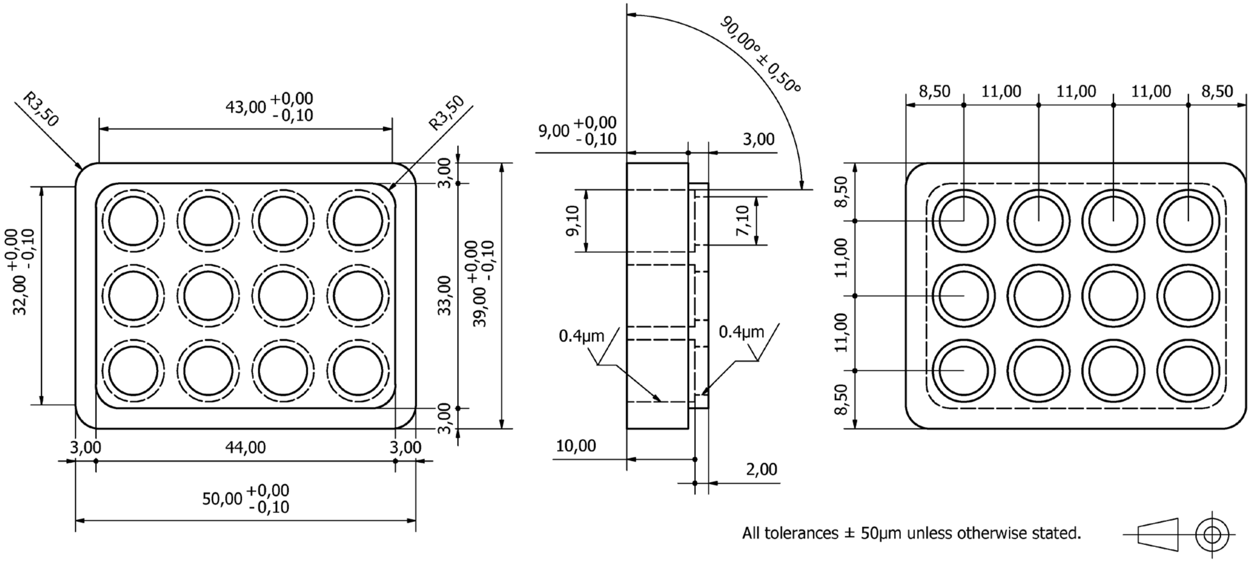

All tolerances ± 50μm unless otherwise stated.

Appendix 12 – High current feedthrough (vacuum side)

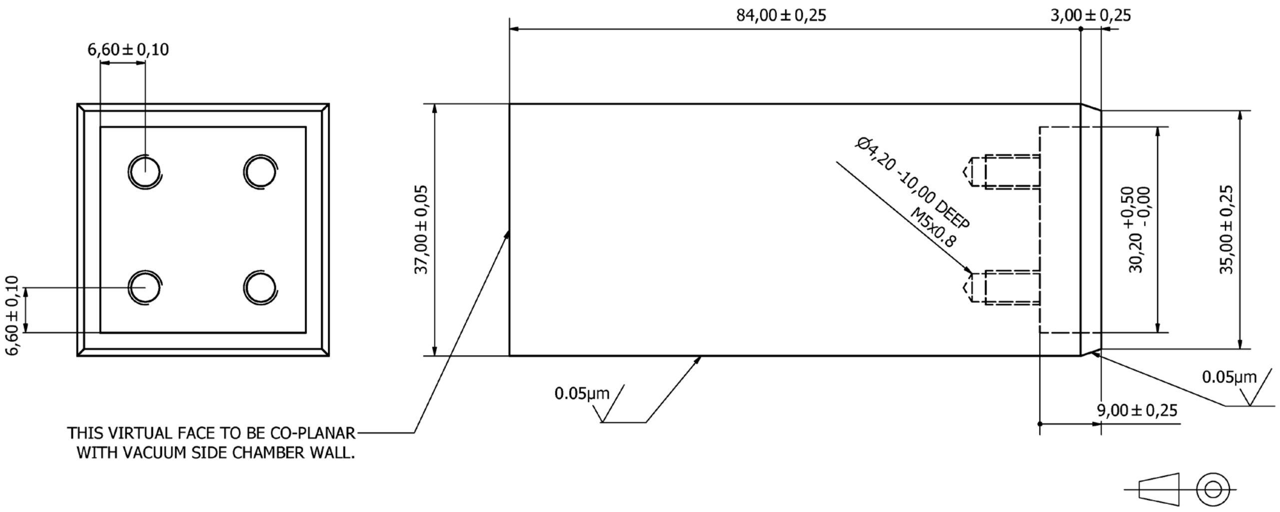

THIS VIRTUAL FACE TO BE CO-PLANAR
WITH VACUUM SIDE CHAMBER WALL.

Appendix 13 – Sample clamp cooling FEM model results

Water Inlet	Total Heat Flux Water In (W)	Total Heat Flux Water Out (W)	Total Heat Flux Sample (W)	Water Flow Rate In (m3/s)	Water Flow Rate In (l/min)	Water Flow Rate Out (m3/s)	Water Flow Rate Out (l/min)	Mean Water Velocity In (m/s)	Mean Water Velocity Out (m/s)	Mean Water Temperature In (K)	Mean Water Temperature Out (K)	Mean Water Pressure In (Pa)	Mean Water Pressure Out (Pa)
Pressure 400000 Pa	1038.96	-1319.76	280.487	0.000134198	8.05188	0.000134538	8.07228	10.8567	10.7922	300	300.506	400000	0
Pressure 400000 Pa	1594.37	-1877.83	284.098	0.000205981	12.35886	0.000206639	12.39834	16.6603	16.7058	300	300.341	400000	0
Pressure 200000 Pa	712.286	-992.685	280.029	9.20E-05	5.52006	9.22E-05	5.53434	7.44314	7.46242	300	300.733	200000	0
Pressure 200000 Pa	1121.4	-1404.6	283.254	0.000144878	8.69268	0.000145345	8.7207	11.718	11.7513	300	300.484	200000	0
Velocity 1 m/s	96.0872	-371.057	274.829	1.24E-05	0.74163	1.24E-05	0.741636	1	0.986065	300	305.414	5540.75	0
Velocity 1 m/s	95.9475	-369.976	274.228	1.24E-05	0.741624	1.24E-05	0.742608	1	1.00003	300	305.418	1209.96	0

Appendix 14 – Clamp cooling circuit modelling

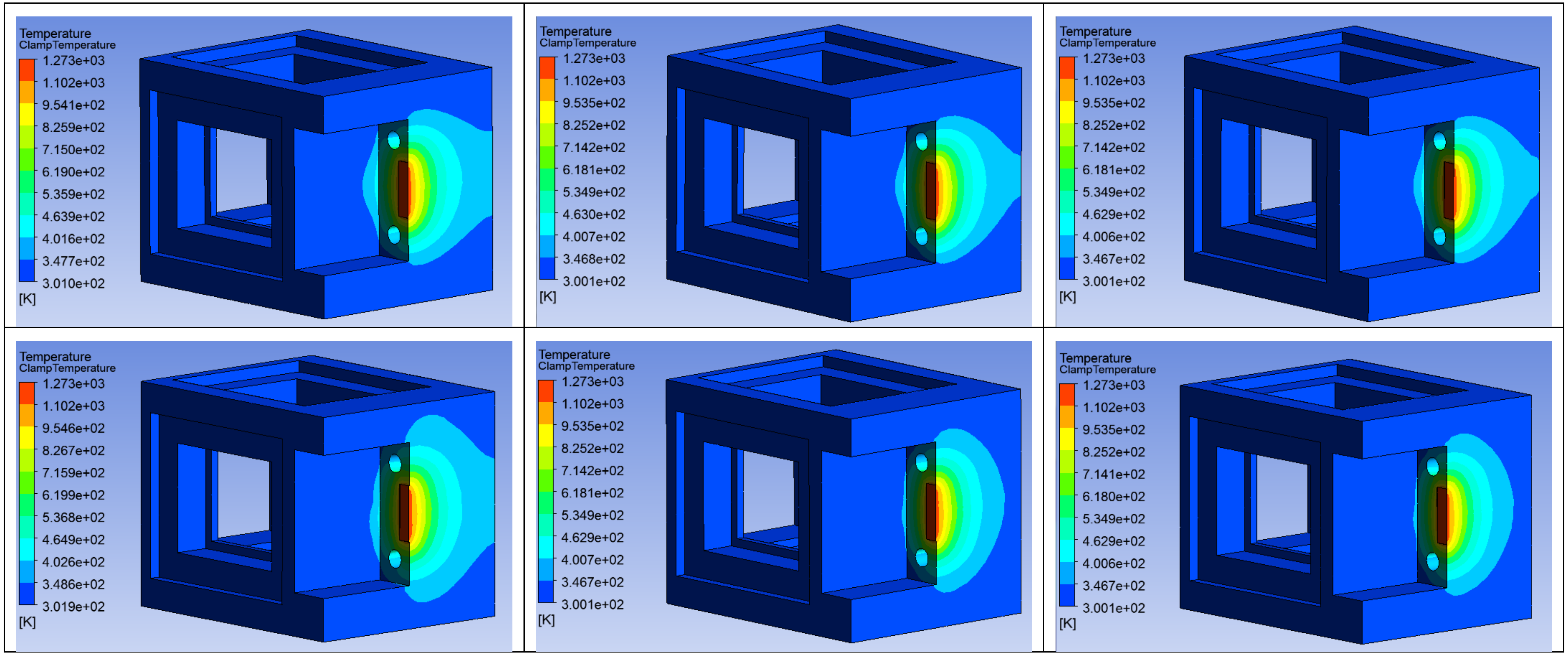

ANSYS Fluent finite element model to compare the cooling power of two different cooling circuit layouts. The top row have a complex internal cooling circuit that wraps around the feedthrough hole and is close to the sample contact. The bottom row use a simpler cooling circuit that is only in the region of the sample contact and can be made by a combination of drilling and welding. Left column: coolant flow rate of 1 m/s. Centre column: fluid pressure drop of 2 bar. Right column: fluid pressure drop of 4 bar.

Appendix 15 – Clamp body (left hand side)

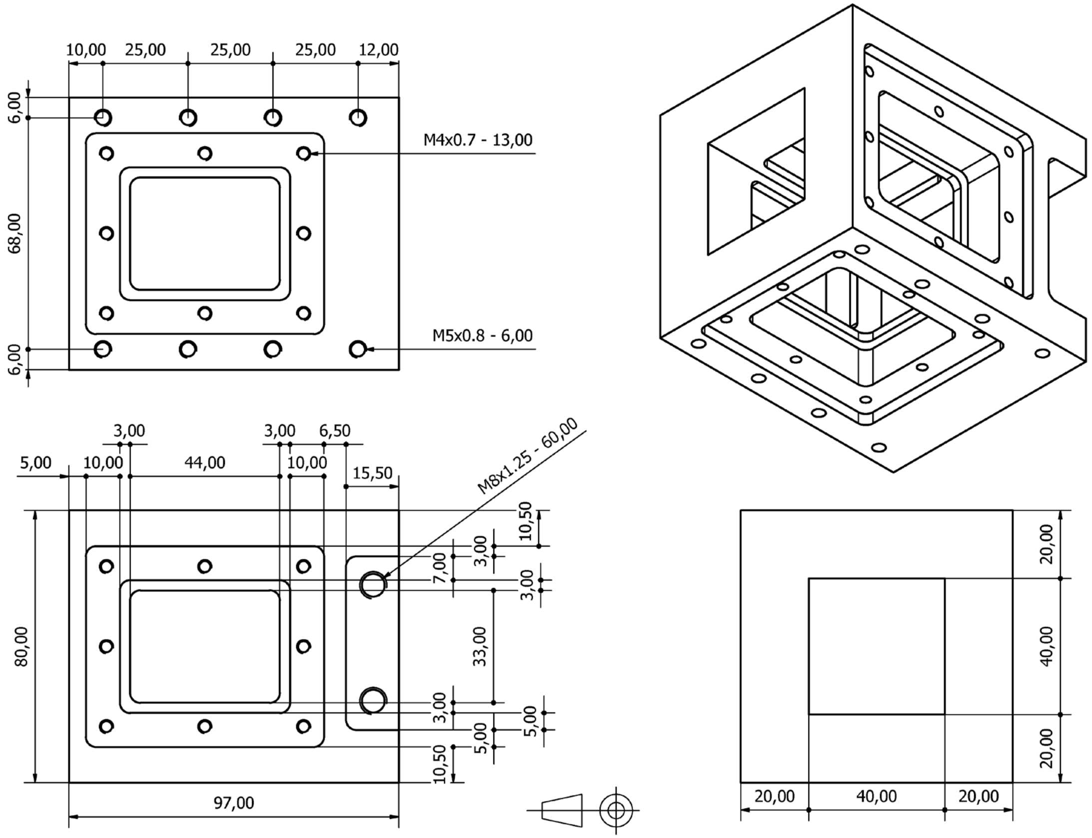

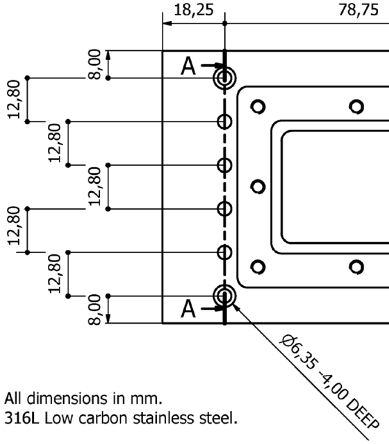

All dimensions in mm.
316L Low carbon stainless steel.

A-A (1 : 1)

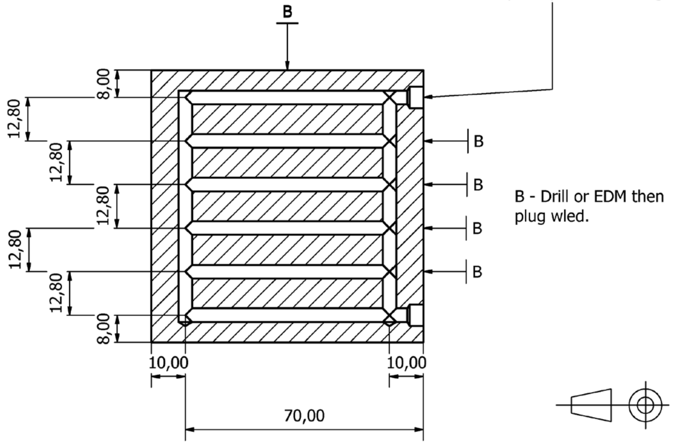

Swagelok VCO Male Tube Weld
SS-4-VCO-3-4MTW to be
welded or brazed here and at
the equivalent fitting below.
Female VCO SS-4-VCO-4
must be in place prior to welding.

B - Drill or EDM then
plug wled.

Appendix 16 – Electrode retaining cap

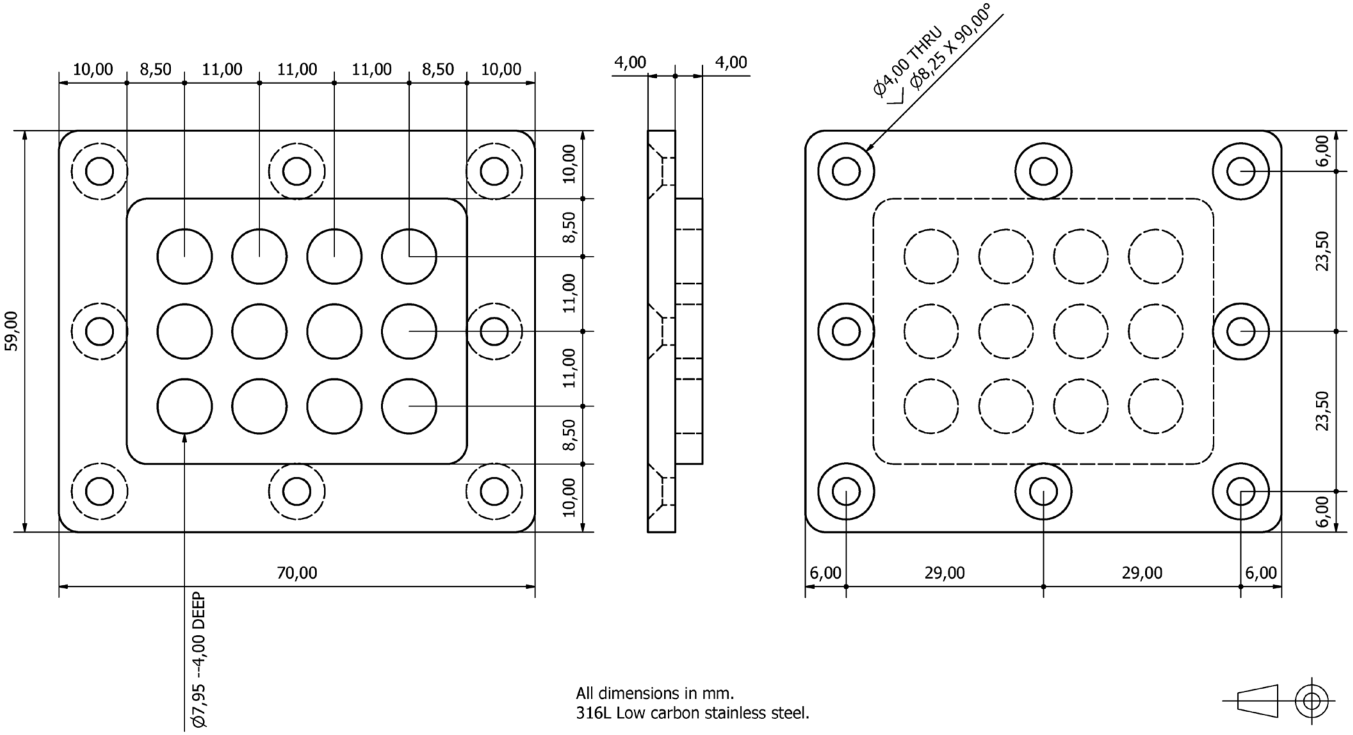

All dimensions in mm.
316L Low carbon stainless steel.

Appendix 17 – Vacuum chamber engineering drawings

Appendix 17A – Front view

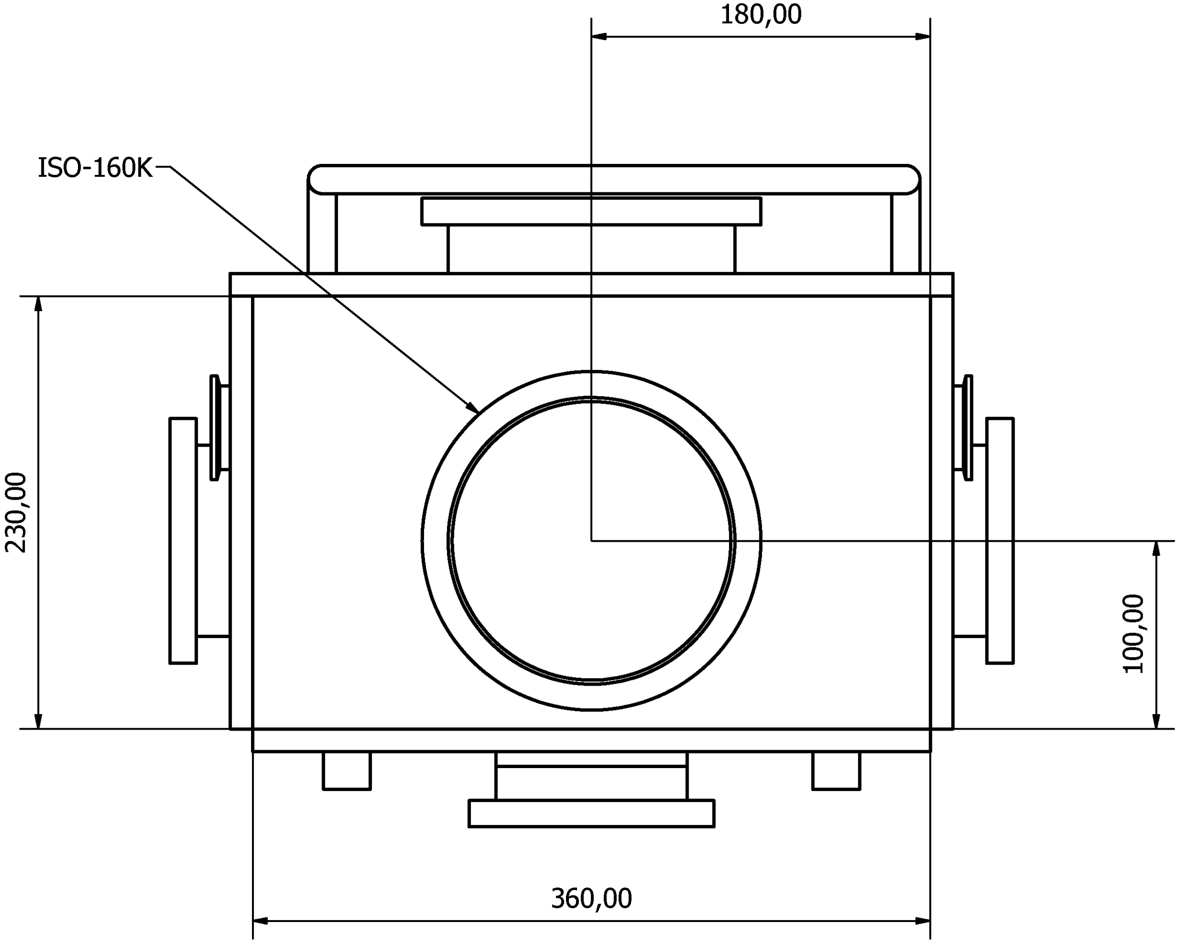

Appendix 17B – Left hand side view

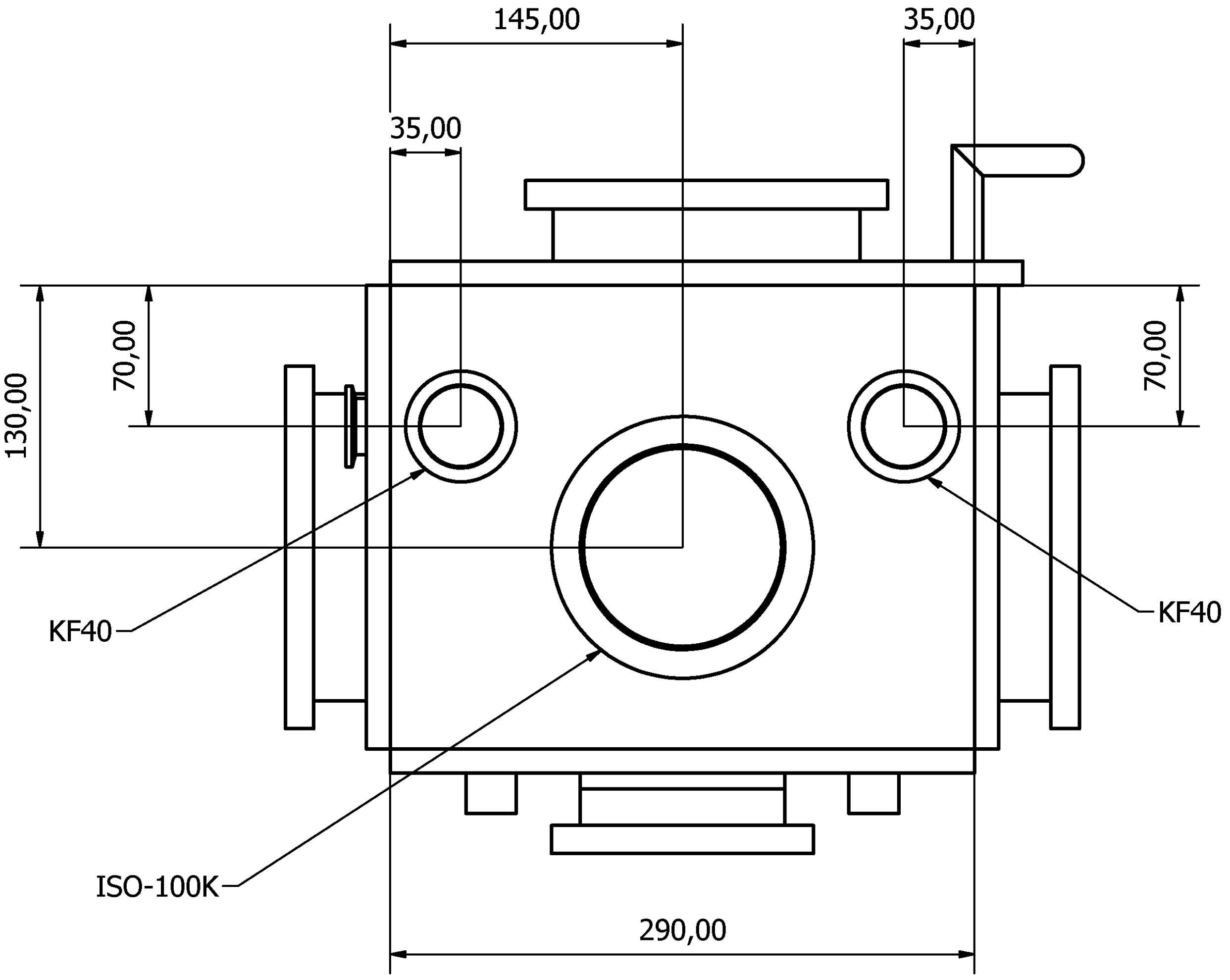

Appendix 17C – Back view

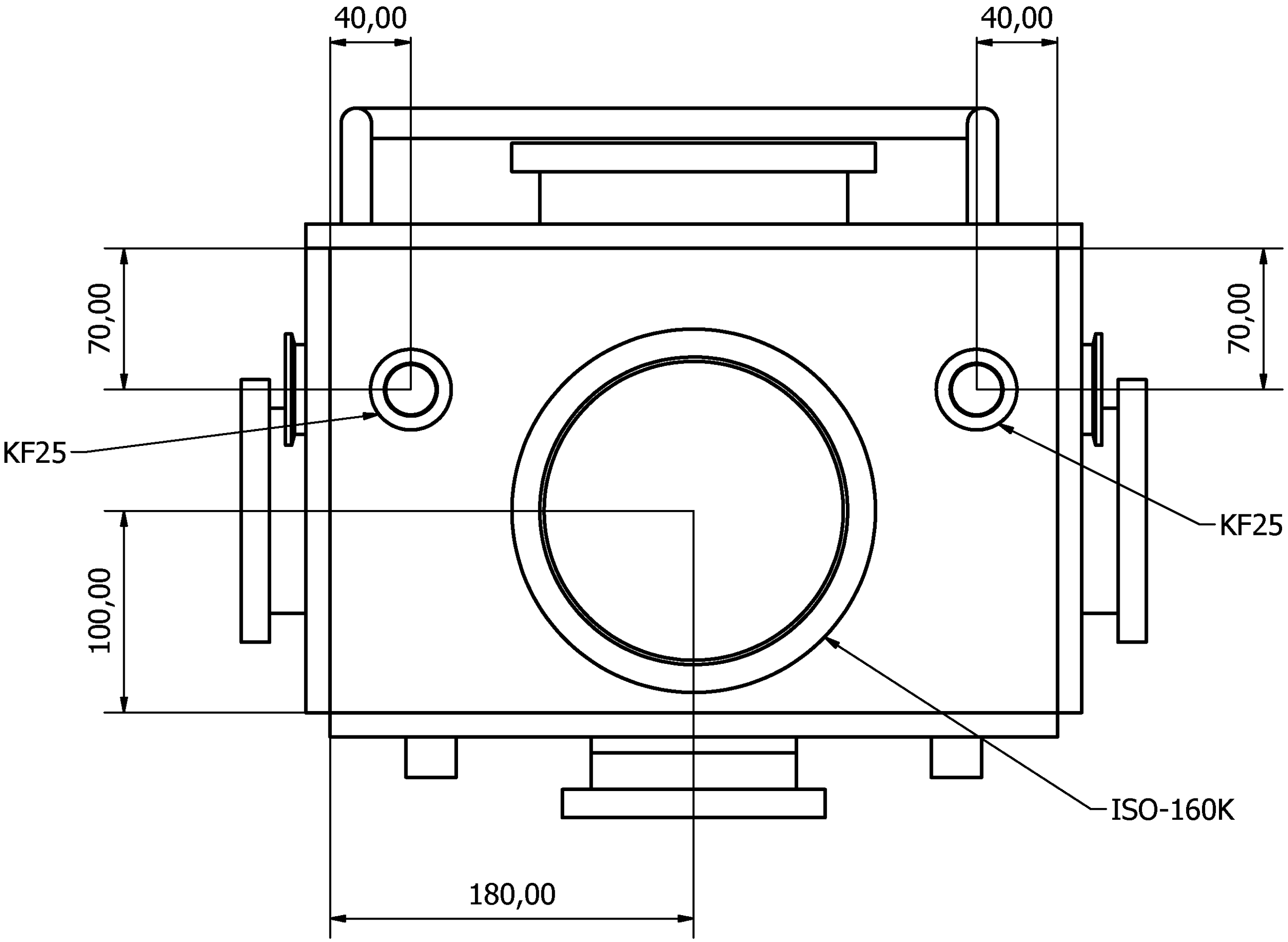

Appendix 17D – Right hand side view

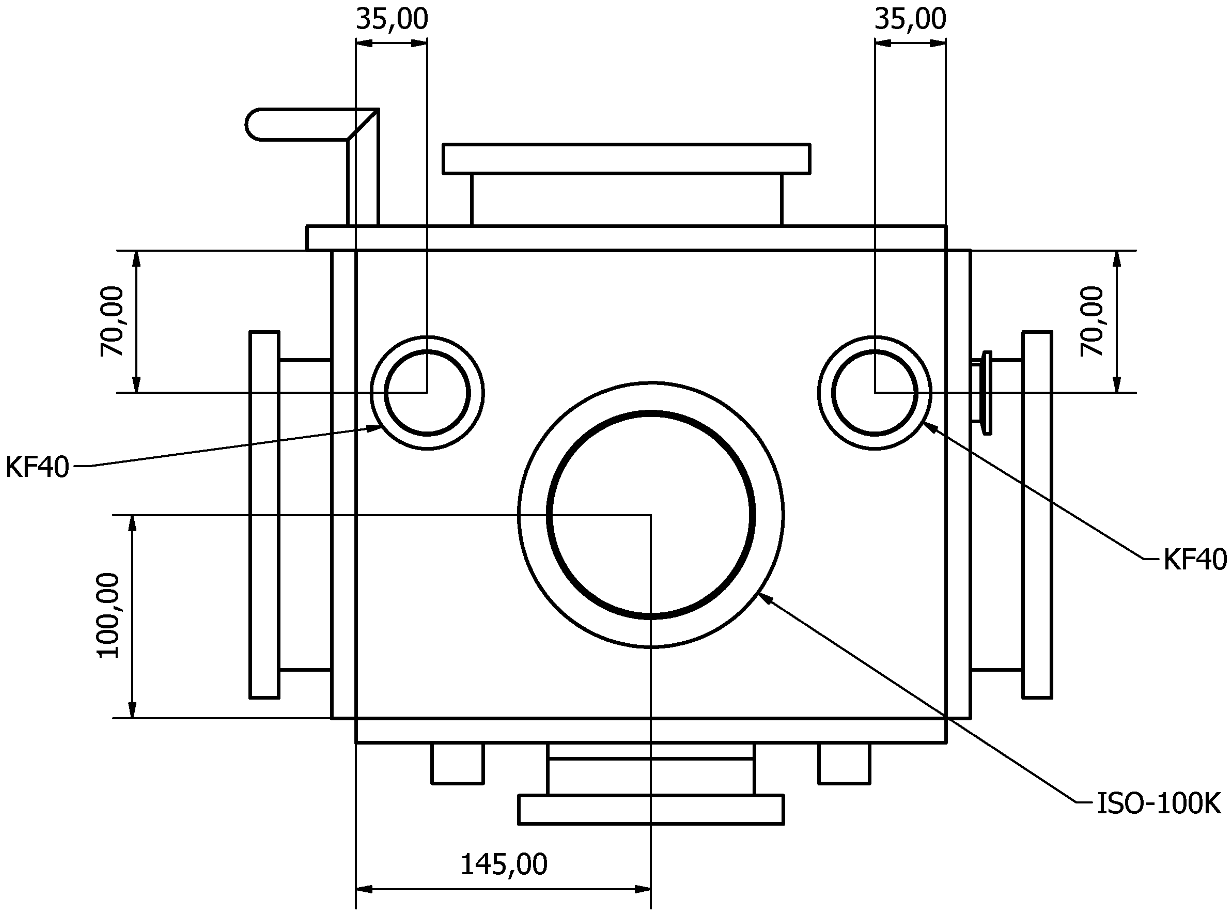

Appendix 17E – Top view

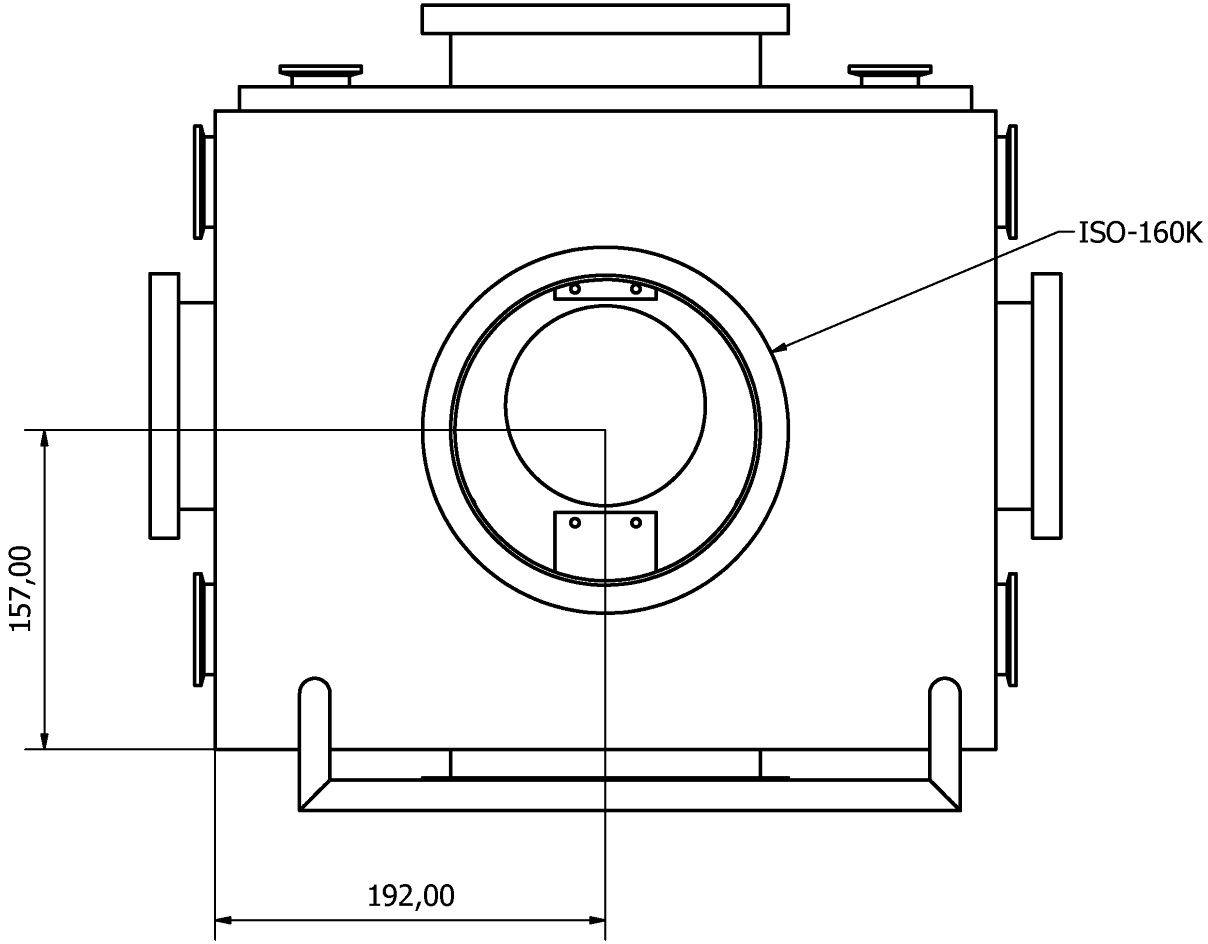

Appendix 17F – Bottom view

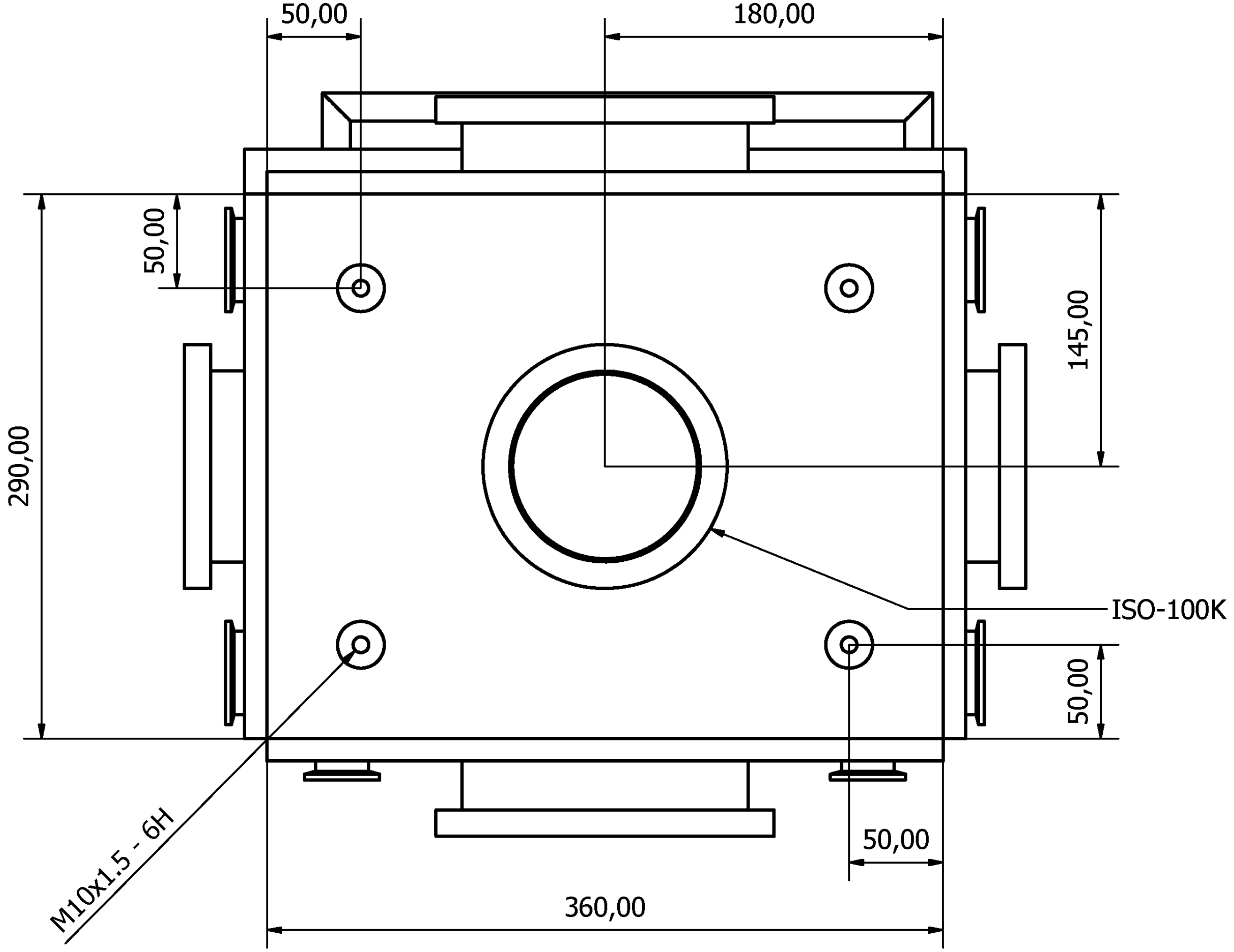

Appendix 17G – Bottom viewed from inside

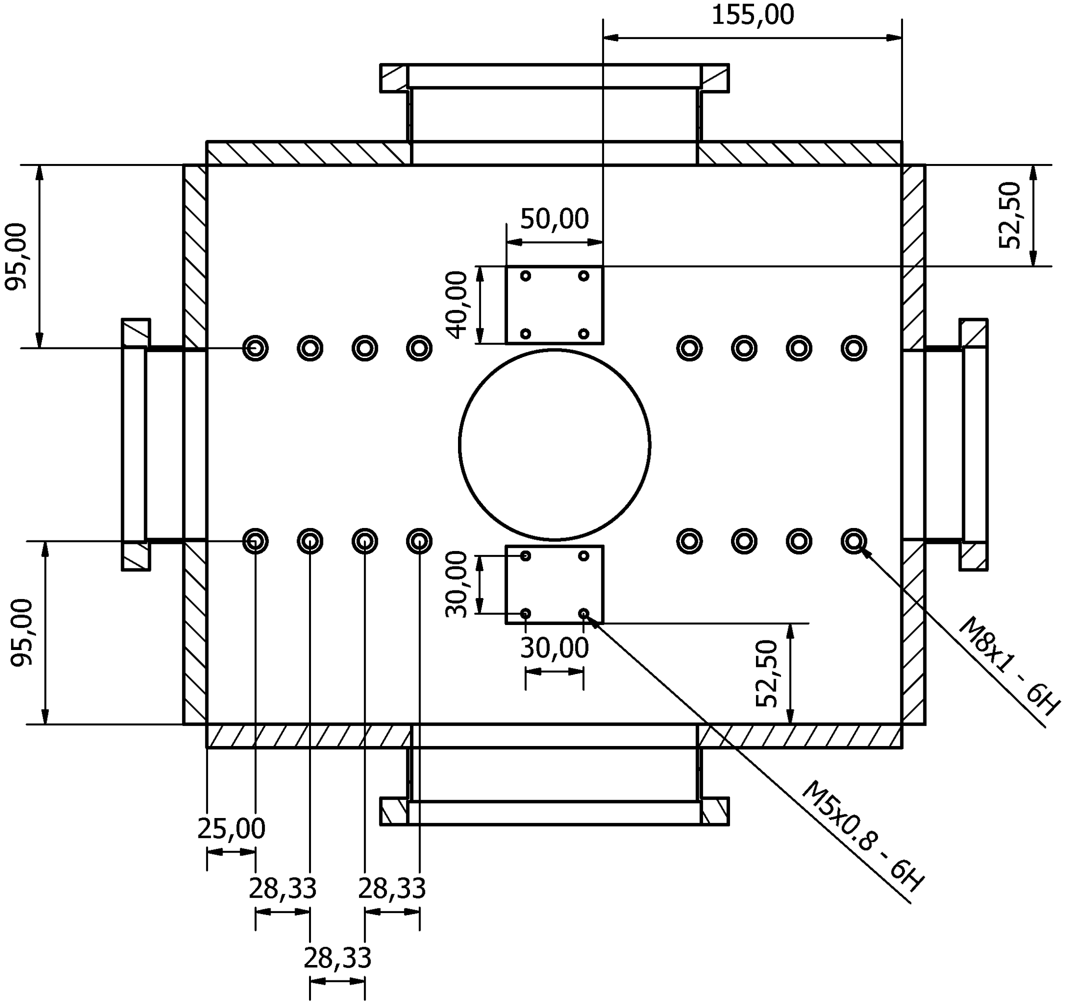

Appendix 18 – Bridge module circuit diagram

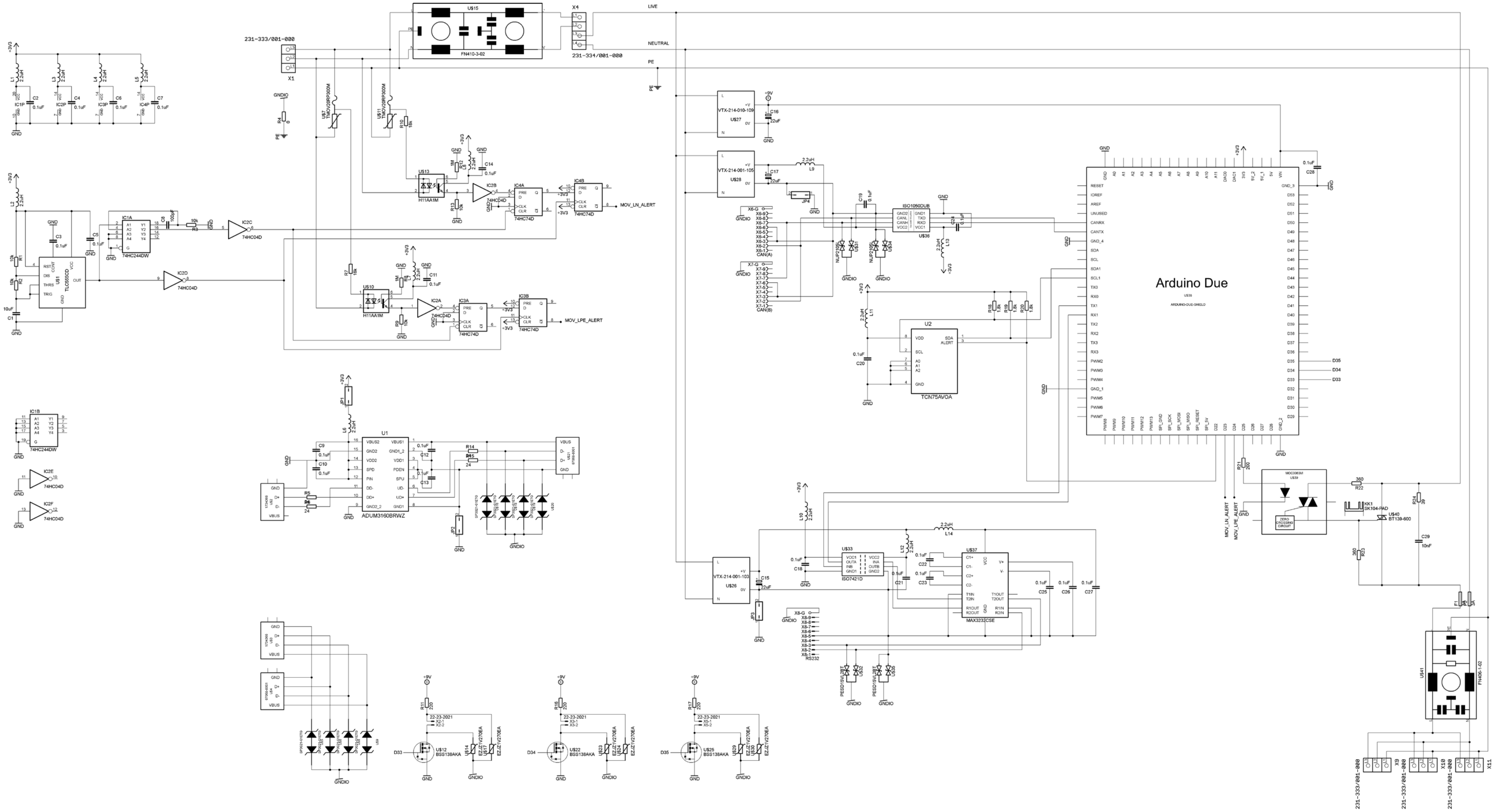

Appendix 19 – Vacuum system control module circuit diagram

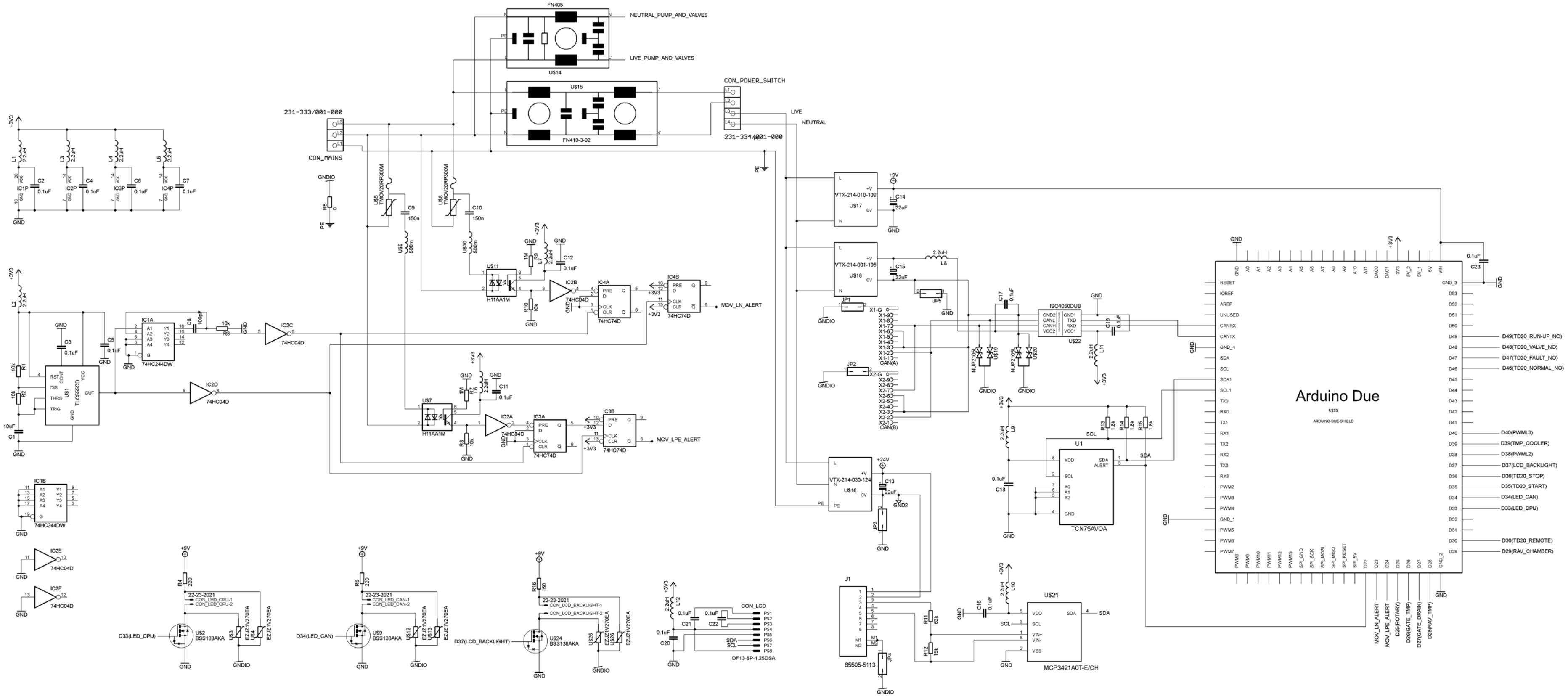

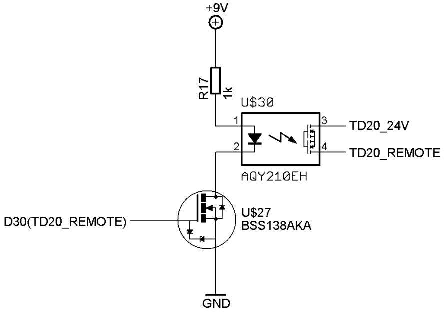
+9V
R17
1k
U$30
1
2
3
4
TD20_24V
TD20_REMOTE
AQY210EH
D30(TD20_REMOTE)
U$27
BSS138AKA
GND

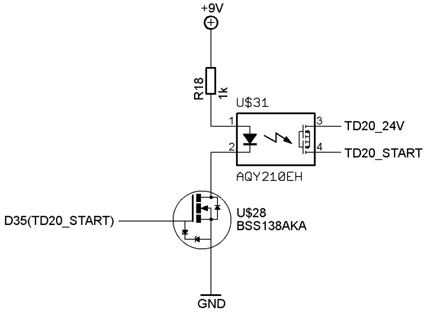
+9V
R18
1k
U$31
1
2
3
4
TD20_24V
TD20_START
AQY210EH
D35(TD20_START)
U$28
BSS138AKA
GND

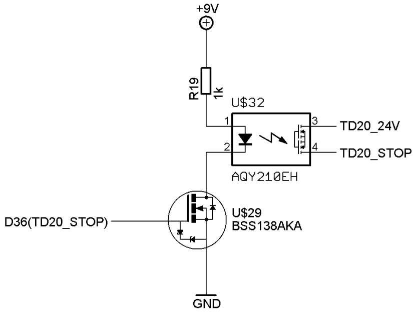
+9V
R19
1k
U$32
1
2
3
4
TD20_24V
TD20_STOP
AQY210EH
D36(TD20_STOP)
U$29
BSS138AKA
GND

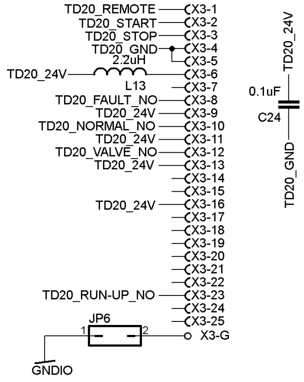
TD20_REMOTE
X3-1
TD20_START
X3-2
TD20_STOP
X3-3
TD20_GND
X3-4
X3-5
2.2uH
TD20_24V
X3-6
L13
X3-7
TD20_FAULT_NO
X3-8
TD20_24V
X3-9
TD20_NORMAL_NO
X3-10
TD20_24V
X3-11
TD20_VALVE_NO
X3-12
TD20_24V
X3-13
X3-14
X3-15
TD20_24V
X3-16
X3-17
X3-18
X3-19
X3-20
X3-21
X3-22
TD20_RUN-UP_NO
X3-23
X3-24
X3-25
JP6
1
2
X3-G
GNDIO
TD20_24V
0.1uF
C24
TD20_GND

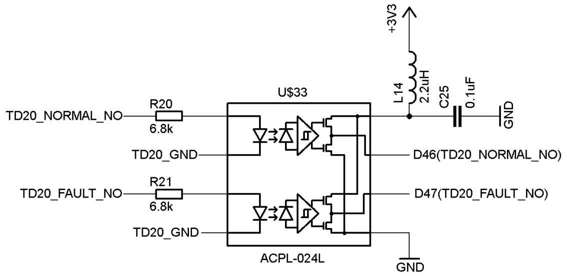
+3V3
L14
2.2uH
C25
0.1uF
GND
U$33
R20
6.8k
TD20_NORMAL_NO
TD20_GND
D46(TD20_NORMAL_NO)
R21
6.8k
TD20_FAULT_NO
D47(TD20_FAULT_NO)
TD20_GND
ACPL-024L
GND

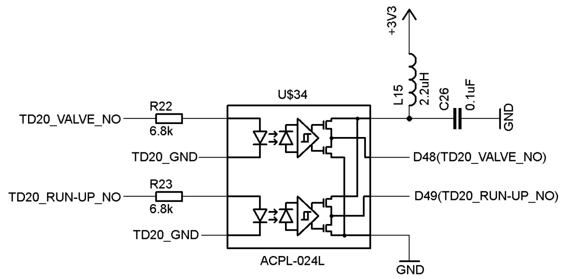
+3V3
L15
2.2uH
C26
0.1uF
GND
U$34
R22
6.8k
TD20_VALVE_NO
TD20_GND
D48(TD20_VALVE_NO)
R23
6.8k
TD20_RUN-UP_NO
D49(TD20_RUN-UP_NO)
TD20_GND
ACPL-024L
GND

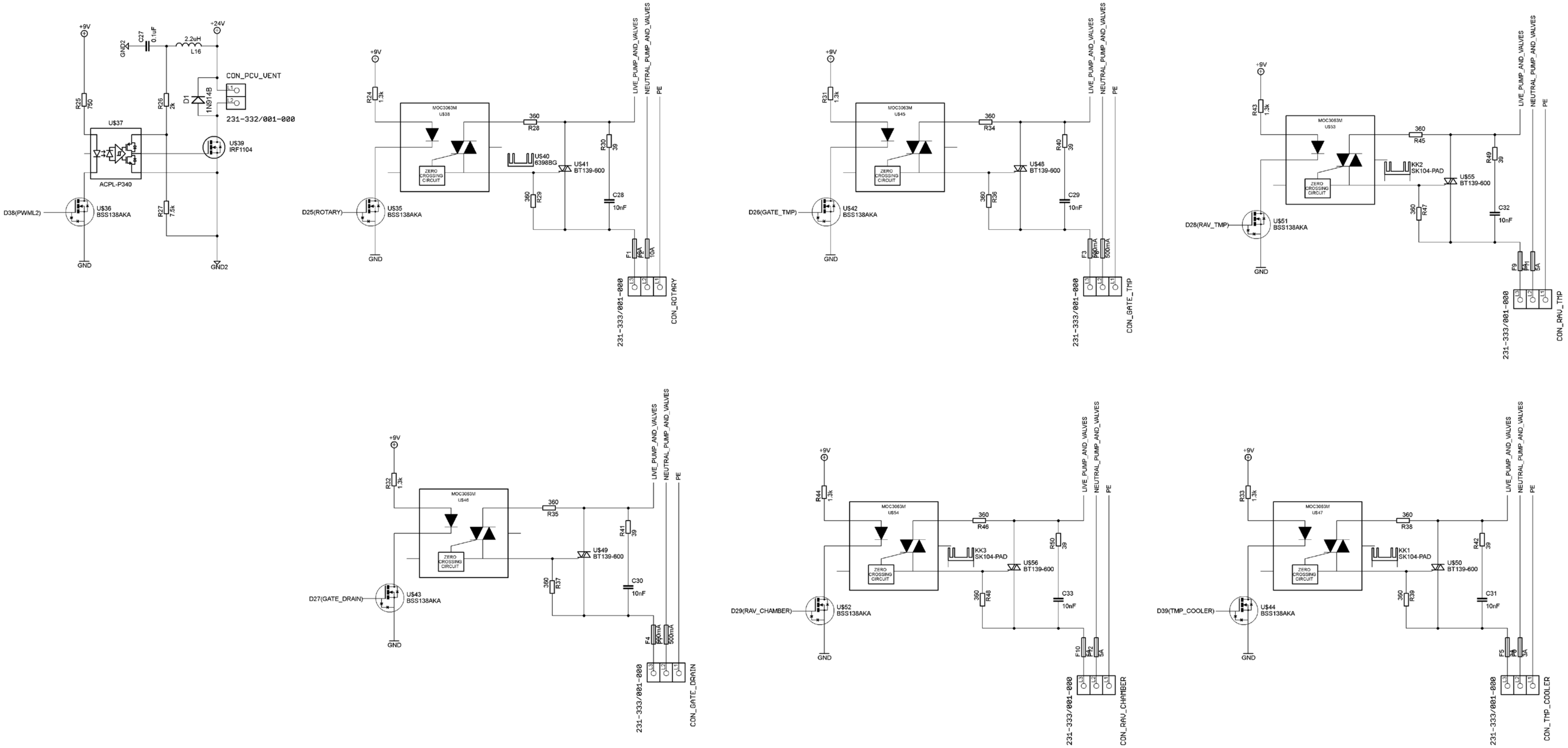
+9V
+24V
GND2
C27
0.1uF
2.2uH
L16
CON_PCU_VENT
R25
750
R26
2k
D1
1N914B
231-332/001-000
U$37
U$39
IRF1104
ACPL-P340
R27
7.5k
D38(PWML2)
U$36
BSS138AKA
GND
MOC3063M
ZERO CROSSING CIRCUIT
LIVE_PUMP_AND_VALVES
NEUTRAL_PUMP_AND_VALVES
PE
R24
1.3k
U$38
360
R28
R30
39
U$40
6398BG
U$41
BT139-600
R29
C28
10nF
D25(ROTARY)
U$35
F1
F2
10A
231-333/001-000
CON_ROTARY
R31
U$45
R34
R40
U$48
R36
C29
D26(GATE_TMP)
U$42
F3
F6
500mA
CON_GATE_TMP
R43
U$53
R45
R49
KK2
SK104-PAD
U$55
R47
C32
D28(RAV_TMP)
U$51
F9
F4
5A
CON_RAV_TMP
R32
U$46
R35
R41
U$49
R37
C30
D27(GATE_DRAIN)
U$43
F4
CON_GATE_DRAIN
R44
U$54
R46
R50
KK3
U$56
R48
C33
D29(RAV_CHAMBER)
U$52
F10
F12
CON_RAV_CHAMBER
R33
U$47
R38
R42
KK1
U$50
R39
C31
D39(TMP_COOLER)
U$44
F5
F8
CON_TMP_COOLER
L1
L2
L3

Appendix 20 – Vacuum system control module additional ADC circuit diagram

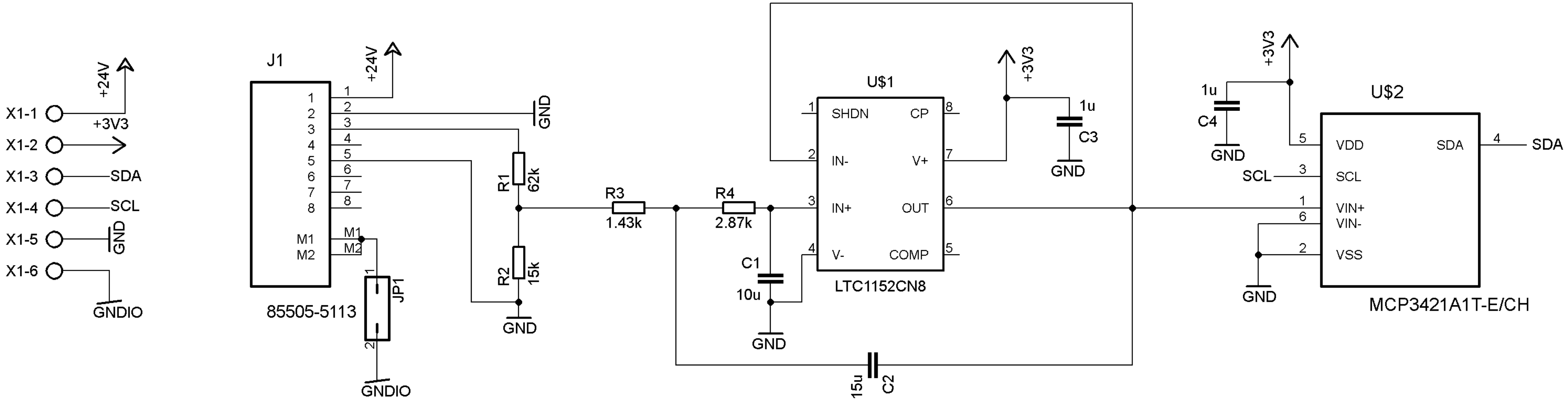

Appendix 21 – Heating control module circuit diagram

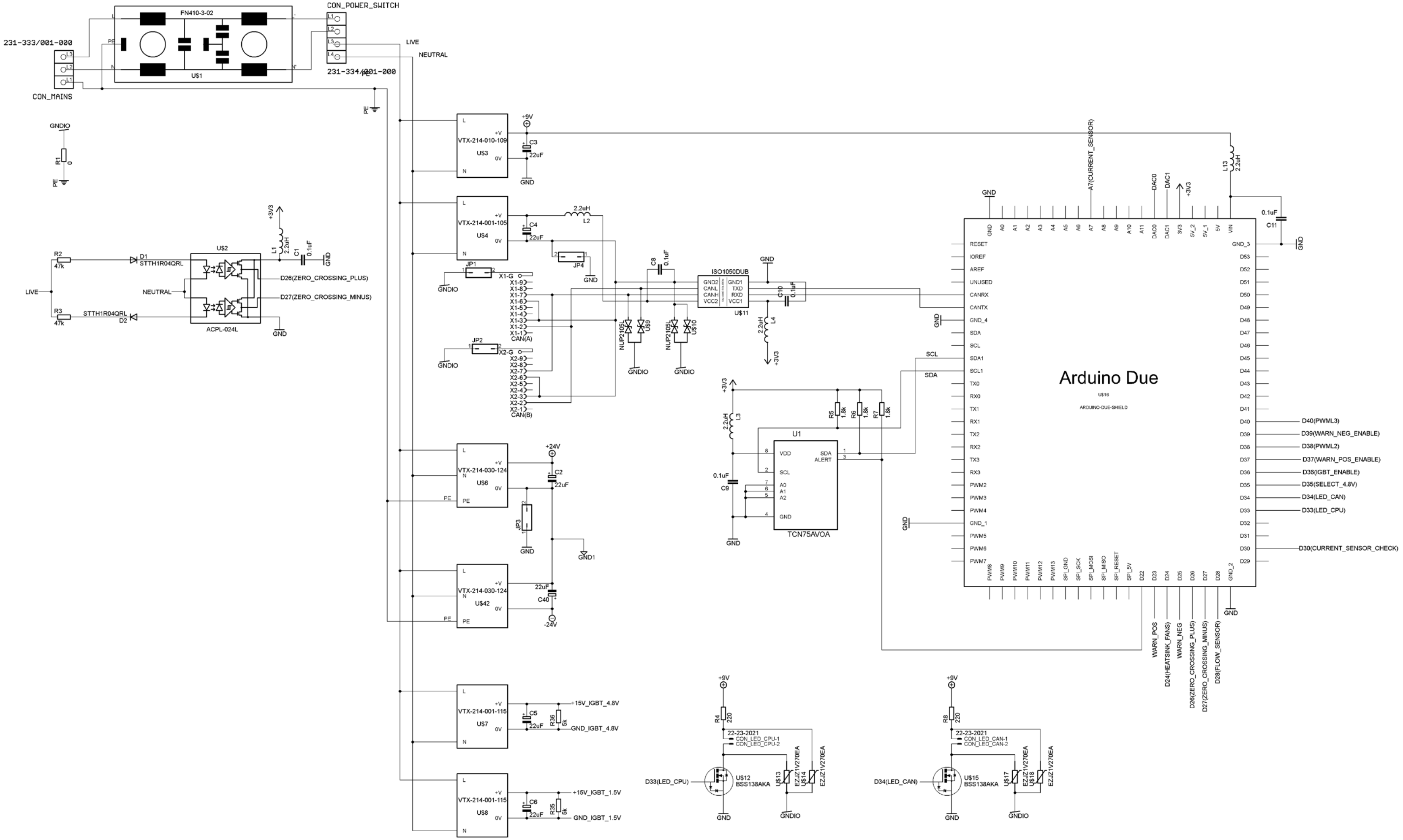

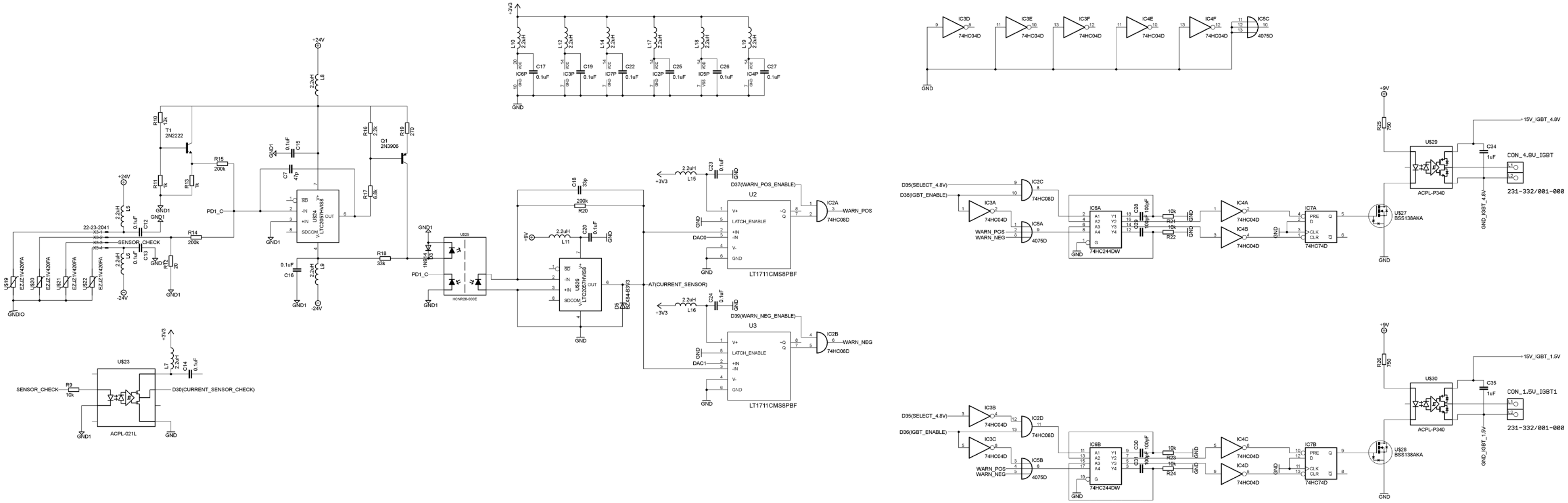
+24V
-24V
+3V3
+9V
GND
GND1
GNDIO
22-23-2041
SENSOR_CHECK
PD1_C
T1 2N2222
Q1 2N3906
R10 10k
R11 1k
R13 1k
R14 200k
R15 200k
R16 2.2k
R17 6.8k
R18 33k
R19 270
R20 200k
L8 2.2uH
L9 2.2uH
C7 47p
C15 0.1uF
C16 0.1uF
C18 33p
U$24 LTC2057HVIS8
U$26 LTC2057HVIS8
U$25 HCNR200-300E
1N914 D3
D5 BZX84-B3V3
A7(CURRENT_SENSOR)
L11 2.2uH
C20 0.1uF
U$19 EZJZ1V420FA
U$20 EZJZ1V420FA
U$21 EZJZ1V420FA
U$22 EZJZ1V420FA
U$23 ACPL-021L
R9 10k
D30(CURRENT_SENSOR_CHECK)
L7 2.2uH
C14 0.1uF
L10 L12 L14 L17 L18 L19 2.2uH
IC6P IC3P IC7P IC2P IC5P IC4P
C17 C19 C22 C25 C26 C27 0.1uF
U2 LT1711CMS8PBF
U3 LT1711CMS8PBF
V+
LATCH_ENABLE
+IN
-IN
V-
DAC0
DAC1
L15 2.2uH
L16 2.2uH
C23 0.1uF
C24 0.1uF
D37(WARN_POS_ENABLE)
D39(WARN_NEG_ENABLE)
IC2A 74HC08D
IC2B 74HC08D
WARN_POS
WARN_NEG
IC3D IC3E IC3F IC4E IC4F 74HC04D
IC5C 4075D
D35(SELECT_4.8V)
D36(IGBT_ENABLE)
IC2C 74HC08D
IC2D 74HC08D
IC3A IC3B IC3C 74HC04D
IC5A IC5B 4075D
IC6A IC6B 74HC244DW
C28 C29 C30 C31 100pF
R21 R22 R23 R24 10k
IC4A IC4B IC4C IC4D 74HC04D
IC7A IC7B 74HC74D
PRE
D
CLK
CLR
U$27 BSS138AKA
U$28 BSS138AKA
R25 750
R26 750
U$29 ACPL-P340
U$30 ACPL-P340
C34 1uF
C35 1uF
15V_IGBT_4.8V
15V_IGBT_1.5V
GND_IGBT_4.8V
GND_IGBT_1.5V
CON_4.8U_IGBT
CON_1.5U_IGBT1
231-332/001-000

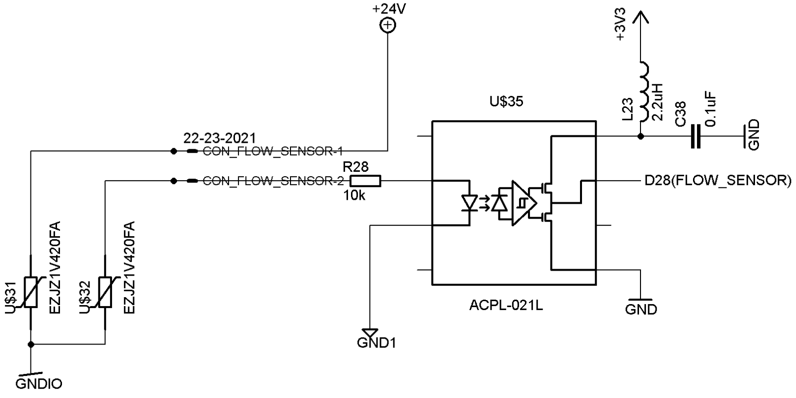
+24V
+3V3
L23
2.2uH
C38
0.1uF
GND
U$35
22-23-2021
CON_FLOW_SENSOR-1
CON_FLOW_SENSOR-2
R28
10k
D28(FLOW_SENSOR)
ACPL-021L
GND
GND1
U$31
EZJZ1V420FA
U$32
EZJZ1V420FA
GNDIO

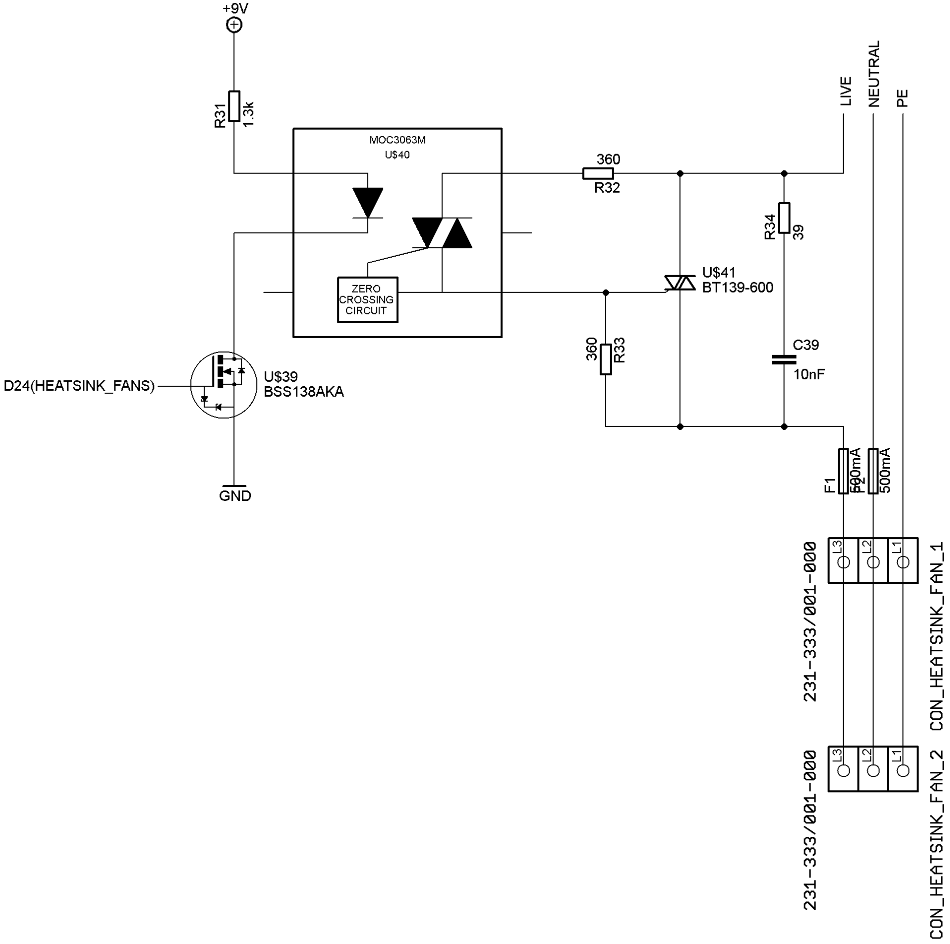
+9V
R31
1.3k
MOC3063M
U$40
ZERO
CROSSING
CIRCUIT
360
R32
LIVE
NEUTRAL
PE
R34
39
U$41
BT139-600
360
R33
C39
10nF
D24(HEATSINK_FANS)
U$39
BSS138AKA
GND
F1
500mA
F2
500mA
L3
L2
L1
231-333/001-000
CON_HEATSINK_FAN_1
L3
L2
L1
231-333/001-000
CON_HEATSINK_FAN_2

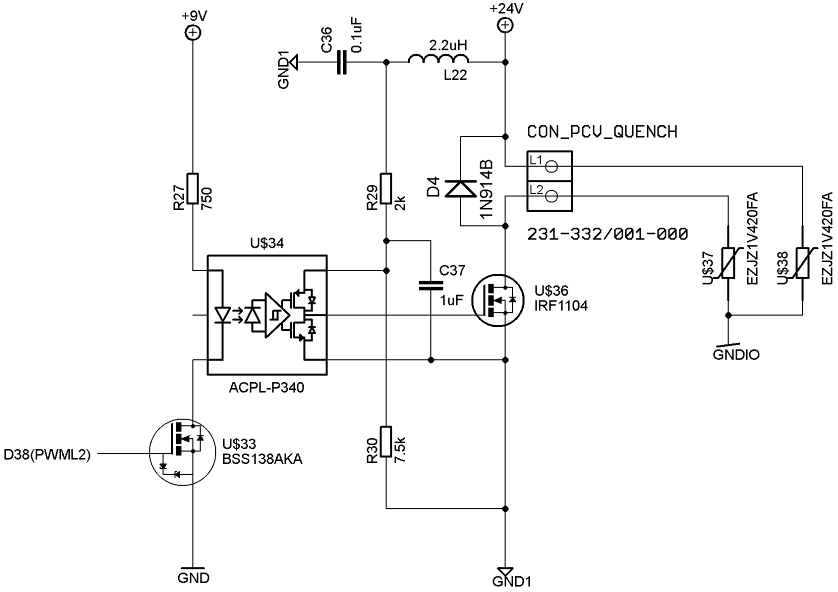
+9V
GND1
C36
0.1uF
2.2uH
L22
+24V
CON_PCV_QUENCH
L1
L2
D4
1N914B
231-332/001-000
R27
750
R29
2k
U$34
C37
1uF
U$36
IRF1104
U$37
EZJZ1V420FA
U$38
EZJZ1V420FA
GNDIO
ACPL-P340
D38(PWML2)
U$33
BSS138AKA
R30
7.5k
GND
GND1

Appendix 22 – Heating control module DAC circuit diagram

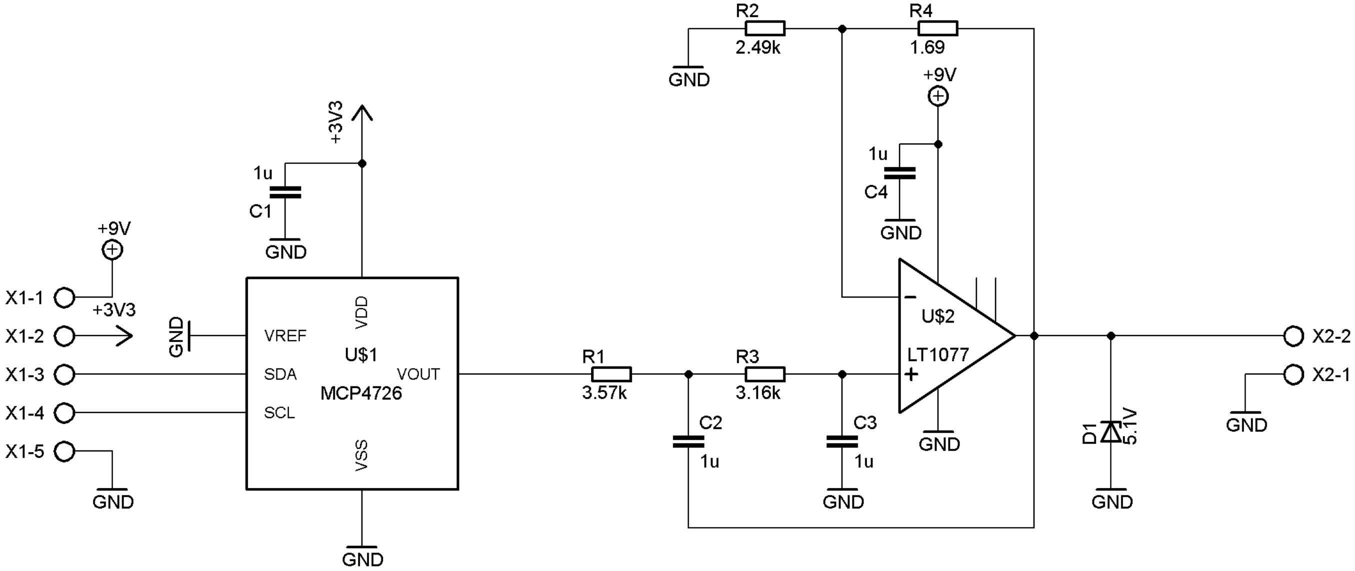

Appendix 23 – Gas control module circuit diagram

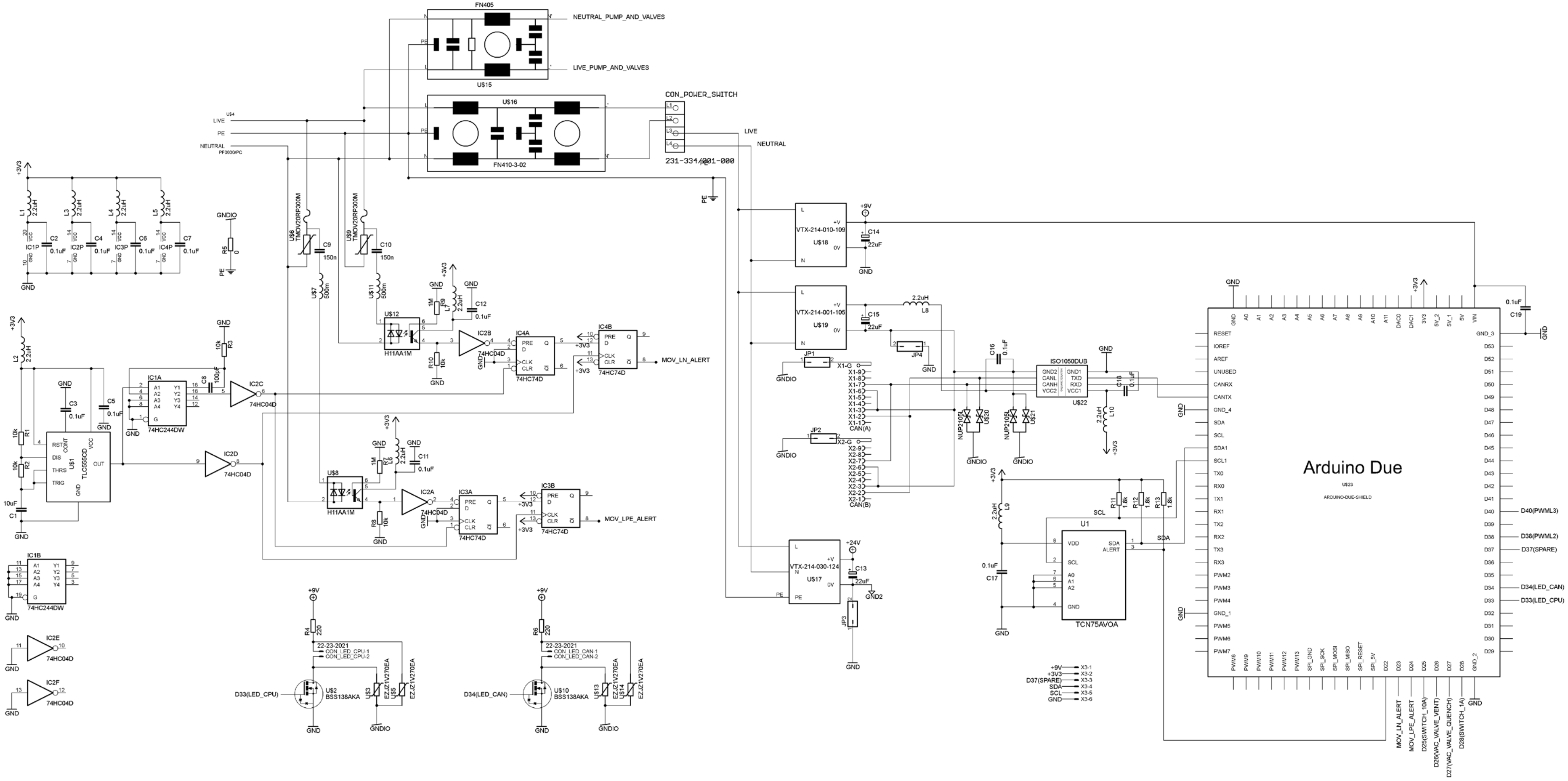

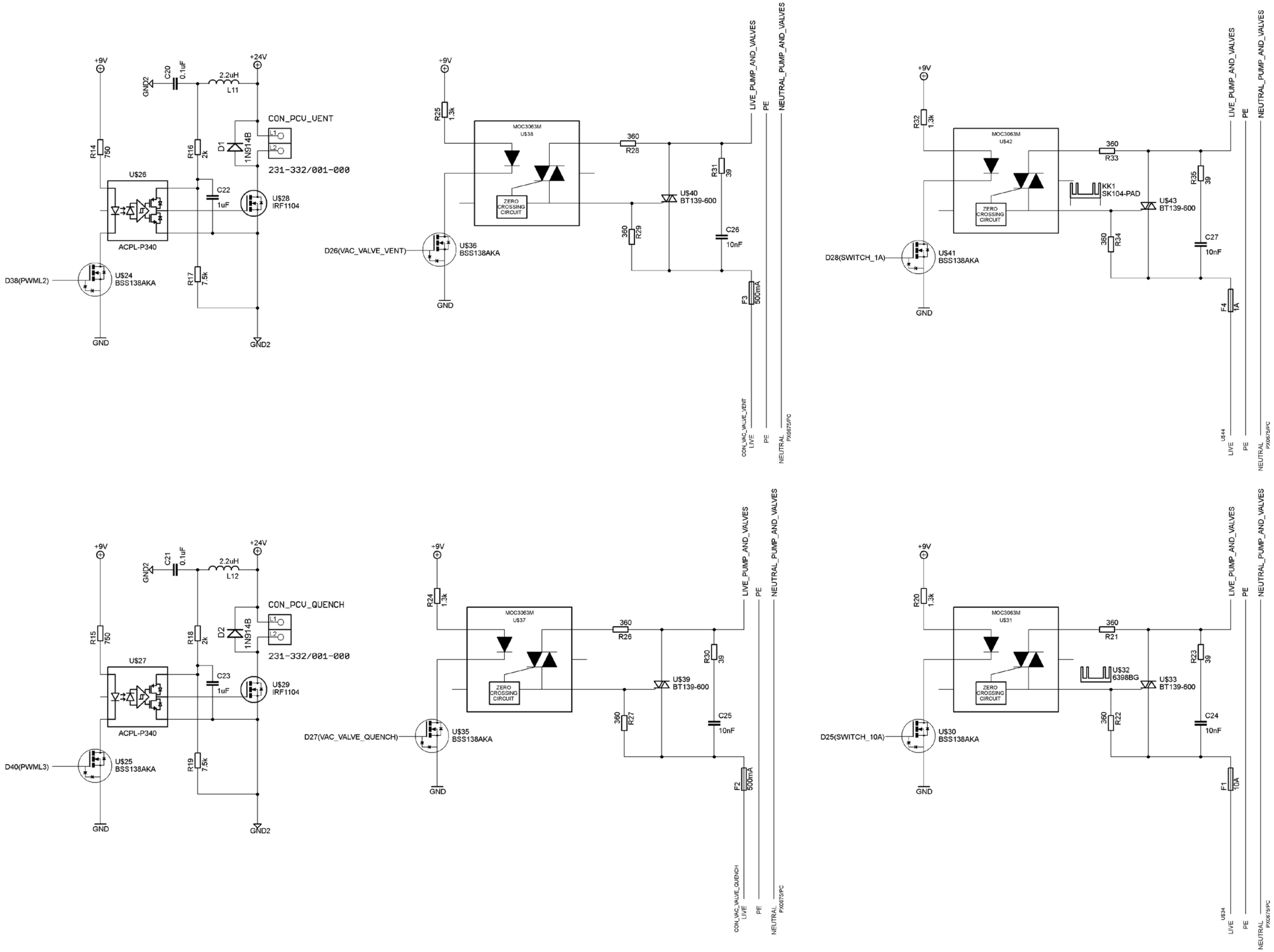

+9V
GND2
C20
0.1uF
2.2uH
L11
+24V
CON_PCV_VENT
L1
L2
D1
1N914B
231-332/001-000
R14
750
R16
2k
C22
1uF
U$28
IRF1104
U$26
ACPL-P340
R17
7.5k
D38(PWML2)
U$24
BSS138AKA
GND
GND2
+9V
R25
1.3k
MOC3063M
U$38
ZERO CROSSING CIRCUIT
360
R28
R31
39
U$40
BT139-600
C26
10nF
360
R29
D26(VAC_VALVE_VENT)
U$36
BSS138AKA
GND
F3
500mA
LIVE_PUMP_AND_VALVES
PE
NEUTRAL_PUMP_AND_VALVES
CON_VAC_VALVE_VENT
LIVE
PE
NEUTRAL
PX0675/PC
+9V
R32
1.3k
MOC3063M
U$42
ZERO CROSSING CIRCUIT
360
R33
R35
39
KK1
SK104-PAD
U$43
BT139-600
360
R34
C27
10nF
D28(SWITCH_1A)
U$41
BSS138AKA
GND
F4
1A
LIVE_PUMP_AND_VALVES
PE
NEUTRAL_PUMP_AND_VALVES
U$44
LIVE
PE
NEUTRAL
PX0675/PC
+9V
GND2
C21
0.1uF
2.2uH
L12
+24V
CON_PCV_QUENCH
L1
L2
D2
1N914B
231-332/001-000
R15
750
R18
2k
C23
1uF
U$29
IRF1104
U$27
ACPL-P340
R19
7.5k
D40(PWML3)
U$25
BSS138AKA
GND
GND2
+9V
R24
1.3k
MOC3063M
U$37
ZERO CROSSING CIRCUIT
360
R26
R30
39
U$39
BT139-600
360
R27
C25
10nF
D27(VAC_VALVE_QUENCH)
U$35
BSS138AKA
GND
F2
500mA
LIVE_PUMP_AND_VALVES
PE
NEUTRAL_PUMP_AND_VALVES
CON_VAC_VALVE_QUENCH
LIVE
PE
NEUTRAL
PX0675/PC
+9V
R20
1.3k
MOC3063M
U$31
ZERO CROSSING CIRCUIT
360
R21
R23
39
U$32
6398BG
U$33
BT139-600
360
R22
C24
10nF
D25(SWITCH_10A)
U$30
BSS138AKA
GND
F1
10A
LIVE_PUMP_AND_VALVES
PE
NEUTRAL_PUMP_AND_VALVES
U$34
LIVE
PE
NEUTRAL
PX0675/PC

Appendix 24 – Instrumentation module circuit diagram

TURN ON THE OUPUT SUPPLY BEFORE THE INPUT SUPPLY!

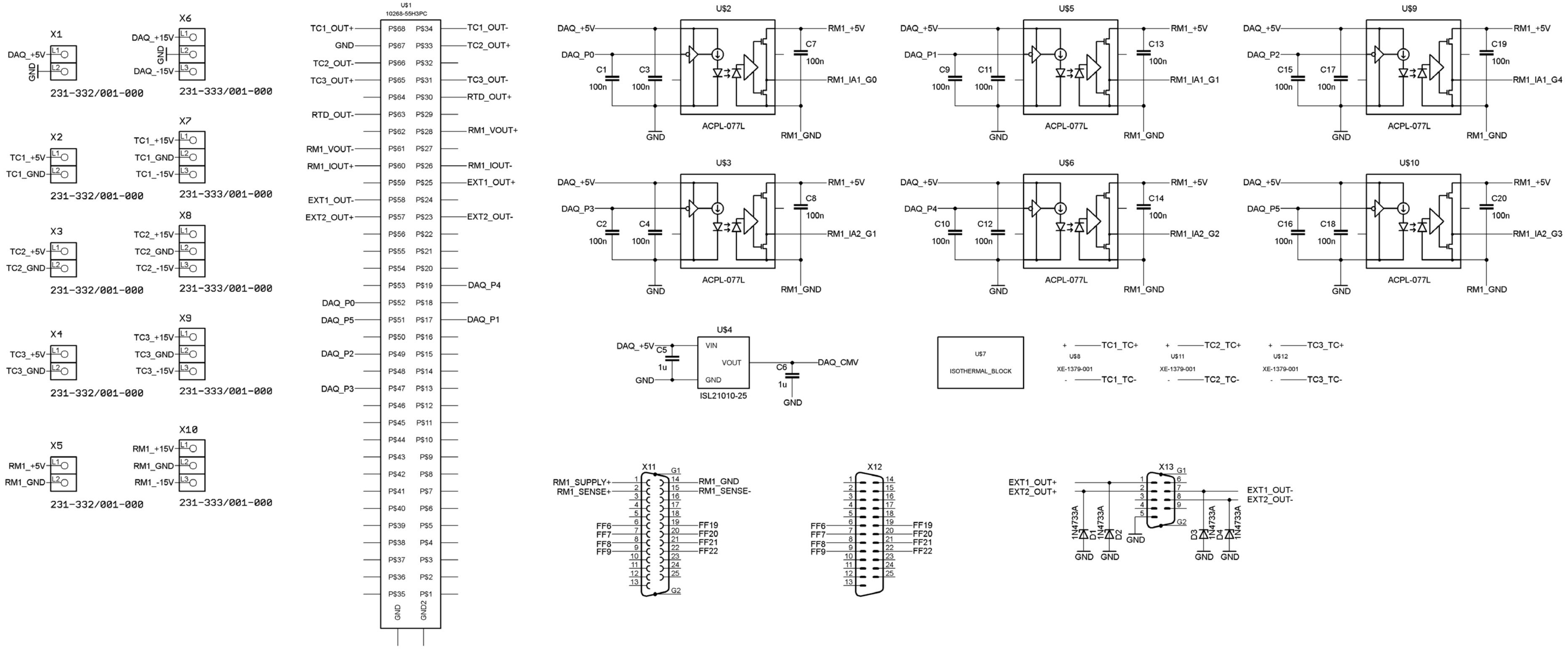

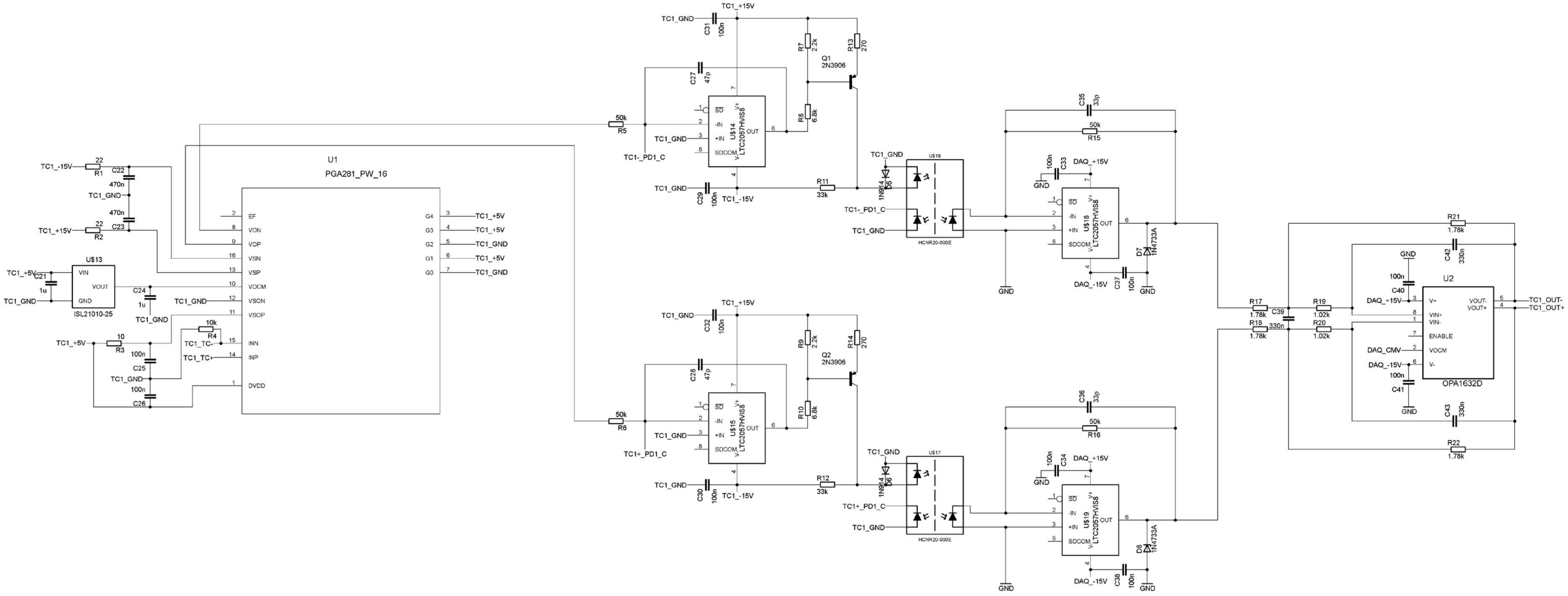
U1
PGA281_PW_16
EF
VON
VOP
VSN
VSP
VOCM
VSON
VSOP
INN
INP
DVDD
G4
G3
G2
G1
G0
TC1_-15V
22
R1
C22
470n
TC1_GND
470n
TC1_+15V
22
R2
C23
U$13
VIN
VOUT
GND
ISL21010-25
TC1_+5V
C21
1u
TC1_GND
C24
1u
TC1_GND
TC1_GND
10k
R4
TC1_TC-
TC1_TC+
TC1_+5V
10
R3
100n
C25
TC1_GND
100n
C26
TC1_+5V
TC1_+5V
TC1_GND
TC1_+5V
TC1_GND
TC1_+15V
TC1_GND
C31
100n
R7
2.2k
R13
270
Q1
2N3906
C27
47p
R8
6.8k
50k
R5
SD
-IN
+IN
SDCOM
V+
V-
U$14
LTC2057HVIS8
OUT
TC1_GND
TC1-_PD1_C
TC1_GND
C29
100n
TC1_-15V
R11
33k
TC1_GND
1N914
D5
U$16
TC1-_PD1_C
TC1_GND
HCNR20-000E
C35
33p
50k
R15
100n
C33
DAQ_+15V
GND
U$18
LTC2057HVIS8
GND
D7
1N4733A
DAQ_-15V
C37
100n
GND
TC1_+15V
TC1_GND
C32
100n
R9
2.2k
R14
270
Q2
2N3906
C28
47p
R10
6.8k
50k
R6
U$15
LTC2057HVIS8
TC1_GND
TC1+_PD1_C
TC1_GND
C30
100n
TC1_-15V
R12
33k
TC1_GND
1N914
D6
U$17
TC1+_PD1_C
TC1_GND
HCNR20-000E
C36
33p
50k
R16
100n
C34
DAQ_+15V
GND
U$19
LTC2057HVIS8
GND
D8
1N4733A
DAQ_-15V
C38
100n
GND
R17
1.78k
R18
1.78k
C39
330n
R19
1.02k
R20
1.02k
R21
1.78k
R22
1.78k
C42
330n
C43
330n
GND
100n
C40
DAQ_+15V
U2
V+
VIN+
VIN-
ENABLE
VOCM
V-
VOUT-
VOUT+
OPA1632D
DAQ_CMV
DAQ_-15V
100n
C41
GND
TC1_OUT-
TC1_OUT+

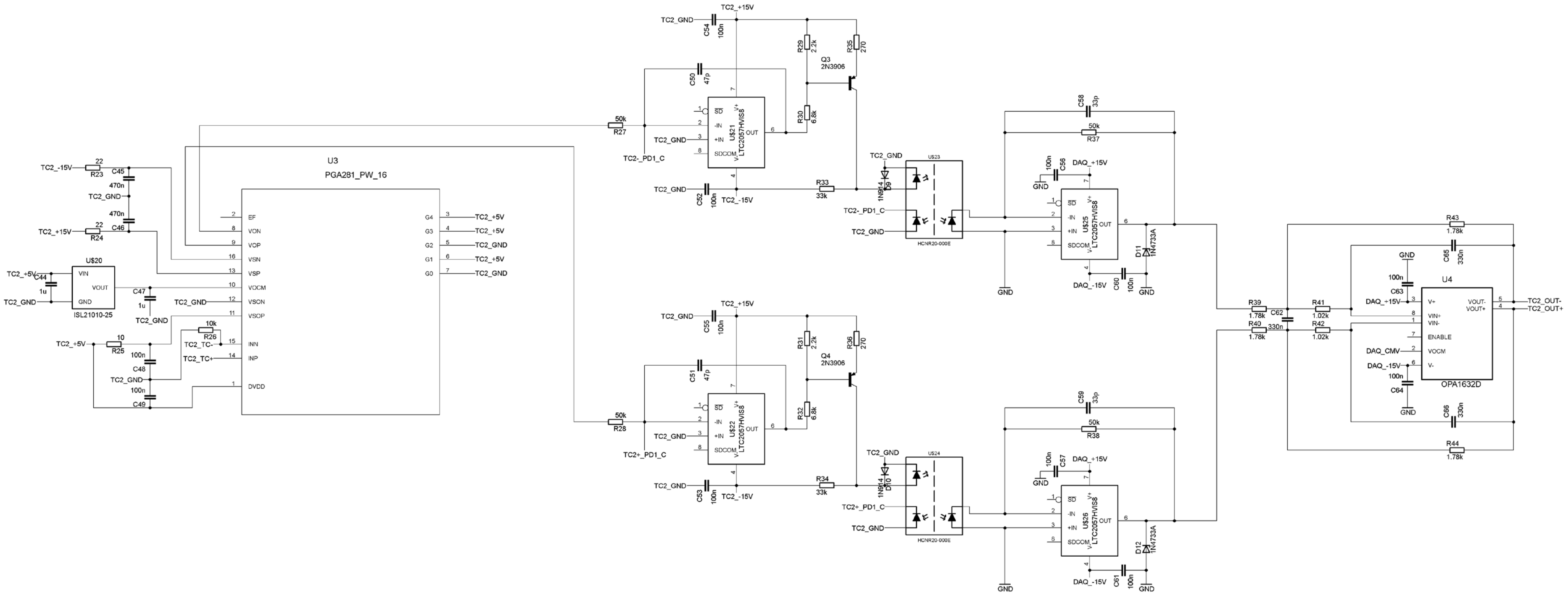
U3
PGA281_PW_16
EF
VON
VOP
VSN
VSP
VOCM
VSON
VSOP
INN
INP
DVDD
G4
G3
G2
G1
G0
TC2_+5V
TC2_+5V
TC2_GND
TC2_+5V
TC2_GND
U$20
VIN
VOUT
GND
ISL21010-25
TC2_-15V
R23
22
C45
470n
TC2_GND
470n
TC2_+15V
R24
22
C46
TC2_+5V
C44
1u
TC2_GND
C47
1u
TC2_GND
TC2_GND
R26
10k
TC2_TC-
TC2_TC+
TC2_+5V
R25
10
100n
C48
TC2_GND
100n
C49
TC2_GND
C54
100n
TC2_+15V
R29
2.2k
R35
270
Q3
2N3906
C50
47p
R30
6.8k
50k
R27
U$21
LTC2057HVIS8
SD
-IN
+IN
SDCOM
OUT
TC2_GND
TC2-_PD1_C
TC2_GND
C52
100n
TC2_-15V
R33
33k
TC2_GND
1N914
D9
U$23
HCNR20-000E
TC2-_PD1_C
TC2_GND
C58
33p
50k
R37
100n
C56
DAQ_+15V
GND
U$25
LTC2057HVIS8
D11
1N4733A
DAQ_-15V
C60
100n
GND
GND
TC2_GND
C55
100n
TC2_+15V
R31
2.2k
R36
270
Q4
2N3906
C51
47p
R32
6.8k
50k
R28
U$22
LTC2057HVIS8
TC2_GND
TC2+_PD1_C
TC2_GND
C53
100n
TC2_-15V
R34
33k
TC2_GND
1N914
D10
U$24
HCNR20-000E
TC2+_PD1_C
TC2_GND
C59
33p
50k
R38
100n
C57
DAQ_+15V
GND
U$26
LTC2057HVIS8
D12
1N4733A
DAQ_-15V
C61
100n
GND
GND
R39
1.78k
C62
R40
1.78k
330n
R41
1.02k
R42
1.02k
R43
1.78k
GND
C65
330n
100n
C63
DAQ_+15V
U4
V+
VIN+
VIN-
ENABLE
VOCM
V-
VOUT-
VOUT+
DAQ_CMV
DAQ_-15V
100n
C64
GND
OPA1632D
C66
330n
R44
1.78k
TC2_OUT-
TC2_OUT+

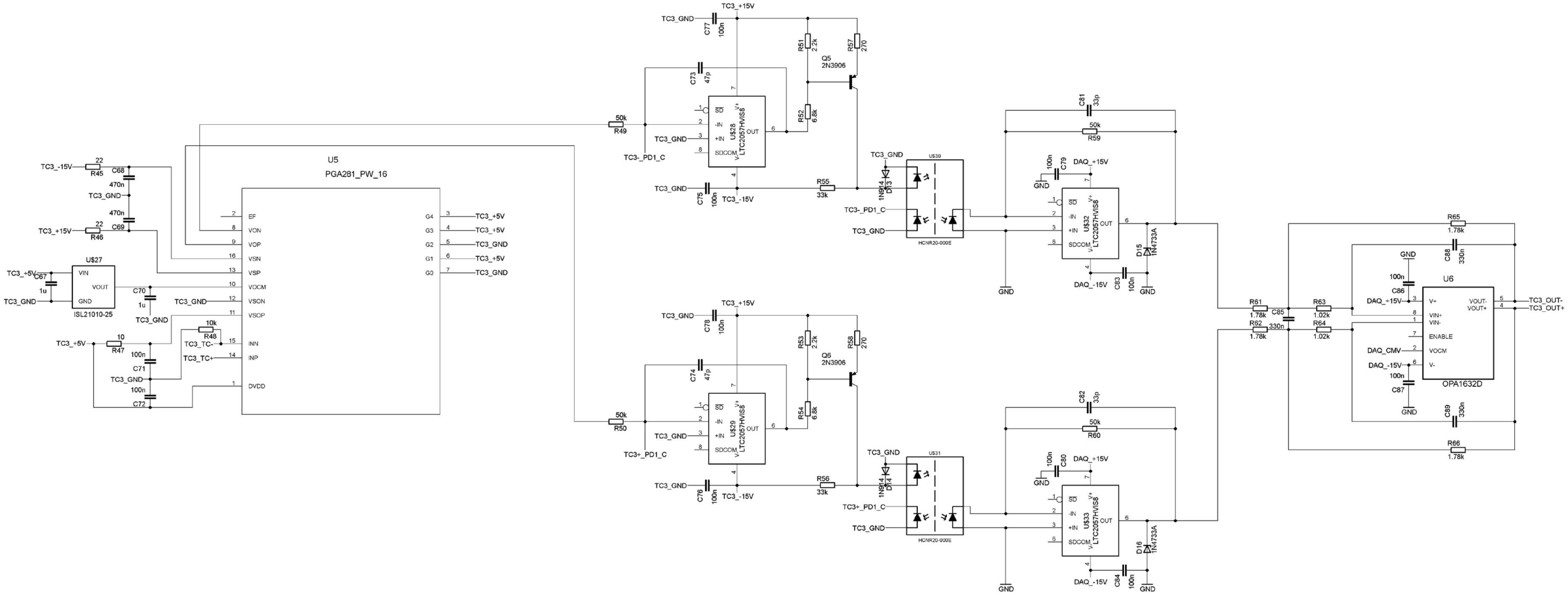
U5
PGA281_PW_16
EF
VON
VOP
VSN
VSP
VOCM
VSON
VSOP
INN
INP
DVDD
G4
G3
G2
G1
G0
TC3_+5V
TC3_+5V
TC3_GND
TC3_+5V
TC3_GND
TC3_-15V
22
R45
C68
470n
TC3_GND
470n
TC3_+15V
22
R46
C69
U$27
VIN
VOUT
GND
ISL21010-25
TC3_+5V
C67
1u
TC3_GND
C70
1u
TC3_GND
TC3_GND
10k
R48
TC3_TC-
TC3_TC+
TC3_+5V
10
R47
100n
C71
TC3_GND
100n
C72
TC3_GND
TC3_+15V
C77
100n
C73
47p
R51
2.2k
R57
270
Q5
2N3906
R52
6.8k
50k
R49
U$28
LTC2057HVIS8
SD
-IN
+IN
SDCOM
V+
V-
OUT
TC3_GND
TC3-_PD1_C
TC3_GND
C75
100n
TC3_-15V
R55
33k
TC3_GND
1N914
D13
U$30
HCNR20-000E
TC3-_PD1_C
TC3_GND
C81
33p
50k
R59
100n
C79
DAQ_+15V
GND
U$32
LTC2057HVIS8
D15
1N4733A
DAQ_-15V
C83
100n
GND
GND
TC3_GND
TC3_+15V
C78
100n
C74
47p
R53
2.2k
R58
270
Q6
2N3906
R54
6.8k
50k
R50
U$29
LTC2057HVIS8
TC3_GND
TC3+_PD1_C
TC3_GND
C76
100n
TC3_-15V
R56
33k
TC3_GND
1N914
D14
U$31
HCNR20-000E
TC3+_PD1_C
TC3_GND
C82
33p
50k
R60
100n
C80
DAQ_+15V
GND
U$33
LTC2057HVIS8
D16
1N4733A
DAQ_-15V
C84
100n
GND
GND
R61
1.78k
R62
1.78k
C85
330n
R63
1.02k
R64
1.02k
R65
1.78k
C88
330n
GND
100n
C86
DAQ_+15V
U6
OPA1632D
V+
VIN+
VIN-
ENABLE
VOCM
V-
VOUT-
VOUT+
DAQ_CMV
DAQ_-15V
100n
C87
GND
C89
330n
R66
1.78k
TC3_OUT-
TC3_OUT+

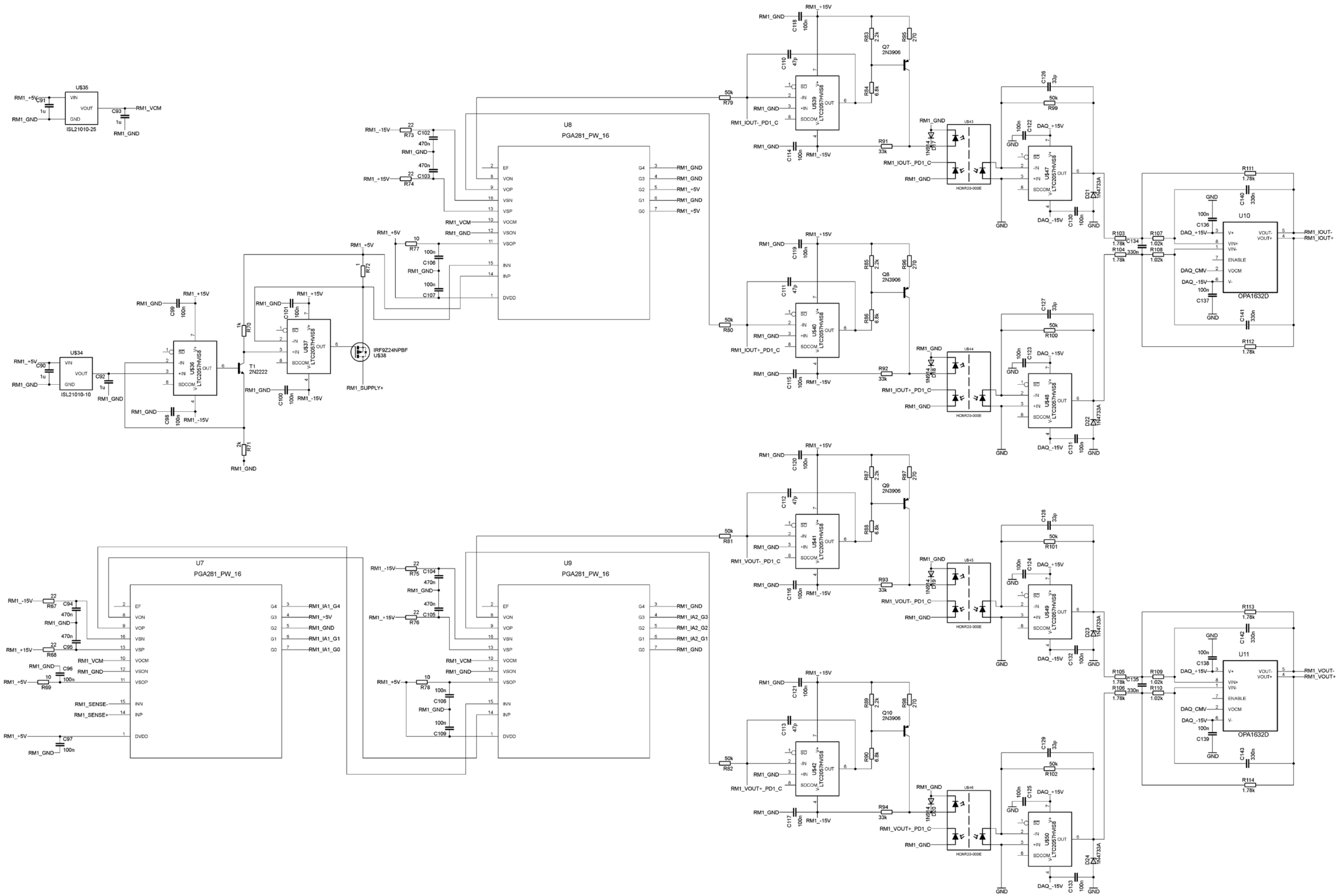
U$35
ISL21010-25
RM1_+5V
RM1_GND
RM1_VCM
U$34
ISL21010-10
U8
PGA281_PW_16
U7
PGA281_PW_16
U9
PGA281_PW_16
T1
2N2222
IRF9Z24NPBF
U$38
RM1_SUPPLY+
LTC2057HVIS8
Q7
2N3906
Q8
2N3906
Q9
2N3906
Q10
2N3906
HCNR200-000E
1N4733A
U10
OPA1632D
U11
OPA1632D
RM1_IOUT-
RM1_IOUT+
RM1_VOUT-
RM1_VOUT+
RM1_SENSE-
RM1_SENSE+
RM1_IOUT-_PD1_C
RM1_IOUT+_PD1_C
RM1_VOUT-_PD1_C
RM1_VOUT+_PD1_C
RM1_IA1_G4
RM1_IA1_G1
RM1_IA1_G0
RM1_IA2_G3
RM1_IA2_G2
RM1_IA2_G1
DAQ_+15V
DAQ_-15V
DAQ_CMV
RM1_+15V
RM1_-15V
GND

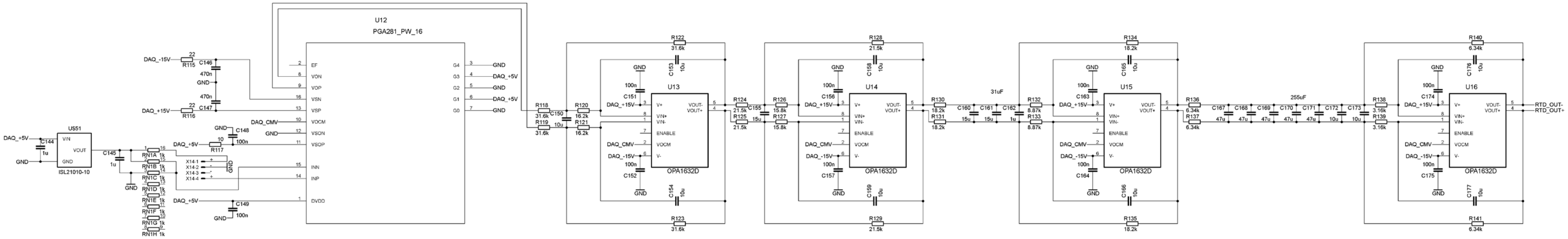
U$51
ISL21010-10
VIN
VOUT
GND
DAQ_+5V
C144
1u
C145
1u
RN1A 1k
RN1B 1k
RN1C 1k
RN1D 1k
RN1E 1k
RN1F 1k
RN1G 1k
RN1H 1k
X14-1
X14-2
X14-3
X14-4
DAQ_-15V
DAQ_+15V
R115
R116
22
C146
C147
470n
R117
10
C148
C149
100n
DAQ_CMV
U12
PGA281_PW_16
EF
VON
VOP
VSN
VSP
VOCM
VSON
VSOP
INN
INP
DVDD
G4
G3
G2
G1
G0
R118
R119
31.6k
C150
10u
R120
R121
16.2k
R122
R123
31.6k
C151
C152
C153
C154
U13
OPA1632D
V+
VIN+
VIN-
ENABLE
VOCM
V-
VOUT-
VOUT+
R124
R125
21.5k
C155
15u
R126
R127
15.8k
R128
R129
21.5k
C156
C157
C158
C159
U14
OPA1632D
R130
R131
18.2k
C160
C161
C162
15u
15u
1u
31uF
R132
R133
8.87k
R134
R135
18.2k
C163
C164
C165
C166
U15
OPA1632D
R136
R137
6.34k
C167
C168
C169
C170
C171
C172
C173
47u
47u
47u
47u
47u
10u
10u
255uF
R138
R139
3.16k
R140
R141
6.34k
C174
C175
C176
C177
U16
OPA1632D
RTD_OUT-
RTD_OUT+

Appendix 25 – Analogue signal isolator analysis

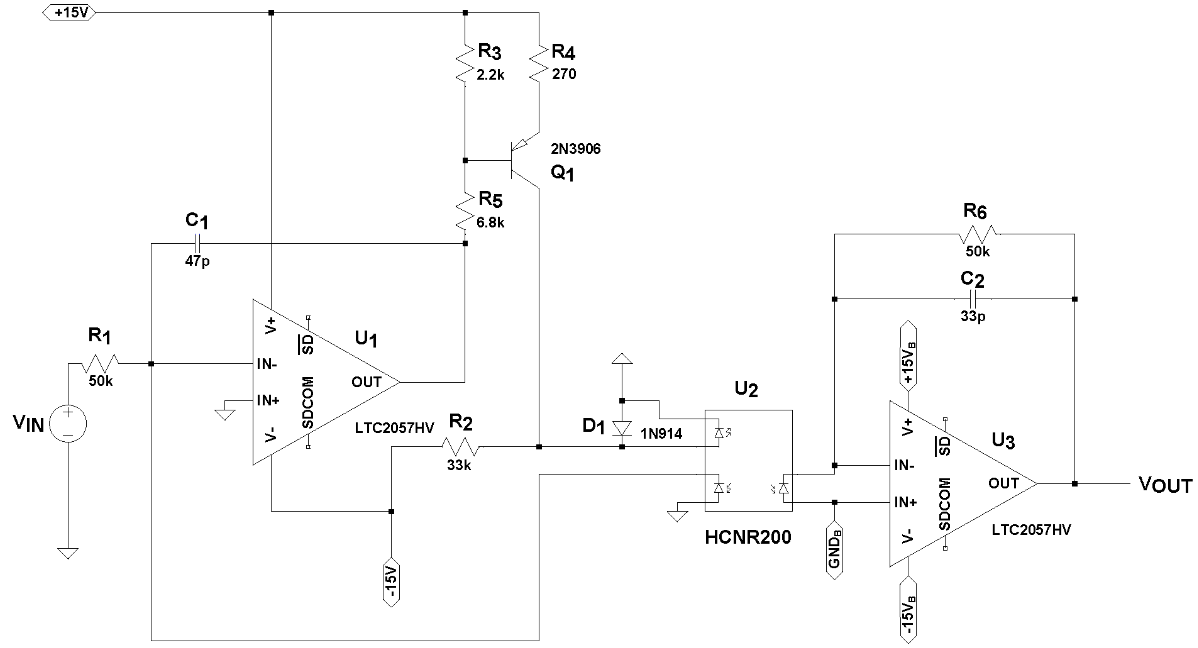

This appendix provides a basic circuit analysis of the electrical isolation circuit that is used for the analogue instrumentation signals; for a general description of this circuit please see section 3.5.3. In this circuit analysis it will be assumed that the input impedances of U_1 and U_3 are sufficiently high that current flow into the input terminals can be ignored; that the spectrum of V_{IN} is of low frequency and that C_1 and C_3 can be considered to be open circuit; and, that as the LED of U_2 will be forward biased that D_1 can be ignored.

To start the analysis, let us consider how the collector current of Q_1 is determined by V_{U1} (the output voltage of U_1. The base voltage of Q_1 is set be the potential divider formed by R_3 and R_5.

$$V_B = (15 - V_{U1})\frac{R_5}{R_3 + R_5} \qquad \text{A.25.1}$$

The emitter voltage is the sum of the base voltage and the emitter base voltage.

$$V_E = V_B + V_{EB} \qquad \text{A.25.2}$$

We can assume that as Q_1 is conducting that V_{EB} is approximately 0.7 V.

$$V_E = (15.7 - V_{U1})\frac{R_5}{R_3 + R_5} \tag{A.25.3}$$

The emitter current is equal to the current through R_4, which can be calculated as the positive supply voltage less the emitter voltage divided by R_4.

$$I_E = \frac{15 - V_E}{R_4} \tag{A.25.4}$$

Let us assume that the current gain of Q_1 is sufficiently large that the collector current is approximately equal to the emitter current. If we then substitute the expression for V_E into the above expression, we can then obtain the collector current as a function of V_{U1}.

$$I_C \simeq \frac{15}{R_4} - \frac{15.7R_5}{R_4(R_3 + R_5)} + \frac{V_{U1}R_5}{R_4(R_3 + R_5)} \tag{A.25.5}$$

As the LED of U2 is turned on, let us assume that the forward voltage is equal to 1.6 V. The current through R2 can then be calculated.

$$I_{R2} = \frac{1.6 - (-15)}{R_2} \tag{A.25.6}$$

Using Kirchoff's current law, we can then determine the current through the LED.

$$I_{LED} = I_C - I_{R2} \tag{A.25.7}$$

Into which we can substitute equations A.25.5 and A.25.6.

$$I_{LED} = \frac{15}{R_4} - \frac{15.7R_5}{R_4(R_3 + R_5)} + \frac{V_{U1}R_5}{R_4(R_3 + R_5)} - \frac{16.6}{R_2} \tag{A.25.8}$$

If we substitute in the values of the resistors: R_3 = 2.2 kΩ, R_4 = 270 Ω, and R_5 = 6.8 kΩ.

$$I_{LED} = 2.80 \times 10^{-3} V_{U1} + 6.09 \times 10^{-3}\text{A} \tag{A.25.9}$$

This analysis of the operation of Q_1 proves that the LED current is a function of V_{U1}, and that the LED is forward biased with an input voltage of zero.

Now let us consider the input amplifier, U_1. The output voltage of U_1, V_{U1}, is the difference between the voltage at the non-inverting and inverting inputs of U_1 multiplied by the open-loop gain of U_1, A_1.

$$V_{U1} = A_1(V_{1+} - V_{1-}) \qquad \text{A.25.10}$$

As the non-inverting input is connected to the input ground, the voltage at that terminal is zero.

$$V_{1+} = 0 \qquad \text{A.25.11}$$

The voltage at the inverting terminal is equal to the input voltage less the voltage drop across R_1. The voltage drop across R_1 is equal to the value of R_1 multiplied by the current flowing through R_1, which is equal to the current flowing through the input side photodiode of U_2, I_{PD1}.

$$V_{1-} = V_{IN} - R_1 I_{PD1} \qquad \text{A.25.12}$$

The datasheet for the HCNR200 optocoupler tells us that the photodiode current is a function of the LED current.

$$I_{PD1} = f_1(I_{LED}) \qquad \text{A.25.13}$$

We know from equation A.25.9 that I_{LED} is function of the output voltage of U_1, so we know that the photodiode current must also be a function of V_{U1}.

$$I_{PD1} = g(V_{U1}) \qquad \text{A.25.14}$$

This can then be substituted into the expression for V_{1-}.

$$V_{1-} = V_{IN} - R_1 g(V_{U1}) \qquad \text{A.25.15}$$

This can now be inserted into the expression for V_{U1}.

$$V_{U1} = A_1 R_1 g(V_{U1}) - A_1 V_{IN} \qquad \text{A.25.16}$$

Now rearranging for V_{IN}.

$$V_{IN} = \frac{A_1 R_1 g(V_{U1}) - V_{U1}}{A_1} \quad \text{A.25.17}$$

$$\therefore V_{IN} = R_1 g(V_{U1}) - \frac{V_{U1}}{A_1} \quad \text{A.25.18}$$

As the open loop gain of U_1 will be very large.

$$R_1 g(V_{U1}) \gg \frac{V_{U1}}{A_1} \quad \text{A.25.19}$$

$$\Rightarrow V_{IN} \simeq R_1 g(V_{U1}) \quad \text{A.25.20}$$

If we now look at the output stage amplifier U_3, the output voltage is again equal to the difference between the input terminals multiplied by the open loop gain, A_3.

$$V_{OUT} = A_3(V_{3+} - V_{3-}) \quad \text{A.25.21}$$

The non-inverting input is connected to the output ground.

$$V_{3+} = 0 \quad \text{A.25.22}$$

The voltage at the inverting input is equal to V_{OUT} less the voltage drop across R_6. The current through R_6 is equal to the current through the output photodiode, I_{PD2}.

$$V_{3-} = V_{OUT} - R_6 I_{PD2} \quad \text{A.25.23}$$

The HCNR200 datasheet also tells us that the output photodiode current is a function of the LED current.

$$I_{PD2} = f_2(I_{LED}) \quad \text{A.25.24}$$

As with the input photodiode, we can state that the output photodiode current is a function of the output voltage of U_1.

$$I_{PD2} = h(V_{U1}) \quad \text{A.25.25}$$

Substituting into A.25.23.

$$V_{3-} = V_{OUT} - R_6 h(V_{U1}) \tag{A.25.26}$$

This can now be combined with equation A.25.21.

$$V_{OUT} = A_3 R_6 h(V_{U1}) - A_3 V_{OUT} \tag{A.25.27}$$

$$\therefore (1 + A_3)V_{OUT} = A_3 R_6 h(V_{U1}) \tag{A.25.28}$$

$$\therefore V_{OUT} = \frac{A_3 R_6 h(V_{U1})}{1 + A_3} \tag{A.25.29}$$

As the open loop gain of U$_3$ is very large.

$$A_3 \gg 1 \tag{A.25.30}$$

$$\Longrightarrow \frac{A_3}{1 + A_3} \simeq 1 \tag{A.25.31}$$

Which allows equation A.25.29 to be simplified.

$$V_{OUT} \simeq R_6 h(V_{U1}) \tag{A.25.32}$$

We can now obtain an expression for the gain by diving equation A.25.32 by equation A.25.20.

$$\frac{V_{OUT}}{V_{IN}} = \frac{R_6 h(V_{U1})}{R_1 g(V_{U1})} \tag{A.25.33}$$

For an ideal device the ratio of the current, K$_3$, in both photodiodes is one.

$$K_3 = \frac{I_{PD2}}{I_{PD1}} = 1 \tag{A.25.34}$$

$$\Longrightarrow \frac{f_2(I_{LED})}{f_1(I_{LED})} = 1 \tag{A.25.35}$$

$$\Longrightarrow \frac{h(V_{U1})}{g(V_{U1})} = 1 \tag{A.25.36}$$

$$\Longrightarrow \frac{V_{OUT}}{V_{IN}} = \frac{R_6}{R_1} \tag{A.25.37}$$

Appendix 26 – Run heat treatment activity diagram

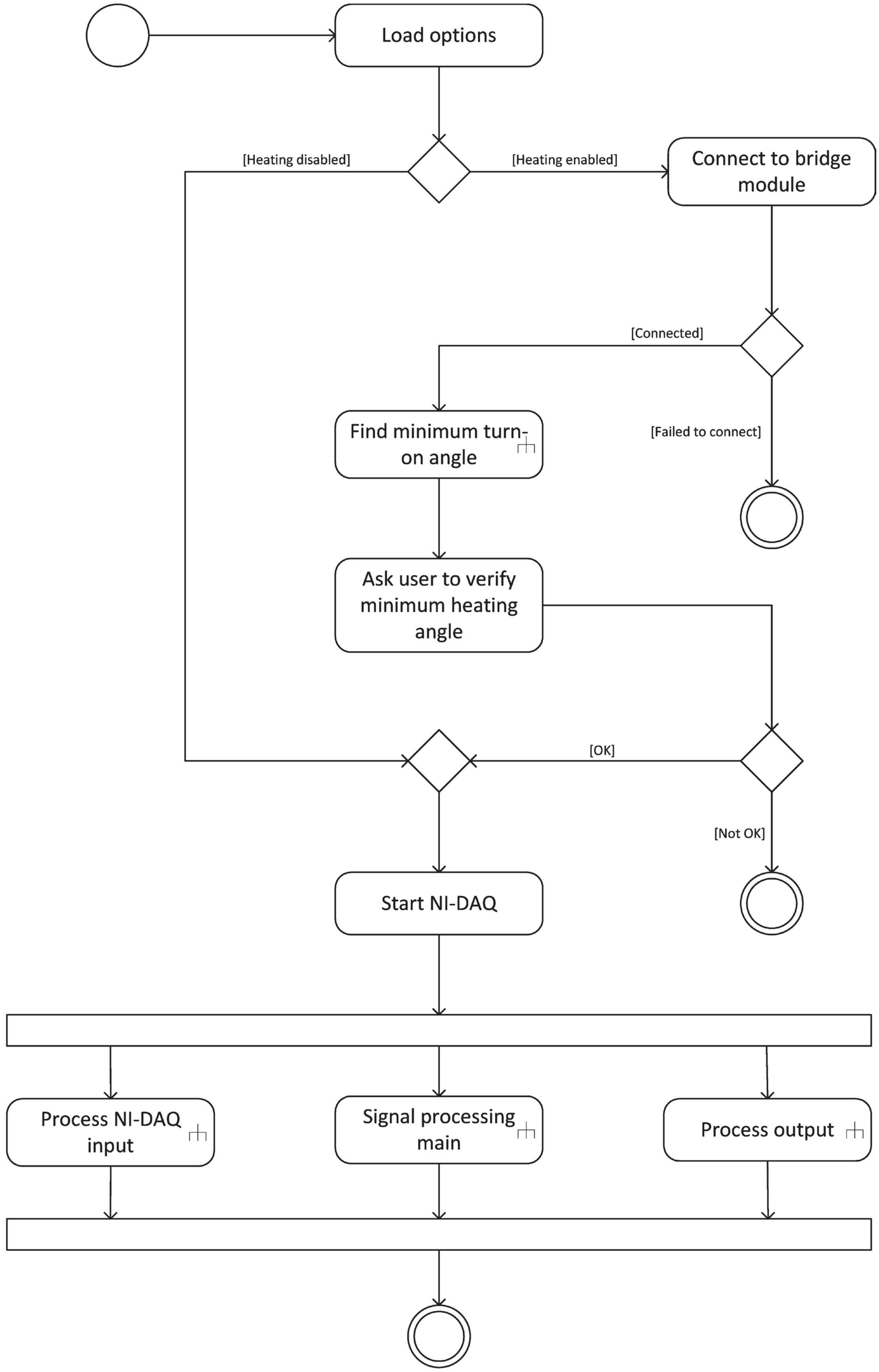

Appendix 27 – Find minimum turn-on angle activity diagram

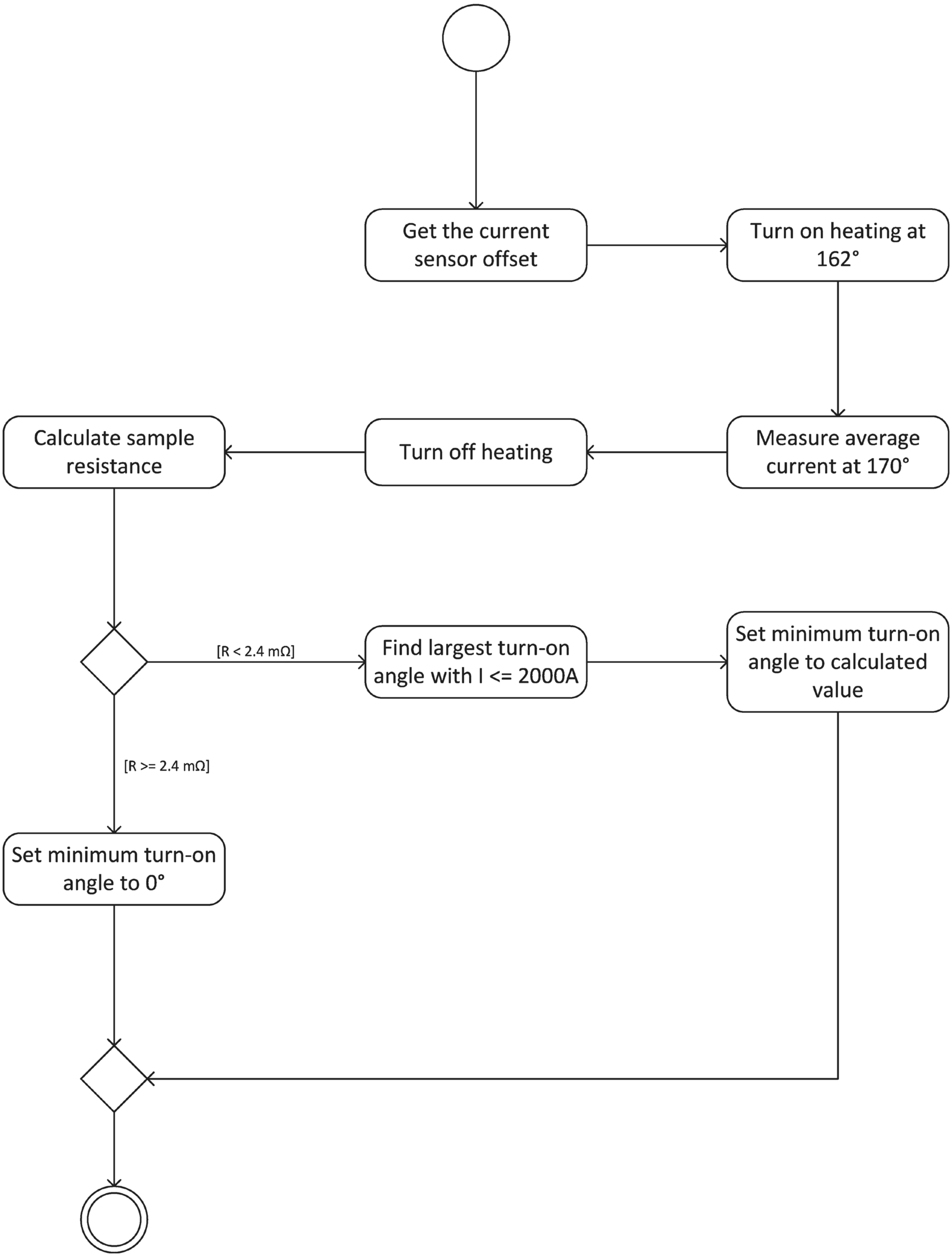

Appendix 28 – Process NI-DAQ input activity diagram

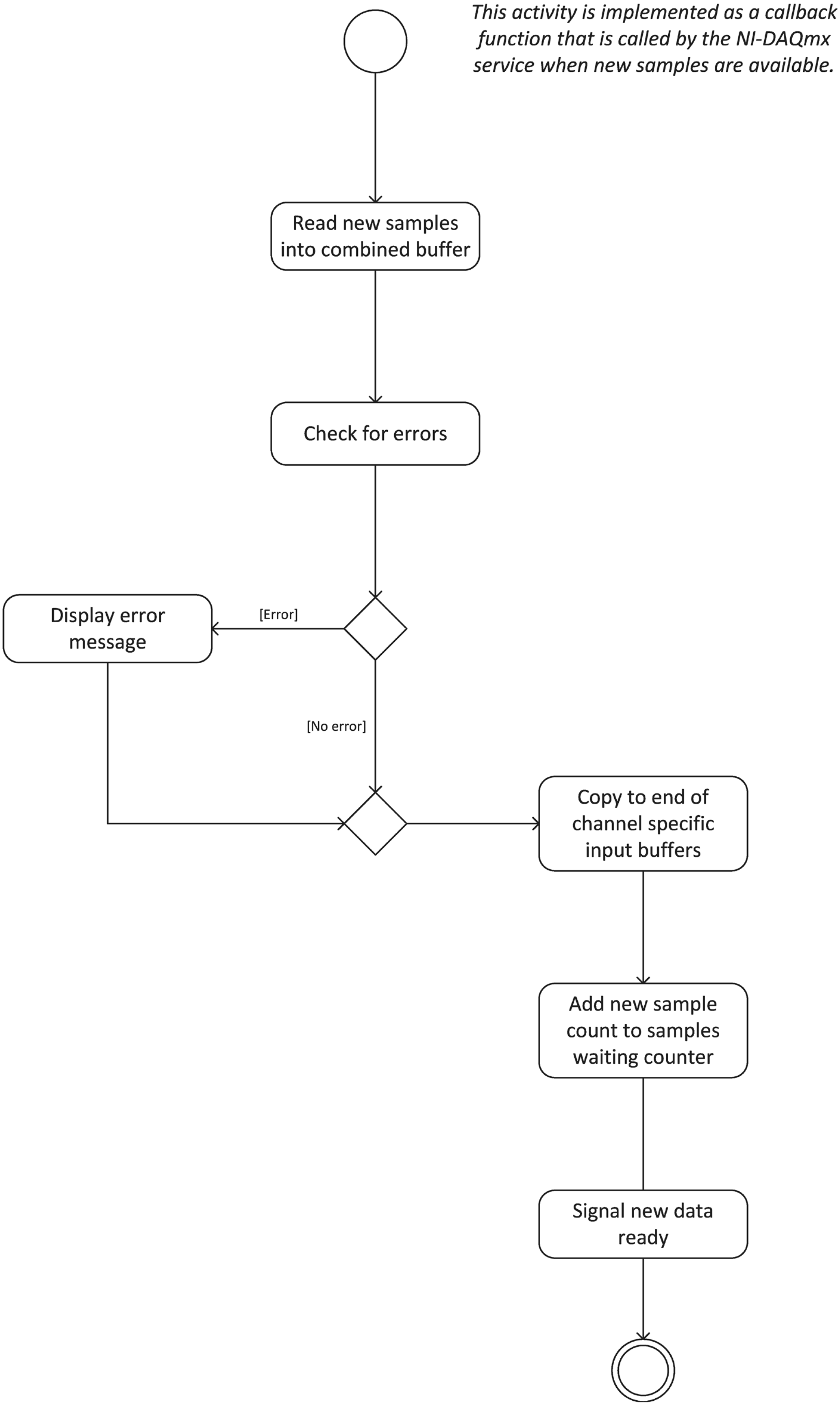

Appendix 29 – Signal processing main activity diagram

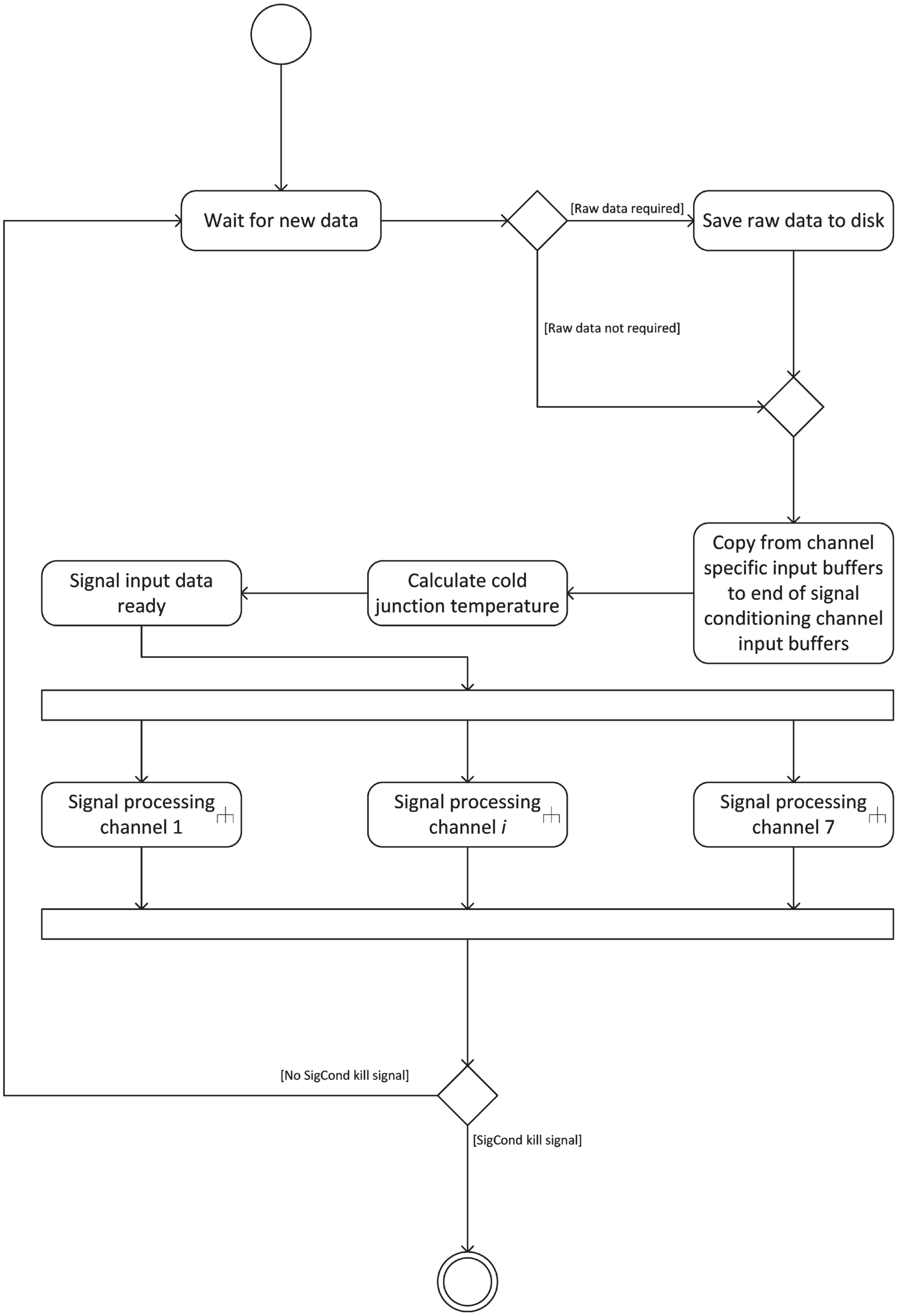

Appendix 30 – Signal processing channel activity diagram

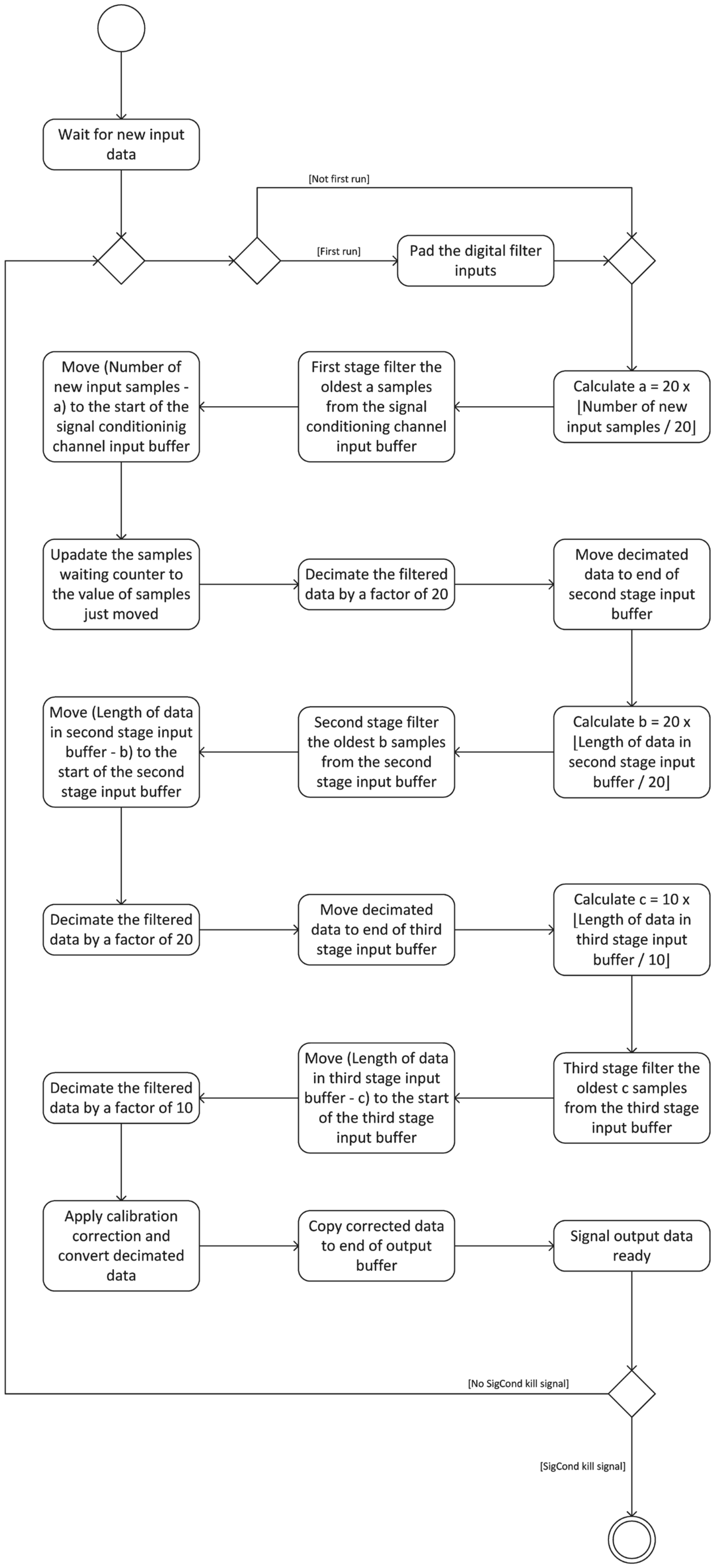

Appendix 31 – Process output activity diagram

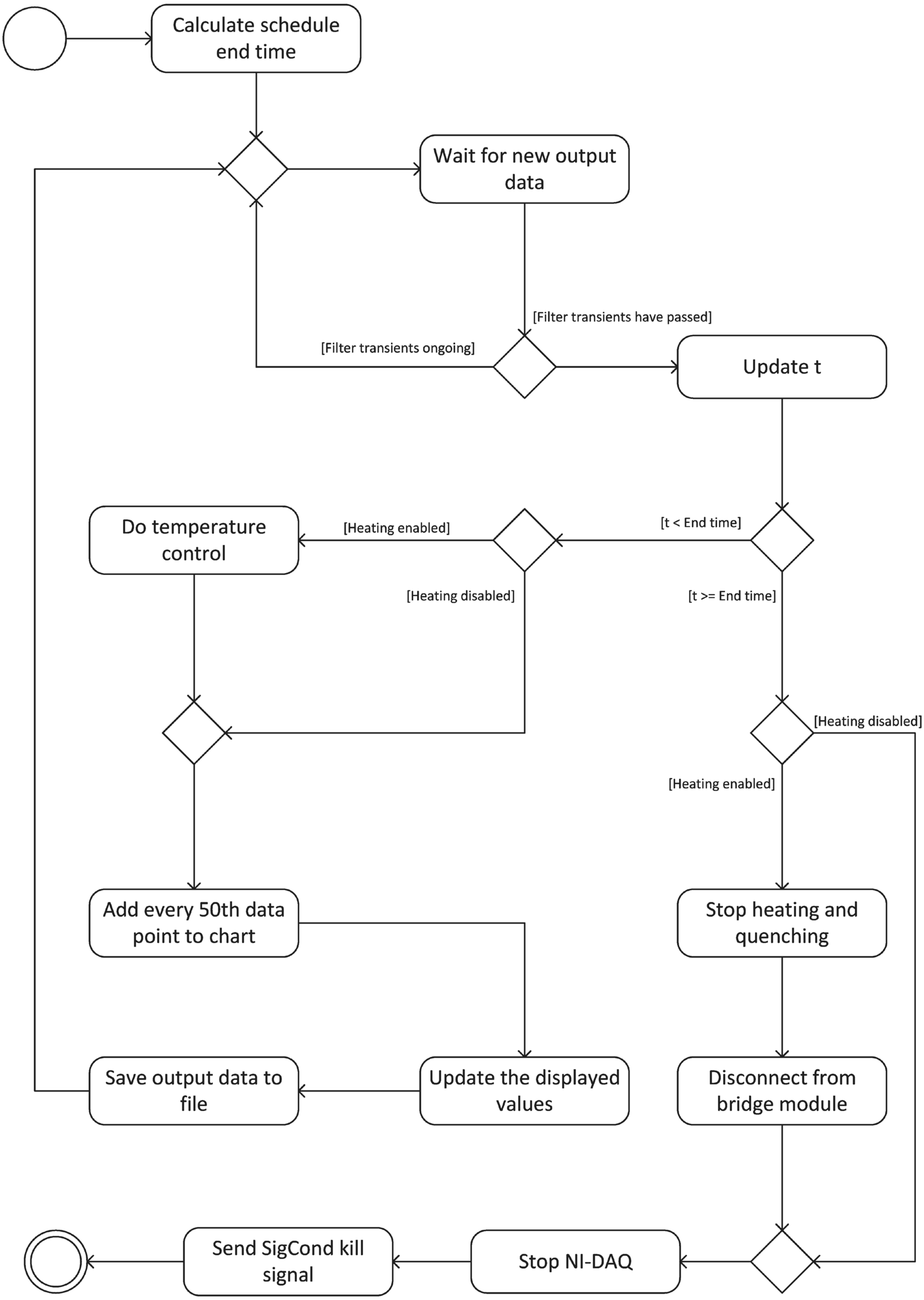

Appendix 32 – Signal processing channel data flow diagram

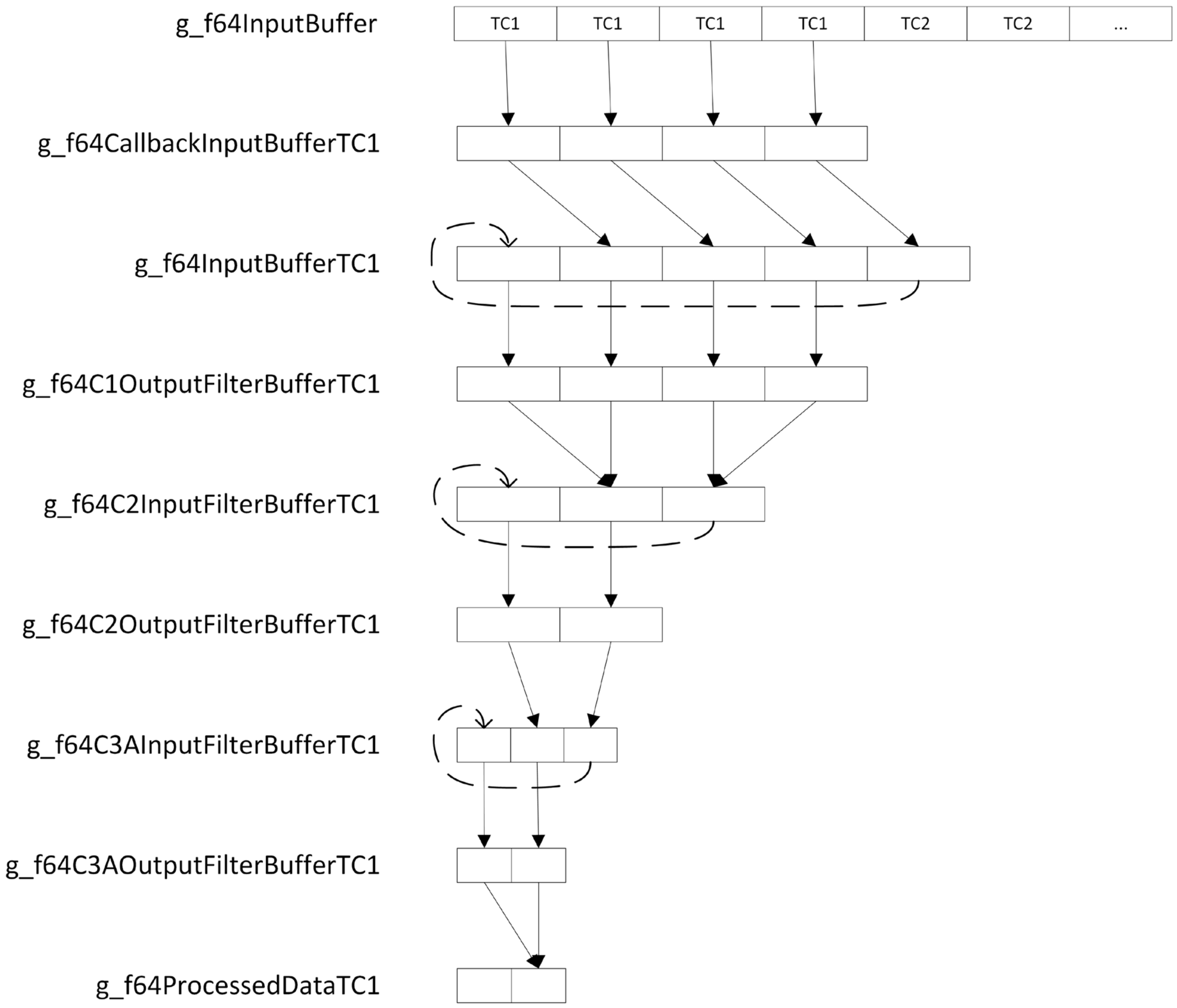

Split data by channel.

Copy data to end of local buffer.

Filter oldest integer multiple of 20 samples.
Move leftover samples to start of buffer.

Decimate by a factor of 20. Move
to end of next stage buffer.

Filter oldest integer multiple of 20 samples.
Move leftover samples to start of buffer.

Decimate by a factor of 20. Move
to end of next stage input buffer.

Filter oldest integer multiple of 10 samples.
Move leftover samples to start of buffer.

Decimate by a factor of 10. Apply
calibration correction and convert.
Move to end of output buffer.

Appendix 33 – Multirate filter combinations

Stages	MPS	Total storage	Total delay	Delay Excluding Last Stage	Decimation factors	N1	N2	N3	N4	N5	N6	N7	N8
1	3.09E+10	154651	0.386625	0	4000	154651							
2	1.31E+08	2566	0.388178	0.001577	80, 50	632	1934						
2	1.62E+08	2341	0.388483	0.001982	100, 40	794	1547						
2	2.02E+08	2237	0.389058	0.002495	125, 32	999	1238						
2	2.59E+08	2258	0.390022	0.003223	160, 25	1290	968						
2	3.27E+08	2403	0.39057	0.00407	200, 20	1629	774						
2	4.13E+08	2683	0.39203	0.005155	250, 16	2063	620						
2	6.88E+08	3826	0.395593	0.008592	400, 10	3438	388						
2	8.84E+08	4730	0.397297	0.011048	500, 8	4420	310						
2	1.55E+09	7927	0.40533	0.01933	800, 5	7733	194						
2	2.06E+09	10467	0.413275	0.025775	1000, 4	10311	156						
2	6.19E+09	31009	0.462325	0.077325	2000, 2	30931	78						
3	33124000	717	0.395987	0.008988	20, 20, 10	156	173	388					
3	40498000	722	0.39605	0.00905	25, 16, 10	196	138	388					
3	40748000	684	0.3978	0.01155	25, 20, 8	196	178	310					
3	51567250	687	0.405983	0.019983	32, 25, 5	250	243	194					
3	63229000	788	0.39638	0.00938	40, 10, 10	313	87	388					
3	63618500	701	0.40608	0.02008	40, 20, 5	313	194	194					
3	63926200	728	0.41408	0.02658	40, 25, 4	313	259	156					
3	78880000	791	0.398227	0.011977	50, 10, 8	392	89	310					
3	79072500	742	0.406353	0.020352	50, 16, 5	392	156	194					

Stages	MPS	Total storage	Total delay	Delay Excluding Last Stage	Decimation factors	N1	N2	N3	N4	N5	N6	N7	N8
3	79259200	755	0.414228	0.026727	50, 20, 4	392	207	156					
3	80887800	1090	0.463353	0.078353	50, 40, 2	392	620	78					
3	1.27E+08	924	0.406977	0.020978	80, 10, 5	632	98	194					
3	1.27E+08	1098	0.463977	0.078977	80, 25, 2	632	388	78					
3	1.59E+08	1066	0.407233	0.021233	100, 8, 5	794	78	194					
3	1.59E+08	1054	0.415233	0.027733	100, 10, 4	794	104	156					
3	1.59E+08	1182	0.464232	0.079232	100, 20, 2	794	310	78					
3	2E+08	1238	0.41562	0.02812	125, 8, 4	999	83	156					
3	2E+08	1325	0.464683	0.079683	125, 16, 2	999	248	78					
3	2.58E+08	1533	0.408423	0.022422	160, 5, 5	1290	49	194					
3	3.26E+08	1838	0.41757	0.03007	200, 5, 4	1629	53	156					
3	3.26E+08	1863	0.46657	0.08157	200, 10, 2	1629	156	78					
3	4.13E+08	2261	0.41828	0.03078	250, 4, 4	2063	42	156					
3	4.13E+08	2266	0.467655	0.082655	250, 8, 2	2063	125	78					
3	6.88E+08	3594	0.470593	0.085593	400, 5, 2	3438	78	78					
3	8.84E+08	4561	0.473548	0.088548	500, 4, 2	4420	63	78					
3	2.06E+09	10421	0.488275	0.103275	1000, 2, 2	10311	32	78					
4	17404500	430	0.407417	0.021417	10, 10, 8, 5	78	80	78	194				
4	17439200	418	0.415418	0.027917	10, 10, 10, 4	78	80	104	156				
4	26134750	450	0.40875	0.02275	16, 10, 5, 5	125	82	49	194				
4	31959750	464	0.408788	0.022787	20, 8, 5, 5	156	65	49	194				
4	32104200	447	0.417938	0.030437	20, 10, 5, 4	156	82	53	156				
4	32183800	472	0.466938	0.081937	20, 10, 10, 2	156	82	156	78				

Stages	MPS	Total storage	Total delay	Delay Excluding Last Stage	Decimation factors	N1	N2	N3	N4	N5	N6	N7	N8
4	32976800	485	0.470988	0.085987	20, 20, 5, 2	156	173	78	78				
4	39812200	471	0.41805	0.03055	25, 8, 5, 4	196	66	53	156				
4	39928800	477	0.418737	0.031237	25, 10, 4, 4	196	83	42	156				
4	39971800	482	0.468113	0.083113	25, 10, 8, 2	196	83	125	78				
4	40350800	490	0.47105	0.08605	25, 16, 5, 2	196	138	78	78				
4	40657000	515	0.47405	0.08905	25, 20, 4, 2	196	178	63	78				
4	50366000	534	0.409023	0.023022	32, 5, 5, 5	250	41	49	194				
4	62894200	564	0.41838	0.03088	40, 5, 5, 4	313	42	53	156				
4	63081800	556	0.47138	0.08638	40, 10, 5, 2	313	87	78	78				
4	63909200	682	0.48908	0.10408	40, 25, 2, 2	313	259	32	78				
4	78632800	632	0.419228	0.031727	50, 5, 4, 4	392	42	42	156				
4	78726800	618	0.471603	0.086602	50, 8, 5, 2	392	70	78	78				
4	78789000	622	0.474478	0.089478	50, 10, 4, 2	392	89	63	78				
4	79242200	709	0.489228	0.104228	50, 20, 2, 2	392	207	32	78				
4	1.27E+08	832	0.472178	0.087177	80, 5, 5, 2	632	44	78	78				
4	1.59E+08	980	0.475483	0.090482	100, 5, 4, 2	794	45	63	78				
4	1.59E+08	1008	0.490233	0.105233	100, 10, 2, 2	794	104	32	78				
4	2E+08	1176	0.475932	0.090932	125, 4, 4, 2	999	36	63	78				
4	2E+08	1192	0.49062	0.10562	125, 8, 2, 2	999	83	32	78				
4	3.26E+08	1792	0.49257	0.10757	200, 5, 2, 2	1629	53	32	78				
4	4.13E+08	2215	0.49328	0.10828	250, 4, 2, 2	2063	42	32	78				
4	8.84E+08	4552	0.499798	0.114798	500, 2, 2, 2	4420	22	32	78				
5	13894200	354	0.418535	0.031035	8, 5, 5, 5, 4	63	40	42	53	156			

Stages	MPS	Total storage	Total delay	Delay Excluding Last Stage	Decimation factors	N1	N2	N3	N4	N5	N6	N7	N8
5	16632800	358	0.419418	0.031918	10, 5, 5, 4, 4	78	40	42	42	156			
5	17036800	342	0.472368	0.087368	10, 8, 5, 5, 2	78	64	44	78	78			
5	17323000	344	0.475668	0.090667	10, 10, 5, 4, 2	78	80	45	63	78			
5	17422200	372	0.490418	0.105418	10, 10, 10, 2, 2	78	80	104	32	78			
5	25656800	365	0.47247	0.08747	16, 5, 5, 5, 2	125	40	44	78	78			
5	31733000	383	0.475888	0.090887	20, 5, 5, 4, 2	156	41	45	63	78			
5	32087200	401	0.492938	0.107937	20, 10, 5, 2, 2	156	82	53	32	78			
5	39618600	414	0.476425	0.091425	25, 5, 4, 4, 2	196	41	36	63	78			
5	39795200	425	0.49305	0.10805	25, 8, 5, 2, 2	196	66	53	32	78			
5	39911800	431	0.493738	0.108738	25, 10, 4, 2, 2	196	83	42	32	78			
5	40647000	506	0.5003	0.1153	25, 20, 2, 2, 2	196	178	22	32	78			
5	62877200	518	0.49338	0.10838	40, 5, 5, 2, 2	313	42	53	32	78			
5	78615800	586	0.494228	0.109228	50, 5, 4, 2, 2	392	42	42	32	78			
5	78779000	613	0.500727	0.115728	50, 10, 2, 2, 2	392	89	22	32	78			
5	1.59E+08	971	0.501733	0.116732	100, 5, 2, 2, 2	794	45	22	32	78			
5	2E+08	1167	0.502182	0.117182	125, 4, 2, 2, 2	999	36	22	32	78			
5	4.13E+08	2214	0.505155	0.120155	250, 2, 2, 2, 2	2063	19	22	32	78			
6	10018600	298	0.476523	0.091523	5, 5, 5, 4, 4, 2	40	40	41	36	63	78		
6	13877200	308	0.493535	0.108535	8, 5, 5, 5, 2, 2	63	40	42	53	32	78		
6	16615800	312	0.494418	0.109418	10, 5, 5, 4, 2, 2	78	40	42	42	32	78		
6	17313000	335	0.501918	0.116917	10, 10, 5, 2, 2, 2	78	80	45	22	32	78		
6	31723000	374	0.502138	0.117138	20, 5, 5, 2, 2, 2	156	41	45	22	32	78		
6	39608600	405	0.502675	0.117675	25, 5, 4, 2, 2, 2	196	41	36	22	32	78		

Stages	MPS	Total storage	Total delay	Delay Excluding Last Stage	Decimation factors	N1	N2	N3	N4	N5	N6	N7	N8
6	39902200	430	0.505613	0.120613	25, 10, 2, 2, 2, 2	196	83	19	22	32	78		
6	78606200	585	0.506103	0.121103	50, 5, 2, 2, 2, 2,	392	42	19	22	32	78		
6	2E+08	1167	0.507495	0.122495	125, 2, 2, 2, 2, 2,	999	17	19	22	32	78		
7	10008600	289	0.502773	0.117773	5, 5, 5, 4, 2, 2, 2	40	40	41	36	22	32	78	
7	16606200	311	0.506293	0.121293	10, 5, 5, 2, 2, 2, 2	78	40	42	19	22	32	78	
7	39593400	405	0.507988	0.122988	25, 5, 2, 2, 2, 2, 2	196	41	17	19	22	32	78	
8	9993400	289	0.508085	0.123085	5, 5, 5, 2, 2, 2, 2, 2	40	40	41	17	19	22	32	78

Appendix 34 – Thermocouple channel one calibration data

Nominal (V)	Input (V)	Measured (V)	Error (°C)	Calibrated (V)	Cal. Error (°C)
1E-06	897.5000E-9	383.3908E-6	64.610	792.535E-9	-0.018
5E-06	4.9035E-6	387.5117E-6	64.630	4.989E-6	0.014
10E-6	9.9210E-6	392.4736E-6	64.620	10.041E-6	0.020
39E-6	39.0026E-6	420.9362E-6	64.516	39.024E-6	0.004
790E-6	787.6655E-6	1.1558E-3	62.179	787.288E-6	-0.064
1.6E-3	1.5869E-3	1.9410E-3	59.809	1.587E-3	-0.010
2.4E-3	2.3790E-3	2.7190E-3	57.442	2.379E-3	0.021
3.2E-3	3.1730E-3	3.4989E-3	55.043	3.173E-3	0.025
4.0E-3	3.9666E-3	4.2781E-3	52.619	3.967E-3	0.001
4.7E-3	4.6682E-3	4.9670E-3	50.486	4.668E-3	-0.012
5.5E-3	5.4615E-3	5.7464E-3	48.123	5.462E-3	0.022
6.3E-3	6.2546E-3	6.5251E-3	45.689	6.254E-3	-0.019
7.1E-3	7.0485E-3	7.3046E-3	43.263	7.048E-3	-0.051
7.9E-3	7.8507E-3	8.0933E-3	40.979	7.851E-3	0.085
8.7E-3	8.6441E-3	8.8724E-3	38.566	8.644E-3	0.062
9.5E-3	9.4372E-3	9.6513E-3	36.152	9.437E-3	0.035
10.3E-3	10.2350E-3	10.4342E-3	33.656	10.235E-3	-0.064
11.1E-3	11.0289E-3	11.2141E-3	31.285	11.029E-3	-0.048
11.9E-3	11.8312E-3	12.0022E-3	28.898	11.831E-3	-0.025
13.0E-3	12.9166E-3	13.0689E-3	25.724	12.917E-3	0.060
15.7E-3	15.6058E-3	15.7100E-3	17.594	15.606E-3	-0.014
18.3E-3	18.1864E-3	18.2444E-3	9.802	18.186E-3	-0.093
20.9E-3	20.7939E-3	20.8068E-3	2.185	20.794E-3	0.071
23.5E-3	23.3744E-3	23.3415E-3	-5.569	23.374E-3	-0.005
26.0E-3	25.8548E-3	25.7783E-3	-12.928	25.855E-3	0.002

Nominal is the voltage selected on the Time Electronics 404N. Input is the voltage measured by the Agilent 34420A. Measured is the voltage output from the Quenching Simulator Control Panel. Error is the difference between the measured and input voltages multiplied by 5.92µV / °C to give an estimate of the temperature measurement error for a type R thermocouple without voltage measurement calibration. Calibrated is the thermocouple voltage calculated using the correction polynomial (equation 3.5.3) using the measured voltage. Cal. Error is the difference between the calibrated and input voltages multiplied by 5.92µV / °C.

Appendix 35 – Thermocouple channel two calibration data

Nominal (V)	Input (V)	Measured (V)	Error (°C)	Calibrated (V)	Cal. Error (°C)
1E-06	894.1000E-9	88.1429E-6	14.738	753.713E-9	-0.024
5E-06	4.9162E-6	92.2511E-6	14.753	4.915E-6	0.000
10E-6	9.9395E-6	97.1981E-6	14.740	9.926E-6	-0.002
39E-6	39.0118E-6	126.0032E-6	14.694	39.102E-6	0.015
790E-6	787.7260E-6	864.8968E-6	13.036	787.534E-6	-0.032
1.6E-3	1.5871E-3	1.6546E-3	11.402	1.587E-3	0.059
2.4E-3	2.3794E-3	2.4361E-3	9.581	2.379E-3	-0.053
3.2E-3	3.1736E-3	3.2207E-3	7.954	3.174E-3	0.039
4.0E-3	3.9670E-3	4.0035E-3	6.160	3.967E-3	-0.038
4.7E-3	4.6686E-3	4.6964E-3	4.697	4.669E-3	0.021
5.5E-3	5.4620E-3	5.4798E-3	3.019	5.462E-3	0.067
6.3E-3	6.2550E-3	6.2620E-3	1.167	6.255E-3	-0.062
7.1E-3	7.0490E-3	7.0462E-3	-0.484	7.049E-3	0.018
7.9E-3	7.8513E-3	7.8380E-3	-2.247	7.851E-3	0.005
8.7E-3	8.6446E-3	8.6213E-3	-3.935	8.645E-3	0.051
9.5E-3	9.4378E-3	9.4037E-3	-5.749	9.438E-3	-0.028
10.3E-3	10.2355E-3	10.1916E-3	-7.417	10.236E-3	0.053
11.1E-3	11.0295E-3	10.9744E-3	-9.315	11.029E-3	-0.104
11.9E-3	11.8317E-3	11.7668E-3	-10.963	11.832E-3	0.013
13.0E-3	12.9172E-3	12.8379E-3	-13.400	12.917E-3	-0.034
15.7E-3	15.6066E-3	15.4927E-3	-19.242	15.607E-3	0.068
18.3E-3	18.1873E-3	18.0390E-3	-25.063	18.187E-3	-0.022
20.9E-3	20.7948E-3	20.6117E-3	-30.921	20.794E-3	-0.062
23.5E-3	23.3755E-3	23.1590E-3	-36.572	23.376E-3	0.075
26.0E-3	25.8558E-3	25.6057E-3	-42.254	25.856E-3	-0.021

Nominal is the voltage selected on the Time Electronics 404N. Input is the voltage measured by the Agilent 34420A. Measured is the voltage output from the Quenching Simulator Control Panel. Error is the difference between the measured and input voltages multiplied by 5.92µV / °C to give an estimate of the temperature measurement error for a type R thermocouple without voltage measurement calibration. Calibrated is the thermocouple voltage calculated using the correction polynomial (equation 3.5.3) using the measured voltage. Cal. Error is the difference between the calibrated and input voltages multiplied by 5.92µV / °C.

Appendix 36 – Thermocouple channel three calibration data

Nominal (V)	Input (V)	Measured (V)	Error (°C)	Calibrated (V)	Cal. Error (°C)
1E-06	868.1000E-9	133.7610E-6	22.448	780.384E-9	-0.015
5E-06	4.8900E-6	137.7493E-6	22.442	4.845E-6	-0.008
10E-6	9.9195E-6	142.7456E-6	22.437	9.937E-6	0.003
39E-6	38.9928E-6	171.2073E-6	22.334	38.944E-6	-0.008
790E-6	787.7126E-6	905.8860E-6	19.962	787.697E-6	-0.003
1.6E-3	1.5875E-3	1.6905E-3	17.402	1.587E-3	-0.027
2.4E-3	2.3795E-3	2.4674E-3	14.849	2.379E-3	-0.072
3.2E-3	3.1735E-3	3.2471E-3	12.418	3.174E-3	0.010
4.0E-3	3.9671E-3	4.0254E-3	9.845	3.967E-3	-0.058
4.7E-3	4.6688E-3	4.7137E-3	7.591	4.668E-3	-0.098
5.5E-3	5.4621E-3	5.4936E-3	5.318	5.463E-3	0.132
6.3E-3	6.2552E-3	6.2716E-3	2.759	6.256E-3	0.069
7.1E-3	7.0493E-3	7.0510E-3	0.285	7.050E-3	0.090
7.9E-3	7.8517E-3	7.8383E-3	-2.257	7.852E-3	0.067
8.7E-3	8.6447E-3	8.6170E-3	-4.675	8.646E-3	0.136
9.5E-3	9.4380E-3	9.3949E-3	-7.273	9.438E-3	0.020
10.3E-3	10.2356E-3	10.1777E-3	-9.773	10.236E-3	0.014
11.1E-3	11.0295E-3	10.9565E-3	-12.328	11.029E-3	-0.064
11.9E-3	11.8318E-3	11.7444E-3	-14.758	11.832E-3	0.009
13.0E-3	12.9173E-3	12.8092E-3	-18.263	12.917E-3	-0.118
15.7E-3	15.6067E-3	15.4495E-3	-26.558	15.606E-3	-0.064
18.3E-3	18.1875E-3	17.9834E-3	-34.471	18.188E-3	0.000
20.9E-3	20.7950E-3	20.5428E-3	-42.606	20.794E-3	-0.113
23.5E-3	23.3757E-3	23.0773E-3	-50.406	23.376E-3	-0.004
26.0E-3	25.8561E-3	25.5135E-3	-57.871	25.857E-3	0.101

Nominal is the voltage selected on the Time Electronics 404N. Input is the voltage measured by the Agilent 34420A. Measured is the voltage output from the Quenching Simulator Control Panel. Error is the difference between the measured and input voltages multiplied by 5.92µV / °C to give an estimate of the temperature measurement error for a type R thermocouple without voltage measurement calibration. Calibrated is the thermocouple voltage calculated using the correction polynomial (equation 3.5.3) using the measured voltage. Cal. Error is the difference between the calibrated and input voltages multiplied by 5.92µV / °C.

Appendix 37 – Cold junction RTD calibration data

Cal. RTD (°C)	Cold junction RTD (°C)	Error (°C)	Calibrated (°C)	Cal. Error (°C)
21.278	22.61	1.33	21.01	-0.26
21.350	22.75	1.40	21.15	-0.20
21.398	22.81	1.41	21.21	-0.18
24.701	26.26	1.56	24.67	-0.03
24.974	26.95	1.98	25.37	0.39
25.007	26.90	1.89	25.32	0.31
25.308	27.12	1.81	25.54	0.23
25.775	26.96	1.19	25.38	-0.40
25.778	27.81	2.03	26.23	0.45
25.815	27.00	1.19	25.42	-0.40
25.830	27.96	2.13	26.38	0.55
26.060	27.96	1.90	26.38	0.32
26.087	28.01	1.92	26.43	0.34
26.142	28.88	2.74	27.30	1.16
26.257	28.66	2.40	27.08	0.83
26.386	28.96	2.57	27.38	1.00
28.308	28.94	0.63	27.36	-0.95
28.463	29.30	0.84	27.72	-0.74
28.712	29.47	0.76	27.89	-0.82
28.848	29.59	0.74	28.01	-0.83
28.924	29.72	0.80	28.15	-0.78

Cal. RTD is the temperature as measured using the calibrated RTD and Isotech milliK. Error is the difference between the temperature as measured by the calibrated and cold junction RTDs. Calibrated show the output from the calibration correction function when the temperatures in the cold junction RTD column are used for the independent variable. Cal. Error is the temperature difference between the calibrated RTD temperature and the cold junction temperature after the correction function.

Appendix 38 – Resistance measurement current calibration

DMM (I)	Measured (I)	Error (%)	Calibrated (I)	Cal. Error (%)
48.466E-3	50.829E-3	4.88	48.476E-3	0.020
105.220E-3	106.407E-3	1.13	105.203E-3	-0.016
202.076E-3	201.422E-3	-0.32	202.139E-3	0.031
279.948E-3	277.791E-3	-0.77	280.010E-3	0.022
390.491E-3	386.047E-3	-1.14	390.332E-3	-0.041
509.511E-3	503.139E-3	-1.25	509.576E-3	0.013

DMM is the current source output as measured by the calibrated DMM. Measured is the value from QSCP. Error is the difference between these two values. Calibrated is the current calculated by the correction function when the measured values are used for the independent variable. Cal. Error is the difference between the corrected values and the DMM values.

Appendix 39 – Resistance measurement voltage calibration

A_v = 64				
Input (V)	**Measured (V)**	**Error (%)**	**Calibrated (V)**	**Cal. Error (%)**
11.164E-6	348.02E-6	3017.46	38.835E-6	247.865
649.925E-6	981.023E-6	50.94	673.647E-6	3.650
12.906E-3	13.122E-3	1.68	12.870E-3	-0.282
25.839E-3	25.938E-3	0.38	25.784E-3	-0.214
38.866E-3	38.846E-3	-0.05	38.833E-3	-0.085
51.807E-3	51.668E-3	-0.27	51.838E-3	0.059
64.734E-3	64.477E-3	-0.40	64.871E-3	0.212
77.654E-3	76.908E-3	-0.96	77.559E-3	-0.122

A_v = 256				
Input (V)	**Measured (V)**	**Error (%)**	**Calibrated (V)**	**Cal. Error (%)**
11.090E-6	91.490E-6	724.96	21.872E-6	97.216
163.739E-6	242.737E-6	48.25	175.213E-6	7.008
3.268E-3	3.317E-3	1.51	3.290E-3	0.690
6.449E-3	6.327E-3	-1.90	6.336E-3	-1.754
9.730E-3	9.720E-3	-0.11	9.766E-3	0.365
12.907E-3	12.868E-3	-0.30	12.943E-3	0.286
16.187E-3	16.118E-3	-0.43	16.221E-3	0.207
19.369E-3	19.206E-3	-0.84	19.331E-3	-0.194

A_v = 1024				
Input (V)	**Measured (V)**	**Error (%)**	**Calibrated (V)**	**Cal. Error (%)**
11.061E-6	27.015E-6	144.25	14.256E-6	28.888
41.891E-6	57.692E-6	37.72	44.890E-6	7.159
817.063E-6	824.325E-6	0.89	812.630E-6	-0.543
1.595E-3	1.595E-3	-0.02	1.588E-3	-0.420
2.493E-3	2.484E-3	-0.34	2.489E-3	-0.142
3.291E-3	3.275E-3	-0.48	3.294E-3	0.118
4.088E-3	4.065E-3	-0.56	4.104E-3	0.392
4.885E-3	4.812E-3	-1.49	4.873E-3	-0.234

A_v = 4096

Input (V)	Measured (V)	Error (%)	Calibrated (V)	Cal. Error (%)
11.012E-6	10.807E-6	-1.86	10.902E-6	1.237
50.919E-6	50.425E-6	-0.97	51.146E-6	0.588
200.278E-6	197.305E-6	-1.48	200.050E-6	-0.265
399.413E-6	394.644E-6	-1.19	399.539E-6	-0.045
598.734E-6	592.099E-6	-1.11	598.767E-6	0.004
797.942E-6	789.521E-6	-1.06	797.883E-6	0.030
997.277E-6	987.001E-6	-1.03	997.278E-6	0.030
1.197E-3	1.184E-3	-1.06	1.197E-3	-0.024

A_v = 16384

Input (V)	Measured (V)	Error (%)	Calibrated (V)	Cal. Error (%)
3.042E-6	-1.326E-6	-143.60	3.751E-6	23.315
11.232E-6	6.815E-6	-39.33	11.984E-6	6.701
51.980E-6	43.996E-6	-15.36	49.586E-6	-4.605
102.735E-6	96.896E-6	-5.68	103.074E-6	0.331
154.023E-6	147.709E-6	-4.10	154.445E-6	0.274
203.509E-6	196.540E-6	-3.42	203.803E-6	0.145
254.699E-6	247.208E-6	-2.94	255.010E-6	0.122
305.135E-6	296.385E-6	-2.87	304.700E-6	-0.142

A_v = 22528

Input (V)	Measured (V)	Error (%)	Calibrated (V)	Cal. Error (%)
2E-6	3.059E-6	-1.626E-6	3.229E-6	5.574
10E-6	11.314E-6	6.540E-6	11.528E-6	1.894
37E-6	40.505E-6	34.555E-6	39.984E-6	-1.288
74E-6	75.721E-6	69.670E-6	75.622E-6	-0.131
111E-6	111.967E-6	105.591E-6	112.046E-6	0.070
148E-6	149.111E-6	142.241E-6	149.175E-6	0.043
185E-6	186.307E-6	179.312E-6	186.696E-6	0.209
222E-6	222.578E-6	214.505E-6	222.283E-6	-0.133

Appendix 40 – CAN Bus commands

Description	Identifier	Data
Module Varistor Thermal Fuse Failure	07FC003E	Byte 1: Module ID. Byte 0: 1: MOV_LN, 2: MOV_LPE.
Request Module ID and Firmware Version	0AFC0001	N/A
Set status of LED0_GPIO on Due	0AFC0002	0: Turn off. 1: Turn on. 2: Toggle.
Reset all modules	0AFC0003	0xA35DE970
Network connection periodic test message	0CFC0001	N/A
Module reset notification	0CFC0002	Byte 0: Module ID. Byte 1: Firmware Version.
Report Module ID and Firmware Version	0CFC0001	Byte 0: Module ID. Byte 1: Firmware Version.
Change in TD20 error signal. (Vacuum pumping stopped if active).	17DC0000	[b0] Fault NO. 0: No fault. 1: Fault. [b1] Normal NO. 0: Speed < 80%. Speed >= 80%. [b2] Run-up NO. 0: Pump not driven. 1: Pump driven. [b3] Valve and forevacuum NO. 0: Not state 1. 1: Pump running w/o error.
Vacuum chamber pressure reading error.	17DC0001	0: No error. 1: Measuring error. 2: Pressure under range. 3: Pressure over range. 4: Pirani gauge defective.

Description	Identifier	Data
Vacuum chamber pumping stopped due to error reading pressure.	17DC0002	0: No error. 1: Measuring error. 2: Pressure under range. 3: Pressure over range. 4: Pirani gauge defective.
Vacuum chamber venting stopped due to error reading pressure.	17DC0003	0: No error. 1: Measuring error. 2: Pressure under range. 3: Pressure over range. 4: Pirani gauge defective.
Vacuum control module communication error with I2C device.	17DC0004	Byte 0: I2C Device (0: ADC, 1: LCD, 2: Temp). Byte 1: Transfer direction (0: Read, 1: Write). Byte 2: Call location unique ID (see source code). Byte 3: Error code.
Vacuum control module I2C status error.	17DC0005	TWI Status Register.
Bridge Module buffer overflow.	17EC0001	0: Buffer A. 1: Buffer B. 2: Buffer C.
Set vacuum module operating mode.	1ADC0000	0: Manual mode. 1: Automatic mode.
~~Set vacuum gauge model for gauge one.~~	~~1ADC0001~~	~~0: Disable gauge.~~ ~~1: Voltage output.~~ ~~2: Leybold PTR90.~~ ~~3: Edwards APG100.~~
Set voltage calibration coefficient for vacuum gauge one.	1ADC0002	-1.0 < Floating point < 1.0

Description	Identifier	Data
Set voltage calibration offset for vacuum gauge one.	1ADC0003	0.5 < Floating point < 2.0
Set voltage calibration coefficient for vacuum gauge two.	1ADC0004	-1.0 < Floating point < 1.0
Set voltage calibration offset for vacuum gauge two.	1ADC0005	0.5 < Floating point < 2.0
Set chamber gas type.	1ADC0006	0: Air 1: Argon
Reset vacuum control module.	1ADC0063	0xA35DE970
~~Set vacuum module venting PID controller proportional coefficient.~~	~~1ADC0FF2~~	~~PID proportional coefficient (0 < floating point <= 10).~~
Set rotary pump status.	1BDC0000	0: Off. 1: On.
Set turbomolecular pump status.	1BDC0001	0: Off. 1: On.
Set chamber right angle valve status.	1BDC0002	0: Close. 1: Open.
Set turbomolecular pump right angle valve status.	1BDC0003	0: Close. 1: Open.
Set turbomolecular pump gate valve status.	1BDC0004	0: Close. 1: Open.
Set drain (bottom of chamber) gate valve status.	1BDC0005	0: Close. 1: Open.
~~Set argon vent proportional control valve duty cycle.~~	~~1BDC0006~~	~~0 (closed) to 1000 (fully open).~~
Set TMP cooler status.	1BDC0007	0: Off. 1: On.

Description	Identifier	Data
Command vacuum system control module PCB temperature sensor.	1BDC0030	0x{01=R;00=W}{AD}{MS}{LS}. 0x01000000: Read temperature. 0x000100AB: Set configuration to value AB. 0x01010000: Read the configuration.
Pump chamber to specified vacuum.	1BDC0FF0	Target chamber pressure (floating point).
Vent chamber to specified pressure.	1BDC0FF1	Target chamber pressure (floating point).
Stop vacuum system.	1BDC0FF2	Target chamber pressure (floating point).
Vacuum chamber pressure reading.	1DDC0000	Chamber pressure (floating point).
Vacuum chamber pumped to target vacuum.	1DDC0001	Target chamber pressure (floating point).
Vacuum chamber vented to target pressure.	1DDC0002	Target chamber pressure (floating point).
Vacuum system stop request completed.	1DDC0003	Don't care.
Vacuum system control module PCB temperature sensor data.	1DDC0030	Target chamber pressure (floating point).
Critical error message. Immediate stop.	03FC0000	Don't care.
Heating module error - heating disabled.	177C0000	0: Lost communications. 1: Insufficient coolant flow.
Enable heating.	1A7C0000	0: Disable heating. 1: Enable heating.
Enable asymmetric turn-on.	1A7C0001	0: Disable asymmetric turn-on. 1: Enable asymmetric turn-on.
Select voltage output.	1A7C0002	0: Select 1.5V output. 1: Select 4.8V output. 1: Enable asymmetric turn-on.
Set minimum heating turn-on (phase control) angle.	1A7C0003	Phase control angle (floating point).

Description	Identifier	Data
Disable heating turn-on angle automatic reset.	1A7C0004	0: Enable automatic angle reset. 1: Disable automatic angle reset.
Set heating turn-on (phase control) angle.	1B7C0000	Phase control angle (floating point).
Enable cooling fans.	1B7C0001	0: Turn off. 1: Turn on.
Get current sensor value at specified angle. Take a single reading.	1B7C0002	Phase control angle (floating point).
Get current sensor value at specified angle. Take eight readings and return the mean value.	1B7C0003	Phase control angle (floating point).
Specify phase control DAC value.	1B7C0004	DAC value (0 to 4096).
Get coolant flow switch status.	1B7C0005	
Command heating control module PCB temperature sensor.	1B7C0030	0x{01=R;00=W}{AD}{MS}{LS}. 0x01000000: Read temperature. 0x000100AB: Set configuration to value AB. 0x01010000: Read the configuration.
Current sensor data (single reading).	1D7C0002	Bytes 3 and 2 contain the integer ADC value.
Current sensor data (mean value).	1D7C0003	Bytes 3 and 2 contain the integer ADC value.
Coolant flow switch status.	1D7C0005	0: Insufficient coolant flow. 1: Sufficient coolant flow.
Heating control module PCB temperature sensor data.	1D7C0030	Target chamber pressure (floating point).
Debugging test message.	1C7C0000	Byte 0: Module ID.
Gas control module communication error with I2C device.	17BC0004	Byte 0: I2C Device (0: ADC, 1: LCD, 2: Temp). Byte 1: Transfer direction (0: Read, 1: Write). Byte 2: Call location unique ID (see source code). Byte 3: Error code.
Gas control module I2C status error.	17BC0005	TWI Status Register.

Description	Identifier	Data
Reset vacuum control module.	1ABC0063	0xA35DE970
Set inert venting gas vacuum valve status.	1BBC0000	0: Close. 1: Open.
Set inert venting gas proportional control valve duty cycle.	1BBC0001	0 (closed) to 1000 (fully open).
Set inert quenching gas vacuum valve status.	1BBC0002	0: Close. 1: Open.
Set inert quenching gas proportional control valve duty cycle.	1BBC0003	0 (closed) to 1000 (fully open).
Command gas control module PCB temperature sensor.	1BBC0030	0x{01=R;00=W}{AD}{MS}{LS}. 0x01000000: Read temperature. 0x000100AB: Set configuration to value AB. 0x01010000: Read the configuration.
Gas control module PCB temperature sensor data.	1DBC0030	Target chamber pressure (floating point).

Appendix 41 – Bridge module source code

Appendix 42 – Vacuum control module source code

Appendix 43 – Heating control module source code

Appendix 44 – Gas control module source code

Appendix 45 – Quenching simulator control panel header file

Appendix 46 – Quenching simulator control panel source code